Ingeniería e Investigación
Journal

Abbreviated Journal Title: **Ing. Investig.**

Frequency
Quarterly, three issues per year
April, August and December

Cover Layout
Carlos Andres Ortiz Valle

Proofreader
José Daniel Gutiérrez-Mendoza

Layout Artist
David Mauricio Valero

For additional information contact
revii_bog@unal.edu.co
Bogota - Colombia
April - 2023

Table of Contents

Tabla de Contenido

Research Article/Chemical, Food and Environmental Engineering http://doi.org/10.15446/ing.investig.90309

Protocol to Monitor Water Governance Based on Indicators for Rural Basins

Protocolo para monitorear la gobernabilidad del agua con base en indicadores para cuencas rurales

Carlos A. Caro-Camargo[1], Ernest Bladé i Castellet[2], D. Gerónimo Soler[3], and Juan D. Hernández[4]

ABSTRACT

The use of quality indicators guarantees the accurate monitoring of sustainability processes around the world. This work proposes a protocol to detail the indicators that make up the rural basin management index (GWI) in order to assess the degree of water management in a predominantly rural basin or region. The methodology contemplates the development of indicators to evaluate performance and its monitoring over time as the basis for planning. This research is based on the *in situ* evaluation of four municipalities within the department of Boyacá, Colombia, where there is a lack of a culture regarding the long-term planning and management of water and environmental resources. Water availability is the most sensitive factor in this context. This study raises the need for the use of monitoring systems in sustainability processes at the level of rural basins, as a result of the findings of four study cases, where processes with a low level of sustainability were evidenced.

Keywords: water supply, water availability, administration indicators, governance

RESUMEN

El uso de indicadores de calidad garantiza el seguimiento preciso de los procesos de sostenibilidad en el mundo. Este trabajo propone un protocolo para detallar los indicadores que componen el índice de gestión de cuencas rurales (IGG) con el fin de evaluar el grado de gestión del agua en una cuenca o región predominantemente rural. La metodología contempla el desarrollo de indicadores para evaluar el desempeño y su seguimiento en el tiempo como base para la planificación. Esta investigación se basa en la evaluación *in situ* de cuatro municipios del departamento de Boyacá, Colombia, donde hay ausencia de cultura de planificación y gestión a largo plazo de los recursos hídricos y ambientales. La disponibilidad del agua es el factor más sensible en este contexto. Este estudio plantea la necesidad del uso de sistemas de monitoreo en procesos de sostenibilidad a nivel de cuencas rurales, a raíz de lo encontrado en cuatro casos de estudio, donde se evidenciaron procesos con un bajo nivel de sostenibilidad.

Palabras clave: oferta hídrica, disponibilidad del agua, indicadores de gestión, gobernanza

Received: September 2th, 2020
Accepted: August 18th, 2022

Introduction

The scarcity of water in many countries of the world is not due to supply issues; it has to do with availability, either due to difficult access or lack of resources to satisfy the transportation requirements. In this sense, the quantification of flows or climatological variables for hydrological models must be accompanied, for every basin, by a comprehensive plan that guarantees the union of that supply with water availability. Colombia is listed as the fourth country with the largest number of water resources in the world (Munevar, 2015). However, the crisis generated by the availability of water resources is increasing in some regions, which is mainly due to its growing demand for agricultural, industrial, and domestic uses (Arroyave *et al*., 2012). Therefore, availability is one of the main issues in the management and use of water resources, and the existence of tools that allow for water management is of great importance for decision-making, as they contribute to the implementation of strategic actions (Ferreira, 2018). These tools may be entrusted with the quantification of flows or climatological variables used in hydrological models. These models are generated from a wide variety of software and modeling technologies that support problem-solving related to environmental planning activities (Torres-Bejarano *et al*., 2016).

[1] Civil engineer, Universidad Javeriana, Colombia. PhD in Civil Engineering, Universitat Politecnica de Catalunya, Spain. Affiliation: Full professor, Universidad Santo Tomás, Colombia. Email: carlosandrescaro@gmail.com

[2] Civil engineer, Universitat Politecnica de Catalunya, Spain. PhD in Civil Engineering, Universitat Politecnica de Catalunya, Spain. Affiliation: Full professor, Universitat Politecnica de Catalunya, España. Email: ernest.blade@upc.edu

[3] Informatics engineer, UNAD, Colombia. Master of Software, Universidad Autónoma de Bucaramanga, Colombia. Affiliation: Full professor, Universidad Santo Tomás, Colombia. Email: David.soler@usantoto.edu.co

[4] Civil engineer, Universidad Santo Tomás, Tunja, Colombia. Master of Hydro-Environmental Engineering, Universidad Santo Tomás, Colombia. Affiliation: Consulting engineer. Email: ingjuanhtorres@gmail.com

How to cite: Caro-Camargo, C. A., Bladé i Castellet, E., Soler, G., and Hernández, J. D. (2023). Protocol to monitor water governance based on indicators for rural basins. *Ingeniería e Investigación, 43*(1), e90309. http://doi.org/10.15446/ing.investig.90309

Moreover, any watershed analyzed must have a comprehensive plan that guarantees joint responsibility between its water supply and demand, which can be achieved with institutional strengthening and governance, as well as by considering factors that allow the long-term sustainability of the water resource (Jiménez, 2018). Likewise, there is a serious problem of vulnerability to flooding events, which notorious in flat areas. To this effect, it is necessary to consolidate government policies, together with State will and an action plan that allows for a path that involves the community, State institutions, and scientific organizations. The population's availability of and access to water requires a great deal of investment, both in infrastructure and in the management and handling of natural resources (Huaricallo, 2013). Education should raise awareness in the Colombian community about proper water governance, which guarantees the availability of the resource in all sectors of society, in addition to allowing its sustainable use.

Climate change harms the supply of water resources, causing potentially lasting droughts in some regions and intense rain in others (Echeverría and Cantillo, 2013). This has prompted reflection on the rational and efficient use of water resources in the world, like in macroclimatic contexts present in Colombia (Villate *et al*., 2008). Still, in Latin America, there is a puzzling situation: despite the fact that there are important studies on the number of water supply and numerous flow prediction tools based on high-resolution hydrological models, the results do not contribute to determining the state of this resource with regard to governance comprehensiveness, conflicts, resource availability, distribution, sanitation, and contamination (Granados, 2013). This exposes the existing problem in the field of water administration, which has aroused interest in different sectors of science and social development.

Additionally, in Latin America, the distribution of water availability is uneven. For example, in Mexico, underground supply indices have reached very low levels due to excess extraction, population growth, and agricultural use (González, 2016). In contrast, Brazil, Paraguay, Uruguay, and Argentina own one of the largest groundwater reserves in the world. Accordingly, South America has two of the most important hydrographic watersheds on the planet: the Amazon (Brazil) and Río de la Plata (Argentina). This is why Brazil has 53% of the water in South America and 14% of the world's water. Water availability situation in Peru is classified as "sufficient", while Brazil, Bolivia, Colombia, Venezuela, Argentina, and Chile are classified as rich countries, with indices between 10 000 and 100 000 m^3 of water per person per year (Guzmán-Arias and Calvo-Alvarado, 2013).

Furthermore, climate change interferes with the drinking water supply and sanitation services, as well as with irrigation and industrial processes (Herron and Gómez, 2010). The foregoing has important consequences on the water balance of the ground, which in turn affects the operation of the infrastructure used for the storage, regulation, and distribution of water flows.

Consequently, an increase in flows and runoff occurs, which in turn increases the risk of accidents in communities established in highly vulnerable areas, where extreme variability or reductions in supply can increase rural migration to urban areas until the operating limits of the infrastructure are exceeded, thus leading to a failure in the institutional capabilities for water administration. Likewise, the limitation of water resources can foster competition among users, which leads to an atmosphere of hostility and distrust, thus sparking conflicts over water as a vital resource (Gomez *et al.*, 2010).

Based on the conflict between scarcity, availability, and climate change, an adequate development route for the correct integral management of water resources is establishing a spatial work unit (Guzmán-Arias and Calvo-Alvarado, 2013). In this vein, due to its physical contribution base, the watershed emerges as a basic territorial unit (BID, 2012). This unit has begun to appear as a territorial or border division in many cases. However, it conflicts with the natural political divisions instituted countries or nations, which involve control over the uses of water, thus leading to contamination, *i.e.*, "upstream" damages "downstream".

The integrated administration of watersheds (MICH, by its acronym in Spanish) integrates environmental and socio-economic relations around a generalized level of the watershed through integrated administration plans and regulatory stipulations (NARBO and UNESCO, 2009). Among the strategies used, in the last couple of decades, hydrological and geological models have been developed within the framework of the physical, spatial, and temporal study of processes that take place in the watersheds based on Geographic Information Systems (GIS). These hydrological administration models allow predicting the different responses of the system to certain specific events at different time scales, as well as evaluating uncertainty and correlating the quality of water. The existence of a conceptual or high-resolution hydrogeological model does not ensure an adequate administration of watersheds, but it is a fundamental control tool (Sandoval-Moreno and Günther, 2013). Indeed, some of the most visible limitations in the development of these models at the aggregate or distributed level are the lack of information, the low quality in the execution of the model, and the difficulty of measuring uncertainty, especially during the projection of response models regarding the effects of climate change (Alegre *et al.*, 2014; Caro-Camargo and Gil-Alvarado, 2021).

One of the fundamental aspects in the GICH is institutionality, which also serves as a control mechanism (French, 2016). Since the first United Nations Conference on Water held in Mar del Plata (UN, 1977), institutional, administrative, and economic reforms have been implemented, which are aimed at watershed organizations (committees, councils, *etc.*) and national or regional regulatory authorities (BID, 2012). Thus, in some countries, these reforms have begun to take effect in terms of integrated control systems for hydrographic resources. Chile was the first to modify its water code in 1981, followed by Mexico in 1992, Colombia

in 1993, and Brazil in 1997. The latter, with the creation of water committees and water agencies, and Mexico, with the creation of watershed councils, were the first countries to create entities for the GICH. According to an analysis of MICH in 28 countries, 10 have not implemented any MICH programs or water efficiency plans or have done so without notable results; and 5 countries have partially implemented them. None of the countries analyzed has fully performed the MICH model.

Based on the above, some authors (van Leeuwen *et al*., 2012) have established a series of indicators (24) that can determine the level of sustainability in watersheds at the urban level, with the purpose of determining which aspects can influence decision-making regarding the sustainable development of water resources. This methodology is framed within an ideal of cities called *Blue Cities* (Koop and van Leeuwen, 2015), and reports on the results of said indicators are given through a *Blueprint* (van Leeuwen, 2012). As mentioned before, 25 indicators are determined from the methodology, and each indicator is evaluated from 0 to 10 from official sources. In the end, the arithmetic mean of the indicators is determined in order to establish the BCI (Blue City Index).

It is important to clarify that the BCI is compared in several studies carried out by van Leeuwen (2012) for many cities around the world, as well as other recognized indices such as the Water Exploitation Index (Eurostat, 2016), TPI (Trends and Pressures Index), the European Green City index (Dening, 2009), the World Bank Governance Indicators, the Worldwide Governance Indicators (Kaufmann, 2010), and the Environmental Performance Index (EPI) (Jay *et al*., 2010) while always maintaining adequate correlations that guarantee the suitability of the BCI. Finally, and with the aim to conduct a more specific analysis of the planning and management of water resources in rural contexts, Caro and Bladé (2021) developed a methodology represented in the GWI (Green Watershed Index). To carry out this research, a methodology was implemented which responded to approaches based on the following objectives:

-To review the state of the art regarding methodologies and procedures for evaluating water resources at the level of rural basins around the world.

-To review indicators in the GWI methodology for water management and planning of rural basins.

-To establish a specific work protocol based on the analysis of indicators and on-site experiences.

Methodology

To identify and analyze the GWI, a procedure was carried out which included the interpretation of the model and its application results in four rural municipalities of Colombia. Next, the methodology and procedures used are explained.

Analyzing the indicator of sustainability and water administration

In the last 20 years, a series of methodologies have been established in order to assess the level of sustainability of both rural and urban watersheds. They have been elaborated by determining indicators that allow identifying critical points regarding the administration of water resources, in order to create tools that help to make the best decisions for sustainable water development in the studied watersheds. The above includes the 24 indicators reflected in the Blueprint (conclusions document) (van Leeuwen, 2012), the 18 indicators in the Trends and Pressures Index, and the 30 indicators in the European Green City index, among others.

By analyzing the main indices, it is possible to establish the indicators that allow evaluating the sustainability and use of the world's water resources. Correspondingly, it is possible to understand which of the indicators could have greater relevance for the analysis in the context of rural watersheds.

To select the most relevant indicators, each of them is evaluated, analyzing the importance, development, and impact generated while considering infrastructure maintenance and water demand, quality, and scarcity, *i.e.*, the factors with the highest incidence for each index. As a result of the foregoing, an analysis was carried out regarding 25 indicators related to the quality of the drinking water service offered for a given community, whose characterization depends on various factors associated with the implementation of a supply system. The indicators to be analyzed are: (1) infrastructure maintenance, (2) sanitation, (3) risk, (4) access to water, (5) water demand, (6) water quality, (7) water scarcity, (8) water stress, (9) water footprint, (10) water self-sufficiency, (11) attention to leaks in the implemented system, (12) programs for efficient use and saving of water, (13) biodiversity, (14) environmental efficiency, (15) energy efficiency, (16) attractiveness, (17) human capital, (18) efficiency and water treatment policies, (19) measured public participation, (20) economic efficiency, (21) adaptability to climate change, (22) quality of the information and the knowledge administration system, (23) control plans and measured action, (24) government efficiency, and (25) corruption control.

It should be noted that indicators (2), (3), (4), (5), (6), (7), (18), and (24) can be understood from a perspective of risk and vulnerability; they could be associated with risk as a product of vulnerability (Sosa-Rodríguez, 2010). The description of the *Effectiveness in general water administration* (item 2 in the Table) is the result of a previous summary of indicators 2, 3, 4, 5, 6, 7, 18, and 24. Vulnerability can be defined as the inability of a population to control or handle a threat. Its importance lies in the need to consider not only the quantity but also the quality of water, based on models that allow for the identification of initial and final samples in bodies of water. Thus, after a detailed evaluation, 18 indicators are listed in Table 1.

The selected indicators are adequate for the characterization of a rural watershed within the framework of a drinking water supply system.

Each one of the indicators in Table 1 is considered to adequately evaluate, from a technical point of view, the development and planning of water resources in a rural basin, including indicators such as corruption control (18), whose specific weight is relevant in countries with problems in this regard, thus making it difficult to plan and allocate resources in all sectors, including the water sector.

According to the reference of each of the analyzed indexes, the best way to demonstrate adequate or poor management is one that can be viewed practically and easily. Therefore, we decided to follow the methodology established in the Blue Cities Index (BCI), where each factor or indicator is rated from 0 to 10 depending on the degree of compliance. In this way, a town, province, or department whose rural watersheds fully meet the objectives of each indicator will obtain an average score close to 10. In this case, the above has been established, considering the criteria shown in Tables 2 and 3.

Table 1. Definition of indicators for rural watersheds

ITEM	SOURCE	INDICATORS	DESCRIPTION
1	European green (Dening, 2009)	Infrastructure maintenance	All the technical considerations established in the resolution that grants the water concession, with regard to the hydraulic conditions of the structure, as well as the calibrations of the measurement systems.
2	WMEI (Sosa-Rodríguez, 2010)	Effectiveness in general water administration	It evaluates the supply, water quality, and coverage of the sewerage system.
3	WMVI (Sosa-Rodríguez, 2010)	Water vulnerability	It evaluates physical, economic, social, and political representation conditions.
4	WEI (Eurostat, 2016)	Water risk	Vulnerability and threat.
5	EPI (Jay *et al.*, 2010)	Water stress	It evaluates whether the demand for water resources affects supply. Water stress is considered to exist in a community when there are annual domestic uses per person between 1 000 and 1 700 m^3.
6	EPI (Jay *et al.*, 2010)	Water foorprint	The total volume of freshwater used to produce services in the area of influence.
7	EPI (Jay *et al.*, 2010)	Water self-sufficiency	Self-sufficiency is at 100% when all the necessary water is available and taken from the territory itself.
8	Required by Law 373 of 1997 (Ministerio de Ambiente, 1997)	Gestión y administración del agua	Plans for the efficient use and saving of water by sector
9	BCI (van Leeuwen, 2012)	Biodiversity	Stable ecological conditions of the source's area of influence are observed.
10	Worldwide	Environmental efficiency	Environmental compensations in the areas of direct influence of the water body from which the resource is derived.
11	BCI (van Leeuwen, 2012)	Residual treatment efficiency	Percentage of treated wastewater.
12	BCI (van Leeuwen, 2012)	Attractiveness	Water supports the quality of the rural landscape measured.
13	BCI (van Leeuwen, 2012)	Human capital	Human resources required for the optimal operation of the supply system.
14	BCI (van Leeuwen, 2012)	Measured participation of the public	Participation can be established through annual accountability meetings and community action committees.
15	WEI (Eurostat, 2016)	Economic efficiency	Monthly billing according to the estimated consumption of each user.
16	WEI (Eurostat, 2016)	Adaptability to climate change	Protection systems in flood areas.
17	WEI (Eurostat, 2016)	Quality of information and knowledge of the administration system	Files and records of compliance plans established by the environmental authority, *e.g.*, information systems in which the number of users and the demand required by them are determined; as well as records of system conditions.
18	Worldwide (Kaufmann, 2010)	Corruption control	Strategies generated to improve and supervise the performance of those who are responsible for the administration and operation of the supply system.

Source: Authors

Table 2. General score for the indicators

SCORE	EVALUATION
0-5	Not sustainable
6-8	Mildly sustainable
9-10	Sustainable

Source: Authors

Table 3. Specific evaluation of the administration criteria

SCORE	EVALUATION
0	The activity is not carried out
2	Activity planning begins
4	The operational part of the planning is completed
6	The activity is being developed for execution.
8	The activity is partially carried out
10	The activity is fully carried out

Source: Authors

It should be noted that a watershed belonging to a developed region will surely have its indicators within a highly sustainable framework, and a watershed belonging to a developing region will surely be unsustainable but will be ideally in the planning phase regarding activities to reach the desired sustainability goal.

Individual analysis of indicators

Six distinct degrees of compliance are proposed for each of the indicators. A score from 1 to 10 is assigned, whose rating depends on the quality and use of resources to offer a service. Each of these actions focuses on strategic planning and commissioning of works to satisfy basic needs related to an optimal water supply. These degrees of compliance are shown in Table 3.

Approach to the water administration index in rural watersheds GWI

Regarding the different administration indices proposed by the aforementioned authors, it is evident that these indices are mainly implemented in contexts and watersheds belonging to urban areas. Therefore, we employed those who had greater rural relevance in terms of contexts and rural watersheds and were better adapted to the Latin American reality. The 18 proposed indicators (Table 1) can provide a real overview of what is happening in a town within its rural jurisdiction, thus allowing to determine the solution or follow-up route with regard to watershed administration.

To present an overview of the quality assessment of water administration in rural watersheds, a new index called GWI (Green watersheds Index) is proposed in this work. The GWI evaluates the process of a watershed towards achieving a good service that involves biodiversity, sustainability, water resources, and social well-being.

Defining the GWI

The proposed GWI is obtained from the weighted average of the 18 proposed indicators, which are analyzed via Equation (1).

$$GWI = \frac{Pi*\left(MI + EGH + VH + RI + EH + HA + AUA + UAH + BD + EMA + ETR + A + CH + PP + ECC + ACC + CI + CC\right)}{number\ of\ indicators} \quad (1)$$

where each indicator is evaluated with a value between 1 and 10, depending on the degree of management according to each indicator in the rural region under study for a representative period of time (usually a year). If value of the denominator is equal to the number of indicators (18), it would mean that all the indicators maintain the same significant weight or importance with regard to the region analyzed. If each indicator has different values or weights, the denominator will be the sum of the weights, as shown in Equation (2), where GWI is the rural basin management index, and P is the differentiated weighting coefficient for each of the indicators according to the study area (Caro and Bladé, 2021). The following expression is proposed:

$$GWI = \frac{\sum_{i=1}^{n} F_i * P_i}{\sum P_i} \quad (2)$$

where:

GWI = rural watersheds administration index

n = number of administration indicators.

Fi = numerical result of the administration indicator i

Pi = differentiated weighting coefficient for each of the indicators according to the analyzed area

Weighting factor per indicator

The weighting factor used for each indicator represents its importance or weight within the management of a hydrographic watershed, depending on its spatial and morphometric location. Thus, the indicator of adaptability to climate change will have a greater weight if it corresponds to a watershed located in the coastal zone, in comparison with another watershed located in an area of the interior of the country with a lower morphometric accidentality (Caro, *et al*., 2021).

Results and discussion

The GWI method for the management and planning of water resources was directly implemented in four rural sectors of the Department of Boyacá, Colombia, a typical Andean

region. The conclusions drawn from the implementation of the index allowed suggesting a procedure for the application of each of the management indicators.

Experimental methodology

This chapter describes the procedure used to obtain the GWI in some rural watersheds with consolidated local governments, aiming to determine their degree of development in terms of the supervision and administration of water and environmental resources. Before selecting the watersheds, some premises were defined to give context to the subsequent presentation of results and their analysis:

1. The selected watersheds are located in Colombia, South America, in Boyacá, a department characterized by large rural areas of agricultural use, which is naturally supported by the use of water resources.

2. The human development index for Colombia was 0,764 in 2018 (PNUD, 2020). However, this index is an average, where the lowest rating is applied to rural areas or jurisdictions. Moreover, the country still does not adequately take advantage of the water and environmental potential of rural areas to improve activities such as agriculture or natural tourism.

3. The absence of knowledge regarding water control and administration in many areas or regions of Colombia generates conditions or activities that are beneficial to the communities, but it does so in an isolated or disorganized way, which makes monitoring or control over time a difficult issue, as it generates uncertainty in some indicators, or even loss of information.

The towns selected for analysis were Arcabuco, Chíquiza, Gachantivá, and Villa de Leyva, which belong to the Cane River watershed. Their general characteristics are shown in Table 4.

Table 4. General characteristics of the analyzed towns

Town	Surface (km^2)	Rural population (# hab)	Total, population (# hab)	Rural population (%)	Main economic activity
Gachantivá	66	2 290	2 654	86	Agriculture
Chíquiza	119,5	5 390	5 484	98	Agriculture
Arcabuco	155	3 279	5 240	62	Agriculture and livestock
Villa de Leyva	128	7 058	16 984	42	Tourism, agriculture, and stone, clay, and marble mining

Source: Authors

A survey regarding rural areas and watersheds was applied to the state entities in charge of territorial planning in the towns.

The information collection procedure for each of the selected towns consisted of sending communications directly to the legal representatives of the towns (*i.e.*, the mayors), while also using petition rights addressed to their respective planning and infrastructure secretaries. In these communications, the parameters of the required information are established, as well as the need to notify if it does not exist or is being procured.

Results of the experimental design

This section presents the results obtained by applying the GWI methodology given by Equations (1) and (2) for the evaluation of rural watersheds in the evaluation. It is important to keep in mind that the results are obtained from subjective information issued by the authorities of the state entities (in this case, the towns). Different values may be obtained if these indicators are applied or evaluated from an external audit entity.

For the sake of comparison, Table 5 shows the results for the four studied towns.

Table 5. Results obtained for the analyzed towns

No.	TOWN	INITIAL DATE	FINAL DATE	GWI
1	Gachantivá	01/06/2018	30/06/2018	1,00
2	Chíquiza	01/06/2018	30/06/2018	4,00
3	Arcabuco	01/06/2018	30/06/2018	3,21
4	Villa de Leyva	01/06/2018	30/06/2018	3,90

Source: Authors

The results show a predominance of rural watersheds over urban ones, as well as a lack of control in terms of community participation and the implementation of policies for the administration and use of water and environmental resources. In the case of the corruption control indicator, a high degree of subjectivity is evident, as this information is based on the perception of the community. The issue of corruption is a major concern for Colombian society, and yet it exhibits the highest value in most of the locations studied.

In the case of Gachantivá (GWI = 1,0), which is far from the maximum possible score, the local authorities recognized a lack of control in each of the topics covered by the indicators, clarifying that there is not necessarily a correlation between the activities carried out and the planning and control of said activities, which is evaluated by the index. Moreover, the results obtained for the town of Villa de Leyva (GWI =3,9) do not agree with what was expected, considering that their income from taxes and tourism is high in comparison with most rural towns in Colombia. Still, it reports an index lower than 5.0, which is surprising given its privileged condition. On the other hand, the town of Chíquiza (GWI = 4,0) shows the best overall performance, even without reaching the expected values. However, Chíquiza surpasses Villa de Leyva, the latter being a town with better conditions regarding income and annual budget capacity.

Considering the classification of populations by categories, in the case of Colombia, municipalities are classified in ranks from one to six, in addition to a special category, according to their number of inhabitants and their Free Destination Current Income (ICLD, for its Spanish acronym), following article 6 of Law 617 of 2000. In Gachantivá, there is a lack of historical control, so none of the indicators exceeds the values according with sostenibility which coincides with the category of the municipality (6^{th}). It can be assumed that the resources contributed by the nation are not designated for administration tasks of this type. It is interesting to note that Villa de Leyva, Arcabuco, and Chíquiza, towns that have historically been characterized by problems with access to water, obtained their best ratings in water stress and water self-sufficiency, with a special interest in what they consider as day-to-day deficiencies or immediate needs.

It is worth highlighting the efforts made by the town of Chíquiza towards the implementation of sustainable policies, specifically regarding wastewater treatment, in compliance with the environmental regulations given by the Colombian Ministry of the Environment. Finally, in the analyzed towns and, overall, in the rural towns of Colombia, we can anticipate that there is an absence of planning culture with regard to environmental affairs.

Implementation of the final protocol

Based on the methodology proposed in this research, it is necessary to create a protocol that articulates policies and government entities with the communities in order to ascertain the reality of the administration and use of water resources, aiming to identify the strengths and weaknesses that can be improved over time. All this, without ignoring the particularities of the studied watershed's location.

The protocol covers the identification of the watersheds and the state entities in charge of the control and/or administration of water resources while considering their hierarchy within the national regulations. In the same way, it determines the responsibility of said entities in controlling and monitoring of the indicators of the GWI, which is calculated for the area and year under study. Subsequently, once the GWI index has been calculated and communicated to the legal representative of the entity with the highest hierarchy or the one in charge of monitoring, the monitoring plan is defined and implemented for the future application and recalculation of the GWI index, as well as the improvement plans based on annual feedback with the participation of all stakeholders, including the affected communities. This shows the environmental relevance of the cooperation between all actors in the use of water resources (Caro *et al*., 2020).

This protocol could be subject to modifications depending on the context of each basin, as well as on its country, region, or potential uses. It essentially consists of the following steps:

1. Identification of the type of basin: urban, rural, or semi-rural. It is important to clarify that the proposed methodology is adapted to rural or semi-rural basins, given the characteristics of the indicators proposed for calculating the GWI.

2. Identification of the entities, corporations, or estates responsible for the control or administration of water resources within the basin or region (hereinafter labeled as *B*), as well as of the entity with the highest authority in the province or department (labeled as *A*).

3. Determination of the responsible body (A or B) with regard to the monitoring and control of the component indicators of the GWI, by means of the legal representative the region or basin under study. The responsible person within the selected location will be called *agent C* and may be a natural person or a collegiate body.

4. Delivery to agent C, via the legal representative of the region or basin, of the computational tool for calculating the GWI and the manual for monitoring or implementing it, with the corresponding explanation of each indicator.

5. Quantitative determination of the indicators of the GWI methodology

6. Determination of the GWI index for the study area and year, supported by the computational tool.

7. Socialization of the index, indicators, and procedures by agent C to bodies A and B.

8. Implementation of a monitoring plan by body A for the future determination of the annual GWI and the subsequent implementation of improvement plans.

9. Annual feedback of the processes to agent B and the community of the region or basin.

10. Training plan for the community of the region or basin with regard to the environmental benefits of cooperation between users within the different systems.

Considering that, for each indicator, it is necessary to propose a defined methodology that includes the different parameters outlined in the Technical Regulation of the RAS drinking water sector and Resolution 0330 of 2017 issued by the Ministry of Housing, City, and Territory, as well as the different conditions of the rural watershed available for the supply of water resources, there must be government entities that can provide information through tools such as censuses, which allow typifying the population that benefits from the resource. Likewise, field visits and data collection allow visual inspections and measuring the current state of the hydraulic structures of the concessions (random samples), as well as comparing this information to the indicators established by the aforementioned standard. To this effect, the real conditions of the population must be

verified (including the floating population), thus making it possible to obtain assertive data given the complexity of characterizing a specific area, whose conditions may vary according to the planning, development, and execution of works for supplying drinking water.

It is important to clarify that the implementation of the methodologies presented for each of the 18 indicators considers that the points, watersheds, or regions studied have defined governance structures. For different situations or contexts, this protocol may not have the same effect.

Conclusions

100% of the analyzed case studies obtained GWI values below the minimum acceptable sustainability established by the methodology.

None of the towns analyzed could be considered a sustainable process according to the GWI. The maximum value was obtained by the rural municipality of Chíquiza, with a weighted average of 4.1.

The results obtained for the indicators shows the need for improvement in many of the processes related to the sustainable management and use of water resources in the regions analyzed.

All of the indicators analyzed are applicable in the context of Colombian rural basins. Moreover, based on the above, a methodology for rural basins worldwide can be proposed, as none of the procedures used would generate a regional context failure.

The GWI was analyzed as a tool for measuring the degree of connectivity between the different levels at the rural basin level (upper, middle, and lower basin), its main actors (community, service providers, and the State), and the degree of management of water and environmental resources. The GWI is based on 18 indicators that are evaluated in consecutive periods of time in order to establish the degree of improvement in management over time. The index involves aspects of water and environmental management, infrastructure, biodiversity, political control, and corruption levels, and it assigns a specific weight to each indicator according to the context of the region or area.

According to the results, the proposed protocol suggests management alternatives that can be applied worldwide while considering the local context.

References

Arroyave, J. A., Builes, L. A., and Rodríguez, E. M. (2012). La gestión socio-ambiental y el recurso hídrico. *Journal of Engineering and Technology, 1*(1), 40-48. http://revistas.unilasallista.edu.co/index.php/jet/article/view/212

Banco Interamericano de Desarrollo (BID) (2012). *El reto del manejo integrado de cuencas hidrográficas: análisis de la acción del BID en programas de manejo de cuencas 1989-2010*. https://publications.iadb.org/publications/spanish/document/Nota-tem%C3%A1tica-El-reto-del-manejo-integrado-de-cuencas-hidrogr%C3%A1ficas;-An%C3%A1lisis-de-la-acci%C3%B3n-del-Banco-en-programas-de-manejo-de-cuencas-1989-2010.pdf

Caro, C. A., Bladé, E., and Gerónimo, D. (2020). *Administración del recurso hídrico: Gobernanza del agua en cuencas rurales. Índice GWI*. Editorial Académica Española. https://upcommons.upc.edu/handle/2117/192821

Caro, C. A., and Bladé, E. (2021), Water resources management: Green watershed index (GWI). *IOP Conference Series: Earth and Environmental Science*, *690*(1) 12-33. https://iopscience.iop.org/article/10.1088/1755-1315/690/1/012033

Caro-Camargo, C. A., Gil-Alvarado, L. (2021) Flood risk management contributions in localized areas. *Tecnología y Ciencias del Agua*,*12*(4), 384-420. https://doi.org/10.24850/j-tyca-2021-04-09

Ministerio de Ambiente (1997). *Ley 373 de 1997. Por la cual se establece el programa para el uso eficiente y ahorro del agua*. https://www.minambiente.gov.co/wp-content/uploads/2021/08/ley-373-1997.pdf

Dening, S. (2009). *European Green City Index*. Siemens AG. https://doi.org/www.siemens.com/greencityindex

Echeverría, J., and Cantillo, B. (2013). Instrumentos económicos para la gestión del agua. *Revista de Ciencias Ambientales, 45*(1), 13-22. https://doi.org/10.15359/rca.45-1.2

Eurostat (2016). *Water exploitation index in Europe, 310*. http://maps.eea.europa.eu/EEAViewer/?appid=eaf7bb088ba-548368c6e102c4a876c13

Ferreira, D. F. (2018). *Desarrollo de herramienta para la gestión del recurso hídrico en el embalse San Roque, Córdoba, Argentina* [Undergraduate thesis, Universidad Nacional de Córdoba]. https://rdu.unc.edu.ar/handle/11086/6452

French, A. (2016). ¿Una nueva cultura de agua?: Inercia institucional y gestión tecnocrática de los recursos hídricos en el Perú. *Anthropologica, 34*(37), 61-86. https://doi.org/10.18800/anthropologica.201602.003

González, M. G. (2016). Gestión integral de cuencas hidrográficas: una alternativa a la sustentabilidad de los recursos hídricos en México. *Lacandonia, 10*(1), 91-98. http://www.academia.edu/download/50014962/gestion_integral_de_cuencas.pdf

Granados, A. (2013). *Carbono neutralidad: Avances y desafíos de cara al año 2021. Estado de la nación en desarrollo humano sostenible, XIX Informe*. http://repositorio.conare.ac.cr/handle/20.500.12337/427

Guzmán-Arias, I., and Calvo-Alvarado, J. (2013). Planning water resources in Latin America and the Caribbean. *Revista Tecnología en Marcha*, *26*(1), 3-18. https://doi.org/10.18845/tm.v26i1.1117

Herron, C., and Gómez, R. (Eds.) (2010). *Diálogo regional de política de América Latina y el Caribe. Retos y oportunidades en adaptación al cambio climático en materia de agua: Elementos para una agenda regional*. https://cenida.una.edu.ni/relectronicos/REP40M671.pdf

Huaricallo, D. C. (2013). *Análisis de la gestión del recurso hídrico para consumo humano en la microcuenca Huancho, Huancane – Puno* [Undergraduate thesis, Universidad Nacional del Altiplano].

Jay, E., Esty, D. C., and Levy, M. A. (2010). *Environmental performance index*. http://www.energ-group.com/energy-from-waste/environmental-performance/

Jiménez, D. M. (2018). *Estado de la gestión del recurso hídrico del municipio de Cachipay (Cundinamarca) en su ámbito institucional* [Undergraduate thesis, Universidad Distrital Francisco José de Caldas]. http://hdl.handle.net/11349/13120

Kaufmann, D. (2010). *The worldwide governance indicators: Methodology and analytical issues*. http://hdl.handle.net/10986/3913

Koop, S. H. A., and van Leeuwen, C. J. (2015). Application of the improved city blueprint framework in 45 municipalities and regions. *Water Resources Management, 29*, 4629-4647. https://doi.org/10.1007/s11269-015-1079-7

Munevar, W. G. (2015). Gestión y valor económico del recurso hídrico. *Revista Finanzas y Política Económica, 7*(2), 279-298. https://doi.org/10.14718/rf&pe.v7i2.289

Network of Asian River Basin Organizations (NARBO) and UNESCO World Water Assessment Programme (2009). *IWRM guidelines at river basin level*. UNESCO.

PNUD (2020). *Informe sobre desarrollo humano. Nota informativa para los países acerca del Informe sobre Desarrollo Humano*. https://hdr.undp.org/sites/all/themes/hdr_theme/country-notes/es/COL.pdf

Sandoval-Moreno, A., and Günther, M. G. (2013). La gestión comunitaria del agua en México y Ecuador: otros acercamientos a la sustentabilidad. *Revista Ra Ximhai, 9*(2), 165-179. https://www.redalyc.org/pdf/461/46128964012.pdf

Sosa-Rodríguez, F. S. (2010). Exploring the risks of ineffective water supply and sewage disposal: A case study of Mexico City. *Enviromental Hazards Human and Policy Dimensions, 9*(2), 135-146. https://doi.org/10.3763/ehaz.2010.0016

Torres-Bejarano, F., Padilla, J., Rodríguez, C., Ramírez, H., and Cantero, R. (2016). La modelación hidrodinámica para la gestión hídrica del embalse del Guájaro, Colombia. *Métodos Numéricos Para Cálculo y Diseño en Ingeniería: Revista Internacional, 32*(3), 163-172. https://dialnet.unirioja.es/servlet/articulo?codigo=5992737

United Nations (1977). *Report of the United Nations Water Conference, Mar del Plata, 14-25 March 1977*. https://digitallibrary.un.org/record/724642

van Leeuwen, C. J., Frijns, J., van Wezel, A., and van de Ven, F. H. M. (2012). City blueprints: 24 indicators to assess the sustainability of the urban water cycle. *Water Resources Management, 26,* 2177-2197. https://doi.org/10.1007/s11269-012-0009-1

Villate, J. J., Caro, C. A., and Martínez, E. F. (2008). Efectos de los fenómenos macroclimáticos (El Niño y La Niña) sobre diferentes variables climatólogicas en Boyacá. *Vestigium Ire, 1*(1), 51. http://revistas.ustatunja.edu.co/index.php/ivestigium/article/view/51

Research Article /Chemical, Food and Environmental Engineering http://doi.org/10.15446/ing.investig.97521

Influence of the Solvent on the Extraction of Phenolic Compounds from Coffee Grounds via Soxhlet Leaching

Influencia del solvente en la extracción de compuestos fenólicos de la borra de café mediante lixiviación Soxhlet

Rafael N. Calle-Chumo[1], Diego A. Calle-Chumo[2], Aaron S. Gallegos-Peredo[3], and Pablo I. Jarrín-Oseguera[4]

ABSTRACT

In this study, phenolic compounds were extracted from the essential oil of coffee grounds originated in the coffee industry in the city of Guayaquil, Ecuador. The selected method was Soxhlet leaching, with three types of solvents (methanol, ethanol, and hexane), in its conventional form (solid-liquid), with two polar solvents and one nonpolar solvent, and in four extraction periods (30, 60, 90, and 120 minutes). The highest phenolic concentration and the best associative capacity were obtained with ethanol as the solvent for extraction, while the use of methanol yielded the second-best results. The extraction performance regarding the coffee grounds oil obtained higher results when using methanol, but close values were obtained with ethanol. Methanolic extracts obtained from coffee grounds can cause the formation of undesirable substances and be responsible for the methanolysis of gallic depsides. Therefore, the solvent-assisted technique depends on the selectivity and affinity of the compounds, according to their polar covalent character, the molecular geometry of the solvent, its relationship with its dielectric constant, and the null generation of unwanted reactions during extraction.

Keywords: coffee grounds, solvent, phenolic compounds, Soxhlet leaching

RESUMEN

En este estudio se realizó extracción de compuestos fenólicos a partir del aceite esencial de la borra de café originada en la industria cafetalera de la ciudad de Guayaquil, Ecuador. El método seleccionado fue la lixiviación Soxhlet, con tres tipos de solventes (metanol, etanol y hexano), en forma convencional (sólido-líquido), con dos solventes de carácter polar y un solvente apolar y en cuatro tiempos de extracción (30, 60, 90 y 120 minutos). La mayor concentración fenólica y la mejor capacidad asociativa se obtuvieron con etanol como disolvente de extracción, seguido por el uso del metanol. El rendimiento de extracción del aceite de borra obtuvo mayores resultados al emplear metanol, pero se obtuvieron valores cercanos con el etanol. Los extractos metanólicos obtenidos de la borra de café pueden causar la formación de sustancias no deseables y ser los responsables de la metanólisis de los dépsidos gálicos. Por lo tanto, la técnica asistida por solventes depende de la selectividad y afinidad de los compuestos de acuerdo con su carácter covalente polar, la geometría molecular del solvente, su relación con su constante dieléctrica y la nula generación de reacciones indeseadas durante la extracción.

Palabras clave: borra de café, solvente, compuestos fenólicos, lixiviación Soxhlet

Received: July 28th, 2021
Accepted: August 17th, 2022

[1] Chemical engineer, Universidad de Guayaquil, Ecuador. Master's degree in Chemical Engineering, Universidad de Chile, Chile. Affiliation: Department of Chemical Engineering, Biotechnology, and Materials, Faculty of Physical Sciences and Mathematics, Universidad de Chile, Chile. Email: rcalle@ing.uchile.cl

[2] Chemical engineer, Universidad de Guayaquil, Ecuador. Master's degree in Chemical Engineering, Universidad de Chile, Chile. Affiliation: Department of Chemical Engineering, Biotechnology and Materials, Faculty of Physical Sciences and Mathematics, Universidad de Chile, Chile. Email: dacalle94@hotmail.com

[3] PhD in General Medicine, Universidad Católica de Santiago de Guayaquil, Ecuador. Affiliation: Department of Medical Sciences, Universidad Católica de Santiago de Guayaquil, Ecuador. Email: agallegosp23@gmail.com

[4] Petroleum engineer, Escuela Superior Politécnica del Litoral, Ecuador. Master's Degree in Environmental Fluid Mechanics, Grenoble Alpes University, France. Affiliation: Department of Earth Science Engineering, Escuela Superior Politécnica del Litoral, Ecuador. Email: paisjarr@espol.edu.ec

How to cite: Calle-Chumo, R. N., Calle-Chumo, D. A., Gallegos-Peredo, A. S., and Jarrín-Oseguera, P. I. (2023). Influence of the Solvent on the Extraction of Phenolic Com-pounds from Coffee Grounds via Soxhlet Leaching. *Ingeniería e Investigación, 43*(1), e97521. http://doi.org/10.15446/ing.investig.97521

Introduction

Coffee trees are shrubs that produce fleshy fruits called *coffee cherries*, which are to date considered to be the most popular natural products. The particularity of their structure allows a glimpse into two well-known species in the coffee sector, which, when processed separately, have different organoleptic properties. Industrialization has allowed for a synergy between them, aiming to achieve the characteristic flavor and aroma of coffee (Andrade and Zapata, 2019).

Nowadays, two predominant varieties take up the whole of commercialization. The first one is called *Arabica*, whose peculiarity is its extended flattened shape, with ovals and a thin dividing line in the shape of an "S". In addition, its

properties diffuse a striking aroma, ideal in taste and quality. However, its caffeine percentage is half when compared to its rival. The second variety is *Robusta*, which is characterized by a spherical structure and a slightly straight median line. Its flavor is intense and bitter, and it has greater consistency, tentatively reducing its quality, but it has more caffeine than Arabica (Venegas *et al*., 2018).

Both varieties are detailed in Figure 1, emphasizing their physical structure so they are easily distinguished.

Currently, coffee beans are used in the preparation of drinks for frequent consumption, given their pleasant taste and smell, as well as the stimulating properties of caffeine (Carvajal, 2019). Thus, in response to the high demand for coffee, the industry is constantly growing, increasing the amount of waste generated, which reaches figures of around 6 million tons of remainder (Carvajal, 2019). Pulp, mucilage, parchment, and lint are discarded as by-products of the process. These residues are known as Spent Coffee Grounds (SCG), and they do not have commercial value, so they are disposed of through an adjusted treatment, since their content of tannins, polyphenols, and caffeine has a negative impact on the environment (Silva *et al*., 1998). However, reusing these residues has been proposed for the evaluation of phenolic compounds that represent commercial interest (Magalhães *et al*., 2016).

Figure 1. Structure of the varieties of roasted coffee: a) Arabica species (cultivation altitude between 900 and 2 000 m at temperatures of 15-25 °C), b) Robusta species (cultivation altitude between 0 and 900 m at temperatures of 20-30 °C.
Source: Authors

In light of the above, a coffee industry was selected in Guayaquil, Ecuador, which involved the industrialization of soluble coffee, since a large amount of waste is generated from coffee grounds during its processing, which constitutes an alternative source to obtain phenolic compounds. It is necessary to underline that, given the astringency of coffee, some studies have recommended the possibility of extracting phenolic compounds such as tannins. In this context, to shed light on the issues, our exploration was carried out in an instant coffee factory dedicated to manufacturing two commercial types of coffee: freeze dried (granulated) and spray dried (powder).

The method used to extract phenolic compounds plays an important role in the quality of the extract. There are various types of extraction, *e.g.*, (i) microwave-assisted extraction, (ii) ultrasonic extraction, (iii) accelerated solvent extraction, (iv) supercritical extraction, and (v) ultrasound-assisted techniques, whose extraction results are based on the phenomenon of acoustic cavitation (Soto-García and Rosales-Castro, 2016). Ultrasound induces a series of physical, chemical, and mechanical effects or impacts, causing an increased recovery rate of phenolic compounds (Rodríguez, 2020). In this study, continuous solvent extraction through Soxhlet leaching was implemented, generating the displacement of soluble substances contained in a solid of interest through mass transfer, which was caused by a highly selective solvent that avoids chemical transformations (Gutiérrez, 2017).

Ultimately, the purpose of this study is to detect the influence of the solvent during the extraction of coffee grounds and justify the best option based on its dielectric constant, the degree of intervention during the process, the cost, and the presence of unwanted reactions. Moreover, the quantitative presence of phenolic compounds is determined via UV-VIS spectrophotometry characterization and qualitative staining/precipitation tests.

Methodology

Regardless of the two varieties of the coffee bean, the harvested ripe fruit goes through a transformation process to become the so-called *green coffee*, aiming to strip the grain of the multilayers, in the following order: husk, pulp, mucilage, and parchment. Subsequently, the fruit goes through the roasting process, and the physicochemical characteristics of the accepted grain are evaluated for reception in storage silos, where they are transported to the continuous roaster to acquire their organoleptic properties. The roasting must be uniform, with a residence time of 8-12 minutes at a temperature between 240 and 260 °C, so that the output grain can reduce its humidity, obtain its characteristic structure, and vary its chemical composition (Torres-Valenzuela *et al*., 2019).

From there, the grain goes through a milling stage, where it reaches the required granulometry (300-600 µm). During solid-liquid extraction, the components of the bean, called *coffee extract*, are absorbed into the water. The accumulation of the residues is what is known as *coffee grounds*. Finally, the coffee extract must be centrifuged to enter the final

dryer, which can be done by freeze-drying or atomization (Calle and Mendoza, 2017).

In Table 1, the amounts of the by-products of the process are detailed from 1 000 g of coffee cherry.

Table 1. By-products of coffee cherry processing

Process stage	By-product	Loss (g)
Pulp removal	Pulp	394
Fermentation	Mucilage	216
Drying	Water	171
Threshing	Parchment	35
Roasting	Volatile compounds	22
Beverage preparation	Coffee grounds	104
Total Loss		942

Note: Calculation base of 1 000 g of cherry coffee with 5,8% utilized for beverage preparation
Source: Authors

Coffee grounds are the product of solid-liquid extraction, but some studies have shown that they contain 10-15% of oil on a dry basis (Calle and Mendoza, 2017). Likewise, it has been discovered that only 1% of oil is transmitted to the coffee extract, which makes it possible to work with this by-product in order to obtain phenolic compounds.

Materials and equipment

Coffee grounds (mixture of robust and arabica species in a ratio of 9:1) were obtained from a coffee industry in the city of Guayaquil, Ecuador. All reagents used were of analytical grade: lead acetate $Pb(C_2H_3O_2)_2$ reagent, gelatin-salt reagent (1% gelatin and 10% sodium chloride solution), ferric chloride ($FeCl_3$) reagent, bromine water, and distilled water. The following lab equipment was available: Soxhlet XL equipment, a Rotavapor R-1 020, a 3 840-L centrifuge, and an electric grain mill (HCP).

Sample preparation

For ten weeks, with a periodicity of three days a week, 90 kg of wet coffee grounds were collected. Then, outdoor drying was carried out on concrete surfaces with a slope of 1% in order to avoid entrapment, and, in accordance with the INEN-ISO 712:2013 standard, tests were carried out in a stove until a relative humidity of 5% was reached. In the next step, the particle size was reduced using an electric grain mill, until a granulometry between 250 and 500 µm was obtained.

Solvent selection

The polarization of a substance can be determined, as well as its ability to associate with other molecules through the relationship with its dielectric constant. For this reason, at the atomic scale, molecular polarization can be affirmed when the separation between the centers of gravity of the positive and negative charges is evidenced. For water, this condition is permanent. However, the conditions of other solvents can be predicted according to the molecular geometry of each compound. In other words, for materials or compounds formed by molecules with constant polarity, there is a common characteristic: high dielectric constants (Guadarrama, 2020).

In accordance with the above, and highlighting the use of solvents, Table 2 shows satisfactory characteristics according to the type of bond, the molecular geometry, and the dielectric constant.

Table 2. Solvent characteristics

Solvent	Polarization (bond type)	Molecular geometry	Dielectric constant
Water (H_2O)	Polar covalent (hydrogen bonds)	Angular	78,5
Methanol (CH_3OH)	Polar covalent (dipole-dipole force)	Tetrahedral	33,0
Ethanol (C_2H_5OH)	Polar covalent (dipole-dipole force)	Flat Triangular	24,0
Hexane (C_6H_{14})	Nonpolar covalent (induced dipole force)	Tetrahedral	2,0

Source: Authors

In order to thoroughly examine the factors that influence the selection of the solvent, this study provides an analysis of its intervention in the process and the possible unwanted reactions that may constitute significant hazards.

Soxhlet leaching

366 g of dry and ground residue material (coffee grounds) were selected as a sample for extraction with solvents of increasing polarity. The performance of three different solvents was evaluated: 1 000 mL of 96% Ethanol, 95% Methanol, and 97% Hexane, maintaining temperatures of 80, 67, and 70 °C respectively, in an interval of 120 minutes. Then, for each test, a mixture of solvent with oil extracted from the coffee grounds was obtained and filtered when cold. Later, the solvent was separated using the Rotavapor, and a portion of extracted oil was obtained (Torres, 2020), which was stored for subsequent qualitative and quantitative analysis (López-Bascón and Luque de Castro, 2020).

Quantitative determination of phenolic compounds

The content of phenolic compounds was determined via the Folin-Ciocalteu method, as described by Muñoz-Bernal *et al*. (2017), with some variations. 240 µL of extract were combined with 15 mL of deionized water and 3 mL of the Folin-Ciocalteu (2N) reagent for phenols. After 5 min, 3,8 mL of Na_2CO_3 (8%) and 25 mL of deionized water were added to the mixture. The absorbance was quantified at 760 nm in a UV-VIS spectrophotometer (Mettler Toledo UV7). The content was calculated from a standard of gallic acid in mg

(gallic acid equivalent, GAE) per 100 mg/L, with a regression equation and a gallic acid calibration curve. All experimental conditions and analyses were replicated three times for each extract.

Qualitative determination of phenolic compounds

In the search for phenolic compounds, this research focused on the determination of tannins, due to their high degree of interest within the industry under study. To this effect, the coffee grounds oil obtained via Soxhlet leaching was filtered and deposited in four test tubes, each one with 1 mL aliquots, in order to perform the analysis with precipitation reagents and phenolic compounds staining to identify and differentiate the tannin classification obtained during experimentation.

In the first test tube, the presence of hydrolysable compounds was investigated from a 10% solution of $Pb(C_2H_3O_2)_2$. If there is such presence, the precipitate should be white due to the lead salts linked to phenolic compounds. In the second tube, a gelatin-salt solution scanned for the presence of hydrolysable compounds by means of a white precipitate. The third tube used 10% $FeCl_3$ to detect two types of ferric salts: (i) green staining: non-hydrolysable or condensed compounds; and (ii) blue staining: hydrolysable compounds derived from pyrogallol. Finally, the fourth tube used bromine water for the detection of condensed phenolic compounds (Colina, 2016). The tests were carried out in triplicate for each solvent.

Lead acetate test

1 mL of 10% $Pb(C_2H_3O_2)_2$ was added to 1 mL of the ethanolic and methanolic extracts. Given the presence of a precipitate, the mixture must be isolated, and 5 drops of a dilution of acetic acid (CH_3COOH) must be added. All natural tannins precipitate with lead acetate in neutral solutions; the filtrate does not react with a salt that includes iron. The precipitate of flobatannins (cathekic tannins) is dissolved in diluted CH_3COOH. Finally, the gallotannins precipitate is partially or totally insoluble.

Gelatin-salt test

Three drops of gelatin-salt were added to an extract of 1 mL ethanol and 1 mL methanol. Initially, a compound in the form of a cloud appeared in the solution. Later, the mixture was placed in a centrifuge. After this process, a white precipitate was observed, which indicated the presence of tannins.

Ferric chloride test

Two drops of $FeCl_3$ were added to both, a 1 mL methanolic extract and another 1 mL ethanolic extract. With this test, if it was possible to observe a bluish-black coloration, the presence of tannins in the pyrogallol derivatives was confirmed. On the other hand, if the coloration was green, it meant that the tannins came from catechin.

Bromine water test

Five drops of bromine water were added to two extracts: 1 mL of methanol and 1 mL of ethanol. In this test, it was possible to verify the presence of a cathekic tannin if a precipitate formed.

Results and discussion

Extraction performance

For the extraction of the coffee grounds oil, three different solvents with increasing polarity were used: hexane, ethanol, and methanol. This, in order to determine the highest extraction yield for a 120-minute interval according to the solvents' boiling point. Thus, the first extraction method, which involved hexane, recorded a low yield close to 7% and reported the presence of nonpolar secondary metabolites (Mena-Valdés *et al*., 2015). In the second extraction (ethanol) the presence of polar-related compounds was evidenced, achieving almost 3,3 times the yields of hexane. Finally, methanol extraction surpassed the previous values. Table 3 shows the values achieved by each extract based on the final residence time for the extraction of waste.

Table 3. Solvent extraction performance

Solvent	Yield	Residence time
Hexane	7,2% ±0,11a	120 min
Ethanol	23,8% ±0,27b	120 min
Methanol	27,1% ±0,27b	120 min

Note: Evaluated with a Tukey statistical test with 5% significance
Source: Authors

Finally, based on the results, the yield obtained with the methanolic extract was the highest. Most of the substances or components present in the coffee grounds show an affinity with the methanol compound. However, due to the methanolysis of gallic depsides, this compound is not recommended (Marcelo-Díaz *et al*., 2017). It is also worth noting that the yield percentage measures the number of compounds related to the polar nature of the solvents used for extraction.

Quantitative analysis: UV-VIS spectrophotometry

To compare the effect of the solvents, the influence of their dielectric constant and the type of bond can be evidenced. Average phenol values were obtained from all Soxhlet extraction values. The methanolic extracts showed higher content of polar compounds, while the ethanolic ones had a higher amount of phenolic compounds. In addition, the extracts with hexane were rich in highly unstable, polyunsaturated fatty acids (Corona-Jiménez *et al*., 2016). The results for the total phenol content of the solvents showed significant differences when comparing the extraction times (90 and 120 minutes *vs.* 60 minutes). In the samples with hexane, there were extraction difficulties, which is explained

by its low affinity to hydrophilic compounds, given their nonpolar covalent character. Similarly, there is an influence of the polarity of the solvent on the extraction process. Thus, the highest phenolic compounds were obtained in samples with ethanol. This value decreased during the extraction with methanol, and it remained constant in hexane, with lower values in comparison with the other two solvents.

All experiments were carried out in triplicate for each extract.

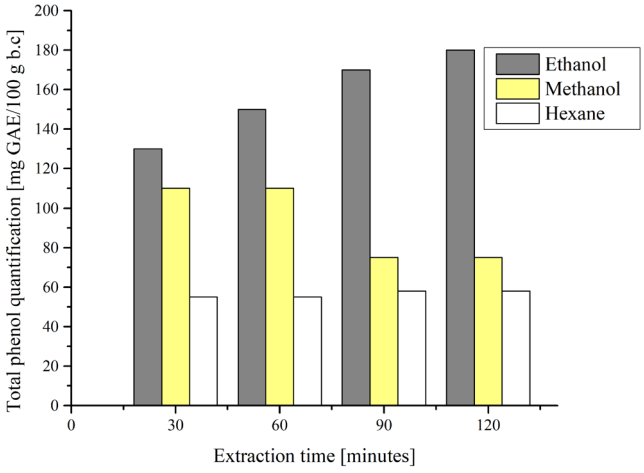

Figure 2. Effect of the solvents during four periods of extraction of phenolic compounds from coffee grounds by means of the Soxhlet method
Source: Authors

The results show a significant difference between the phenolic compounds of the ethanolic and methanolic extracts for different extraction periods. These compounds, which are present in coffee grounds, are characterized by their polar nature. Similarly, the liquid-solid ratio was set for the three types of solvent extraction, and the optimal conditions were an extraction time of 90 min and a 96% ethanol concentration. In comparison with other publications (Marcelo-Díaz *et al.*, 2017), ethanol turned out to be an optimal alternative for the extraction of phenolic compounds, which is due to its polar affinity. Moreover, when it is assisted by ultrasound, an increase in extraction yields can be achieved. Table 4 shows the univariate analysis of variance conducted in order to confirm the influence of the solvent on the Soxhlet-assisted extraction.

Table 4. Univariate analysis of variance

Origin of variations	Sum of squares	Degrees of freedom	Average of squares	F	Probability	Critical F-value
Between groups	20 994	2	10 497	30,68	9,57101E-05	4,26
Within groups	3 079	9	342,1111			
Total	**24 073**	**11**				

Note: One-way ANOVA for three extraction solvents
Source: Authors

The groups in the Table are made up of the three solvents: ethanol, methanol, and hexane. The contrasted hypothesis for the study from the unifactorial ANOVA (H_0) and establishes that there are no significant differences between the solvents. However, the results indicate a probability (P) lower than 0,05, which allows rejecting the null hypothesis. Moreover, since F is greater than the critical F-value, the results obtained from the tests are significant. Similarly, to give greater clarity regarding the choice of the optimal solvent, Table 5 complements the results of the ANOVA with a statistical analysis assisted by the Tukey test.

Table 5. Statistical Tukey analysis

	MeanDiff	SEM	q-Value	Probability	Alpha	Sig.	LCL	UCL
Methanol-Ethanol	-67,5	13,08	7,29878	0,00154	0,05	1	-104,016	-30,984
Hexane-Ethanol	-100,5	13,08	10,86707	8,0804E-05	0,05	1	-137,016	-63,984
Hexane-Methanol	-33	13,08	3,56829	0,07596	0,05	0	-69,516	3,516

Note: If Sig. is equal to 0, the difference of the means is not significant at the 0,05 level. If Sig. is equal to 1, the difference of the means is significant at the 0,05 level.
Source: Authors

By comparing the treatments used, it is observed that the difference between means the corresponding to Methanol-Ethanol and Hexane-Ethanol are large. Therefore, with $p<0,05$, both pairs represent different treatments, which is why ethanol is considered to be the optimal solvent, as it differs significantly with respect to the value of its means. Similarly, Figure 3 shows the data distribution for each solvent extract and the means obtained in triplicate with each extraction method.

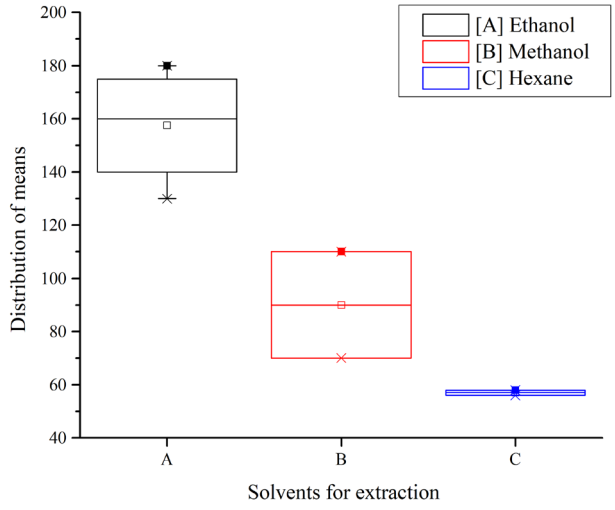

Figure 3. Box-and-whisker plot for three extracts
Source: Authors

Qualitative analysis: coloration and precipitation

For the qualitative identification of the phenolic compounds called *tannins*, this study was framed in the use of ethanolic and methanolic extracts, discarding the extract with hexane

because of its nonpolar affinity. Consequently, given the varieties of phenolic compounds, the study focuses on hydrolysable tannins, as they undergo hydrolysis in the presence of acids, enzymes, and basic media in a polyol or sugar added to the phenolcarboxylic acid. Subcategories are established in relation to the acid used: gallotannins (gallic acid) and ellagitannins (ellagic acid).

Table 6. Qualitative determination of phenolic compounds (tannins)

Extracts	Reagent	Results	Inspection/ verification
Ethanolic extract	Gelatin-salt	-	Absence of precipitate
	Lead acetate	-	Absence of precipitate
	Ferric chloride	+++	Dark green precipitate
	Bromine water	+++	Precipitate
Methanolic extract	Gelatin-salt	-	Absence of precipitate
	Lead acetate	-	Absence of precipitate
	Ferric chloride	++	Green precipitate
	Bromine water	+	Precipitate

(+) Scarce presence, (++) moderate prescence, (+++) abundant presence, (-) not detected
Source: Authors

When precipitated in bromine solutions and treated with acids at high temperatures, the condensed tannins from catechol generate a gradual green polymerization. In this way, the analyses indicate the presence of phenolic compounds such as tannins in coffee grounds, both for ethanolic and methanolic extracts. However, it is clear that there is a greater amount of total phenols in ethanol, which makes it possible to discard the use of methanol as an extraction solvent in this context.

Conclusions

The criterion for selecting the optimal solvent involved a high selectivity or affinity towards polar compounds. Therefore, based on the relationship with its dielectric constant, water is considered an ideal solvent, since soluble compounds (hydrolysable tannins derived from pyrogallol) and their ability to associate with other molecules have been extracted in the different stages of coffee processing. Although the use of methanol has a higher dielectric constant and extraction efficiency, it can cause of the formation of toxic substances and the methanolysis of gallic depsides. Hexane is not favorable either, given that if the dielectric molecules have a temporary dipole moment (nonpolar molecules), their association capacity tends to decrease due to their dielectric constant. In addition, hexane is considered one of the toxic alkanes due to the physiological effect caused by the products of its metabolization. One of them is 2,5-hexadione, which reacts with essential amines and is a neurotoxic agent. Thereupon, ethanol was established as the optimal solvent in this study, in view of its ease of handling, lower toxicity, polar covalent character, relevant dielectric constant, absence of unwanted reactions, and increased yield of phenolic compounds during extraction.

To date, a wide variety of procedures have been used for the purpose of extracting phenolic compounds, but most of them begin with extraction by organic solvents or with some mixture involving them. In particular cases, it is possible to combine and calculate the capacity of a mixture of solvents to induce a dipole moment, since the dielectric constant of the system depends on the constants of each of the substances and their percentage in the mixture. However, harmful effects may be caused by their synergy. Complementary alternatives are needed to improve solvent-assisted extraction on an industrial scale, so as to increase the yield and quality of the extracts. There is a constant search for the correct process variables, as the use of this technology is subject to industrial objectives and operating conditions.

Finally, the solvent-assisted extraction of phenolic compounds constitutes a viable and innovative alternative use of coffee grounds. The results of the one-way ANOVA indicated the influence of the solvent in the extraction process. The null hypothesis was rejected for two reasons: a sufficiently low probability and a very large variability relationship, where F was greater than the critical F-value. In addition, the Tukey test and the box-and-whiskers diagram allowed selecting ethanol as the optimal solvent for the leaching of coffee grounds, given the increased yield of phenolic compounds obtained with a residence time of 120 minutes, which shows promise for subsequent tannin applications in parallel industries.

References

Andrade, H., and Zapata, P. (2019). Desempeño ecofisiológico de café (*Coffea arabica* L.) CV. Castillo a la sombra en San Juan de Rioseco, Colombia. *Revista de Investigación Agraria y Ambiental, 11*(1), 15-27. https://doi.org/10.22490/21456453.2915

Calle, D., and Mendoza, J. C. (2017). *Extracción de taninos de la borra de café mediante lixiviación Soxhlet* [Undergraduate thesis, Universidad de Guayaquil]. http://repositorio.ug.edu.ec/handle/redug/18205

Carvajal, S. (2019). *Aprovechamiento de los desperdicios del café para la elaboración de una Kombucha* (*Medusomyces Gisevi*) *a partir de borras de café* [Undergraduate thesis, Universidad de Guayaquil]. http://repositorio.ug.edu.ec/handle/redug/47059

Colina, A. (2016). *Análisis fitoquímico, determinación cualitativa y cuantitativa de flavonoides y taninos, actividad antioxidante, antimicrobiana de las hojas de "Muehlenbeckia hastulata* (*J.E.Sm*) *I.M. Johnst" de la zona de Yucay* (*Cusco*) [Undergraduate thesis, Universidad Nacional Mayor de San Marcos]. http://cybertesis.unmsm.edu.pe/handle/20.500.12672/7121

Corona-Jiménez, E., Martínez-Navarrete, N., Ruiz-Espinosa, H., and Carranza-Concha, J. (2016). Extracción asistida por ultrasonido de compuestos fenólicos de semillas de chía (*Salvia hispanica* L.) y su actividad antioxidante. *Agrociencia, 50*(4), 403-412.

Guadarrama, A. (2020). *Análisis molecular de la constante dieléctrica en función de la tensión superficial de un fluido polar* [Undergraduate thesis, Universidad Autónoma del Estado de México]. http://hdl.handle.net/20.500.11799/109304

Gutiérrez, L. (2017). *Estudio del tratamiento de minerales sulfurados auríferos mediante procesos secuenciales de flotación, lixiviación alcalina, biolixiviación y cianuración para la recuperación de oro* [Undergraduate thesis, Universidad Nacional Mayor de San Marcos]. http://cybertesis.unmsm.edu.pe/handle/20.500.12672/6616

Instituto Ecuatoriano de Normalización. *NORMA TÉCNICA ECUA-TORIANA NTE INEN-ISO 712:2013*. https://www.normalizacion.gob.ec/buzon/normas/nte-inen-iso-712.pdf

López-Bascón, M. A., and Luque de Castro, M. D. (2020). Soxhlet Extraction. In C. F. Poole (Ed.), *Liquid-Phase Extraction* (pp. 327-354). Elsevier. https://doi.org/10.1016/B978-0-12-816911-7.00011-6

Magalhães, L. M., Machado, S., Segundo, M. A., Lopes, J. A., and Páscoa, R. N. (2016). Rapid assessment of bioactive phenolics and methylxanthines in spent coffee grounds by FT-NIR spectroscopy. *Talanta, 147*, 460-467. https://doi.org/10.1016/j.talanta.2015.10.022

Marcelo-Díaz, R., Luján-Gonzales, V., Ramírez, L., Olano, M., Vargas, A., Rojas, M. L., and Linares, G. (2017). Fenólicos a partir de residuos de café: Optimización del proceso de extracción. *Revista de Investigaciones Altoandinas, 19*(4), 405-410. https://dx.doi.org/10.18271/ria.2017.315

Mena-Valdés, L., Tamargo-Santos, B., Salas-Olivet, E., Plaza-Paredes, L. E., Blanco-Hernández, Y., Otero-González, A., and Sierra-González, G. (2015). Determinación de saponinas y otros metabolitos secundarios en extractos acuosos de *Sapindus saponaria* L. (jaboncillo). *Revista Cubana de Plantas Medicinales, 20*(1), 106-116.

Muñoz-Bernal, O., Torres-Aguirre, G., Núñez-Gastélum, J., de la Rosa, L., Rodrigo-García, J., Ayala-Zavala, J., and Álvarez-Parrilla, E. (2017). Nuevo acercamiento a la interacción del reactivo de Folin-Ciocalteu con azúcares durante la cuantificación de polifenoles totales. *TIP, 20*(2), 23-28. https://doi.org10.1016/j.recqb.2017.04.003

Rodríguez, D. (2020). *Compuestos fenólicos en residuos agroforestales: Una revisión de técnicas de extracción y fuentes disponibles* [Master's thesis, Universidade da Coruña]. http://hdl.handle.net/2183/27189

Silva, M. A., Nebra, S. A., Silva M. M., and Sanchez, C. G. (1998). The use of biomass residues in the Brazilian soluble coffee industry. *Biomass and Bioenergy, 14*(5), 457-467. https://doi.org/10.1016/S0961-9534(97)10034-4

Soto-García, M., and Rosales-Castro, M. (2016). Efecto del solvente y de la relación masa/solvente, sobre la extracción de compuestos fenólicos y la capacidad antioxidante de extractos de corteza de *Pinus durangensis* y *Quercus sideroxyla*. *Maderas. Ciencia y Tecnología, 18*(4), 701-714. https://doi.org/10.4067/S0718-221X2016005000061

Torres, A. (2020). *Rendimiento y caracterización física y química de la oleorresina Foeniculum vulgare (Miller:1769) hinojo extraída mediante el método Soxhlet con solventes etanol y hexano* [Undergraduate thesis, Universidad Nacional José María Arguedas]. http://repositorio.unajma.edu.pe/handle/123456789/593

Torres-Valenzuela, L., Martínez, K., Serna-Jimenez, J., and Hernández, M. (2019). Secado de pulpa de café: condiciones de proceso, modelación matemática y efecto sobre propiedades fisicoquímicas. *Información Tecnológica, 30*(2), 189-200. https://doi.org/10.4067/S0718-07642019000200189

Venegas, S., Orellana, D., and Pérez, P. (2018). La realidad Ecuatoriana en la producción de café. *Revista Científica Mundo de la Investigación y el Conocimiento, 2*(2), 72-91. https://doi.org/10.26820/recimundo/2.(2).2018.72-91

Research Article/Chemical, Food, and Environmental Engineering http://doi.org/10.15446/ing.investig.95432

Evaluation of the Biostability of Elodea (*Egeria densa*) and Orange Peel as Bioadsorbent Materials for Pb (II) and Cr (III) in Solution

Evaluación de la bio-estabilidad de la Elodea (*Egeria densa*) y la cáscara de naranja como bio-adsorbentes de Pb (II) y Cr (III) en solución

Adriana C. Melo-Páez[1], Silvia Y. Narvaéz-Flórez[2], Carmen S. Mosquera-Vivas[3], and Maria J. Calvo-Saad[4]

ABSTRACT

A variety of plant-based materials can be used in innovative methods to treat water pollution through bio-adsorption. This work evaluated, under lab conditions, the presence of native microorganisms in orange peel (OP) and elodea (*Egeria densa*, ELO), the aerobic degradation and biostability of the bio-adsorbents, and the contribution of microorganisms to the bio-adsorption of Pb (II) and Cr (III). The microbial characterization and biostability of OP and ELO were conducted using 2 g of dried bio-adsorbent and a solution of the metallic ions at 450 mg/L. ELO had a larger number of bacteria, fungi, and yeast than OP. After 2 hours of contact with a 450 mg/L Pb (II) and Cr (III) solution, this value decreased by 80-86% in both bio-adsorbents. After 25 days, the microorganisms showed adaptation to the Pb (II) and Cr (III) concentrations. According to the bio-degradation test, OP had a stability of over 7,01 months, while that of ELO was 2,61 months, with a CO_2 value of 1 439,9 mg after 46 days of incubation. The microorganisms tolerated a high metal concentration, but they did not contribute significantly to Cr (III) bio-adsorption in ELO. The microorganisms present in the adsorbents affect the stability of the materials, as the bio-adsorbents provide a nutrient-rich substrate. OP had higher bio-stability and could be used in pilot tests for the treatment of metal-polluted water.

Keywords: bioadsorption, chromium, lead, biodegradation, biostability

RESUMEN

Diversos materiales de origen vegetal pueden utilizarse en métodos innovadores para tratar la contaminación del agua mediante la bioadsorción. Este trabajo evaluó, en condiciones de laboratorio, la presencia de microorganismos nativos en la cáscara de naranja (CN) y elodea (*Egeria densa*, ELO), la degradación aeróbica, la bioestabilidad de los bioadsorbentes y la contribución de los microorganismos en la bioadsorción de Pb (II) y Cr (III). La caracterización microbiana y la estabilidad de CN y ELO se determinaron con 2 g de bioadsorbente seco y una solución de los iones metálicos a una concentración de 450 mg/L. ELO presentó un mayor número de bacterias, hongos y levaduras que CN. Después de 2 horas de contacto con una solución de 450 mg/L de Pb (II) y Cr (III), este valor disminuyó en 80-86% en ambos bioadsorbentes. A los 25 días, los microorganismos mostraron adaptación a las concentraciones de Pb (II) y Cr (III). Según el ensayo de biodegradación, CN presentó una estabilidad de más de 7,01 meses, mientras que la de ELO fue de 2,61 meses, con un valor de CO_2 de 1 439,9 mg a los 46 días de incubación. Los microorganismos toleraron una alta concentración de los metales, pero no contribuyeron significativamente a la bioadsorción del Cr (III) en ELO. Los microorganismos presentes en los adsorbentes afectan a la estabilidad de los materiales, ya que los bioadsorbentes proporcionan un sustrato rico en nutrientes. CN presentó una mayor bioestabilidad y puede ser utilizada en pruebas piloto para el tratamiento de aguas contaminadas con metales.

Palabras clave: bioadsorción, cromo, plomo, biodegradación, bioestabilidad

Received: May 2th, 2021
Accepted: May 25th, 2021

[1] Universidad ECCI, Environmental Engineering Department. Affiliation: GADES research group. E-mail: adrianac.melop@ecci.edu.co

[2] Universidad ECCI, Environmental Engineering Department. Affiliation: GADES research group. E-mail: narvaezflorez@gmail.com

[3] Universidad ECCI, Environmental Engineering Department. Affiliation: GADES research group. E-mail: cmosquerav@ecci.edu.co

[4] Universidad ECCI, Environmental Engineering Department. Affiliation: GADES research group. E-mail: calvo.maria@ecci.edu.co

How to cite: Melo-Páez, A., Narvaéz-Flórez, S., Mosquera-Vivas, C., and Calvo-Saad, M. (2023). Evaluation of the Biostability of Elodea (*Egeria densa*) and Orange Peel as Bioadsorbent Materials for Pb (II) and Cr (III) in Solution. *Ingeniería e Investigación, 43*(1), e95432. http://doi.org/10.15446/ing.investig.88403

Introduction

Metals are considered to be one of the major pollutants of water resources around the world. They are used in various industrial processes, and several tons of waste per year end up in effluents that reach different water sources (Chakraborty *et al*., 2020; Bilal *et al*., 2021). Metals are found naturally in the Earth's crust and are essential in several biochemical processes. However, some of them,

such as cadmium (Cd), lead (Pb), mercury (Hg), chromium (Cr), and copper (Cu), are toxic even at low concentrations and have no known specific biological role (Ballardo de la Cruz *et al*., 2015; Beltrán-Pineda and Gómez-Rodríguez, 2016; Mustapha and Halimoon, 2015). Metal toxicity leads to biological and chemical degradation within ecosystems, affecting environmental and public health (Suárez and Reyes, 2002; Bilal *et al*., 2021).

Pb is a persistent pollutant of environmental interest. It is biomagnified through the different links in the food chain and causes long-term damage (Bedoya-Vélez *et al*., 2019). It inhibits enzymatic activity and affects nucleic acid and protein conformation, as well as cell membrane functions (Jarosławiecka and Piotrowska-Seget, 2014). It can replace metallic ions such as Zn, Ca, and Fe in enzymes that are important for microbial metabolism (Naik and Dubey, 2013). High concentrations of Pb have been found up to a value of 250 ppm (Jarosławiecka and Piotrowska-Seget, 2014) in the effluents derived from industrial activities such as lead battery manufacturing, welding, metal refining, weapons manufacturing, the automotive industry, power plants, and waste incineration, among others (Fernández *et al*., 2020; Naik and Dubey, 2013).

On the other hand, Cr is a transition metal that is found in different oxidation states. The most common states are Cr (VI) and Cr (III). Hexavalent chromium, Cr (VI), is considered toxic and is soluble, but it is rare in nature given its high oxidation state. Trivalent chromium, Cr (III), is less mobile but is frequently present in soil and water samples (Cervantes *et al*., 2001; Mandina *et al*., 2013). For instance, concentrations of Cr (III) up to 450 ppm have been found in tanneries (Pinzón-Bedoya and Cardona-Tamayo, 2010), especially in small industries that lack physicochemical wastewater treatments. These levels exceed the maximum permissible limits established in national environmental legislation (Resolution 0631 of 2015) (Cardona-Guitiérrez *et al*., 2013). Cr (III) interacts electrostatically with anionic groups in DNA phosphates, producing DNA transcription errors and causing mutagenesis. Additionally, Cr (III) affects enzyme structures (Cervantes *et al*., 2001; Joutey *et al*., 2015; Viti *et al*., 2013).

The presence of toxic metals in water sources has driven the development of different water treatment methods. Conventional methods include membrane filtration, electrodialysis, reverse osmosis, nanofiltration, and ultrafiltration (Cervantes *et al*., 2001; Chakraborty *et al*., 2020; Joutey *et al*., 2015; Viti *et al*., 2013). However, electrochemical methods, ionic exchange, precipitation, and recovery by evaporation are expensive techniques and only remove 1 and 100 mg/L of metals (Özer and Özer, 2003). Some methods are costly due to equipment maintenance costs, and state-of-the-art technology is generally too expensive for companies that operate at a local scale. Thus, efforts have been made over the past several years to design alternative biotechnological processes that efficiently remove toxic metals and are easy to operate, widely available, and relatively cheap. One of the alternatives for industrial wastewater decontamination is the use of several types of biomass from plant-based agro-industrial waste as bio-adsorbents. Bioadsorption is defined as the ability to retain metallic ions (adsorbate) present in a liquid phase (solvent) on a solid surface (adsorbent) (Ballardo de la Cruz *et al*., 2015). For instance, elodea (*Egeria densa*, ELO) is a submerged freshwater plant that is found in lakes. This plant is able to take up nutrients from the body of water and perform photosynthesis even with low amounts of CO_2 and light, which makes it highly efficient at colonizing different ecosystems, to the point where it has been deemed an invasive species in many bodies of water (Rimac *et al*., 2018; Yarrow *et al*., 2009). Currently, there are few studies on the use of ELO for metal removal, but, in one study, it was able to remove nearly 91% of Pb (II) from an aqueous solution (Hernández-Gómez *et al*., 2017).

Other potential bio-adsorbents are coconut husk, saw dust-based biochar, and seed composite, which have been used to remove metallic ions from mining effluents and water bodies with an effectiveness between 75 and 96,36% (Fernández *et al*., 2020; Mahour *et al*., 2022; Manyuchi *et al*., 2022). *Cassia fistula* seeds and three different surfaces of modified adsorbent materials retained between 13,22 and 129,3 mg/g of Pb (II) at pH equal to 5,0 and 30 minutes of contact (Hemavathy *et al*., 2021). Orange peel (OP) has been used as a bioadsorbent for Pb, Fe, Cu, Zn, and Cr, with adsorption percentages between 67,2 and 99,5%, where pH and particle size play an important role in the metal retention of the adsorbent surface (Cardona-Guitiérrez *et al*., 2013; Fernández *et al*., 2020; Patiño-Saldivar *et al*., 2021). The removal of contaminants from solutions has also been investigated using tea waste, modified diatomite and bentonite, and the Metal Organic Framework (MOF) to adsorb dyes, metals, and pharmaceutical compounds. For example, carbon from tea waste was able to remove 120,13 mg/g of methylene blue, and UiO- 66 MOF adsorbed 30 mg/g of Cr (VI) and 485,4 mg/g of the pharmaceutical waste diclofenac sodium (Patil *et al*., 2022; Sriram *et al*., 2022a, 2022b; Rego, Sriram, *et al*., 2021a; Rego, Kuriya, *et al*., 2021b; Uthappa *et al*., 2020).

The use of biomaterials provides multiple benefits, as it repurposes solid waste, aids in the management of invasive species, and eliminates pollutants of environmental concern. Furthermore, bioadsorbents are efficient materials in the removal of metals and have a high biodegradation capacity, which is an advantage when they must be disposed of after use (Ojuederie and Babalola, 2017). When considering the use of biomaterials within water treatment systems, it is important to consider their biodegradation and stability in the design features.

During biodegradation, the materials' intrinsic biodegradability behaves as a function of time due to the occurrence of reactions dependent on the interaction with microorganism communities, temperature, and humidity, among other factors (Pischedda *et al*., 2019). Microorganisms

responsible for the biodegradation process can be present in plant matrices, as well as in the effluents to be treated. Through different mechanisms, the microorganisms fragment biomaterials into simpler compounds that are necessary for their metabolic processes (Polman *et al*., 2019). During biodegradation, the carbon present in a material is transformed or mineralized, aerobically or anaerobically, into products such as biomass, water, carbon residues, and carbon dioxide (CO_2), as shown in Equation (1) (Chinaglia *et al*., 2018).

$$C + O_2 \rightarrow CO_2 + H_2O + C_{residual} + C_{biomass} \quad (1)$$

Respiration involves an electron transfer chain from one carrier to another, in which organic compounds (bioadsorbents) act as electron donors to the final electron acceptor (O_2). This chain yields adenosine triphosphate (ATP) and CO_2, among other substances. ATP provides the necessary energy to produce molecular compounds involved in growth, maintenance, and reproduction (Vanrolleghem *et al*., 1999). Biomass is the result of long-term microbial reproduction (Chinaglia *et al*., 2018), while CO_2 and H_2O tend to be the final products of mineralization. Aerobic respiration generates the chemical energy used by microorganisms for their vital functions through the use of organic substrates as electron donors and oxygen as the last electron acceptor (Vanrolleghem *et al*., 1999).

Respirometry techniques can therefore be used to calculate the cumulative production of CO_2 over time, using traps with alkaline solutions such as sodium hydroxide (NaOH) and potassium hydroxide (KOH). The amount of CO_2 generated via microorganism respiration is quantified by titrating the quantity of base that has not reacted with carbon dioxide (Castro-Aguirre *et al*., 2017; Pellizzari-Wielewski *et al*., 2014). This provides a quantification of the materials' biodegradability, which is linked to the ability of organic materials to maintain their physical and chemical properties over time (or biostability). Inevitable changes in the adsorbents' structure lead to a loss of the material's active function (Lemaire, 1997), which highlights the importance of considering these two aspects (biodegradability and biostability) for the scaling of real polluted water treatment systems using biomaterials.

Additionally, bacteria, depending on their morphology, have different mechanisms that influence pollutant absorption (Verma *et al*., 2021). Gram-positive bacteria interact with metals at the extracellular level through electrostatic attraction (Joutey *et al*., 2015; Suárez and Reyes, 2002) to exopolysaccharides conformed of macromolecules as polysaccharides, proteins, and nucleic acids (Naik and Dubey, 2013; Sajna *et al*., 2021). Functional groups such as peptidoglycan carboxylate and teichoic acid phosphate, components of the cell wall, act as anionic sites that bond with the metal cations Pb (II) and Cr (III) (Diep *et al*., 2018; Pérez-Bou *et al*., 2018; Ojuederie and Babalola, 2017; Yin *et al*., 2019). Gram-negative bacteria also have mechanisms of extracellular interaction with metals via through electrostatic attraction (Joutey *et al*., 2015; Suárez and Reyes, 2002), in which functional groups such as phosphoryl in lipopolysaccharide and the components of the external membrane are responsible for the union with metal cations (Pb (II), Cr (III)) (Jarosławiecka and Piotrowska-Seget, 2014; Kadukova, 2016; Naik and Dubey, 2013).

The biostability of bioadsorbents is a poorly studied but important aspect of the design of wastewater treatment with alternative materials. Thereupon, the objectives of this study were 1) to isolate native microorganisms that were tolerant of metals such as Pb (II) and Cr (III), 2) to determine the biostability and biodegradation of plant-based ELO and OP bioadsorbents, and 3) to evaluate the contribution of tolerant microorganisms to metal removal from aqueous solutions.

Materials and methods

Obtaining the bioadsorbents

Orange peel (OP) was obtained from a local market, and elodea (ELO) was collected from Simón Bolivar Metropolitan Park. Both plant-based materials were washed with abundant water and dried at room temperature. The bioadsorbents were chopped into pieces no larger than 1 cm^2 and dried again at room temperature. Then, the bioadsorbents were dried in an oven at 50 °C to constant weight. Each of the plant-based materials was ground in a hand crank mill and sifted to obtain a particle size between 2 000 and 500 µm. The bioadsorbents were then stored in sealed plastic bags at room temperature (Castañeda-Figueredo *et al*., 2022).

Microbial characterization of the bioadsorbents

Microbial characterization of the plant-based materials was performed in order to identify native microorganisms in each bioadsorbent and establish whether they contained microbial strains resistant to Pb (II) and Cr (III). The microorganism concentration in OP and ELO was quantified using the plate count method. Macroscopic morphological characterization (morphotypes) was based on the shape and color of the colony. Subsequently, a test of the microorganisms' resistance to metals in the bioadsorbents over time was done. In this assay, a Pb (II) and Cr (III) solution at 450 mg/L was added to OP and ELO. After 2, 600, and 1 104 hours of contact between the bioadsorbents and metallic ions, the microbial concentration was determined using serial dilutions (from $1x10^{-2}$ to $1x10^{-6}$) and cultures via the plate spread method. Bacteria and fungi were isolated with nutrient agar (NA) (Ben-David and Davidson, 2014) and Sabouraud agar or potato dextrose agar (PDA), respectively. Cultured agars were incubated at 30±1 °C for 24 hours for bacteria and at 25 °C for 3 to 5 days for fungi. All tests were performed in duplicate.

The morphotypes that were most dominant and tolerant of Pb (II) and Cr (III) were selected to be individually isolated in NA using the streaking method, and they were preserved at 4 °C.

Biodegradation and stability study of the bioadsorbents

An incubation test was used to determine the biodegradation of ELO and OP as a function of the microorganisms' metabolic activity by quantifying CO_2 production (respirometry tests). The bio-adsorbents were incubated separately in hermetic glass jars with a 500 mL capacity. At the bottom of each jar, two smaller jars or vials were placed: one (amber) with 10 mL of sterile distilled water to maintain the humidity of the medium, and another one containing 2 g of dried bioadsorbent and 8 mL of a Pb (II) and Cr (III) solution at 450 mg/L (M1) (Figure 1). Controls consisted of 2 g of sterilized plant-based material and 8 mL of distilled water (M2), an empty glass jar (M3), and 8 mL of the Pb (II) and Cr (III) solution (M4). The CO_2 that evolved during the incubation test was trapped with 20 mL of NaOH 1 N placed in 30-mL vials on the upper part of the jar. All setups were evaluated in duplicate. The M1 setup was incubated for 46 days for ELO and 60 days for OP. Control tests M2, M3, and M4 were analyzed three times during the assay (beginning of the test, middle of the test, and end of the test), according to the time established for each matrix. All incubations were performed at room temperature (20±1 °C).

The CO_2 that evolved during the incubation test was quantified by mixing 2 mL of NaOH from each sample with 5 mL of barium chloride $BaCl_2$ 0,5 M. The NaOH that did not react to the CO_2 was titrated with hydrochloric acid (HCl) 0,5N (Equations (2)-(4)).

$$2NaOH_{(aq)} + CO_{2(g)} \rightarrow Na_2CO_{3(aq)} + H_2O_{(l)} \quad (2)$$

$$Na_2CO_{3(aq)} + BaCl_{2(aq)} \rightarrow BaCO_{3(s)} + 2NaCl_{(aq)} \quad (3)$$

$$NaOH_{(aq)} + HCl_{(aq)} \rightarrow NaCl_{(aq)} + H_2O_{(l)} \quad (4)$$

Figure 1. Respirometry setup for biodegradation and stability of bioadsorbents
Source: Authors

The stability of bioadsorbents in terms of the product lifespan was established according to Leejarkpai *et al*. (2011). The theoretical amount of CO_2 ($ThCO_2$) in grams was computed according to Equation (5), and the biodegradation percentage for ELO and OP was obtained from the produced amount of CO_2, as shown in Equation (6):

$$ThCO_2 = M_{TOT} \times C_{TOT} \times \frac{44}{12} \quad (5)$$

$$Biodegradation(\%) = \frac{(CO_2)_T - (CO_2)_B}{ThCO_2} \times 100\% \quad (6)$$

where $ThCO_2$ is the theoretical amount of CO_2 that each bio-adsorbent can produce (g); M_{TOT} is the amount of dried solids (g) added at the beginning of the test; C_{TOT} is the ratio of total organic carbon present in the samples' dried solids; 44 and 12 are the molecular weights of CO_2 and carbon, respectively; $(CO_2)_T$ is the accumulated amount of CO_2 (g) released from each setup; and $(CO_2)_B$ is the accumulated amount of CO_2 from the blank (g).

Biostability was estimated through a zero-order kinetic equation, as shown in Equation (7) (Pinchao-Pinchao *et al*., 2019).

$$(B) = (B_0) + k_0 t \quad (7)$$

where (B) is the percent biodegradation at time t, (B_0) is the initial percent biodegradation, and k_0 is the constant velocity.

Pb (II) and Cr (III) bioadsorption

The bioadsorption of Pb (II) and Cr (III) over time was evaluated in ELO with and without the predominant and metal-tolerant morphotypes (B1, B2, and B3). ELO was used for this test because it had more microorganisms than OP. The bioadsorption of Pb (II) and Cr (III) was tested using three treatments (T1, T2, and T3) in 100 mL Erlenmeyer flasks. Treatment 1 (T1) consisted of 1 g of sterilized ELO with 45 mL of a Pb (II) and Cr (III) solution at 50 mg/L, and an aliquot (5 mL) of each bacterium with a cell concentration of 0,550 of absorbance –approximately $5{,}8x10^8$ cells according to the McFarland scale (EB1, EB2, and EB3). The bacteria were isolated separately through colony suspension in peptone water, followed by a reading in the spectrophotometer at a wavelength of 600 nm. Treatment 2 (T2) consisted of 1 g of sterilized bioadsorbent with 50 mL of the metal solution (MEL). Treatment 3 (T3) was prepared with an aliquot (5 mL) of each bacterium and 45 mL of the metal solution (MB1, MB2, and MB3). In T3, the nutrient broth was provided as a carbon source to support the bacteria's metabolism. All of the treatments were kept at room temperature (20±1 °C) under constant agitation at 120 rpm for 5 days. Every 12 hours, two tests were retrieved for each treatment, and the solution was filtered through 0,45 µm membranes. The filtrates were

preserved with nitric acid (HNO_3) at 65%, and the metals were quantified via atomic absorption spectrophotometry. For each assay, a microbial growth control was performed which consisted of a streaking culture in AN and Sabouraud agar or PDA. The control was verified every 24 hours throughout the test. The adsorbed quantity and removal percentages were calculated using the following Equations:

$$q_t = \frac{mg\ of\ adsorbed\ Cr\ or\ Pb}{kg\ of\ bioadsorbent} \quad (8)$$

$$\%\,Removal = \frac{m_0 - m_f}{m_0} \times 100\% \quad (9)$$

where q_t is the amount adsorbed (mg/kg), m_0 is the initial mass of the metal ions, and m_f is the final mass of metal ions.

The adsorption kinetics of Pb (II) and Cr (III) in ELO were fit to two linear forms of kinetic reaction models (*i.e.*, pseudo-first-order and pseudo-second-order equations) (Tran *et al.*, 2017).

$$ln\left(q_e - q_t\right) = k_1 \times t + ln\left(q_e\right) \quad (10)$$

$$\frac{t}{q_t} = \left(\frac{1}{q_e}\right) \times t + \frac{1}{k_2 \times q_e^2} \quad (11)$$

where q_e is the amount of adsorbate uptake per mass of adsorbent at equilibrium, k_1 (1/time) is the rate constant of the pseudo-first-order equation, and k_2 (mass/mass x time) is the rate constant of the pseudo-second-order model.

Statistical analysis

A one-way ANOVA (analysis of variance) was used to determine whether there were any statistically significant differences between the means of Pb (II) and Cr (III) bioadsorption and the results of plant-based materials biodegradation. The normality, homogeneity, and multiple comparisons of means were evaluated with Shapiro-Wilk, Levene, and Tukey tests. All statistical analyses were performed with the OriginPro software and considered an alpha-value of 0,05.

Results and discussion

Microbial characterization of the bioadsorbents

ELO had a higher abundance of microorganisms than OP (Figure 2). Without metals, the ELO had 6,84x10^6 CFU/g of bacteria and 7,35x10^5 CFU/g of fungi and yeast. After 2 hours of contact with the Pb (II) and Cr (III) solution, there was an 80% decrease in both groups. In the absence of metals, OP had 5,50x10^2 CFU/g of bacteria and 1,00x10^3 CFU/g of fungi and yeast, and there was an 86,0% decrease in bacteria and an 84,3% decrease in fungi and yeast after 2 hours of contact with metals.

Exposure to the Pb (II) and Cr (III) solution clearly inhibited microbial growth. After 2 hours of contact, toxic metals can disable cell enzymes, causing irreversible damage and modifying the active conformation of biological molecules (Beltrán-Pineda and Gómez-Rodríguez, 2015), leading to a decrease in the number of viable organisms.

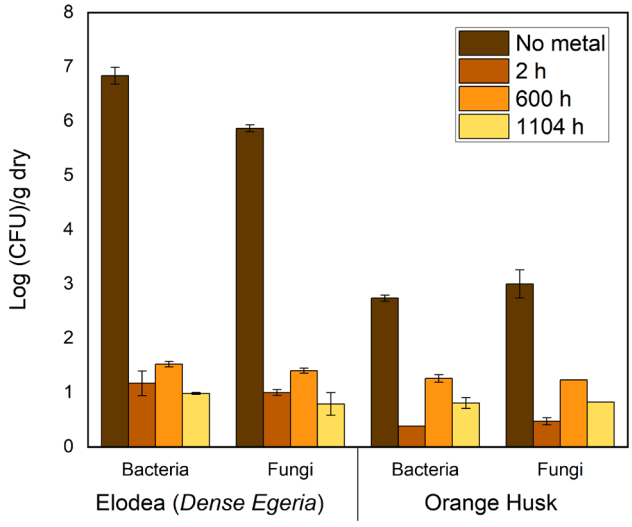

Figure 2. Average count (log) for bacteria, fungi, and yeast in ELO and OP bioadsorbents in the presence and absence of Pb (II) and Cr (III) (450 mg/L)
Source: Authors

Although the number of microorganisms decreased in the presence of metals over time, there was an apparent microbial adaptation in both bioadsorbents after 600 h of contact with the Pb (II) and Cr (III) solution. This demonstrates an active metabolism, in which the nutrients present in ELO and OP act as the main source of carbon and energy (Mehrotra *et al.*, 2021). The easily biodegradable and available organic substrates stimulate microbial growth and respiration (Guerrero-Ortiz *et al.*, 2012) since they are the source of carbon and nitrogen (Table 1) for microorganisms. Macronutrients used as a source of nitrogen are important elements for the synthesis of nucleic acids, phospholipids, protein, and stabilization of the cell wall in the microbial cell.

There was microbial growth in the presence of Pb (II) and Cr (III) over the full course of the test, possibly due to the development of tolerance and/or resistance mechanisms in the microorganisms. These aspects allowed the survival of several strains under the conditions of their environment (*e.g.*, humidity, pH, temperature), including the presence of toxic elements (Yin *et al.*, 2019; Muñoz-Silva *et al.*, 2019). Based on the observed microbial growth in ELO over 60 days, three bacterial morphotypes were identified which were tolerant to Pb (II) and Cr (III). All three formed round colonies, which were pink (B1), yellow (B2), or white (B3). In the case of OP, there was little microbial growth compared to ELO.

With respect to fungi, there was mycelial growth with sporulation starting on day 19 for OP (with black pigments) and on day 25 for ELO (with white pigments and radial growth between 1 and 3 cm). The proliferation of fungi –especially those with morphologies with 1 to 3 cm of growth– can be problematic for filter design because they can plug filters, obstructing the flow of water to be treated. There may be viable alternative treatments using fungi that take advantage of their contaminant-adsorption properties (*e.g.*, using pulverized biomass), but further investigation of those possibilities is needed.

Table 1. Nutrients present in ELO and OP on a dry basis are used by microorganisms as a source of carbon and other nutrients

		ELO	OP	Sources
Carbon source		Organic matter 84-75%	Carbohydrates in 21,40%	Mora-Ortiz (2009); Virreira-Flores and Góngora-Pereira (2014); Correa et al. (2003); Ulloa-Espinosa (2012); Cerón-Salazar and Cardona-Alzate (2011)
		Organic carbon 28,90%	Protein 8,60%	
		Ethereal extract 10,90%	Neutral sugars 3,80	
Other nutrients	P	1,90 g kg-1	21 mg/100 g	
	K	15,60 g kg-1	21,20 mg/100 g	
	Ca	27,60 g kg-1	27,34 mg/100 g	
	S	3,20 g kg-1	-	
	Mg	4,90 g kg-1	8,64 mg/100 g	

Biodegradation and biostability of the bioadsorbents

Measuring CO_2 via respirometry tests is a reliable method for quantifying microorganisms' metabolic activity, as it measures microbial respiration, which is indispensable for the cell's vital functions. Figures 3a, 3b, and 3c show the CO_2 evolution and microbial growth in the bioadsorbents ELO and OP over time, respectively. According to CO_2 production, ELO presented the highest microbial activity. After 46 days of incubation, 1 439,9 mg of CO_2 were found in M1 (ELO + metals at 450 mg/L), followed by M2 (ELO + sterile distilled water) with 114,4 mg of CO_2. The control samples (M3 and M4) had a low production of CO_2. As for OP, CO_2 production was 114,4 mg in M1, 44 mg in M3, and 33 mg in M2 and M4 (Figures 3a and 3b) after 60 days of incubation. The amount of CO_2 in ELO (M1) ranged between 200,75 and 870,65 mg from day 5 to day 19. Then, it showed high microbial growth, with bacterial counts of 10^6 up to 10^8. For OP, M1 showed an increase in CO_2 from 11,0 mg to 544,5 mg between days 5 and 32 (Figure 3b). The values of CO_2 for both bioadsorbents evidenced the active metabolism of bacteria, fungi, and yeast. Furthermore, there were bacteria present ($3{,}6 \times 10^3$ CFU) in the sterilized (M2) ELO material, indicating the presence of high-temperature-resistant spores. However, by day 28, there was no microbial growth because no nutrients were included to allow their growth (Beltrán-Pineda and Gómez-Rodríguez, 2015). Meanwhile, OP did not show significant microbial growth on day 0. The behavior of CO_2 over time is explained by bacterial growth, which was higher in ELO (Figure 3c).

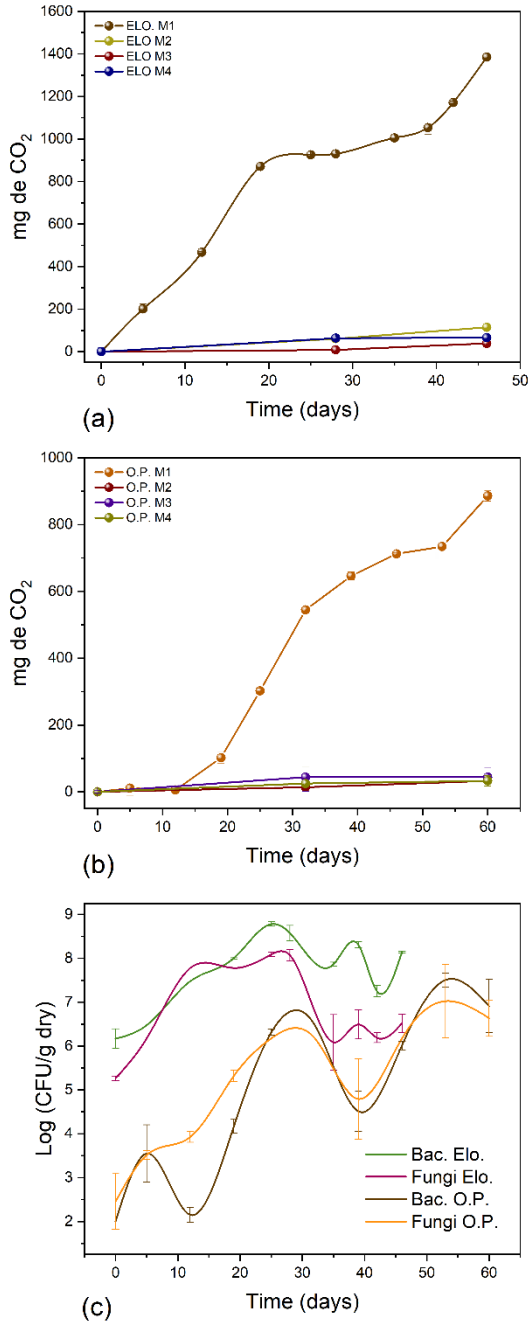

Figure 3. Microbial growth (bacteria, fungi, and yeast). a), b) CO_2 production from respirometry techniques in the presence of Pb (II) and Cr (III) at 450 mg/L; c) microbial growth in ELO and OP.
Source: Authors

Guerrero-Ortiz *et al.* (2012) reported values of CO_2 evolution of 649,44 mg over 30 days of incubation and 3 735,87 mg of accumulated C-CO_2 from the biodegradation of organic fertilizers made from *Lupinus montanus* due to the material's biological activity. When evaluating rice chaff biodegradation under greenhouse conditions, Pedraza (2014) obtained values of 140 mg of CO_2 and 233 mg of CO_2 in an incubation period of 60 days. In this study, ELO was an easily biodegradable plant-based material in the presence of water. Furthermore, the amounts of microbial growth indicate an active metabolism, even in the MI treatment,

in which they were exposed to high concentrations of Pb (II) and Cr (III) (450 mg/L), demonstrating that there were bacteria with tolerance and/or resistance mechanisms in both bioadsorbents (Bedoya *et al*., 2019). Such behavior is an indirect measure of metal degradation through catabolic reactions, as evaluated with respirometry techniques (Merchán *et al*., 2009). When ELO becomes saturated with the metal ions and therefore loses its bioadsorbent capacity, incineration is a suitable method of disposal.

When comparing the production of CO_2 with microbial growth over time (Figure 3), there is a direct relationship with microbial development phases. There was an exponential phase between days 5 and 25 for ELO and between days 5 and 32 for OP (Figure 3a and 3b) during which the plant-based materials were easily biodegradable. This was followed by a stationary phase between days 25 and 30 for ELO and days 39 and 53 for OP in the CO_2 production curve. Finally, there was a cell death phase. During the last few days of the test, there was a slight growth, since dead microbes can be a substrate for successive microbial populations (Pérez-Bou *et al*., 2018).

Figure 4 and Table 2 show the biodegradation of ELO and OP over time and their fit to a zero-order kinetic (Equation 7), respectively. Zero-order kinetics explain the biodegradation data of ELO by 92,74% and OP by 95,16%, according to the values of the coefficient of determination (R^2). The product lifespan for ELO was 78 days or 2,6 months, and OP showed stability over 211,6 days or 7 months in the presence of the metal ions (Table 2). Biodegradation velocity for ELO is higher, which is possibly due to the absence of lignin in this plant's cell wall. On the other hand, OP can be regarded as a more biostable material in aqueous solutions due to the presence of lignin (3,2±0,4) (Cerón-Salazar and Cardona-Alzate, 2011). Lignin provides rigidity to the cell wall of the OP and is considered resistant to degradation, even more than cellulose (Polman *et al*., 2021). This enables a more complex structure in OP and a slower degradation (Abdel-Hamid *et al*., 2013; Pedraza, 2014). Pinchao-Pinchao *et al*. (2019) found biodegradation of natural fique (*Furcraea andina*) and cotton (*Gossypium barbadense*) fibers of 6,1 and 29,9 months, respectively.

Table 2. Zero-order kinetic of the bioadsorbents ELO and OP

Bioadsorbent	ELO	OP
Linear equation	y= 1,25x + 6,45	y= 0,46 x – 2,39
k_0 **constant (%/d)**	1,23	0,46
R^2	0,93	0,95
Time for 100% biodegradation (days)	78,34	211,58
Time for 100% biodegradation (months)	2,61	7,05

Pb (II) and Cr (III) bioadsorption

ELO was chosen as the bioadsorbent in which to test the capacity of its associated microbes in order to remove Pb(II) and Cr(III) because it had more microbial growth, including strains that were tolerant to the metals of interest. According to Bojórquez *et al*. (2019), microbial population growth (*i.e.*, increasing cell density) can increase the total availability of active sites for metal adsorption over time. Figure 5 shows the amount of Pb (II) and Cr (III) adsorbed in ELO with the presence (EB1, EB2, and EB3) and absence (MEL) of microorganisms, as well as the adsorbed quantity of metals by microorganisms (MB1, MB2, and MB3) over time. The adsorption kinetic data of Pb (II) and Cr (III) in ELO with and without microorganisms (EB1-EB3 and MEL) were well fitted by the linear form of the pseudo-second-order equation (R^2 > 0,99). There is an affinity between bioadsorbent and metallic ions, which are attracted to the solid (Andrago, 2011) starting at 6 hours of contact. After 12 hours, small fluctuations occurred in the retention of Pb (II) and Cr (III) in ELO with and without microorganisms. At 12 hours, a state of equilibrium was reached between metals, ELO, and microorganisms. Hemavathy *et al*. (2021) reported that the pseudo-first-order equation fitted well to adsorption kinetic data of Pb (II) in *Cassia fistula* seeds. The pseudo-first-order model is only appropriate for the initial 20-30 minutes of the contact time between metal and bioadsorbent (Tran *et al*., 2017).

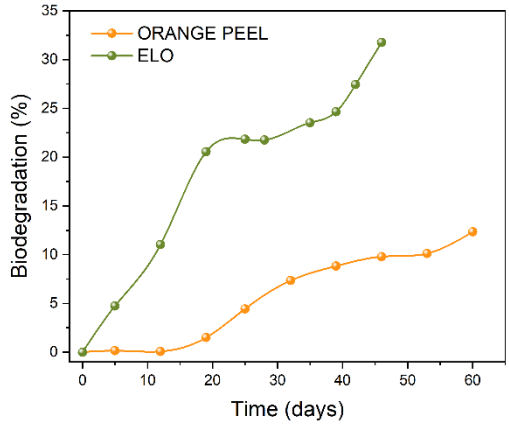

Figure 4. Biodegradation for bioadsorbents ELO and OP
Source: Authors

The adsorption capacities of Pb (II) at 120 hours of contact were 2 424,75, 2 257,25, 2 151,25, 152,25, 431,43, 115,88, and 2 256,88 mg/kg for EB1, EB2, EB3, MB1, MB2, MB3, and MEL, respectively. Moreover, the adsorption capacities of Cr (III) at 120 hours of contact were 2 273,63, 2 249,55, 2 264,80, 107,00, 85,95, 238,50, and 2 428,20 mg/kg for EB1, EB2, EB3, MB1, MB2, MB3, and MEL, respectively. These results showed that individually selected bacteria did not generate significant changes in metal concentrations, which limits their use for this purpose. ELO is a viable bioadsorbent for Pb (II) and Cr (III) removal, and it provides nutrients and substrate for microorganisms as well as metal adsorption sites. Martínez-Vásquez and Serna-Flórez (2020) studied the retention ability for Pb (II) and Cr (III) from adsorption kinetics with passion fruit rind (*Passiflora edulis*) and elodea (*Egeria densa*) in an aqueous solution. They found retention values for Pb (II) of 825,33 mg/kg and for Cr (III) of 666,43 mg/kg for passion fruit rind, and retention values for Pb (II) of 200,16 mg/kg and for Cr (III) of 114,83 mg/kg for

elodea in an optimal time of 60 minutes. Hernández-Gómez *et al*. (2017) evaluated the bioadsorption ability of Pb (II) in synthetic solutions using elodea, pea pods, and coffee grounds as bioadsorbents. They found a greater efficiency in ion removal, with 91% for Elodea and 72,6% for pea pods.

The treatments EB1, EB2, and EB3 did not increase the removal of Cr (III) by the bioadsorbent. The bacteria labeled as EB1 increased Pb (II) adsorption in ELO (Table 3) with a p-value < 0,05. There was no significant metal removal by bacteria in treatment T3 (MB1, MB2, and MB3; p-value > 0,05). The treatment T3 showed the lowest adsorption of Pb (II) and Cr (III) in comparison with the MEL treatment (ELO showed high removal of metallic ions, 88,79-94,34%). Thus, the ELO-associated bacteria can persist in environments polluted with these metals, but they did not use Pb (II) and Cr (III) for their metabolic processes. This was further confirmed by growing cultures in nutrient agar to identify microbial growth for each treatment over time. For ELO treatments, there was growth (+), while, in the inoculated MB1, MB2, and MB3, growth was absent (-) (Table 3). This may be because, at a concentration of 50 mg/L, the metals saturated the cell membrane, disabling the metal resistance mechanisms (Jarosławiecka and Piotrowska-Seget, 2014).

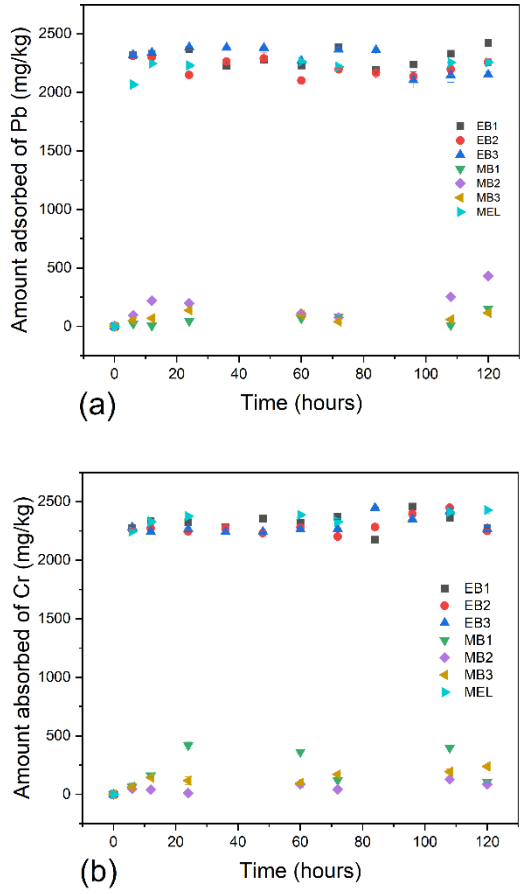

Figure 5. Bioadsorption for metals in the presence and absence of elodea and microorganisms. a) Pb (II) adsorption, and b) Cr (III) adsorption. Treatment 1 (EB1, EB2, and EB3), treatment 2 (MEL), and treatment 3 (MB1, MB2, and MB3).
Source: Authors

Table 3. Removal percentage for Pb (II) and Cr (III) in the presence and absence of elodea and microorganisms

	Presence (+) / absence (-) of ELO	Pb (II) removal, %	Cr (III) removal, %	Presence (+)/ absence (-) of microbial growth
EB1	+	93,62±2,40	92,92±1,51	+
EB2	+	88,63±3,08	91,19±3,03	+
EB3	+	91,34±3,89	91,44±2,32	+
MEL	+	88,88±2,64	94,35±2,32	+
MB1	-	2,22±2,08	9,32±6,11	-
MB2	-	7,92±4,92	2,52±1,56	-
MB3	-	3,27±1,45	5,83±2,40	-

T1: microorganism and ELO (EB1, EB2 and EB3); T2: ELO without microorganism (MEL); T3: microorganism without ELO (MB1, MB2 and MB3)

Source: Authors

Conclusions

The study confirmed the potential of ELO and OP as bioadsorbents for metallic ion removal. Biostability and microbial characterizations demonstrated that OP had a longer lifespan than ELO (7,05 months *vs.* 2,61 months) and less microbial growth. Meanwhile, ELO contained a high abundance of native microorganisms that were resistant to Pb (II) and Cr (III). The abundant microbes in ELO degrade the plant-based material faster (higher CO_2 production in the respirometry test). Furthermore, the microorganisms present in ELO did not contribute significantly to metal retention, meaning that it is mainly the plant material itself that is responsible for metal adsorption, except for the bacteria EB1, which led to a small but significant increase in Pb (II) adsorption. The pseudo-second-order model was observed as the appropriate fittest one for Pb (II) and Cr (III) adsorption in ELO. Finally, it is our opinion that OP is the better material for filter development to be applied in polluted water treatment systems.

References

Abdel-Hamid, A. M., Solbiati, J. O., and Cann, I. K. O. (2013). Insights into lignin degradation and its potential industrial applications. *Advances in Applied Microbiology*, *82*, 1-28. https://doi.org/10.1016/B978-0-12-407679-2.00001-6

Andrago, D. (2011). *Estudio isotérmico de biosorción de cromo y cadmio en solución acuosa utilizando residuos de césped* [Undergraduate thesis, Universidad Politécnica Salesiana Quito]. http://dspace.ups.edu.ec/handle/123456789/1348

Ballardo de la Cruz, C. E., Merino-Rafael, F. A., and Gutiérrez-Moreno, S. M. (2015). Evaluación de la capacidad de bioadsorción de Cadmio (II) y Plomo (II) mediante el uso de biomasa bacteriana muerta en soluciones acuosas. *Ciencias Biológicas*, *2*, 95-106. https://revistasinvestigacion.unmsm.edu.pe/index.php/Theo/index

Bedoya-Vélez, J. M., Castaño, G., and Ochoa-Agudelo, S. (2019). Tolerancia al plomo de aislamientos nativos de

Pseudomonas spp. de aguas residuales del Valle de Aburrá. *Revista Colombiana de Biotecnología*, *21*(1), 135-143. https://doi.org/10.15446/rev.colomb.biote.v21n1.65146

Beltrán-Pineda, M. E., and Gómez-Rodríguez, A. M. (2016). Biorremediación de metales pesados Cadmio (Cd), Cromo (Cr) y Mercurio (Hg). Mecanismos bioquímicos e ingeniería genética: una revisión. *Revista Facultad de Ciencias Básicas*, *12*(2), 172-97. http://dx.doi.org/10.18359/rfcb.2027

Beltrán-Pineda, M. E., and Gómez-Rodríguez, A. M. (2015). Metales pesados (Cd, Cr y Hg): su impacto en el ambiente y posibles estrategias biotecnológicas para su remediación. *Revista I3+*, *2*(2), 82-112. https://doi.org/10.24267/23462329.113

Ben-David, A., and Davidson, E. (2014). Estimation method for serial dilution experiments. *Journal of Microbiological Methods*, *107*, 214-221. http://dx.doi.org/10.1016/j.mimet.2014.08.023

Bilal M., Ihsanullah, I., Younas, M., and Shah, M. U. H. (2021). Recent advances in applications of low-cost adsorbents for the removal of heavy metals from water: A critical review. *Separation and Purification Technology*, *278*, 119510. https://doi.org/10.1016/j.seppur.2021.119510

Bojórquez, C., Frías-Espericueta, M.G., Gómez-Gil, B., and Voltolina, D. (2019). Biosorption of cadmium and lead using suspended and immobilized *Enterobacter cloacae* at different pH. *Revista Internacional de Contaminación Ambiental*, *35*(1), 259-264. https://doi.org/10.20937/RICA.2019.35.01.19

Castañeda-Figueredo, J. S., Torralba-Dotor, A. I., Pérez-Rodríguez, C. C., Moreno-Bedoya, A. M., and Mosquera-Vivas, C. S. (2022). Removal of lead and chromium from solution by organic peels: effect of particle size and bio-adsorbent. *Heliyon, 8*, e10275. https://doi.org/10.1016/j.heliyon.2022.e10275

Castro-Aguirre, E., Auras, R., Selke, S., Rubino, M., and Marsh, T. (2017). Insights on the aerobic biodegradation of polymers by analysis of evolved carbon dioxide in simulated composting conditions. *Polymer Degradation and Stability*, *137*, 251-271. https://doi.org/10.1016/j.polymdegradstab.2017.01.017

Cardona-Gutiérrez, A. F., Cabañas-Vargas, D. D., and Zepeda-Pedreguera, A. (2013). Evaluación del poder biosorbente de cáscara de naranja para la eliminación de metales pesados, Pb (II) y Zn (II). *Ingeniería*, *17*(1), 1-9. https://www.redalyc.org/pdf/467/46729718001.pdf

Cerón-Salazar, I., and Cardona-Alzate, C. (2011). Evaluación del proceso integral para la obtención de aceite esencial y pectina a partir de cáscara de naranja. *Ingeniería y Ciencia*, *13*, 65-86. http://www.scielo.org.co/pdf/ince/v7n13/v7n13a04.pdf

Cervantes, C., Campos-García, J., Devars, S., Gutiérrez-Corona, F., Loza-Tavera, H., Torres-Guzmán, J., and Moreno-Sánchez, R. (2001). Interactions of chromium with microorganisms and plants. *FEMS Microbiology Reviews*, *25*(3), 335-47. https://doi.org/10.1111/j.1574-6976.2001.tb00581.x

Chakraborty, R., Asthana, A., Singh, A. K., Jain, B., and Susan, A. B. H. (2020). Adsorption of heavy metal ions by various low-cost adsorbents: a review. *International Journal of Environmental Analytical Chemistry*, *102*(2), 342-379. https://doi.org/10.1080/03067319.2020.1722811

Correa, M., Velini, E., and Arruda, D. (2003). Composição química e bromatológica de *Egeria densa*, *Egeria najas* e *Ceratophyllum demersum*. *Planta Daninha*, *21*, 7-13. https://doi.org/10.1590/S0100-83582003000400002

Chinaglia, S., Tosin, M., and Degli-Innocenti, F. (2018). Biodegradation rate of biodegradable plastics at molecular level. *Polymer Degradation and Stability*, *147*, 237-244. https://doi.org/10.1016/j.polymdegradstab.2017.12.011

Diep, P., Mahadevan, R., and Yakunin, A. F. (2018). Heavy metal removal by bioaccumulation using genetically engineered microorganisms. *Frontiers in Bioengineering and Biotechnology*, *6*, 00157. https://doi.org/10.3389/fbioe.2018.00157

Fernández, M., Flórez, D., Yactayo, M., Lovera, D., Quispe, J., Landauro, C., and Pardave, C. (2020). Remoción de metales pesados desde efluentes mineros, mediante cáscaras de frutas. *Aibi Revista de Investigación, Administración e Ingeniería*, *8*(1), 21-28. https://doi.org/10.15649/2346030x.627

Guerrero-Ortiz, P. L., Quintero-Lizaola, R., Espinoza-Hernández, V., Benedicto-Valdés, G. S., and Sánchez-Colín, M. (2012). Respiración De CO_2 como indicador de la actividad microbiana en abonos orgánicos de lupinus. *Terra Latinoamericana*, *30*(4), 355-62. http://www.redalyc.org/articulo.oa?id=57325814007

Hemavathy, R. V., Saravanan, A., Senthil Kumar, P., Vo, D.-V. N., Karishma, S., and Jeevanantham, S. (2021). Adsorptive removal of Pb (II) ions onto surface modified adsorbents derived from *Cassia fistula* seeds: Optimization and modelling study. *Chemosphere*, *283*, 131276. https://doi.org/10.1016/j.chemosphere.2021.131276

Hernández-Gómez, R. C., Garzón-Gutiérrez, J., La Rotta- La Rotta, M., and Guerra-Rodríguez, J. (2017). Evaluación de la capacidad de bioadsorción de plomo (ll) presente en afluentes sintéticos, utilizando bioadsorventes de origen vegetal. *Publicaciones e Investigación*, *12*(1), 115-125. https://repository.unad.edu.co/handle/10596/29768

Jarosławiecka, A., and Piotrowska-Seget, S. (2014). Lead resistance in micro-organisms. *Microbiology*, *160*(Part 1), 12-25. https://doi.org/10.1099/mic.0.070284-0

Joutey, N., Sayel, H., Bahafid, W., and Ghachtouli, N. (2015). Mechanisms of hexavalent chromium resistance and removal by microorganisms. *Reviews of Environmental Contamination and Toxicology*, *233*, 45-69. https://doi.org/10.1007/978-3-319-10479-9_2

Kadukova, J. (2016). Surface sorption and nanoparticle production as a silver detoxification mechanism of the freshwater alga *Parachlorella kessleri*. *Bioresource Technology*, *216*, 406-413. https://doi.org/10.1016/j.biortech.2016.05.104

Leejarkpai, T., Suwanmanee, U., Rudeekit, Y., and Mungcharoen, T. (2011). Biodegradable kinetics of plastics under controlled composting conditions. *Waste Management*, *31*(6), 1153-1161. https://doi.org/10.1016/j.wasman.2010.12.011

Lemaire, F. (1997). *The problem of the biostability in organic substrates*. Institut National de la Reacherche Agronomique.

Mahour, S., Verma, S. K., and Srivastava, S. (2022). Functionalized agro-waste for toxic metal remediation from water bodies: A green pre-treatment process. *Materials Today: Proceedings*, *50*(Part 3), 287-292. https://doi.org/10.1016/j.matpr.2021.06.330

Mandina, S., Chigondo, F., Shumba, M., Nyamunda. B. C., and Sebata, E. (2013). Removal of chromium (VI) from aqueous solution using chemically modified corncorb-activated carbon: Equilibrium and kinetic studies. *Environmental Progress and Sustainable Energy*, *32*(3), 673-680. https://doi.org/10.1002/ep.11684

Manyuchi, M. M., Sukdeo, N., and Stinner, W. (2022). Potential to remove heavy metals and cyanide from gold mining wastewater using biochar. *Physics and Chemistry of the Earth, Parts A/B/C*, 103110. https://doi.org/10.1016/j.pce.2022.103110

Martínez-Vásquez, A, F., and Serna-Flórez, M, A. (2020). *Comparación de la capacidad de retención del plomo y cromo en los bioadsorbentes de cascara de naranja* (*Cistrus sinensis*)*, cascara de maracuya* (*Passiflora edulis*) *y elodea* (*Egeria densa*) [Undergraduate thesis, Universidad ECCI]. http://dspace.ups.edu.ec/handle/123456789/20073

Mehrotra, T., Dev, S., Banerjee, A., Chatterjee, A., Singh, R., and Aggarwal, S. (2021). Use of immobilized bacteria for environmental bioremediation: A review. *Journal of Environmental Chemical Engineering*, *9*(5), 105920. https://doi.org/10.1016/j.jece.2021.105920

Merchán, J. P., Ballesteros, D., Jiménez, I. C., Medina, J. A., and Álvarez, O. (2009). Estudio de la biodegradación aerobia de almidón termoplástico (TPS). *Revista Latinoamericana de Metalurgia y Materiales*, *1*(1), 39-44. http://hdl.handle.net/1992/55329

Mora-Ortiz, L. (2009). *Crecimiento sobre buchón y elodea de Pleurotus ostreatus y efecto de esta especie fúngica sobre la digestibilidad del sustrato lignocelulósico como potencial alimento para rumiantes* [Undergraduate thesis, Universidad Javeriana]. http://hdl.handle.net/10554/8443

Muñoz-Silva, L., Olivera-Gonzales, P., Santillán-Torres, M., and Tamariz-Angeles, C. (2019). Heavy Metals Tolerant Microorganisms from Mine Tailing Wastelands Santa Rosa, Jangas (Peru). *Revista Peruana de Biología*, *26*(1), 109-18. http://dx.doi.org/10.15381/rpb.v26i1.15914

Mustapha, M. U., and Halimoon, N. (2015). Screening and Isolation of heavy metal tolerant bacteria in industrial effluent. *Procedia Environmental Sciences*, *30*, 33-37. https://doi.org/10.1016/j.proenv.2015.10.006

Naik, M., and Dubey, S. (2013). Lead resistant bacteria: Lead resistance mechanisms, their applications in lead bioremediation and biomonitoring. *Ecotoxicology and Environmental Safety*, *98*, 1-7. http://dx.doi.org/10.1016/j.ecoenv.2013.09.039

Ojuederie, O., and Babalola, O. (2017). Microbial and plant-assisted bioremediation of heavy metal polluted environments: A review. *International Journal of Environmental Research and Public Health*, *14*(12), 1504. https://doi.org/10.3390/ijerph14121504

Özer, A., and Özer, D. (2003). Comparative study of the biosorption of Pb (II), Ni (II) and Cr (VI) ions onto *S. cerevisiae*: Determination of biosorption heats. *Journal of Hazardous Materials*, *100*(1-3), 219-229. https://doi.org/10.1016/S0304-3894(03)00109-2

Patil, C. S., Gunjal, D. B., Naik, V. M., Waghmare, R. D., Dongale, T. D., Kurkuri, M. D., Kolekar, G. B., and Gore, A. H. (2022). Sustainable conversion of waste tea biomass into versatile activated carbon: Application in quick, continuous, and pressure filtration of miscellaneous pollutants. *Biomass Conversion and Biorefinery, 2022,* s13399-021-02125-1. https://doi.org/10.1007/s13399-021-02125-1

Patiño-Saldivar, L., Hernández, J. A., Ardila, A., Salazar-Hernández, M., Talavera, A., and Hernández-Soto, R. (2021). Cr (III) removal capacity in aqueous solution in relation to the functional groups present in the orange peel (*Citrus sinensis*). *Applied Sciences*, *11*(14), 6346. https://doi.org/10.3390/app11146346

Pedraza, D. (2014). *Evaluación de la actividad enzimática de aislamientos microbianos celulolíticos y lignolíticos, y su aplicación en la degradación de tamo de arroz* (*Oryza sativa*) [Master's thesis, Universidad Nacional de Colombia]. https://repositorio.unal.edu.co/handle/unal/75010

Pellizzari-Wielewski, L., Zuccolotto, T., Soares, M., Tentler-Prola, L. D., and Vinicius, M. (2014). A tecnologia de remoção de fósforo: Gerenciamento do elemento em resíduos industriais. *Revista Ambiente e Agua*, *9*(3), 445-458. https://doi.org/10.4136/1980-993X

Pérez-Bou, L., Salgado-Bernal, I., Larrea-Duarte, C., Martínez-Sardiñas, A., Cruz-Arias, M., and Carballo-Valdés, M. (2018). Biosorción microbiana de metales pesados: caracteristicas del proceso. *Revista Cubana de Ciencias Biológicas*, *6*(1), 1-12.

Pinchao-Pinchao, Y. A., Osorio-Mora, O., Checa-Coral, O., and Tobar, E. (2019). Study on the rate and time of biodegradation under controlled conditions of natural fibers of fique (*Furcraea andina*) and cotton (*Gossypium barbadense*). *Información Tecnológica*, *30*(4), 59-67. https://doi.org/10.4067/S0718-07642019000400059

Pinzón-Bedoya, M. L., and Cardona-Tamayo, A. M. (2010). Influence of the pH in the Biosorption of Cr(III) on orange shell: Determination of the conditions operation in discontinuous process. *Bistua, Revista de la Facultad de Ciencias Básicas*, *8*(1), 21-30. https://www.redalyc.org/pdf/903/90315226003.pdf

Pischedda, A., Tosin, M., and Degli-Innocenti, F. (2019). Biodegradation of plastics in soil: The effect of temperature. *Polymer Degradation and Stability*, *170*, 109017. https://doi.org/10.1016/j.polymdegradstab.2019.109017

Polman, E. M. N., Gruter, G.-J. M., Parson, J. R., and Tietema, A. (2021). Comparison of the aerobic biodegradation of biopolymers and the corresponding bioplastics: A review. *Science of the Total Environment*, *753*, 141953. https://doi.org/10.1016/j.scitotenv.2020.141953

Rego, R. M., Sriram, G., Ajeya, K. V., Jung, H.-Y., Kurkuri, M. D., and Kigga, M. (2021a). Cerium based UiO-66 MOF as a multipollutant adsorbent for universal water purification. *Journal of Hazardous Materials*, *416*, 125941. https://doi.org/10.1016/j.jhazmat.2021.125941

Rego, R. M., Kuriya, G., Kurkuri, M. D., and Kigga, M. (2021b). MOF based engineered materials in water remediation: Recent trends. *Journal of Hazardous Materials*, *403*, 123605. https://doi.org/10.1016/j.jhazmat.2020.123605

Rimac, A., Stankovic, I., Alegro, A., Gottstein, S., Koletic, N., Vukovic, N., Segota, V., and Zizic-Nakic, A. (2018). The Brazilian elodea (*Egeria densa* Planch) invasion reaches Southeast Europe. *BioInvasions Records*, *7*(4), 381-389. https://doi.org/10.3391/bir.2018.7.4.05

Sajna, K.V., Sharma, S., and Nadda, A. K. (2021). Microbial exopolysaccharides: An introduction. In K. V. Sajna, A. Sharma, A. K. Nadda (Eds.), *Microbial Exopolysaccharides as Novel and Significant Biomaterials* (pp. 1-18). Springer. https://doi.org/10.1007/978-3-030-75289-7_1

Sriram, G., Bendre, A., Altalhi, T., Jung, H.-Y., Hegde, G., and Kurkuri, M. (2022a). Surface engineering of silica based materials with Ni-Fe layered double hydroxide for the efficient removal of methyl orange: Isotherms, kinetics, mechanism and high selectivity studies. *Chemosphere*, *287*(Part 1), 131976. https://doi.org/10.1016/j.chemosphere.2021.131976

Sriram, G., Bendre, A., Mariappan, E., Altalhi, T., Kigga, M., Ching, Y. C., Jung, H.-Y., Bhaduri, B., and Kurkuri, M. (2022b). Recent trends in the application of metal-organic frameworks (MOFs) for the removal of toxic dyes and their removal mechanism – A review. *Sustainable Materials and Technologies*, *31*, e00378. https://doi.org/10.1016/j.susmat.2021.e00378

Vanrolleghem P. A., Spanjers H., Petersen B., Ginestet P., and Takacs I. (1999). Estimating (combination of) activated sludge model No.1 parameters and components by respirometry. *Water Science and Technology*, *39*(1), 195-214. https://doi.org/10.1016/S0273-1223(98)00786-0

Suárez, P., and Reyes, R. (2002). La incorporación de metales pesados en las bacterias y su importancia para el ambiente. *Interciencia*, *27*(4), 160-164. https://www.redalyc.org/pdf/339/33906702.pdf

Tran, H. N., You, S.-J., Hosseini-Bandegharaei, A., and Chao, H.-P. (2017). Mistakes and inconsistencies regarding adsorption of contaminants from aqueous solutions: A critical review. *Water Research*, *120*, 88-116. https://doi.org/10.1016/j.watres.2017.04.014

Ulloa-Espinosa, C. (2012). *Estudio de las opciones de reutilización energética o material de Cáscaras de Naranja* [Undergraduate thesis, Universidad de San Francisco de Quito]. http://repositorio.usfq.edu.ec/handle/23000/6983

Uthappa, U. T, Sriram, G., Arvind, O. R., Kumar, S., Jung, H.-Y., Neelgund, G. M., Losic, D., and Kurkuri, M. D. (2020). Engineering MIL-100(Fe) on 3D porous natural diatoms as a versatile high performing platform for controlled isoniazid drug release, Fenton's catalysis for malachite green dye degradation and environmental adsorbents for Pb^{2+} removal and dyes. *Applied Surface Science*, *528*, 146974. https://doi.org/10.1016/j.apsusc.2020.146974

Verma, S., Bhatt, P., Verma, A., Mudila, H., Prasher, P., and Rene, E. R. (2021). Microbial technologies for heavy metal remediation: effect of process conditions and current practices. *Clean Technologies and Environmental Policy, 2021*, s10098-021-02029-8. https://doi.org/10.1007/s10098-021-02029-8

Virreira-Flores, J., and Góngora-Pereira, O. (2014). *Caracterización fisicoquímica de las cáscaras de naranja* (*Citrus sinensis L.*) *y Pomelo* (*Citrus grandis*) [Undergraduate thesis, Universidad Nacional de la Amazonía Peruana]. http://repositorio.unapiquitos.edu.pe/handle/20.500.12737/4258

Viti, C., Marchi, E., Decorosi, F., and Giovannetti, L. (2013). Molecular mechanisms of Cr (VI) resistance in bacteria and fungi. *FEMS Microbiology Reviews*, *38*(4), 633-659. https://doi.org/10.1111/1574-6976.12051

Yarrow, M., Marín, V. H., Finlayson, M., Tironi, A., Delgado, L. E., and Fischer, F. (2009). The ecology of *Egeria densa* planchon (liliopsida: Alismatales): A wetland ecosystem engineer. *Revista Chilena de Historia Natural*, *82*(2), 299-313. https://doi.org/10.4067/S0716-078X2009000200010

Yin, K., Wang, Q., Lv, M., and Chen, L. (2019). Microorganism remediation strategies towards heavy metals. *Chemical Engineering Journal*, *360*, 1553-1563. https://doi.org/10.1016/j.cej.2018.10.226

Research Article/Chemical, Food, and Environmental Engineering http://doi.org/10.15446/ing.investig.97254

Obtaining Biodiesel from Fat Extracted from Solid Waste Produced in the Fleshing Stage of Leather Manufacturing

Obtención de biodiésel a partir de grasa extraída de residuos sólidos producidos en la etapa de descarnado en la fabricación de cuero

Ángel Díaz-Burgos[1], Carol Castillo-Parra[2], Pablo Fernández-Izquierdo[3], David Arturo-Perdomo[4] and Juan J. Lozada-Castro[5]

ABSTRACT

Tallow is produced in leather manufacturing, particularly in the fleshing stage. It contains large amounts of fat, which, in most industrial plants, pollutes water and soil due to poor disposal. In order to take advantage of this solid waste, chemical processes have been applied to transform the fats extracted from tallow into biodiesel. In this work, an extraction technique involving non-polar solvents pressurized at 15 psi. With gasoline, a 51,0% fat recovery was obtained. The quality of the extracted fat was determined by analyzing density, viscosity, melting point, moisture, acidity, and acidity, peroxides, saponification, and iodine indices. Biodiesel was obtained via transesterification reactions with methanol and sodium hydroxide. The content of methyl esters produced in the reaction was characterized by means of gas chromatography coupled with mass spectrometry, where the methyl esters of palmitic and oleic fatty acids were identified as major components.

Keywords: pressurized solvent, fat, transesterification, biodiesel, tallow, solid waste

RESUMEN

El sebo se produce en la fabricación de cuero, particularmente en la etapa de descarnado, y contiene grandes cantidades de grasa que, en la mayoría de las plantas industriales, contaminan el agua y el suelo debido a la mala eliminación. Para aprovechar este recurso se han aplicado procesos químicos para transformar las grasas extraídas del sebo en biodiesel. En este trabajo se aplicó una técnica de extracción con disolventes apolares presurizados a 15 psi. Con gasolina se obtuvo una recuperación de grasa del 51,0 %. La calidad de la grasa extraída se determinó analizando densidad, viscosidad, punto de fusión, humedad, acidez e índices de acidez, peróxidos, saponificación y yodo. El biodiesel se obtuvo mediante reacciones de transesterificación con metanol e hidróxido de sodio. El contenido de los ésteres metílicos producidos en la reacción se caracterizó mediante cromatografía de gases acoplada a espectrometría de masas, donde se identificaron los ésteres metílicos de los ácidos grasos palmítico y oleico como componentes principales.

Palabras clave: solventes presurizados, grasas, transesterificación, biodiesel, sebo, residuos sólidos

Received: July 13th, 2021
Accepted: August 19th, 2022

[1] Chemist, Universidad de Nariño, Colombia. Affiliation: Grupo de Investigación Estudio de Sistemas Contaminantes, Universidad de Nariño, Colombia. Email: angeldb022@gmail.com

[2] Chemist, Universidad de Nariño, Colombia. MSc in Water Management, Universidad de Buenos Aires, Argentina. Affiliation: Grupo de Investigación Estudio de Sistemas Contaminantes, Universidad de Nariño, Colombia. Email: carol.castillop@gmail.com

[3] Biologist, Universidad de Nariño, Colombia. PhD in Biological Sciences, University of Havana, Cuba. Affiliation: Associate professor of the Department of Biology, Grupo de Investigación en Biotecnología Microbiana, Universidad de Nariño, Colombia. Email: pabfdez@gmail.com

[4] Chemist, Universidad de Nariño, Colombia. Affiliation: Grupo de Investigación Estudio de Sistemas Contaminantes y Laboratorio de Cromatografia, Universidad de Nariño, Colombia. Email: davechem06@gmail.com

[5] Chemist and Biologist, Universidad Santiago de Cali, Colombia. PhD in Analytical Chemistry, Universidad Complutense de Madrid, Spain. Affiliation: Associate professor, Grupo de Investigación Estudio de Sistemas Contaminantes, Universidad de Nariño, Colombia. Email: jjlccc2121@hotmail.com

How to cite: Díaz-Burgos, A., Castillo-Parra, C., Fernández-Izquierdo, Arturo-Perdomo, D., and Lozada-Castro, J. J. (2023). Obtaining biodiesel from fat extracted from solid waste produced in the fleshing stage of leather manufacturing. *Ingeniería e Investigación, 43*(1), e97254. http://doi.org/10.15446/ing.investig.97254

Introduction

Today, there is a high dependence on oil for the production of fuels. This industry includes numerous processes, such as exploration, drilling, extraction, refining, *etc.*, all of which require a high consumption of resources (Sayaddi *et al.*, 2022). Fuels obtained from petroleum are an environmental concern, given that combustion results in high amounts of greenhouse gases and acid rain (Nandhini *et al.*, 2022). Since the beginning of the 21st century, the growing energy demand has sparked great interest in the production and use of biofuels (Bosu *et al.*, 2022). One of the biofuels that has impacted the current economy is biodiesel, a renewable energy source. It is estimated that the annual global production of biodiesel is approximately 35 billion liters (Naylor and Higgins, 2017). These fuels are composed of mixtures of methyl esters derived from the fatty acids that are part of the triacylglycerides from both vegetable

oils and animal fats (Verma and Sharma, 2016), which have physicochemical properties similar to those of commercial diesel (Alptekin *et al*., 2012).

Belén (Nariño, Colombia) is a township with more than 2 500 inhabitants, which is located at 1°35'43" N, 77°00'57" W. Its economy depends on the production of leather, as more than 85% of its inhabitants participate in this activity. Currently, there are 43 tanneries in the urban area, and an average of 29 000 cowhides is treated every month. In this township, the leather industry has grown by tradition. These activities have a high environmental impact due to the amount of waste produced, including the tallow obtained in the fleshing stage of the leather tanning process, which accounts for 60 ton/month of the total residues, which are disposed of in dumps in the open or on the banks of the rivers (Díaz-Burgos, 2019). These substances contaminate water sources because they are very stable and change the composition of the water through oxidation (Vidales-Olivo *et al*., 2010). It is therefore necessary to develop technologies in order to utilize these resources. The fats present in tallow also contain between 75 and 80% of triacylglycerides, which makes them suitable for the production of biodiesel for vehicular applications with internal combustion engines (Šánek *et al*., 2015).

Biodiesel is formed by transesterification reactions, in which the triacylglycerides present in vegetable oils and animal fats react in the presence of KOH with an alcohol, thus obtaining alkyl esters as by-product (Ranjitha *et al*., 2020), which correspond to each of the fatty acids that form the triacylglycerides and glycerin (Knothe and Razon, 2017). Research has also been conducted on the use of enzymatic methods for the production of biodiesel with animal fat (Pollardo, 2017). Several sources of raw materials are used, the most common being: oil seeds such as soybean, rapeseed, palm oil, and bovine tallow from the food industry (Yuan, *et al*, 2017). Therefore, the objective of this work was the obtaining of biodiesel from bovine tallow, a solid waste generated in the leather tanning process.

Materials and methods

Reagents and materials

Hexane 95% alkane mix, ammonium sulfate (99,5%), potassium hydroxide (85%), methanol ACS (99,9%), sodium sulfate (99%), phenolphthalein solution (1%), acetic acid (99,5%), and chloroform ACS (98%) were obtained from Panreac. Ethanol (99,8%), potassium iodide (98%), and potassium iodate (99,5%) were obtained from Merck. Anhydrous sodium carbonate was obtained from Carlo Erba. Isopropanol (99, 5%) was obtained from Aldrich.

The materials used were a homemade pressure extractor, a magnetic stirrer hot plate (Heidolph Instruments 101142642) and a Radwag analytical balance (AS 220/C/2 366202).

Methods

Samples: Tallow was collected at the end of the fleshing stage from La Sociedad Curtimebres de Cueros Belén [The Belén Leather Tanning Society], in the town of Belén, Nariño, Colombia. 1,0 kg samples were collected in plastic bags and then frozen in order to delay the decomposition process until the moment of processing (Ranjitha *et al*., 2020). The solid wastes were washed with distilled water and solid ammonium sulfate (99,5%) for approximately 30 minutes. Acetic acid (99,5%) was then added until a pH value close to 7 was observed. The residues were cut manually into pieces measuring approximately 1 cm, which were then packed and stored in a refrigerator at -4 °C.

Fat extraction with pressurized solvent: An extraction technique involving a pressurized solvent (Figure 1a) was implemented for the fat extraction procedure. A sample holder was incorporated to this effect, as well as a container used to collect the extracted fat. The solvent was deposited at the bottom, outside of the grease collection container (Figure 1b).

To optimize the fat extraction process, a central composite 2^2 design with two star points was used. The factors were the type of solvent (A), the extraction time (B), and the amount of solvent (C). The response variable was the percentage of fat recovery, as shown in Table 1, where the levels for each one of the factors, as well as their corresponding) units have been included.

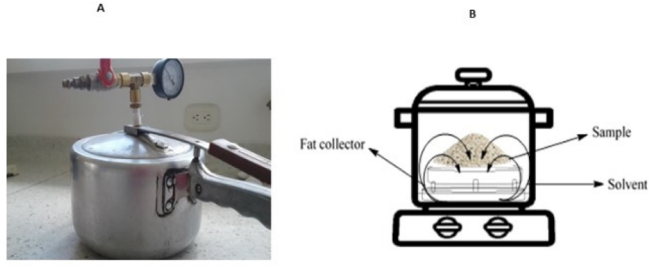

Figure 1. a) Conventional pressure vessel, b) internal pressure vessel system
Source: Authors

Table 1. Factors and levels in central composite 2^2 design + star points

Factors	Level codes	Specifications
Solvent type	-2; -1; 0; 1; 2	-2 isopropanol, -1 petroleum ether, 0 hexane, 1 gasoline, 2 chloroform
Time	0,5; 1; 2; 3; 3,5	Hours
Quantity of solvent	25; 50; 100; 150; 175	mL

Source: Authors

According to the experimental design, between 25 and 175 mL of isopropanol (-2) solvent, petroleum ether (-1), hexane (0), gasoline (1), and chloroform (2) were added to the pressure system. Later, 100 g of tallow were added to the sample holder, and the container was hermetically sealed and heated to a pressure of 103,4 kPa. The extraction was carried out in intervals from 0,5 to 3,5 h according to the experimental design. Finally, the employed solvent was released using the lid valve, and it was recovered from the condensation for later use. The lid was removed, as well as the sample holder from inside the pressure system. The extracted fat was deposited in a beaker and left to cool for 30 min in order to determine its mass.

Chemical analysis of extracted fats: The chemical properties were determined through the methodologies described in Table 2.

Table 2. Chemical properties of the extracted fat

Parameter	Method
Acidity index Acidity	ICONTEC NTC 218
Saponification value	ICONTEC NTC 335
Iodine value	ICONTEC NTC 283
Peroxide value	ICONTEC NTC 236
Moisture	ICONTEC NTC 287

Note: NTC: Colombian technical standard
Source: Authors

Obtaining biodiesel from the extracted fat: In a round-bottom flask equipped with a condenser, 30 g of fat were heated to a temperature of 110 ˚C for 10 min. The reaction mixture was allowed to cool until it reached 100 ˚C, and then 40 mL of a solution composed of 0,5 g of potassium hydroxide (solid 85%) dissolved in 40 mL of methanol was added (Kubendran *et al*., 2017). Finally, the reaction was continued at reflux, with constant stirring for 2 hours, according to the methods proposed by Bhatti *et al*. (2008), Jain *et al*. (2011), and Mata *et al*. (2011). The aforementioned amount of methanol is necessary (it was experimentally determined), considering that tallow is a residue from a biological source (variable composition) that does not allow accurately establishing a stoichiometric relationship.

Biodiesel cleaning: The reaction mixture was taken to a separatory funnel and left to stand for 3 h at room temperature. The upper part was separated (biodiesel) and washed with distilled water at 85 ˚C until the pH was 7. It was then dried with 1,0 g of sodium sulfate anhydrous, shaken for 60 min, and then filtered and stored in amber glass containers (Mata *et al*., 2011). The physicochemical properties of the obtained product were then determined as follows: density using the ASTM D1298 method and the kinematic viscosity using the ASTM D 445 method, according to research reported by Srinivasan *et al*. (2020), and the acid number using NTC 218 of ICONTEC (Colombian Institute of Technical Standards). The materials and reagents are specified in each one of the applied methodologies.

Chromatographic characterization of biodiesel: The characterization of the produced biodiesel was carried out using a Shimadzu GCMS-QP2010S gas chromatograph/mass spectrometer (Kyoto, Japan). 200 µL of biodiesel were dissolved in 2 mL of hexane, and an Agilent DB-5MS chromatographic column (Santa Clara, CA, USA) (30 m x 0,25 mm x 0,25 µm) was used with the following temperature program: 40 ˚C initial temperature; increase to 300 ˚C for 5 min at 10 ˚C /min; split injector 1:50 at 250 ˚C; and a mass detector at 300 ˚C. The amount of sample injected into the equipment was 1,0 µL.

Results and discussion

Sample treatment: Through the chemical treatment of tallow, changes in its organoleptic properties were observed. Due to the presence of calcium hydroxide and impurities that adhere to the samples in the peeling process, such as sand, stone, and vegetal material, a variation in the grey color of the samples was noted. Finally, tallow acquired a white coloration, the unpleasant odor disappeared, and the material had a clear and clean appearance.

Fat extraction with pressurized solvent: The central composite experimental 2^2 design + star points allowed for the identification of the factors that impact fat extraction in greater magnitudes. The results of the 16 experiments are presented in Table 3.

According to an ANOVA conducted on the complete factorial design, it could be determined that the solvent is the most relevant factor in fat extraction, with a p-value of 0,0006 less than 0,05 at a significance level of 95%, with an R^2 value of 90,53% and an adjusted R^2 of 76,33%, *i.e.*, greater than 70%, which indicates that the variability in the percentage of fat recovery is explained in great magnitude by the factors studied. Therefore, an adequate estimation of the regression coefficients for the adjusted statistical model and the regression equation can be made in order to predict the percentage of fat recovered by varying the experimental factors, as shown in Equation (1).

$$\begin{aligned} \%\,\boldsymbol{RF} = {} & 44,2026 + 6,19082 \times A - 0,108802 \times \\ & B - 0,0502297 \times C - 3,06168 \times A^2 - \\ & 0,28125 \times AB + 0,006475 \times AC - 0,0370247 \times \\ & B^2 + 0,019125 \times BC + 0,000132974 \times C^2 \end{aligned} \quad (1)$$

where % RF is the percentage of fat recovery, A is the type of solvent, B is the time, C is the quantity of solvent, and AA, AB, AC, BB, BC, and CC are the interactions between the factors.

The response surface plot that demonstrates the adjusted model determined by Equation (1) is depicted in Figure 2.

It is observed that, at times greater than 1 h and when the level-1 solvent (gasoline) is used, the percentages of recovery reach up to 50%.

Table 3. Central composite experimental 2^2 design + star points

Type of solvent	Time (hours)	Amount of solvent (mL)	Fat recovery (%)
-1	3	150	36,91
1	3	150	51,65
-2	2	100	28,34
0	2	175	46,35
-1	1	50	33,67
1	3	50	49,81
1	1	50	48,24
-1	1	150	30,39
0	0.5	100	39,57
1	1	150	49,17
0	3.5	100	46,86
0	2	100	44,08
-1	3	50	33,45
0	2	100	44,08
2	2	100	40,98
0	2	25	42,17

Source: Authors

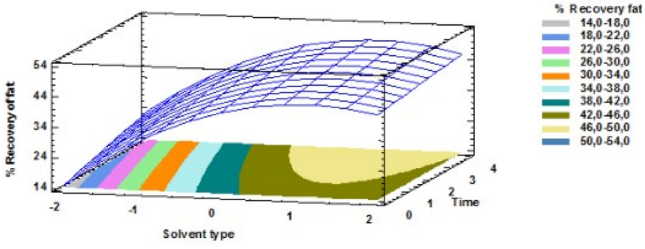

Figure 2. Response surface plot of interaction between solvent type and extraction time
Source: Authors

Commercial gasoline was the solvent that extracted the highest amount of grease, reaching 51,50% in a 3 h period, using 150 mL of solvent and the pressurized extraction technique with solvents in liquid-gas equilibrium, as described in this work. These results are related to the mixture of hydrocarbons present in gasoline (Hua *et al*., 2018) which provide a lipophilic and apolar environment that favors fat recovery. These values are higher than those obtained with other techniques that have been used for the extraction of fat in this type of waste, using hexane and soxhlet equipment and achieving fat recovery values of up to 11,5%. It is clear that the proposed method has the following advantages: small amounts of solvent are required, commercial gasoline is inexpensive, it has short extraction times, and the solvent used is 70% recovered and can be reused for these same purposes. The risks at work using gasoline (as it is highly flammable and hazardous) are reduced by controlling the experimental conditions of extraction. At the end of the processes and through gas chromatography, it was possible to demonstrate that tallow was obtained without any contaminant, since there is no interference in chemical characterization.

Characterization of the physical and chemical properties of extracted fat: It was observed that the fat is yellow and has a smooth texture, its melting point falls in a range between 38-39 °C, the density is 0,8932 g / cm^3, and its dynamic viscosity is 6,93 cP at 60 °C. Table 4 shows the chemical properties observed.

Table 4. Chemical properties of extracted fat

Parameter	Method	Units	Results
Acidity index Acidity	ICONTEC NTC 218	mg KOH / g % oleic acid	1,64 0,82
Saponification value	ICONTEC NTC 335	mg KOH /g of fat	188,43
Iodine value	ICONTEC NTC 283	g I_2/100 g	33,21
Peroxide value	ICONTEC NTC 236	meq O_2/Kg	5,47

Source: Authors

The acidity, saponification, and acidity indices indicate that the degradation of the fat is low, since it contains a low amount of free fatty acids, favoring the extraction of biodiesel. In the transesterification reaction, there are no secondary reactions that alter the composition of the biofuel. The iodine value indicates the low content of unsaturated fatty acids, which confers a great stability of the fat to the oxidative processes, as well as to the mixture of methyl esters present in the biodiesel (de Freitas *et al*., 2019). The peroxide value indicates the stability of the fat once extracted, and the low content of water remaining in the fat is due to the implemented extraction system, which allows for water to be eliminated in the form of steam through the upper valve (Rahman *et al*., 2015), as shown in Figure 1a.

Characteristics of the biodiesel: Biodiesel is a slightly viscous liquid with a pleasant aroma, which is a characteristic of esters, with a translucent yellow coloration. When in contact with the flame, it is consumed in a controlled manner, and no sudden reaction to heat is observed. Its density is 880 kg/m^3, and it has an acid number of 0,078 mg KOH/g and a viscosity of 3,25 mm^2/s at 40 °C (Srinivasan *et al*., 2020). These values fit the range proposed by the international norms, *i.e.*, ASTM D6751 (ASTM International, 2013), as well as by European standards (EN 14214) (European Committee for Standardization, 2003), which regulate the properties of biofuels. According to the chromatographic analysis (Figure 3), the main components of the methyl esters were palmitic and oleic acids, with 20,10% and 15,7%, respectively (Table 5). These values are confirmed by Sandhya *et al*. (2016) with values of 46,60% for palmitic acid and 32,2% for oleic acid; as well as by Moraes *et al*. (2008), who reported values of 26,18% for palmitic acid and 30,09% for oleic acid.

Economic feasibility: 50% of tallow is composed of fat. Approximately 800 mL of biodiesel are produced from each kg of tallow. With 60 tons being produced in the municipality of Belén, approximately 24 000 liters of biodiesel per month can be produced. This amount of biodiesel can be an alternative for the energy needs of the leather production plants, or it can be sold to generate new economic resources. Although Belén is a township with an industrial inclination located in the southwest of Colombia, the applied technology shows low levels of productivity. The leather produced in this industrial area is not competitive, and the profitability of the industry is low. The main limitation to access new markets is the environmental impact caused by solid and liquid waste, so it is necessary to open new production lines such as biodiesel produced from fat contained in tallow. This technology will allow improving profitability while reducing the negative environmental impact of tanneries (Nandhini *et al.*, 2022).

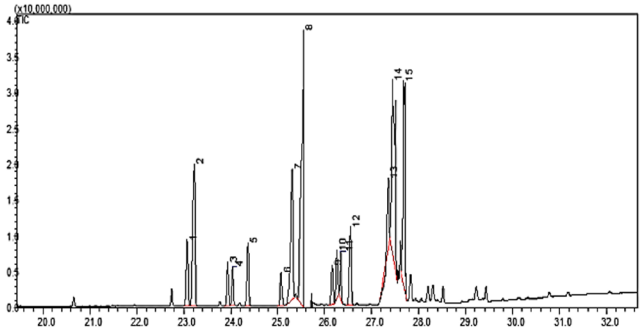

Figure 3. TIC Chromatogram of methyl esters of acids (biodiesel): 1) miristoleic; 2) miristic; 3) decanoic; 4) arachidic; 5) pentanoic; 6) hexadecanoic; 7) palmitoleic; 8) palmitic; 9) isomargaric; 10) isoheptadecanoic; 11) 8-octanoic (2-methylcyclopropyl); 12) heptadecanoic; 13) elaidic; 14) oleic; 15) stearic
Source: Authors

Table 5. Methyl ester components of the biodiesel produced

Peak no.	Fatty acid	Methyl esters (%)
1	Miristoleic acid	3,40
2	Miristic acid	11,20
3	Decanoic acid	2,35
4	Arachidic acid	2,20
5	Pentanoic acid	3,60
6	Hexadecanoic acid	1,90
7	Palmitoleic acid	10,00
8	Palmitic acid	20,10
9	Isomargaric acid	2,20
10	Isoheptadecanoic acid	3,20
11	8- (2-methylcyclopropyl) octanoic acid	2,75
12	Heptadecanoic acid	5,10
13	Elaidic acid	5,90
14	Oleic acid	15,70
15	Stearic acid	10,60

Source: Authors

Conclusions

The extraction technique presented in this work, which incorporates the use of a pressurized solvent, proved to be more efficient, with a fat recovery percentage of 51%, short extraction times, and the use of small amounts of solvent in comparison to conventional techniques such Soxhlet extraction. This results in lower production costs of biodiesel from tallow. It was observed that commercial gasoline is a good solvent for the extraction of fat, and it is easy to acquire and relatively inexpensive. The characteristics of the biodiesel obtained from tallow using the extraction technique constitute a novelty of this work.

The physical and chemical properties of the extracted fat indicate that it is an excellent raw material for the production of biodiesel. In the transesterification process, there are no secondary reactions derived from fat degradation processes, thus allowing to obtain high-quality biodiesel. The biodiesel has good characteristics that are in the ranges reported by technical standards ASTM D6751 (ASTM International, 2013) and EN14214, and it shows good a performance, considering that, from 30 g of raw material used in the transesterification reaction, 22,09 g of biodiesel were extracted.

After extracting the fat from the tallow, a solid residue remains, which is mainly collagen. Studies should be carried out to propose its application as a filling material in filters to remove heavy metals from wastewater.

Acknowledgements

We would like to thank the Center for Environmental Studies (CEA), Department of Exact Sciences, Universidad de Nariño,as well as the Chromatography Lab of the same university.

References

Alptekin, E., Canakci, M., and Sanli, H. (2012). Evaluation of leather industry wastes as a feedstock for biodiesel production. *Fuel, 95*, 214–220. https://doi.org/10.1016/j.fuel.2011.08.055

ASTM International (2013). *ASTM D6751-12: Standard specification for biodiesel fuel blend stock (B100) for middle distillate fuels*. ASTM International. https://doi.org/10.1520/D6751-12

ASTM International (2017). *ASTM D1298-12b: Standard test method for density, relative density, or API gravity of crude Petroleum and Liquid petroleum products by hydrometer method*. ASTM International. https://www.astm.org/d1298-12br17.html

ASTM International (2013). *ASTM D445-06: Standard test method for kinematic viscosity of transparent and opaque liquids (and calculation of dynamic viscosity)*. ASTM International. https://www.astm.org/d0445-21e01.html

Bhatti, H. N., Hanif, M. A., Qasim, M., and Ata-ur-Rehman. (2008). Biodiesel production from waste tallow. *Fuel, 87*(13-14), 2961-2966. https://doi.org/10.1016/j.fuel.2008.04.016

Bosu, S., and Rajamohan, N. (2022). Nanotechnology approach for enhancement in biohydrogen production – Review on applications of nanocatalyst and life cycle assessment. *Fuel, 323*, 124351. https://doi.org/10.1016/j.fuel.2022.124351

de Freitas, O. N., Cardoso Rial, R., Fontoura Cavalheiro, L., Dos Santos Barbosa, J. M., Domingues-Nazário, C. E., and Viana, L. H. (2019). Evaluation of the oxidative stability and cold filter plugging point of soybean methyl biodiesel/bovine tallow methyl biodiesel blends. *Industrial Crops and Products, 140*, 111667. https://doi.org/10.1016/j.indcrop.2019.111667

Díaz-Burgos A. (2019). *Obtención de biodiesel a partir de sebo bovino aislado de los residuos sólidos producidos en el proceso de descarnado en el curtido de cuero* [Unpublished undergraduate thesis, Universidad de Nariño, Colombia].

European Committee for Standardization (2003). *Liquid petroleum products - Fatty acid methyl esters (FAME) for use in diesel engines and heating applications - Requirements and test methods. Method EN 14214*. European Committee for Standardization

Hua, Y., Liu, F., Wu, H., Lee, C. F., and Wang, Z. (2018). Experimental evaluation of various gasoline surrogates based on soot formation characteristics. *Energy and Fuels, 32*(11), 11961-11969. https://doi.org/10.1021/acs.energyfuels.8b02931

ICONTEC (2011). *Grasas y aceites vegetales y animales* (*NTC 218, 236, 283, 287, and 335*). Instituto Colombiano de Normas Técnicas y Certificación.

Jain, S., Sharma, M. P., and Rajvanshi, S. (2011). Acid base catalyzed transesterification kinetics of waste cooking oil. *Fuel Processing Technology, 92*(1),32-38. https://doi.org/10.1016/j.fuproc.2010.08.017

Knothe, G., and Razon, L. F. (2017). Biodiesel fuels. *Progress in Energy and Combustion Science, 58*, 36-59. https://doi.org/10.1016/j.pecs.2016.08.001

Kubendran, D., Salma-Aathika, A. R., Amudha, T., Thiruselvi, D., Yuvarani, M., and Siva-Nesan, S. (2017). Utilization of leather flesh-ing waste as a feedstock for sustainable biodiesel production. *Energy Sources, Part A: Recovery, Utilization and Environmental Ef-fects, 39*(15),1587-1593. https://doi.org/10.1080/15567036.2017.1349218

Mata, T. M., Cardoso, N., Ornelas, M., Neves, S., and Caetano, N. S. (2011). Evaluation of two purification methods of biodiesel from beef tallow, pork lard, and chicken fat. *Energy and Fuels, 25*(10), 4756-4762. https://doi.org/10.1021/ef2010207

Nandhini, R., Berslin, D., Sivaprakash, B., Rajamohan, N. and, Vo, D.-V. (2022). Thermochemical conversion of municipal solid waste into energy and hydrogen: A review. *Environmental Chemistry Letters, 20*, 1645-1669. https://doi.org/10.1007/s10311-022-01410-3

Naylor, R. L., and Higgins, M. M. (2017). The political economy of biodiesel in an era of low oil prices. *Renewable and Sustainable Energy Reviews, 77*, 695-705. https://doi.org/10.1016/j.rser.2017.04.026

Pollardo, A.A., Lee, H.S., Lee, D., Kim, S., Kim, J.(2017). Effect of supercritical carbon dioxide on the enzymatic production of biodiesel from waste animal fat using immobilized Candida antarctica lipase B variant. *BMC Biotechnology*,*17*(1), 70. https://doi.org/10.1186/s12896-017-0390-1

Rahman, M. H., Hossain, M. M., Rahman, S. M. E., Amin, M. R., and Oh, D. H. (2015). Evaluation of physicochemical deterioration and lipid oxidation of beef muscle affected by freeze-thaw cycles. *Korean Journal for Food Science of Animal Resources, 35*(6), 772-782. https://doi.org/10.5851%2Fkosfa.2015.35.6.772

Ranjitha, J., Gokul Raghavendra, S., Vijaya-lakshmi, S., and Deepanraj, B. (2020). Production, optimization and engine characteristics of beef tallow biodiesel rendered from leather fleshing and slaughterhouse wastes. *Biomass Conversion and Biorefinery, 10*(3), 675-688. https://doi.org/10.1007/s13399-019-00501-6

Sandhya, K. V., Abinandan, S., Vedaraman, N., and Velappan, K. C. (2016). Extraction of fleshing oil from waste limed fleshings and biodiesel production. *Waste Management, 48*, 638-643. https://doi.org/10.1016/j.wasman.2015.09.033

Šánek, L., Pecha, J., Kolomazník, K., and Bařinová, M. (2015). Biodiesel production from tannery fleshings: Feedstock pretreatment and process modeling. *Fuel, 148*(148), 16–24. https://doi.org/10.1016/j.fuel.2015.01.084

Sayaddi, R. A., Rajamohan, N., and Vasseghian, Y. (2022). Enhanced production of biodiesel using nanomaterials: A detailed review on the mechanism and influencing factors. *Fuel, 319*, 123862. https://doi.org/10.1016/j.fuel.2022.123862

Srinivasan, G. R., Shankar, V., Chandra Sekharan, S., Munir, M., Balakrishnan, D., Mohanam, A., and Jambulingam, R. (2020). Influence of fatty acid composition on process optimization and characteristics assessment of biodiesel produced from waste animal fat. *Energy Sources, Part A: Recovery, Utilization and Environmental Effects*, 1771477. https://doi.org/10.1080/15567036.2020.1771477

Verma, P., and Sharma, M. P. (2016). Review of process parameters for biodiesel production from different feedstocks. *Renewable and Sustainable Energy Reviews, 62*, 1063-1071. https://doi.org/10.1016/j.rser.2016.04.054

Vidales-Olivo, M. P. A., Leos-Magallanes, M. Y., and Campos-Sandoval, M. G. (2010). Extracción de grasas y aceites en los efluentes de una Industria Automotriz. *Ciencia y Tecnológía, 40*(40), 29-34. https://www.redalyc.org/pdf/944/94415759007.pdf

Yuan, M., Chen, Y., Chen, J., and Luo, Y. (2017). Dependence of cold filter plugging point on saturated fatty acid profile of biodiesel blends derived from different feedstocks. *Fuel, 195*, 59-68. https://doi.org/10.1016/j.fuel.2017.01.054

Research Article/Civil and Sanitary Engineering http://doi.org/10.15446/ing.investig.88403

HFFB Test and Wind-Induced Vibration Analysis on 1 000 kV Transformer Frame

Prueba HFFB y análisis de vibraciones eólicas en una estructura de transformadores de 1 000 kV

Wennian Shang[1], Jun Gong[2], Xudong Zhi[3], and Haoyang Wang[4]

ABSTRACT

In order to propose a complete, wind-resistant design method for ultra-high voltage (UHV) transformer frames, the wind-induced vibration characteristics of a 1 000 kV transformer frame (TF1000) were studied using a high-frequency force balance (HFFB) test. Five section models and one whole model of the TF1000 were designed and constructed using 3D printing, and these were evaluated in a wind tunnel by means of HFFB tests for multiple loading scenarios. The finite element method (FEM) was used on the test data to analyze the wind-induced vibration on the TF1000. The results demonstrate that the shape factor of the TF1000 is significantly affected by the flow field type and solidity ratio; the minimum value occurs when the wind direction is between 30 and 45°. Moreover, all the shape factor values obtained by the test are larger than those established by the Chinese code. The wind-induced vibration analysis indicates that the most unfavorable wind direction for the TF1000 is approximately 60°, with a wind-induced vibration coefficient between 1,7 and 3,9.

Keywords: high-frequency force balance test, finite element analysis, 1000 kV transformer frame, shape factor, wind-induced vibration coefficient

RESUMEN

Para proponer un método completo y resistente al viento para estructuras de transformadores de tensión ultra alta (UHV), se estudiaron las propiedades de vibración eólica de una estructura de transformadores de alta presión de 1 000 kV (TF1000) mediante una prueba de equilibrio de fuerzas de alta frecuencia (HFFB). Se diseñaron y elaboraron cinco modelos de sección y un modelo integral para el TF1000 utilizando impresión 3D y se evaluaron en un túnel de viento mediante pruebas HFFB para varios escenarios de carga. Se utilizó el método de los elementos finitos (FEM) en los datos de prueba para analizar la vibración eólica en el TF1000. Los resultados demuestran que los factores de forma del TF1000 se ven significativamente afectados por el tipo de campo de flujo y la relación de solidez; el valor más bajo ocurre cuando la dirección del viento está entre 30 y 45°. Además, todos los factores de forma obtenidos en la prueba fueron superiores a los valores prescritos en el código chino. El análisis de las vibraciones eólicas indica que la dirección del viento más desfavorable para el TF1000 es aproximadamente 60°, con un coeficiente de vibración eólica entre 1,7 y 3,9.

Palabras clave: prueba de equilibrio de fuerzas de alta frecuencia, análisis de elementos finitos, estructuras de transformadores de 1000 kV, factor de forma, factor de vibración eólica

Received: June 18th, 2020
Accepted: June 13th, 2022

Introduction

The 1 000 kV ultra-high voltage (UHV) power grid has high transmission capacity and efficiency with small losses, which is consistent with the aims of the power industry to promote sustainable development and meet its strategic needs. However, the impact of natural disasters on the UHV power grid may be very serious. For example, transformer frames, which have characteristics common with high-rise (Music and Soto, 2021) and long-span structures, are susceptible to ice and earthquake loads (Gong *et al*., 2020a, 2020b, 2021, 2022), as well as to wind loads, and they are prone to vibration fatigue damage and collapse under extreme conditions.

Wind engineering research methods include theoretical analysis (Shiotani and Iwatani, 1980; Solari, 1983;

[1] Master in Civil Engineering, Harbin Institute of Technology, China. Affiliation: Professorate senior engineer, Shandong Electric Power Engineering Consulting Institute Co., Ltd., Ji'nan, China.

[2] PhD in Civil Engineering, Harbin Institute of Technology, China. Affiliation: Lecturer, School of Civil Engineering and Geomatics, Southwest Petroleum University, Chengdu, China.

[3] PhD in Civil Engineering, Harbin Institute of Technology, China. Affiliation: Full professor, School of Civil Engineering, Harbin Institute of Technology, Harbin, China.

[4] Master's student in Civil Engineering, School of Civil Engineering, Harbin Institute of Technology, Harbin, China

* Corresponding author: Jun Gong, jun.gong@swpu.edu.cn

How to cite: Shang, W., Gong, J., Zhi, X., and Wang, H. (2023). HFFB Test and Wind-Induced Vibration Analysis on 1 000 kV Transformer Frame. *Ingeniería e Investigación, 43*(1), e88403. https://doi.org/10.15446/ing.investig.88403

Davenport, 1967; Balendra *et al*., 1989), field measurement, and wind tunnel testing. Wind tunnel tests, widely used in long-span space structures and high-rise structures, include the model multi-point synchronous pressure test (Zou, 2013), the aero-elastic model test (Wang, 2011), and the high-frequency force balance (HFFB) test (Bernardini *et al*., 2013). The HFFB test allows calculating the wind-induced response of a structure by measuring the bending moment and force on the model under a wind load by using a highly sensitive balance installed at the bottom. Put forward in the 1980s, the HFFB method has been widely used to study wind-induced vibration responses of high-rise structures. Xiao and Li (2011) carried out HFFB tests to investigate the complex characteristics of wind-induced vibration responses of UHV DC transmission towers. Their results suggest that an HFFB-based modified vibration method reliably and conveniently calculates wind-induced vibration responses and equivalent wind loads on a transmission tower (Xiao and Li, 2011). Gu *et al*. (2000) used the HFFB technique to study the dynamic responses and equivalent wind loads of the Shanghai Jin Mao Building. Their test results show that the vibration response to crosswinds is larger than that to winds in the downwind direction. Moreover, the interference caused by surrounding buildings reduces the average aerodynamic coefficient while increasing the pulse dynamic coefficient (Gu *et al*., 2000). Yu (2007) investigated the three-dimensional (3D) wind load of the He'nan Broadcast and TV Tower based on the HFFB test and analyzed the characteristics of the wind-induced vibration responses and frequency spectrum of the structure in all wind directions (Yu, 2007). Huang and Gu (2005) studied the interference effects on wind-induced torsional loads between two tall buildings with square cross-sections. Using the HFFB technique, they presented the values of the interference factor of the mean, root mean square (RMS), and peak torsional loads for various configurations (Huang and Gu, 2005).

The numerical method offers low-cost and high-efficiency research advantages. Therefore, it has been extensively used by many scholars to study the wind-induced vibration responses of high-rise structures. Kapania and Yang (1984) analyzed the random wind responses of a cooling tower using the Monte Carlo simulation approach and compared the time-domain responses of the structure for five wind models (Kapania *et al*., 1984). Xiao (2009) studied the 3D wind-induced vibration response of a transmission tower using the wind tunnel aero-elastic model test method and the finite element buffeting analysis method (Xiao, 2009). Guo *et al*. (2006) analyzed the wind-induced dynamic response in the time domain of the Zhoushan long span transmission tower using the finite element method (FEM) and conducted wind tunnel aero-elastic model tests. They found that the system response can be divided into background and resonant responses, as long as the influence of transmission lines is considered (Guo *et al*., 2006). Lou *et al*. (1996) carried out the wind tunnel aero-elastic model test on a 183 m high self-supporting tower. They also performed numerical computations on the buffeting response in the frequency-domain based on quasi-steady theory and the space truss model (Lou *et al*., 1996). Yu (2018) investigated the wind-induced vibration responses of a single-column lightning rod, a single span, and three spans of the lightning rod structures in the time domain. They proposed a simplified calculation method for the wind-induced vibration response of the lightning rod structure (Yu, 2018).

Altogether, the abovementioned research shows that wind-induced vibration analysis has been successfully used in high-rise buildings, and that significant progress has been made in the field of transmission towers. However, there have been few similar efforts on the UHV transformer frame, and there are currently no provisions in the design code specifying the values of wind loads. Hence, in order to propose a complete, wind-resistant design method for the UHV transformer frame, this research studied the wind-induced vibration characteristics of a 1 000 kV transformer frame (TF1000) based on the HFFB test. First, the general features of the HFFB test are introduced, including the experimental equipment and design, the construction of the experimental model, and the test plan. Then, the test data were analyzed carefully to obtain the shape factor. Futhermore, the wind-induced vibration response of the TF1000 was numerically analyzed using the FEM.

Experimental conditions

A UHV TF1000 in the Shandong province, China, was selected as the analytical model to perform the wind tunnel test and numerical studies. A 70 m high prototype TF1000 spanning 49 m was assembled using two columns with a variable cross-section and one equal section beam made of Q355 steel tubes, as shown in Figure 1. The designation Q355 means a nominal yield strength of 355 MPa. In the basic design, the wind pressure of the structure is 0,56 kPa. The influence of the transmission lines and electrical equipment under wind loads on the wind-induced vibration response of the TF1000 was not considered in this study.

Test equipment

The HFFB test on the TF1000 was performed in a small test section at the Wind Tunnel and Water Flume of the Harbin Institute of Technology (WTWF-HIT). The laboratory is a closed reflux wind tunnel with two test sections. The dimensions of the small test section are $4 \times 3 \times 25$ m. The wind speed can be adjusted continuously, and the maximum wind speed in the empty tunnel is 44 m/s. Moreover, the turbulence, the mean velocity deviation, and the flow deflection angle of the wind field are less than 1,0, $\pm$2,0, and 1,0%, respectively. Furthermore, the wind tunnel is equipped with an automatic turntable system 2,4 m in diameter, which can be adjusted in a counterclockwise direction to any angle from 0 to 360° with a maximum error of 1°.

The experiment involved the test equipment and a data acquisition system, which included the HFFB, an

anemometer, and a signal analysis system. The HFFB (ATI delta ip68 si-660-60, ATI Industrial Automation, Inc., Apex, North Carolina, USA) is a six-component force sensor that can simultaneously provide force information in a 3D space, which consists of the forces and torques in three directions (*Fx*, *Fy*, *Fz*, *Tx*, *Ty*, and *Tz*) (Figure 2a), whose sampling frequency is 1 kHz. A Cobra probe 3D pulsating wind speed meter was used to measure the wind speed in different wind fields. Its sampling frequency is more than 2 kHz, and it can measure turbulence within ±45 degrees of wind direction. This meter is highly suitable for situations involving high turbulence and an unknown wind direction (Figure 2b).

Figure 1. TF1000 prototype
Source: Authors

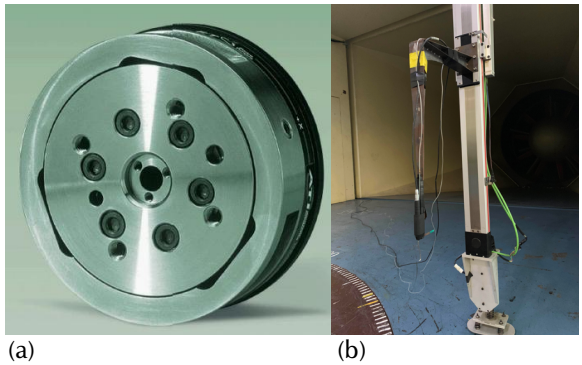

(a) (b)

Figure 2. Test equipment: a) multi-axis force/torque sensor, b) Cobra probe 3D pulsating wind speed meter
Source: Authors

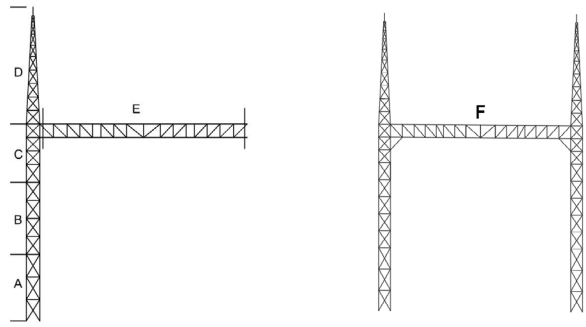

(a) (b)

Figure 3. Experimental model designations: a) A, B, C, D, and E correspond to section models of the OLF1000; b) F corresponds to the whole model of the TF1000
Source: Authors

Design and construction of the experimental model

In this experiment, five section models (A, B, C, D, E) and one whole model (F) were designed for testing, as shown in Figure 3. In a HFFB test, if the reduced-scale factor of the experimental model is too large, then its structural stiffness is very poor; and, if the factor is too small, then too many measurement errors will occur. A reduced-scale factor of 1:50 was selected for test models A, B, C, and D, and a factor of 1:100 was selected for models E and F. The frontal and lateral windshield areas measure 0,0495 and 0,0249 m^2, respectively, and their corresponding solidity ratios are 0,4 and 0,2%, respectively, which meets the requirements of the wind tunnel test. Furthermore, due to the complex layout of the TF1000, 3D printing technology was used to construct the experimental models. Stereolithgraphy apparatus (SLA) photosensitive resin was selected as the printing material because of its light weight, high strength, and rigidity. The 3D printing equipment (iSLA550, ZRapid Tech, Suzhou, China) and experimental models are shown in Figures 4 and 5, respectively.

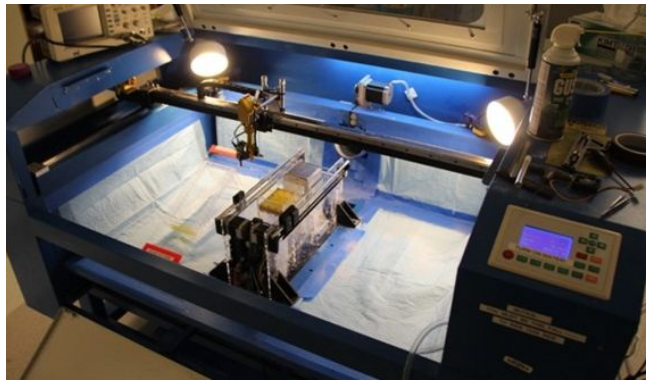

Figure 4. 3D printing equipment
Source: Authors

Test plan

TF1000s are mostly located in landforms that offer few sheltered structures. These correspond to Landforms

A and B in the Chinese code (China Architecture and Building Press, 2012). Landform B has rougher terrain than Landform A. The experimental flow fields used in the HFFB test consisted of one uniform flow field and two turbulent flow fields corresponding to Landforms A and B. The turbulent flow fields were set up using Ding's method, which was thoroughly presented in a study on passive simulation test technology of near-earth turbulence (Ding, 2013).

The highest position of the experimental model was selected as the reference height, and the wind speed was set to 12 m/s in the HFFB test. To ensure the stability of the test data, the initial test data points were discarded. Three samples were collected for each test condition, and each sampling lasted for 90 s. Moreover, before the test, the HFFB was adjusted to align its *x* axis positive direction with the incoming flow direction, *i.e.*, the initial state to which the experimental model was fixed. The initial state was set as the wind direction 0° angle. From this point, every 15° change in the wind direction angle was set as a test condition. The HFFB test of models A~F under three flow fields and different wind directions was planned according to Table 1. Because the height of Model E is low (it is the crossbeam of the TF1000), the wind speed at each point is the same. Thus, only a uniform flow field was applied to model E. Model F (*i.e.*, the whole TF1000) is symmetrical; only half of the structure was placed on the force balance. The other half was also placed in the wind field to simulate the real wind field environment, as shown in Figure 6.

Figure 5. Experimental models constructed by 3D printing: (a) Experimental models; (b) Model A in testing
Source: Authors

Table 1. Test schedule

MODEL	Solidity Ratio		Reduced-scale factor	Wind direction angle	Flow field
	Front	Side			
A	0,400	0,222	1:50	0~90°	Uniform, A, and B
B	0,308	0,217	1:50	0~90°	
C	0,391	0,322	1:50	0~90°	
D	0,322	0,313	1:50	0~90°	
E	0,270	0,177	1:50	0~90°	
F	0,361	0,278	1:100	0~90°	
F	0,361	0,278	1:100	180~270°	

Source: Authors

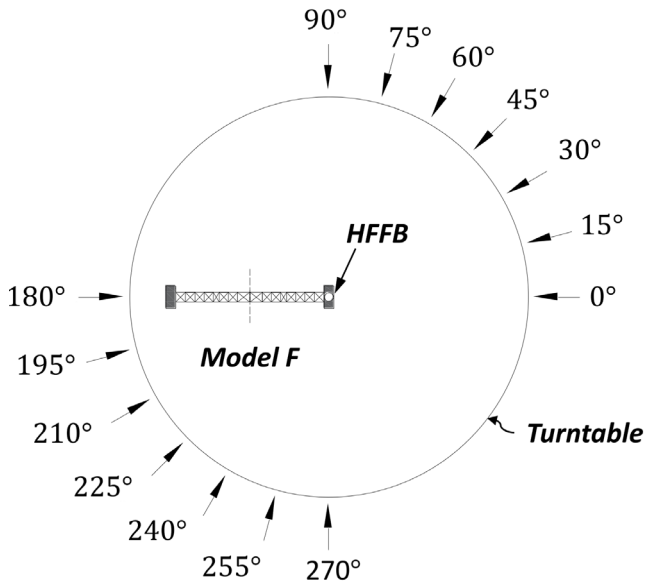

Figure 6. Wind direction angle
Source: Authors

Experimental data analysis

Experimental data processing method

The aerodynamic coefficient is the ratio of the actual wind load on the structure to the theoretical value of the average wind load obtained from the average test wind speed and the reference area. It reflects the influence of the aerodynamic shape of the structure on the distribution of the wind load. To convert the test data into a wind load time history applied to the real structure, the test data obtained by the wind tunnel test were expressed by the dimensionless aerodynamic coefficient, which is calculated as follows:

$$C_x = F_x / \left(0,5\rho V_\infty^2 S\right) \quad (1)$$

$$C_y = F_y / \left(0,5\rho V_\infty^2 S\right) \quad (2)$$

$$C_{mz} = M_z / \left(0,5\rho V_\infty^2 SB\right) \quad (3)$$

where B is the bottom width of the structure perpendicular to the wind direction; V_∞ is the wind speed; ρ is the air density; S is the projected area of structural members along the wind direction; F_x, F_y, and M_z are the forces and torque along the x, y, and z axes, respectively, as obtained by the HFFB test; and C_x, C_y, and C_{mz} are the aerodynamic coefficient components along the x, y, and z axes, respectively.

The wind factor of the structure can be divided into the drag (*i.e.*, shape factor) and lift coefficients. Since the lift coefficient has little effect on the structure, this study focused on analyzing the drag coefficient, which is obtained by combining the aerodynamic coefficients along the *x*

and *y* axes, as shown in Equation (4), where α is the wind direction angle.

$$C_D = C_x \cos(\alpha) + C_y \sin(\alpha) \quad (4)$$

Experimental results

Figure 7 shows the shape factors of models A~F under different wind direction angles. As the wind direction angle changed from 0~90°, the shape factor of each experimental model initially decreased and then increased as the wind direction angle increased. The wind direction angles corresponding to the minimum shape factor of each model were slightly different, assuming values between 30 and 45°. Moreover, the shape factor decreased in flow fields A and B, as well as in the uniform flow field, and it changed gradually with the wind direction angle in a uniform flow field. Therefore, the type of flow field affects the wind load distribution of the TF1000. Figure 8 compares the shape factor of four section models in flow fields A and B, as well as in the uniform flow field. The results show that the shape factor of Models A, B, C, and D decreased under the same wind direction angle, which indicates that this factor is mainly related to the windshield area (Table 2).

Figure 9 illustrates that the shape factor measurements obtained in the HFFB test are larger than the Chinese code's recommended values (China Architecture and Building Press, 2012). This is because the code only considers the solidity ratio and the shape of the member section in determining the shape factor of a high-rise tower structure (Table 3). According to the wind direction defined in Figure 10, the TF1000 columns and crossbeam members are too complex and diverse to rely on the code method in determining its shape factor.

Table 2. Windshield area of section models (cm²)

Section model	Model A	Model B	Model C	Model D
Downwind	71,12	61,04	59,24	52,60
Crosswind	81,68	73,48	63,72	52,60

Source: Authors

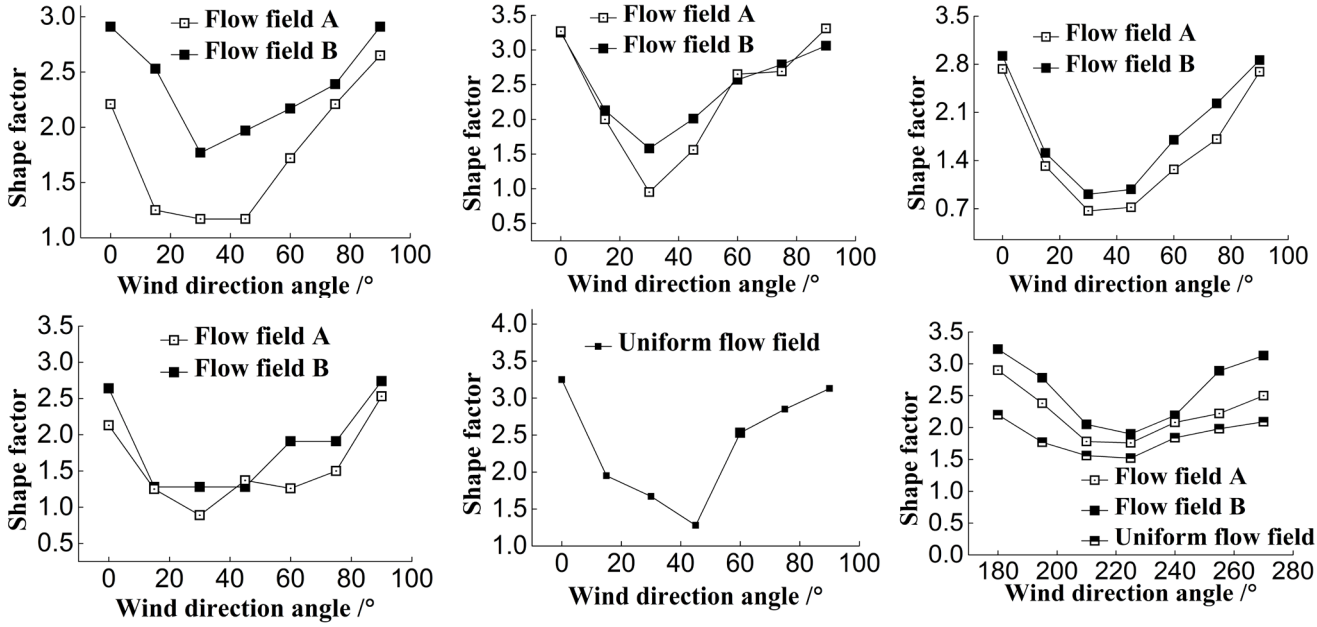

Figure 7. Shape factors: a) Model A, b) Model B, c) Model C, d) Model D, e) Model E, f) Model F
Source: Authors

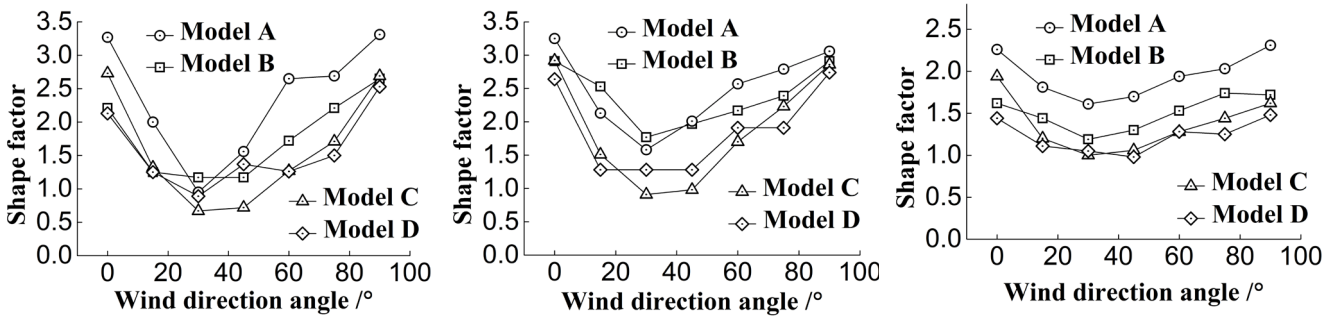

Figure 8. Shape factors of models A~D under same flow field: a) flow field A, b) flow field B, c) uniform flow field
Source: Authors

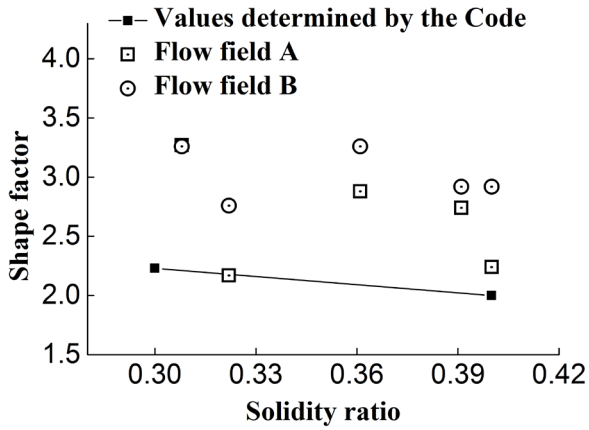

Figure 9. Comparison of shape factors (testing and code)

Table 3. Specifications for the shape factor of tower structures

Solidity ratio	Wind direction I	Wind direction II	
		Single angle steel	Combined angle steel
≤0,1	2,6	2,9	3,1
0,2	2,4	2,7	1,9
0,3	2,2	2,4	2,7
0,4	2,0	2,2	2,4
0,5	1,9	1,9	2,0

Source: China Architecture and Building Press (2012)

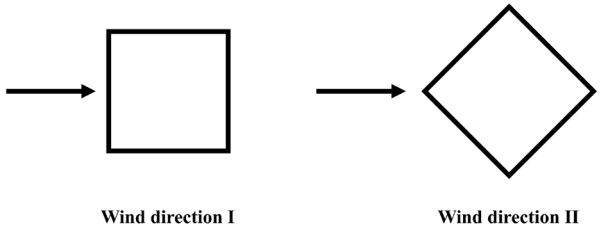

Figure 10. Wind direction of the tower structure showing rectangle outline
Source: Authors

Analysis of wind-induced vibration response based on the FEM

The wind-induced vibration analysis of the TF1000 based on FEM is presented in this section. The wind load distribution of four section models measured via the HFFB test is used to solve the corresponding wind load time history of the TF1000 nodes, which is applied to the TF1000's finite element model (FE model) in order to perform a nonlinear calculation of the wind-induced vibration responses along and across the wind direction.

FE model

The FE model used in the wind-induced vibration analysis aimed to simulate the members of the TF1000 with 16 kinds of pipe section sizes, whose maximum and minimum values were ϕ377×12 mm and ϕ89×6 mm, respectively. Members with the same node were connected rigidly, while members of the TF1000 columns were fixed to the ground. Additionally, the ideal elastic-plastic constitutive model was adopted for the analysis. Its modulus of elasticity was 206 GPa, its Poisson's ratio 0,3, its steel density 7 850 kg/m^3, and its yield strength 345 MPa. Rayleigh damping was used for dynamic analysis with a ratio of 0,02. The established FE model is shown in Figure 11.

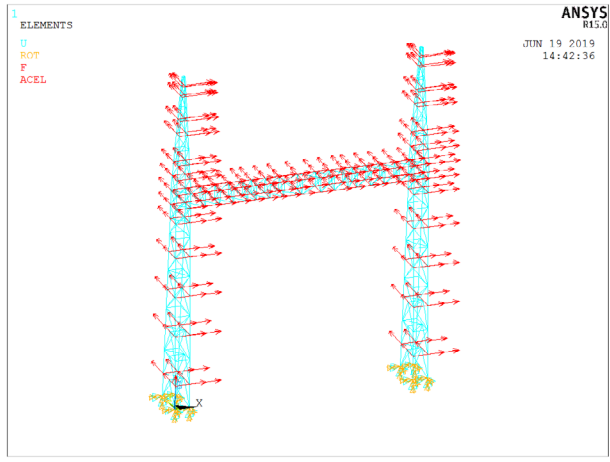

Figure 11. Analytical model of the TF1000 for studying wind-induced vibration response
Source: Authors

Wind loads

The TF1000 was divided into five section models (*i.e.*, A ~ E) in HFFB test, and the aerodynamic coefficients of each section model were transformed into the wind load time history at different heights via the force formula, a function of the aerodynamic coefficient, wind speed, and windshield area. The detailed steps to obtain the wind load time history are as follows:

i) HFFB tests were carried out on experimental models A, B, C, D and E to obtain aerodynamic coefficients. Then, the mean values of the aerodynamic coefficients in the *x* and *y* directions were determined through Equations (5) and (6), where i = A ~ E.

$$\mu_{iX} = mean\left(C_{FX}(t)\right) \tag{5}$$

$$\mu_{iY} = mean\left(C_{FY}(t)\right) \tag{6}$$

ii) The wind load actually borne by the TF1000 was then assumed to be composed of the loads on five section models. Equations (7) and (8), which are applicable at any time, were solved, where $F(X)_{\text{total}}$ and $F(Y)_{\text{total}}$ are the forces of Model F in the *x* and *y* directions, respectively; u_{hi} is the wind speed at the corresponding height of section model *i*; and A_{iX} and A_{iY} are windshield areas in the *x* and *y* directions of section model *i*, respectively.

$$F(X)_{\text{toal}} = \sum_{i=A}^{E} \mu_{iX} \cdot \frac{1}{2} \rho u_{hi}^2 \cdot A_{iX} \quad (7)$$

$$F(Y)_{\text{toal}} = \sum_{i=A}^{E} \mu_{iY} \cdot \frac{1}{2} \rho u_{hi}^2 \cdot A_{iY} \quad (8)$$

iii) Wind loads on the whole model F were distributed to each section model, and then the total load time history of each section model was distributed to each node according to Equations (9) and (10), where λ_L and λ_V are the reduced-scale factors of length and wind speed, respectively. The load distribution is shown in Figure 11.

$$F(X)_i = \frac{\mu_{iX} \cdot \frac{1}{2} \rho u_{hi}^2 \cdot A_{iX}}{\sum_{i=A}^{E} \mu_{iX} \cdot \frac{1}{2} \rho u_{hi}^2 \cdot A_{iX}} \cdot F(X)_{\text{toal}} \cdot \lambda_L^2 \cdot \lambda_V^2 \quad (9)$$

$$F(Y)_i = \frac{\mu_{iY} \cdot \frac{1}{2} \rho u_{hi}^2 \cdot A_{iY}}{\sum_{i=A}^{E} \mu_{iY} \cdot \frac{1}{2} \rho u_{hi}^2 \cdot A_{iY}} \cdot F(Y)_{\text{toal}} \cdot \lambda_L^2 \cdot \lambda_V^2 \quad (10)$$

It should be noted that the effect of turbulence on the vertical distribution of the wind load is ignored in this study because the wind-induced response of the TF1000 is mainly caused by the superposition of the wind load horizontal distribution.

Wind-induced vibration analysis

Wind-induced vibration response: Figure 12 shows the changes in the average displacement at different heights of the TF1000 with the wind direction angle in different flow fields. The results show that, as the height on the TF1000 increases, the nodal displacement increases continuously under the action of the wind load at the same wind direction angle, and the displacement at the top of the column reaches the maximum value. Moreover, regardless of the flow field (A or B), as the wind direction angle increases from 0 to 90°, the displacement in the *x* and *y* directions initially increases and then decreases. In addition, when the wind direction angle is 60°, the average displacement reaches the maximum value, thus suggesting that the most unfavorable wind direction for the TF1000 is 60°.

Wind-induced vibration coefficient (*WVC*): Figure 13 shows the WVCs of the TF1000 under different wind direction angles. The results suggest that the WVC in the *y* direction

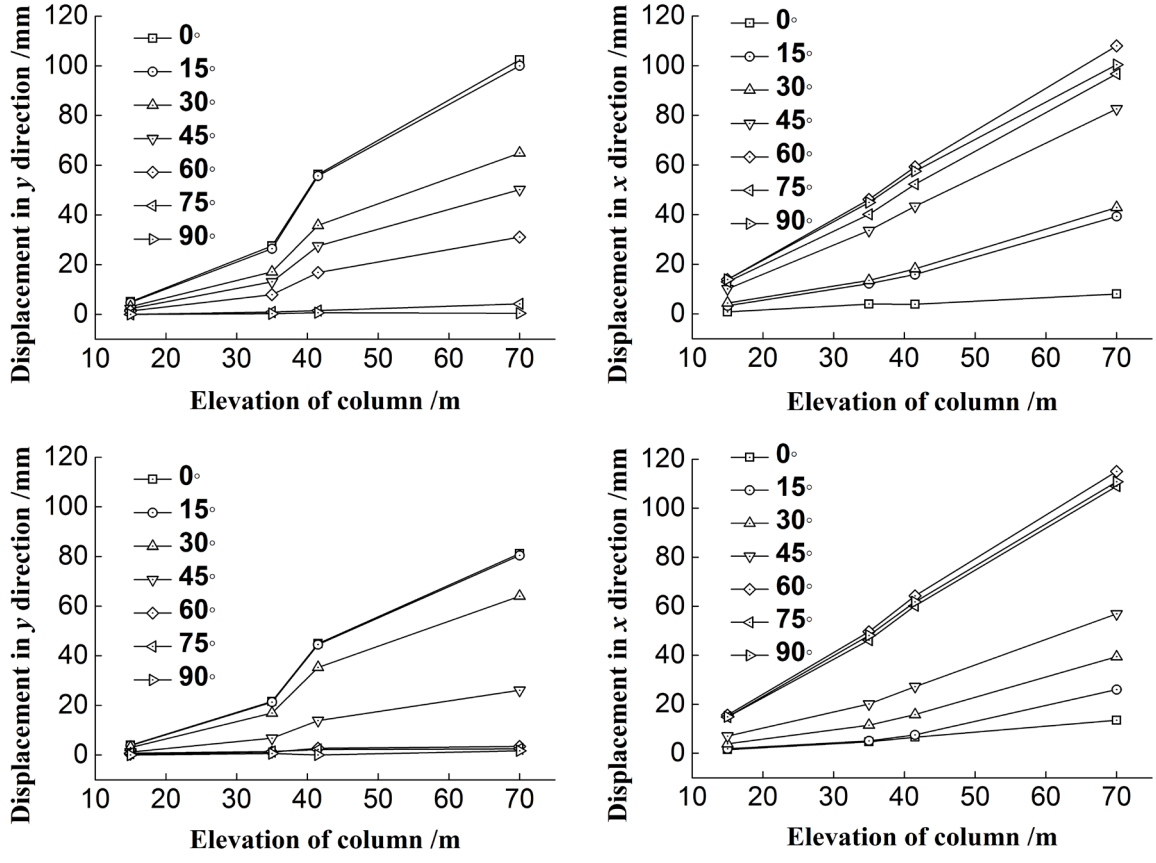

Figure 12. Wind-induced vibration responses: a) displacement along the *y* axis under flow field A, b) displacement along the *x*-axis under flow field A, c) displacement along the *y* axis under flow field B, d) displacement along the *x* axis under flow field B
Source: Authors

increases along with the increase in the height of the TF1000 column that is subjected to the same wind direction angle. The WVC also increases as the wind direction angle increases within a certain range. In the *x* direction, two WVC trends at various heights and different wind direction angles are apparent: one trend involves an initial increase, followed by a decrease; and the other one is the reverse of the first. Additionally, under flow field B, the WVC values are greater than those under flow field A, which indicates that the flow field has an effect on the WVC. Finally, the WVC values of the TF1000 range from 1,7 to 3,9. This range may be a useful reference for engineering design.

Conclusions

This work studied the experimental and numerical responses of the TF1000 under different wind loads. Five section models and one whole model of the TF1000, designed and constructed by means of 3D printing, were evaluated under multiple loading cases in the wind tunnel via the HFFB test. The test data were used in the FEM to conduct wind-induced vibration analysis. The key findings and conclusions are summarized below:

i) The wind direction angle corresponding to the minimum shape factor of each model is between 30 and 45°. The shape factor measurements obtained in the HFFB test are generally larger than those determined by the Chinese code (China Architecture and Building Press, 2012). This significantly indicates that the method mentioned in the code underestimates the design wind load, and the results in this paper can provide a reference for improving it. The shape factor distribution is influenced by the flow field and windshield area, and the larger the windshield area, the larger the shape factor.

ii) As the wind direction angle increases from 0 to 90°, the displacements in the *x* and *y* directions initially increase and then they decrease. When the wind direction angle is 60°, the average displacement reaches the maximum value, indicating that the most unfavorable wind direction for the TF1000 is 60°.

(3) The WVC values under flow field B are greater than those under flow field A, which indicates that the flow field affects the WVC. The WVC values of the TF1000 range from 1,7 to 3,9, which may be useful reference values in engineering design.

Acknowledgements

This work was conducted with financial support from Heilongjiang Province Natural Science Foundation, China [Grant No. JQ2020E004], the Young Scholars Development Fund of SWPU [Grant No. 202299010016], and the R&D project of Shandong Electric Power Engineering Consulting Institute Corp., Ltd. [Project designation: 37-2018-24-K0005].

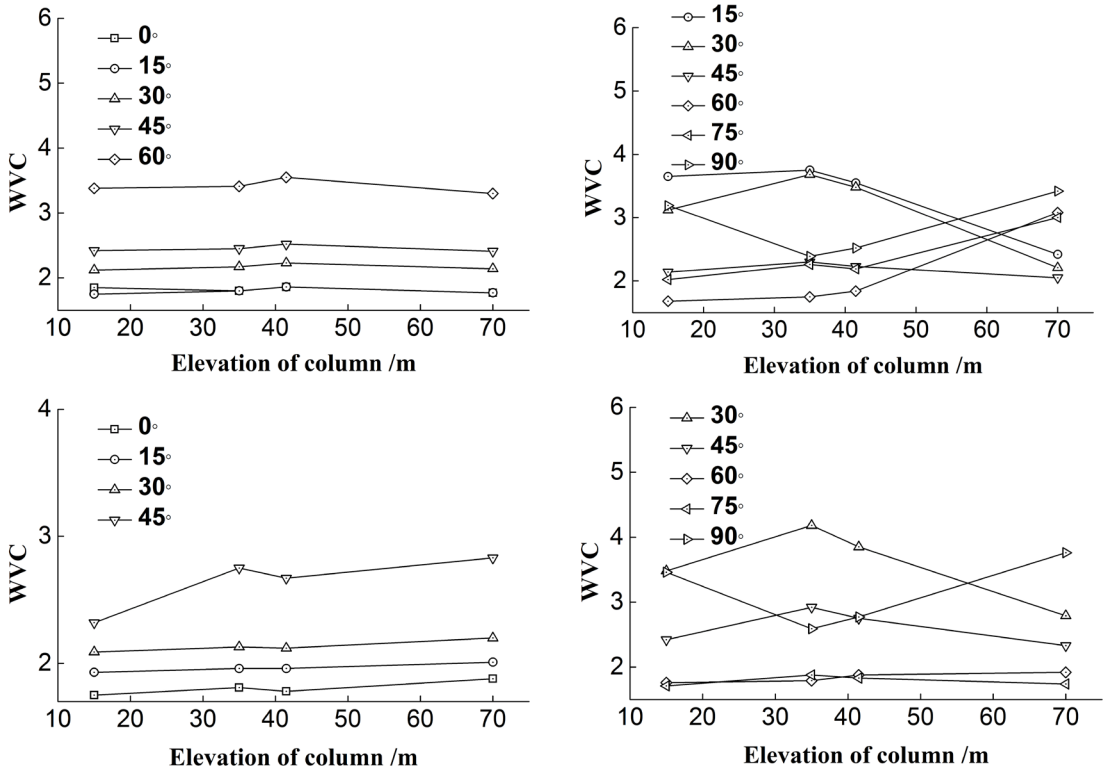

Figure 13. WVCs: a) WVC along the *y* axis under flow field A, b) WVC along the *x* axis under flow field A, c) WVC along the *y* axis under flow field B, d) WVC along the *x* axis under flow field B
Source: Authors

References

Balendra, T., Nathan, G., and Kang, K. H. (1989). A deterministic model for along-wind motion of buildings. *Engineering Structures, 11*(1), 16-22. https://doi.org/10.1016/0141-0296(89)90028-X

Bernardini, E., Spence, S. M., and Kareem, A. (2013). A probabilistic approach for the full response estimation of tall buildings with 3D modes using the HFFB. *Structural Safety, 44*, 91-101. https://doi.org/10.1016/j.strusafe.2013.06.002

China Architecture and Building Press (2012). *Load code for the design of building structures.* China Architecture and Building Press.

Davenport, A. G. (1967). Gust loading factors. *Journal of the Structural Division, 93*(3), 11-34. https://doi.org/10.1061/JSDEAG.0001692

Ding, S. (2013). *Experimental study on the passive simulation of turbulence in the boundary layer* [Master's thesis, Harbin Institute of Technology]. https://kns.cnki.net/KCMS/detail/detail.aspx?dbname=CMFD201401&filename=1014003202.nh

Music, J. and Soto, F. (2021). Characterization of high-rise reinforced concrete buildings located in Antofagasta, Chile, by means of structural indexes. *Ingeniería e Investigación, 41*(3), e90430. https://doi.org/10.15446/ing.investig.v41n3.90430

Gong, J., Zhi, X., Shang, W., and Fan, F. (2020a). Shaking table test and numerical analysis of dynamic coupling effect between suspended system and OLF1000. *Engineering Structures, 207*, 110224. https://doi.org/10.1016/j.engstruct.2020.110224

Gong, J., Zhi, X., Shang, W., Fan, F., and Wang, H. (2020b). Shaking table test on 1000kV frame by considering coupling action of transmission lines under longitudinal excitations. *China Civil Engineering Journal, 53*(3), 51-59. https://doi.org/10.15951/j.tmgcxb.2020.03.007

Gong, J., Zhi, X., and Fan, F. (2021). Effect of incident directionality on seismic responses and bearing capacity of OLF1000. *Engineering Structures, 242*, 112542. https://doi.org/10.1016/j.engstruct.2021.112542

Gong, J., Zhi, X., Shao, Y., Dai, K., and Zhong, J. (2022). Directionality effect in the seismic fragility of long-span supporting frames in ultrahigh-voltage substation. *Soil Dynamics and Earthquake Engineering, 159*, 107322. https://doi.org/10.1016/j.soildyn.2022.107322

Gu, M., Zhou, Y., Zhou, F., Xiang, H., and Jiang, H. (2000). Study on wind loads and wind-induced vibration of the Jin Mao Building using high-frequency-force-balance method. *Journal of Building Structures, 21*(4), 55-61. https://doi.org/10.14006/j.jzjgxb.2000.04.008

Guo, Y., Sun, B., and Ye, Y. (2006). Time-domain analysis on wind-induced dynamic response of long span power transmission line systems. *China Civil Engineering Journal, 39*(12), 12-17. https://t.cnki.net/kcms/detail?v=5MN-u6HS-5jy6PDZHNTSt6QFmIiEMLKCT2MSzC__6iozaf2xnI-JK7wc1kp5YvKzkRi5Jet9UVYWaXTMdg8F42mn2McCeCtY-6pL5jqMhuO_66ii13DFenQAA==&uniplatform=NZKPT

Huang, P., and Gu, M. (2005). Experimental study of interference effects on wind-induced torsional responses between tall buildings. *Journal of Building Structures, 26*(4), 86-91. https://doi.org/10.14006/j.jzjgxb.2005.04.014

Kapania, R. K., and Yang, T. (1984). Time domain random wind response of cooling tower. *Journal of Engineering Mechanics, 110*(10), 1524-1543. https://doi.org/10.1061/(ASCE)0733-9399(1984)110:10(1524)

Lou, W., Sun, B., and Tang, J. (1996). Wind tunnel test and numerical computation on wind-induced vibration for tall lattice tower. *Journal of Vibration Engineering, 9*(3), 108-112. https://doi.org/10.16385/j.cnki.issn.1004-4523.1996.03.017

Shiotani, M., and Iwatani, Y. Gust structures over flat terrains and their modification by a barrier. *Wind Engineering: Proceedings of the Fifth International Conference*, *1*, 203-214. https://doi.org/10.1016/B978-1-4832-8367-8.50024-3

Solari, G. (1983). Analytical estimation of the alongwind response of structures. *Journal of Wind Engineering and Industrial Aerodynamics, 14*(1-3), 467-477. https://doi.org/10.1016/0167-6105(83)90047-8

Wang, C. (2011). *Investigation on wind-induced vibration of long-span steel trussed arch bridges* [Doctoral thesis, Chongqing University]. https://kns.cnki.net/KCMS/detail/detail.aspx?dbname=CDFD1214&filename=1011293153.nh

Xiao, Z. (2009). *Wind-induced response analysis and equivalent wind loads of UHV transmission tower* [Master's thesis, Chongqing University]. https://kns.cnki.net/KCMS/detail/detail.aspx?dbname=CDFD0911&filename=2009148381.nh

Xiao, Z., and Li Z. (2011). Research on equivalent wind loads of UHV transmission tower based on high frequency force balance tests[J]. *Power System Technology*. *35*(05), 27-32. https://doi.org/10.13335/j.1000-3673.pst.2011.05.034

Yu, H. (2007). *Wind tunnel experiment and wind-induced response analysis of complex high-rising structures* [Doctoral thesis, Tongji University]. https://kns.cnki.net/KCMS/detail/detail.aspx?dbname=CDFD9908&filename=2007222887.nh

Yu, P. (2018). *Study on along-wind vibration response of lightning rod structures in substations* [Master's Thesis, Zhengzhou University]. https://kns.cnki.net/KCMS/detail/detail.aspx?dbname=CMFD201802&filename=1018088566.nh

Zou, Y. (2013). *Study on wind effects and wind-tunnel test method for super large cooling towers group* [Doctoral thesis, Hunan University]. https://kns.cnki.net/KCMS/detail/detail.aspx?dbname=CDFD1214&filename=1014237999.nh

Research Article/Civil and Sanitary Engineering http://doi.org/10.15446/ing.investig.99281

Comparison between a traditional Colombian Structural Design and the Use of Viscous-Type Energy Damping Systems (2021)

Comparación entre un diseño estructural colombiano tradicional y el uso de disipadores de energía de tipo viscoso (año 2021)

Andres F. Ordoñez-Ruiz[1], William A. Parra-Moreno[2], and Alfer L. Silva-Ceron[3]

ABSTRACT

This paper compares a traditional Colombian structural design to the same structure with viscous-type energy dampers, considering both structural behavior and construction costs. To this effect, a building was designed: first, in accordance with the Colombian Seismic-Resistant Construction Regulations (NSR-10); and then according to the recommendations of American Society of Civil Engineers (ASCE, 2017) with regard to damping systems. Finally, the quantities and construction costs were calculated. As a result, an unconventional structure was obtained which was more expensive than a traditionally designed building. Still, said structure had less cross-sections, stresses, and displacements. The above demonstrates that, while the initial cost of this method may be higher, the extra cost can be offset when an earthquake occurs, as the building has better earthquake resistance.

Keywords: damping, structures, budget, seismic control

RESUMEN

Este trabajo compara un diseño estructural convencional colombiano frente a la misma estructura con disipadores de energía de tipo viscoso, considerando tanto el comportamiento estructural como el costo de construcción. Para ello se diseñó una edificación: en primera instancia, bajo los parámetros del Reglamento Colombiano de Construcción Sismorresistente (NSR-10); y luego cumpliendo con las recomendaciones de la American Society of Civil Engineering (ASCE, 2017) con respecto a sistemas de disipación. Por último, se calcularon las cantidades y los costos de construcción. Como resultado, se obtuvo una estructura más costosa que una edificación diseñada convencionalmente. De todas maneras, dicha estructura tenía menos secciones transversales, esfuerzos y desplazamientos. Lo anterior evidenció que, aunque el costo inicial de este método es más alto, el costo adicional puede ser compensado en el momento en que se presenta un sismo, pues la edificación es más sismorresistente.

Palabras clave: disipadores, estructuras, presupuesto, control sísmico

Received: November 11th, 2021
Accepted: August 19th, 2022

Introduction

In the search of solutions to the threat posed by earthquakes, alternative design methods such as energy dissipation systems have been developed, which implement viscous-fluid devices (Enriquez *et al*., 2020; Hanson, 1993). These devices seek to improve the response of structures to severe earthquakes by incorporating damping and reducing angular distortions, seismic shear, pseudo-acceleration spectrum, and the steel area (Cano-Lagos and Zumaeta-Escobedo, 2012).

When designing buildings, structural engineers always seek to ensure excellent rigidity, resistance, and ductility, aiming to obtain acceptable failure mechanisms in the engineering design. However, since the priority is to save people's lives, elements of the structure can fail, to the point that the building becomes uninhabitable, as long as the structure itself does not collapse. Thus, plastic deformation energy (E_{SD}) plays a vital role in energy dissipation (Rochel Awad, 2012). Conversely, seismic control systems take advantage of the other terms in the energy balance equation (1), such as the mass kinetic energy (E_k), the inherent damping energy of the structure (E_D), and the elastic deformation energy (E_{SS}). These are usually quantified in an additional term (damping energy due to supplementary devices, E_H) (Oviedo and Duque, 2006). This, in order for the structure not to require plastic hinges to dissipate the input energy (E_I).

[1] Civil Engineering. Universidad del Cauca, Colombia. Email: orandres@unicauca.edu.co

[2] Civil Engineering. Universidad del Cauca, Colombia. Email: williamparra@unicauca.edu.co

[3] Civil Engineering. Universidad del Cauca, Colombia. Affiliation: PhD student in Civil Engineering, Universidad EAFIT, Colombia. Assistant professor, Universidad del Cauca, Colombia. Email: alfer@unicauca.edu.co

How to cite: Ordoñez-Ruiz, A. F., Parra-Moreno, W. A., and Silva-Ceron, A. L. (2023). Comparison between a traditional Colombian structural design and the use of viscous-type energy damping systems (2021). *Ingeniería e Investigación, 43*(1), e99281. http://doi.org/10.15446/ing.investig.99281

$$E_K + E_D + E_{SS} + E_{SD} + E_H = E_I \quad (1)$$

In particular, energy damping systems are highly recommended because they take part in passive control systems, which do not require regular maintenance or an activation system. Moreover, viscous-type energy dampers have many benefits, such as simple installation, high resistance, versatility, longevity, and manageable design. Part of that versatility lets designers use these devices in different structures (León-Joya, 2016; Zhou *et al.*, 2020), reinforce old buildings (Hesam *et al.*, 2017), combine them with other control seismic systems (Zhen *et al.*, 2020), or even protect adjacent buildings (Bhaskararao and Jangid, 2007; Patel and Jangid, 2013). Additionally, this control system is one of the most studied mechanisms to protect buildings, with many positive results (Li and Huo, 2010).

Viscous-type energy dissipation devices are elements that transfer highly viscous fluids from one compartment to another through small orifices, taking advantage of the energy loss generated by the fluid during each oscillation of the structure. Because the dissipator behaves according to the laws of fluid mechanics, the value of the resistive force (F) varies with respect to the translational speed of the dissipator (V). Nevertheless, the parameters C (Damping constant) and α (Velocity coefficient) are used to define the dampers in the structure:

$$F = CV^{\alpha}$$

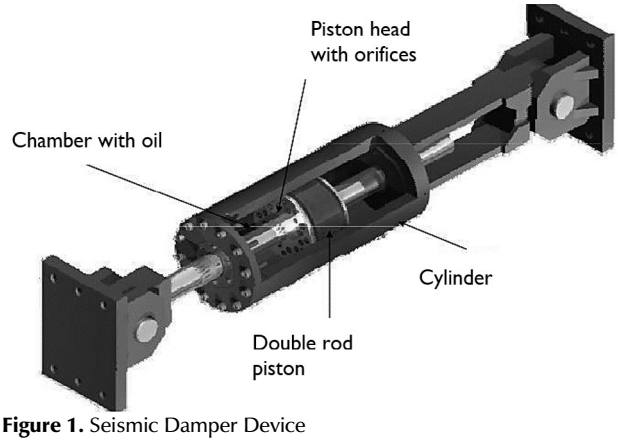

Figure 1. Seismic Damper Device
Source: DISIPA Ingenieros (2021)

Hence the philosophy of this project, whose objective is to compare the performance of two models of the same building. The first model was built using the parameters of the Colombian Construction Regulation (NSR-10), following a traditional design based on the combination of resistance, durability, deformability, and energy absorption through damage. The second model used viscous-type energy dissipation devices, which increase energy absorption and reduce damage (Colunga-Tena and Gama-Contreras, 2017). This, in order to observe the effectiveness of these design mechanisms in a practical environment from an economic perspective.

Methodology

To carry out this study, the aforementioned structures were exposed to a time-history analysis using representative earthquakes for the area under study. The design and analysis of the structures were performed with the help of the academic versions of the Etabs V18.1 and Safe V16.0.2 software. This made it possible to compare the structural behavior of the two alternatives and, through a budget analysis, to carry out a cost-benefit comparison.

A building for residential use was used in the evaluation. It has a normal occupancy (use group I, NSR-10), consisting of five floors, an elevator, and a staircase, with a height of approximately 15,2 m. The structure is based on moment-resisting frames, a gabled roof, composite slabs in metaldeck, and cementation using combined footings and a foundation slab. The building is located on D-type quality soil. On the other hand, the unconventional building has the same components and two viscous dampers for each direction in every story with a diagonal bracing scheme, as shown in Figure 2.

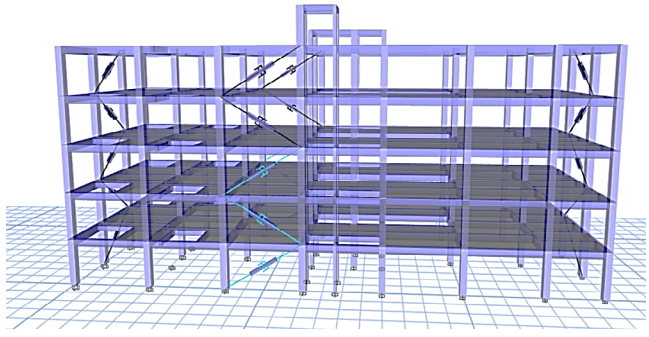

Figure 2. Structural model
Source: Authors

According to the General Study of Seismic Threats of Colombia carried out by the Colombian Association of Seismic Engineering (AIS), there are two dominant seismogenic sources in the study area: active and subduction. In this sense, the seismic records listed in Tables 1 and 2 were based on a study of the micro seismic zoning of Popayán, which was conducted by Universidad de Los Andes (AIS *et al.*, 2010). These records were obtained from the Pacific Earthquake Engineering Research database, the Colombian Seismic Network, and the National Geological Survey of Mexico.

Table 1. Subduction quakes

ID	Country	Date	Magnitude	Distance (km)	Time (s)
San Fernando	USA	9/02/1971	6,6	27	60,19
Imperial Valley	USA	15/10/1979	6,5	36	103,80
Irpinia	Italy	23/11/1980	6,5	33	38,26
Northridge	USA	17/01/1994	6,7	35	39,98
Armenia	Colombia	25/01/1999	6,3	38	144

Source: Authors

Table 2. Active source quakes

ID	Country	Date	Magnitude	Distance (Km)	Time (sec)
Nuxco	Mexico	15/07/1996	6,5	20	83,00
La Unión	Mexico	10/12/1994	6,3	20	54,94
Copala	Mexico	24/10/1993	6,2	19	58,87
Las Vigas	Mexico	25/04/1989	6,5	19	34,39

Source: Authors

Based on these seismic records, an elastic review of the two structures was carried out, where the adequate dynamic behavior was verified, with fundamental translational modal shapes and other requirements of Colombian regulation. Next, the structures were designed, assigning the steel required by either the regulation or the analysis in each structural element, which was conditioned by the design spectrum in each case.

In particular, the design of viscous dampers was established by calculating the maximum capacity force required by the device, determined by means of the equation of the dissipator (2) and the damping coefficient C, which was obtained from the objective viscous damping (β_{vis}) (Fuentes-Sadowski, 2019; Genatios and Lafuente, 2016). The starter viscous damping ratio was determined via Equation (3) in order to estimate a value according to the relation between the objective drift (δ_{Obj}, NSR-10) and the maximum drift (δ_{Max}) of the building analyzed without dampers. Here, the inherent damping (β_0) was taken as 5%.

$$\frac{\delta_{Max}}{\delta_{Obj}} = \frac{2,31 - 0,41Ln(\beta_0)}{2,31 - 0,41Ln(\beta_{vis} + \beta_0)} \quad (2)$$

Next, a damping constant was determined with the properties of the dampers, the structure, and its modal response in a nonlinear analysis (Dall'Asta *et al.*, 2016). The parameters φ_i, φ_{rj}, A, and w are the vibration mode, the relative displacement, the amplitude, and the frequency, respectively, of the fundamental time period of the structure. θ_j is the inclination angle of the dissipator, m_i is the floor mass, and λ are values that depend on the gamma function and the velocity coefficient α (NEHRP, 2020).

$$B = \frac{2.31 - 0.41Ln(\beta_0)}{2.31 - 0.41Ln(\beta_{eff})} \quad (3)$$

As the seismic response in each direction of the structure differs, the damping constant is calculated independently, given that the direction of the structure that is flexible requires greater damping than the other one, which has less flexibility. This means that greater resistive forces are needed. When the output force from the dampers is limited, the structural members and connections are more economical. As a result, the damping constants for the structure under analysis were determined through several iterations whose aim was always to obtain the best behavior and the lowest cost for the devices.

Table 3: Damping constant used in the design

Story	Coef. x (tonf*(s/m)1+α)	Coef. y (tonf*(s/m)1+α)
5	100	100
4	100	100
3	150	180
2	150	180
1	150	180

Source: Authors

The most efficient placement of dampers will be in the perimeter of the structure, aiming to control any torsional motion of the building with respect to its center of mass in its fundamental shape modals. Moreover, for low-rise buildings, dampers are typically placed at all floor levels to capture and absorb the energy at its source throughout the structure (Taylor Devices Inc., 2022; Díaz, 2014). It is important to note that the metallic elements that transfer the earthquake force to the devices had to be designed with a safety factor of 1,5.

The expected viscous damping ratios (β_{vis}) are usually different from the starter ones because the placement is not considered in the estimation. The damping constant was modified in order to obtain the best results. In this framework, the viscous damping ratios were 10,7% in the X-direction and 8,4% in the Y-direction.

Finally, the amount of material required and the construction costs of each of the alternatives were calculated, and a budget analysis considering only the structural elements was carried out to fulfil the aim of the research.

Result analysis

In order to characterize the results and define the most favorable alternative, the following parameters were evaluated: displacements, energy balance, basal shear, accelerations, element design, and construction costs. These parameters showed the most significant differences among the two alternatives.

Displacements

The first significant change that could be observed in the designs was a reduction in displacements. In the unconventional model, these were reduced by 28,61% in the X-direction and 27,11% in the Y-direction, *i.e.*, with respect to the structure without dampers (Arlinton, 2020; Marko, *et al.*, 2004). Depending on the design, a reduction of up to 80% can be achieved (Sajjan and Biradar, 2018). This allowed the project to comply with regulations without the need for additional modifications. These results are shown in Tables 4 and 5.

Table 4. Displacements of the unconventional model in the X-X direction

Floor	Height (m)	Without dissipation (mm)	With dissipation (mm)	Reduction (%)
Story 5	15,30	133,115	94,999	28,63%
Story 4	12,24	122,951	87,482	28,85%
Story 3	9,18	101,15	72,193	28,63%
Story 2	6.,20	69,068	49,330	28,58%
Story 1	3,06	29,801	21,464	27,98%
Base	0	**Average**		28,61%

Source: Authors

Table 5. Displacements of the unconventional model in the Y-Y direction

Floor	Height (m)	Without dissipation (mm)	With dissipation (mm)	Reduction (%)
Story 5	15,30	138,430	100,938	27,08%
Story 4	12,24	127,504	91,543	28,20%
Story 3	9,18	103,932	74,743	28,08%
Story 2	6,12	69,050	50,075	27,48%
Story 1	3,06	28,475	20,830	26,85%
Base	0	**Average**		27,11%

Source: Authors

As for the traditionally designed building, much larger cross-sections were required, as well as two additional columns, in order to increase the rigidity of the building and thus guarantee the maximum displacement allowed by the regulations. The results for this case are presented in Table 6.

Table 6. Displacements of the conventional model

Floor	Height (m)	X-X (mm)	Y-Y (mm)
Story 5	15,30	100,18	99,96
Story 4	12,24	91,46	89,51
Story 3	9,18	74,48	71,30
Story 2	6,12	49,419	46,24
Story 1	3,06	20,24	18,13
Base	0		

Source: Authors

Based on the above, the two structures were compared, whose displacements were similar in order to comply with the regulations. However, it should be noted that the dimensions and properties of the structural element sections in the two structures are different: they are greater in the conventional model.

Energy balance

The reduction in the non-traditional model's displacements was mainly produced by the redistribution of the earthquake's energy in the structure. The damping devices take up to 64,63% of the input energy, while the overall damping of the structure only takes 34,84%, leading to reductions in the stresses on the structure and in the damage to structural elements.

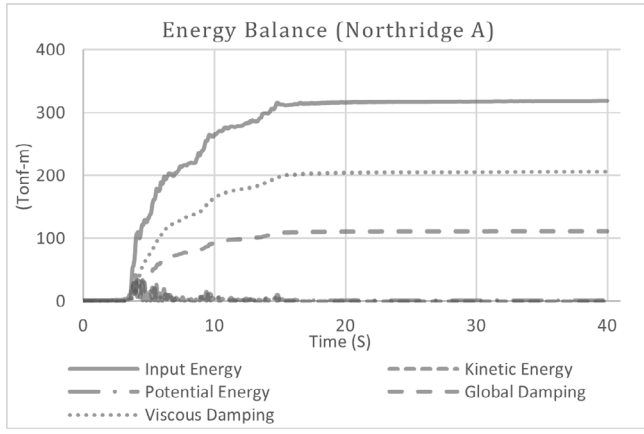

Figure 3. Balance of energy in the unconventional model
Source: Authors

On the other hand, in the conventional model, the energy of the incoming earthquake is dissipated through the inherent damping of the structure, which is determined by the energy dissipation capacity of the materials. Thus, the building can enter the inelastic range, generating plastic hinges and damages to structural and non-structural elements, which means increased reparation costs to rehabilitate the building.

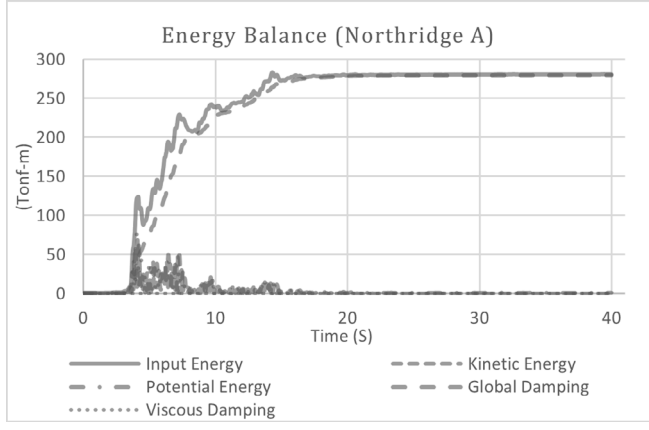

Figure 4. Balance of energy in the conventional model
Source: Authors

Figure 5 presents the comparison of the maximum energy values, where the great difference in the energy distribution of the two studied models can be observed. In particular, the energy of the earthquake taken by the global damping of the structure is reduced from 98,69 to 34,84%, reducing 63,85% of the earthquake's energy, a value close to the energy assumed by the viscous damping (64,63%) in the non-traditional model. Moreover, the kinetic and potential energy were reduced, thus improving behavior in the first moments of an earthquake.

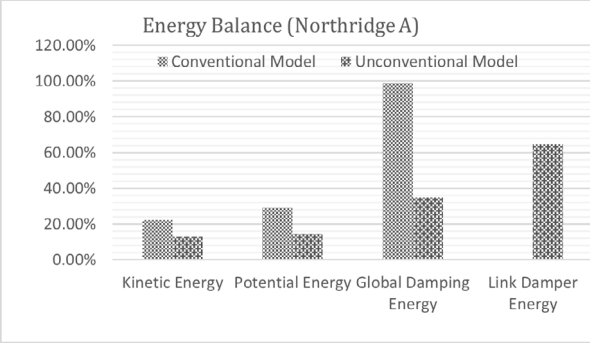

Figure 5. Maximum energy values
Source: Authors

Stresses

The concept of *basal shear* is used to quantify and show the difference in terms of stresses between the two models as a response of the structure against ground motion. Thus, this difference shows the reduction of the structural elements in seismic demand. Figure 6 compares the shear stresses of the models under study. The model with dissipators reduced an average 36,21% of the stresses present in the conventional structure, which leads to a lower demand on the structural elements in the design.

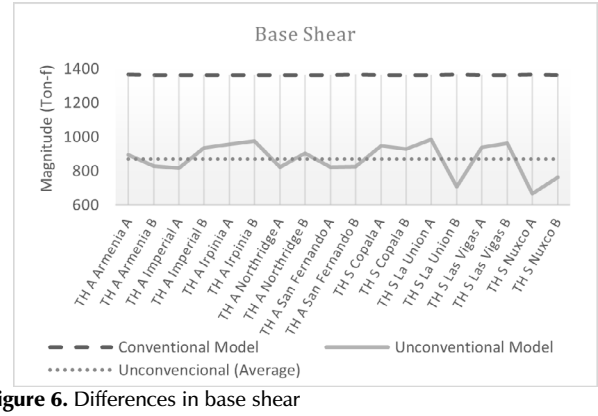

Figure 6. Differences in base shear
Source: Authors

At the same time, the inclusion of dissipators increased the axial forces in the columns adjacent to the devices, which implies that their capacity must be improved (Figure 7) (Guevara-Huatuco and Arias-Torres, 2012). However, it is noteworthy that the increase in the capacity of these columns did not exceed what was required in the conventional model.

Accelerations

Additionally, the acceleration of each floor and model was determined in order to observe the reduction in the output accelerations of the earthquakes. There was indeed an average decrease of 21,21%, which confirms the redistribution of energy, where the kinetic energy of the mass had less participation and consequently less force on the oscillations of the structure.

In particular, the structure presented a reduction of 21,63% in the X-direction and of 17,46% in the Y-direction. The latter was slightly lower because, in this direction, the structure is more flexible and less redundant, with just four columns against the eight columns in the other direction.

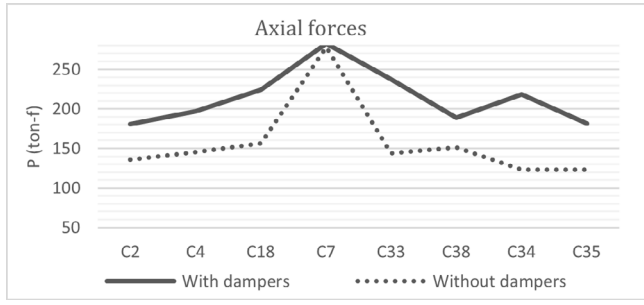

Figure 7. Axial forces in the columns adjacent to the devices
Source: Authors

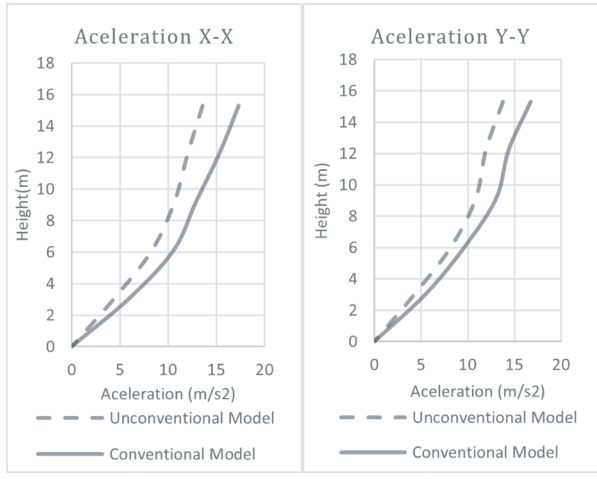

Figure 8. Output accelerations
Source: Authors

Design and budget

Finally, the variation in the quantities of concrete and steel for the construction of each design model was determined. Since the implementation of dampers causes a reduction in the cross-sections, the characteristics of the materials and the spectrum of pseudo-accelerations of the unconventional design led to a quantity reduction, and therefore to a cost reduction of 6,97% for concrete and 10,53% for steel (Table 7).

Table 7. Quantities of concrete and steel

Concrete			
Design	**Conventional**	**Unconventional**	**Variation (%)**
Quantity (m³)	515,850	494,365	4,16%
Cost ($)	275 136,950	255 958,167	6,97%
Steel			
Design	**Conventional**	**Unconventional**	**Variation (%)**
Quantity (m³)	75 301,185	67 369,346	10,53%
Cost ($)	274 322,217	245 426,526	10,53%

Source: Authors

It should be noted that the reduction with respect to the amounts of steel and concrete in the unconventional design takes place differently depending on the structural element, namely cementation, columns, and floor beams. Figure 9 shows that columns benefit the most from the implementation of viscous fluid dampers, as these allow for the greatest reduction of concrete and steel, whereas the difference is not as large in the foundations and floor beams.

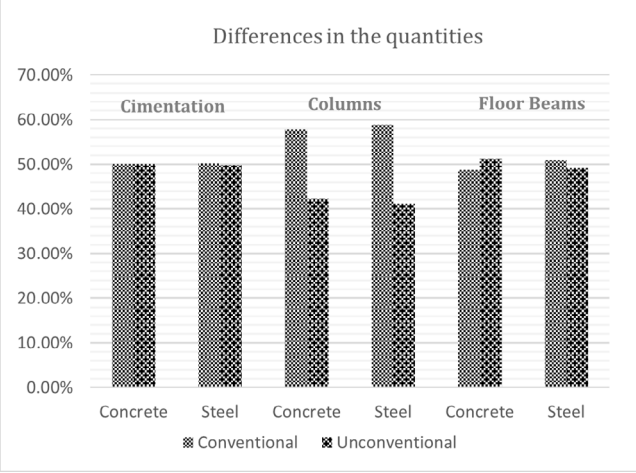

Figure 9. Quantities according to the structural elements
Source: Authors

As for the total construction costs of each building, the conventional model would be valued at $700 639 558 COP, while the unconventional design would have a cost of $ 1 245 065 084 COP, approximately 77,7% higher than the former. However, considering the finishing costs of the building and the repairs made to a structure in the event of an earthquake, the extra cost of the dissipators can be justified (Benavides-Ortiz, 2015).

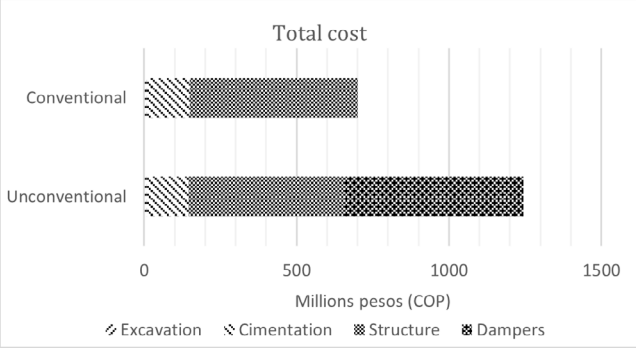

Figure 10. Budget
Source: Authors

According to the background of this research, the rate of increase in the construction costs of a model with viscous dampers under similar conditions is 1,7 with respect to the conventional model, which is close to the value obtained. In addition, to equalize the investment costs, the building should be higher than 18 stories, considering that this value varies depending on the level of importance, type of soil, and area of seismic threat (Benavides-Ortiz, 2015)

Conclusions

According to the information collected through this study, the following remarks can be made:

For the design with viscous fluid dissipators, one of the most important considerations to take into account is the determination of the energy dissipation coefficient C, as values between 100- and 300-tons force · (s / m) $^{1+\alpha}$ are recommended so that the devices are not oversized, expensive, or wasteful.

As a result of the time-history analysis of the unconventional model, the structure exhibits displacement reductions of 28,61 and 27,11%, as well as reducing 21,21% of the floor accelerations and 64,63% of an incoming earthquake's energy, which leads to better structural behavior and greater safety during earthquakes.

Depending on the results, a decrease in the rigidity demand of the structure is noted, due to the fact that the devices absorb a large amount of the input seismic energy. This allows thinner sections to have better behavior and meets the required maximum parameter of angular distortion (Oviedo, 2012).

The building with viscous-type energy dissipators has a better structural performance, since there are less displacements and stresses, thus causing a reduction in sections and materials. While the conventional structure is the most economical construction option, the structural elements of the building were placed under greater stresses.

Despite the many benefits entailed by the implementation of viscous dampers, the process can be very expensive and unfeasible in some cases. However, it should be noted that the use of these devices can be justified in more flexible or more important buildings (Cevasco-Beramendi and Condo Vargas, 2020).

Building structures designed with energy dissipators are an option that should be given greater consideration, as the benefits transcend structural health and human safety. In rare earthquakes, important structures must have a structural performance that is difficult to achieve with conventional designs.

Although the implementation of viscous dampers has an additional cost, the structure requires fewer repairs because it minimizes its incursion into the inelastic range, thus reducing costs and times associated to the possible suspension of service in the building.

The lack of knowledge about the feasibility of using control systems in Colombia was made evident, so research in this area becomes extremely important.

References

AIS, UNIANDES, and INGEOMINAS (2010). *Estudio general de la Amenaza Sísmica de Colombia*. Asociación Colombiana de Ingeniera Sismica.

Arlinton, C. B. (2020). *Influencia de los disipadores de fluido viscoso en el reforzamiento del edificio centro cultural de la Universidad Señor de Sipán* [Undergraduate thesis, Universidad Señor de Sipán]. https://repositorio.uss.edu.pe/handle/20.500.12802/9119

American Society of Civil Engineers (ACSE) (2017). *Minimum design loads and associated criteria for buildings and other structures*. ACSE. https://doi.org/10.1061/9780784414248

Asociación Colombiana de Ingeniería Sísmica (2010). *Reglamento Colombiano de Construcción Sismo Resistente NSR-10, Tomo 2*. ACIS.

Benavides-Ortiz, C. I. (2015). *Analisis comparativo de costos de estructuras de base fija vs. estructuras con elementos disipadores de energía*. Universidad del Valle.

Bhaskararao, A. V., and Jangid, R. S. (2007), Optimum viscous damper for connecting adjacent SDOF structures for harmonic and stationary white-noise random excitations. *Earthquake Engineering Structural Dynnamics, 36*(4), 563-571. https://doi.org/10.1002/eqe.636

Cano-Lagos, H., and Zumaeta-Escobedo, E. I. (2012). *Diseño estructural de una edificación con disipadores de energía y análisis comparativo sísmico entre el edificio convencional y el edificio con disipadores de energía para un sismo severo* [Undergraduate thesis, Universidad Peruana de Ciencias Aplicadas]. http://hdl.handle.net/10757/301565

Cevasco-Beramendi, R. F., and Condo-Vargas, P. (2020). *Análisis del comportamiento sísmico dinámico de un edificio multifamiliar de 37 niveles con disipadores de fluido viscoso en la victoria* [Undergraduate thesis, Universidad Ricardo Palma]. https://hdl.handle.net/20.500.14138/3568

Colunga-Tena, A., and Gama-Contreras, A. (2017). Determinación de parámetros de diseño sísmico para marcos dúctiles de concreto reforzado con disipadores de energía histeréticos. *Revista Sul-Americana de Engenharia Estrutural*, *14*(1), 36-58. https://doi.org/10.5335/rsaee.v14i1.6496

Dall'Asta, A., Tubaldi, E., and Ragni, L. (2016) Influence of the nonlinear behavior of viscous dampers on the seismic demand hazard of building frames. *Earthquake Engineering Structural Dynnamics*, *45*(1), 149-169. https://doi.org/10.1002/eqe.2623

Díaz, M. A. (2014). *Evaluación del proyecto estructural y optimización del diseño con disipadores de energía viscosos taylor para una edificación esencial de 6 pisos* [Undergraduate Thesis, Universidad Privada Antenor Orrego]. https://repositorio.upao.edu.pe/handle/20.500.12759/637

DISIPA Ingenieros (2021, August 30). *Energy Dampers* [Figure]. http://www.disipaing.com/disipadores-energia/

Enriquez, A., Marulanda, J., & Thomson, P. (2018). *Análisis comparativo entre un reforzamiento convencional y tres alternativas de repotenciación con dispositivos de con-trol pasivo para una clínica construida antes del CCCSR-84* [Master's thesis, Universidad del Valle]. https://1library.co/document/yr35l67y-analisis-comparativo-reforzamiento-convencional-alternativas-repotenciacion-dispositivos-electronico.html

Fuentes-Sadowski, J. C. (2019). *Procedimientos para el análisis y diseño de estructuras con sistemas de disipación de energía en el Perú* [Master's thesis, Pontificia Universidad Católica del Perú]. http://hdl.handle.net/20.500.12404/15624

Genatios, C., and Lafuente, M. (2016). *Introducción al uso de aisladores y disipadores en estructuras.* CAF-Banco de Desarrollo de América Latina Serie GeóPolis. http://scioteca.caf.com/handle/123456789/1213

Guevara-Huatuco, D. N., and Arias-Torres, P. O. (2012). *Diseño de un edificio aporticado con amortiguadores de fluido-viscoso en disposición diagonal* [Undergraduate Thesis, Pontificia Universidad Catolica del Perú]. http://hdl.handle.net/20.500.12404/1477

National Earthquake Hazards Reduction Program (NEHRP) (2020). *NEHRP recommended provisions for seismic regulations for new buildings and other structures* (vol. I). Federal Emergency Management Agency. https://www.fema.gov/sites/default/files/2020-10/fema_2020-nehrp-provisions_part-1-and-part-2.pdf

Hanson, R. D. (1993). Supplemental damping for improved seismic performance. *Earthquake Spectra, 9*(3), 319-334. https://doi.org/10.1193/1.1585719

Hesam, P., Irfanoglu, A., and Hacker, T. J. (2017). Effective viscous damping in reinforced concrete buildings : Estimation based on measured strong motion response. *16th World Conference on Earthquake*, *2393*, 9. http://wcee.nicee.org/wcee/article/16WCEE/WCEE2017-2393.pdf

León-Joya, L. T. (2016). *Disipadores y aisladores sísmicos, modelo de puente vehicular con disipador y sin disipador de energía, comparación de la respuesta sísmica* [Undergraduate thesis, Universidad Católica de Colombia]. http://repository.ucatolica.edu.co/handle/10983/13931

Li, H., and Huo, L. (2010). Advances in structural control in civil engineering in China. *Mathematical Problems in Engineering, 2010*, 936081. https://doi.org/10.1155/2010/936081

Marko, J., Thambiratnam, D., and Perera, N. (2004). Influence of damping systems on building structures subject to seismic effects. *Engineering Structures*, *26*(13), 1939-1956. https://doi.org/10.1016/j.engstruct.2004.07.008

Oviedo, J. A. (2012). Influence of the story stiffness of reinforced concrete frame with proportional hysteretic dampers on the seismic response. *Revista EIA, 9*(17), 121-137. https://revistas.eia.edu.co/index.php/reveia/article/view/455

Oviedo, J. A., and Duque, M. del P. (2006). Sistemas de control de respuesta sísmica en edificaciones. *Revista EIA, 3*(6), 105-120. https://revistas.eia.edu.co/index.php/reveia/article/view/163

Patel, C. C., and Jangid, R. S. (2013). Dynamic response of identical adjacent structures connected by viscous damper. *Structural Control and Health Monitoring*, *21*, 205-224. https://doi.org/10.1002/stc.1566

Rochel Awad, R. (2012). *Análisis y diseño sísmico de edificios* (2nd ed.). Fondo Editorial Universidad EAFIT.

Sajjan, P., and Biradar, P. (2018). Study on the effect of viscous damper for Rcc frame structure. *IJRET: International Journal of Research in Engineering and Technology, 5*(9), 31-36. https://doi.org/10.15623/ijret.2016.0509005

Taylor Devices Inc. (2022). *Fluid viscous dampers manual*. https://www.taylordevices.com/damper-manual/

Zhen, L., Dejian, L., Leihua, P., Yao, L., Kepei, C., and Qianqiu, W. (2020). Study on the damping efficiency of continuous beam bridge with constant cross-section applied by lead rubber bearings and fluid viscous dampers. *Noise and Vibration Worldwide*, *51*(4-5), 85-92. https://doi.org/10.1177/0957456520901353

Zhou, P., Liu, M., Li, S., Li, H., and Song, G. (2020). Experimental study on seismic control of towers in cable-supported bridges by incorporating fluid viscous dampers between sub-towers. *Advances in Structural Engineering*, *23*(10), 2086-2096. https://doi.org/10.1177/1369433220908031

Research Article/Electrical, Electronic, and Telecommunications Engineering https://doi.org/10.15446/ing.investig.90968

Modeling and Control of Small-Scale Underground Mine Ventilation Networks

Modelado y control de redes de ventilación de minas subterráneas de pequeña escala

Oscar-Oswaldo Rodríguez-Díaz [1], Edinson Franco-Mejía [2], and Esteban Rosero [3]

ABSTRACT

This paper presents a nonlinear model and a control strategy to regulate airflow in small-scale underground mine ventilation networks. In underground ventilation control systems, a sensor and an actuator for each branch are usually considered. However, in small-scale underground mines, it is too expensive to have automatic doors for controlling the airflow in each tunnel, as well as to install flow and gas sensors in each branch. In order to regulate airflow in small-scale underground ventilation networks, the number of sensors and actuators is regarded as a limitation for practical installation. This work presents an alternative modeling of the network, with direct control of the airflow in each tunnel, by varying the speed of the fans available on the external surface of the mine. A state space model is presented, and a linear quadratic controller with integral action and a state estimator is designed. To validate the model and the controller, a network ventilation system for a small-scale mine with nine branches (tunnels) and two actuators (fans) is presented.

Keywords: ventilation, modeling, control systems, mines

ABSTRACT

Este artículo presenta un modelado no lineal y una estrategia para el control del flujo de aire en redes de ventilación de minas subterráneas de pequeña escala. Para los sistemas de control de ventilación subterránea usualmente se consideran un sensor y un actuador en cada rama. Sin embargo, en las minas subterráneas de pequeña escala, es muy costoso colocar puertas automáticas para controlar el flujo de aire en cada túnel, así como instalar sensores de flujo y gas en cada rama. Con el fin de regular el flujo de aire en redes de ventilación subterránea de pequeña escala, se considera el número de sensores y actuadores como una limitante para la instalación práctica. Este trabajo presenta una alternativa para el modelado de la red, con control directo del flujo de aire en cada túnel, a través de la variación de velocidad de los ventiladores disponibles en la superficie externa de la mina. Se presenta un modelo de espacio de estado y se diseña un controlador cuadrático lineal con acción integral y un estimador de estado. Para validar el modelo y el controlador, se presenta un sistema de red de ventilación para una mina de pequeña escala con nueve ramas (túneles) y dos actuadores (ventiladores).

Palabras clave: ventilación, modelado, sistema de control, minas

Received: October 15th, 2020
Accepted: May 10th, 2022

Introduction

The mining industry is an important contributor to the economies of many countries. Due to its characteristics, underground mining is considered to be a dangerous activity, with high rates of accidents reported each year Knights and Scanlan (2019); Wang and Du (2020). For this reason, substantial academic and industrial research has been focused on improving safety conditions in underground mining operations, focusing on the niche of knowledge in what is known as Industry 4.0. Pałaka *et al.* (2020) show the impact of this technology on the workers of underground coal mines. Ventilation systems play a key role in underground coal mine safety due to the presence of dangerous gases such as methane. The problems around modeling and controlling mine ventilation systems have been studied since the 1960s, Tolmachev (1966),(Petrov *et al.*, 1992). A nonlinear dynamic model for ventilation systems based on Kirchhoff's laws is presented by Hu et al. (2003), which allows modeling large-scale ventilation networks and airflow control in each tunnel. A similar model is proposed by Zhu *et al.* (2014), who include external perturbation in the model and design an H_1 optimal controller. In Sui *et al.* (2016), the analysis of a large ventilation network with 11 nodes and 17 branches is proposed. In the aforementioned studies, a fully equipped network was considered in order to control the dynamic behavior of airflow in the tunnels, namely that there were sensors throughout the network and automatic doors working as actuators in every branch. An example for this type of instrumentation is shown in Kozielski *et al.* (2021),

[1] Electronics engineer, Universidad Pedagógica y Tecnológica de Colombia, Colombia. MSc in Engineering-Automation, Universidad Nacional de Colombia, Colombia. PhD student at Universidad del Valle, Colombia. Affiliation: Assistant professor at the Electronics Engineering School, Universidad Pedagógica y Tecnológica de Colombia. Email: oscar.rodriguez@uptc.edu.co

[2] Electrical engineer, Universidad del Valle, Colombia. PhD in Engineering at Universidad del Valle, Colombia. Affiliation: Full professor at the School of Electrical and Electronics Engineering, Universidad del Valle, Colombia. Email: edinson.franco@correounivalle.edu.co

[3] Mechanical engineer, Universidad del Valle, Colombia. PhD in Engineering with an emphasis in Control Systems, Hamburg University of Technology, Germany. Affiliation: Assistant professor at the School of Electrical and Electronics Engineering, Universidad del Valle, Colombia. Email: esteban.rosero@correounivalle.edu.co

How to cite: Rodríguez-Díaz, O.O., Franco-Mejía, E., and Rosero E. (2023). Modeling and Control of Small-Scale Underground Mine Ventilation Networks. *Ingeniería e Investigación, 43*(1), e90968. https://doi.org/10.15446/ing.investig.90968

where data collected from 28 different sensors placed at various locations of an underground coal mine were made available for analysis or research.

In developing countries, it is common to find small-scale mining facilities whose complete measurements and network actuation are not available due to their high cost and lack of resources. It is therefore necessary to design control strategies for ventilation networks of underground mines while considering the availability of sensors and actuators. A typical scenario is a ventilation system with a reduced number of fans working as actuators.

From a control perspective, Rodriguez-Diaz *et al.* (2021) show the application of a classic control strategy in a prototype for underground mining built in GipsaLab (France). Raji *et al.* (2020) show control strategies to manipulate airflow and reduce energy costs. Moreover, Rasool *et al.* (2020) show the tuning of multiple controllers for an HVDC system-based optimization technique. Applications of modern control strategies for ventilation networks can be found throughout the literature Jing *et al.* (2020); Ren and Cao (2020); Nardo and Yu (2021), where the use of techniques such as artificial intelligence and on-demand ventilation are employed. In addition, in a study by de Villiers *et al.* ((2019), the evaluation of auxiliary fan performance in underground mining highlights the engineering challenges involved in optimizing airflow.

This study proposes another solution starting with a model based on the analysis provided by Hu *et al.* (2003), as well as a control design for ventilation systems in underground small-scale mines with reduced measurements and actuators. The control aim is to regulate the airflow in a work area (a branch of the ventilation network) by means of the control action provided only by the fans available in the mine. The designed controller is based on the optimization of sensors and actuators.

Summers and Lygeros (2014) have focused on the problem of optimal placement of sensors and actuators in complex dynamic networks. Moreover, control theory uses the representation in state space and the concepts of observability and controllability to reduce the number of devices needed in a control system **?**.

The paper is organized as follows: Section 1 provides a brief introduction; Section 2 presents the modeling procedure; Section 3 presents a specific application where the ventilation system of a typical underground small-scale coal mine is considered, proposes a controller design, and presents the results obtained; and Section 4 outlines the conclusions and future research areas.

Modeling of ventilation networks in underground mines

Electric circuit theory can be used to analyze the dynamic behavior of mine ventilation systems, particularly the well known non-planar circuit analysis (topological analysis).

This work demonstrates a static analysis of the network under study. First, a representation of the ventilation network as a non-planar circuit is presented, identifying the elements in the system and organizing them according to the equivalent circuit. Then, the tree in the network must be defined. A tree is defined by considering a set of nodes and branch lines constituting a path without closing any mesh and passing every node just once. Including the branches with air fans in the definition of trees is recommended for analyzing the system. The branches that are not part of the trees are called *links*. Thus, it is possible to state that

n_n = *Amount of nodes in the network*,
n_r = *Amount of branch lines in the network*,
n_{rs} = *Amount of branch lines without a fan*,
$l_1 = n_r - (n_n - 1)$ = *Link number*
m = *Amount of air fans*

Static model of the network

The following conditions are assumed Hu *et al.* (2003):

1. The air is incompressible. Therefore, the air density is constant in all branches of the mine Danko ((2017).
2. The temperature in all the branches of mine is constant.

These assumptions are made based on the typical conditions found in small-scale mines.

Airflow equations without direct fan action

Considering the connections in a ventilation network, air mass conservation at the nodes can be expressed in terms of airflow quantities, *i.e.*, the sum of the airflow entering the node is equal to the sum of the outgoing airflow. Kirchhoff's current law applied to the ventilation network can be expressed as follows:

$$\sum_{j=1}^{n_{rs}} E_{Qij} Q_j = 0, \quad i = 1, \cdots, (n_{rs} - l_1), \tag{1}$$

or, equivalently,

$$E_Q Q = 0, \tag{2}$$

where Q represents the vector values of airflow quantities in the branches. The values of E_{Qij} are defined as follows:

$$E_{Q_{ij}} = \begin{cases} 1, & \text{if branch } \boldsymbol{j} \text{ is connected to the node } \boldsymbol{i} \\ & \text{and airflow leaves the node } \boldsymbol{i} \\ -1, & \text{if branch } \boldsymbol{j} \text{ is connected to the node } \boldsymbol{i} \\ & \text{and airflow enters the node } \boldsymbol{i} \\ 0, & \text{if branch } \boldsymbol{j} \text{ is not connected to the node } \boldsymbol{i} \end{cases}$$

The airflow in a ventilation network is associated with the current flow in an electric circuit. To explain the concept, a mathematical representation of the analysis of node i in matrix form is shown in Figure 1, as given by

$$\begin{bmatrix} -1 & -1 & -1 & -1 \end{bmatrix} \begin{bmatrix} Q_1 \\ Q_2 \\ Q_3 \\ Q_4 \end{bmatrix} = 0.$$

Then, for a system with $p = (n_{rs} - l_1)$, it is possible to express the following:

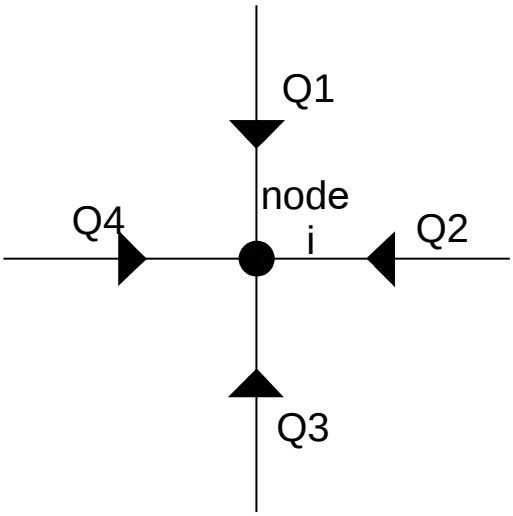

Figure 1. Example of bifurcation in an underground mine
Source: Authors

$$\underbrace{\begin{bmatrix} a_{11} & a_{12} & a_{13} & \dots & a_{1n_{rs}} \\ a_{21} & a_{22} & a_{23} & \dots & a_{2n_{rs}} \\ \vdots & \vdots & \vdots & \ddots & \vdots \\ a_{p1} & a_{p2} & a_{p3} & \dots & a_{pn_{rs}} \end{bmatrix}}_{E_Q} \underbrace{\begin{bmatrix} Q_1 \\ Q_2 \\ \vdots \\ Q_{n_{rs}} \end{bmatrix}}_{Q} = 0.$$

Airflow equations with direct action of fans e_{Qm}

At nodes where an air fan actuator is located, the equivalent of Kirchhoff's current law can be expressed as

$$\sum_{j=1}^{n_{rs}} e_{Qij} Q_j = Q_{mi}, \quad i = 1, \cdots, m, \tag{3}$$

or, equivalently

$$e_{Qm} Q = Qm, \tag{4}$$

where e_{Qm} is a matrix with dimensions $m \times n_{rs}$, and m is the amount of the air fans in the network. $e_{Qm_{ij}}$ is defined as

$$e_{Qm_{ij}} = \begin{cases} 1, & \text{if branch } \boldsymbol{j} \text{ is connected to the node } \boldsymbol{i} \\ & \text{and airflow leaves node } \boldsymbol{i} \\ -1, & \text{if branch } \boldsymbol{j} \text{ is connected to the node } \boldsymbol{i} \\ & \text{and airflow enters node } \boldsymbol{i} \\ 0, & \text{if branch } \boldsymbol{j} \text{ is not connected to the node } \boldsymbol{i} \end{cases}$$

For a ventilation network with m fans, Equation (4) can be written as

$$\underbrace{\begin{bmatrix} b_{11} & b_{12} & b_{13} & \dots & b_{1n_{rs}} \\ b_{21} & b_{22} & b_{23} & \dots & b_{2n_{rs}} \\ \vdots & \vdots & \vdots & \ddots & \vdots \\ b_{m1} & b_{m2} & b_{p3} & \dots & b_{mn_{rs}} \end{bmatrix}}_{e_{Qm}} \underbrace{\begin{bmatrix} Q_1 \\ Q_2 \\ \vdots \\ Q_{n_{rs}} \end{bmatrix}}_{Q} = \underbrace{\begin{bmatrix} Q_{f1} \\ Q_{f2} \\ \vdots \\ Q_{fm} \end{bmatrix}}_{Q_m}.$$

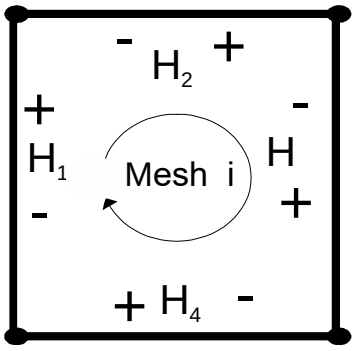

Figure 2. Pressure drops for a mesh in an underground mine
Source: Authors

Pressure drop equations without direct fan action

In an ventilation network, as in an electrical network, the Kirchhoff voltage law holds, *i.e.*, the algebraic sum of pressure drops in a closed trajectory is zero, Hartman *et al.* (1997):

$$\sum_{j=1}^{n_{rs}} E_{Hij} H_j = 0, i = 1, ..., (l_1 - m), \tag{5}$$

or, equivalently

$$E_H H = 0, \tag{6}$$

where l_1 is the amount of links, namely the number of branches in the co-tree; and the column vector H contains the pressure drop variables in the branches where the air fans do not have direct action. The terms of the E_H matrix are defined as

$$E_{H_{ij}} = \begin{cases} 1, & \text{if branch } \boldsymbol{j} \text{ is connected to the mesh } \boldsymbol{i} \text{ and} \\ & \text{airflow is in same direction as the loop} \\ -1, & \text{if branch } \boldsymbol{j} \text{ is connected to the mesh } \boldsymbol{i} \text{ and} \\ & \text{airflow is in the opposite direction to the loop} \\ 0, & \text{if branch } \boldsymbol{j} \text{ is not connected to the mesh } \boldsymbol{i}. \end{cases}$$

According to the example in Figure 2, Equation (6) can be written as follows:

$$\begin{bmatrix} -1 & -1 & -1 & -1 \end{bmatrix} \begin{bmatrix} H_1 \\ H_2 \\ H_3 \\ H_4 \end{bmatrix} = 0.$$

For a ventilation network with p meshes, where $p = l_1 - m$, Equation (6) can be written as

$$\underbrace{\begin{bmatrix} a_{11} & a_{12} & a_{13} & \dots & a_{1n_{rs}} \\ a_{21} & a_{22} & a_{23} & \dots & a_{2n_{rs}} \\ \vdots & \vdots & \vdots & \ddots & \vdots \\ a_{p1} & a_{p2} & a_{p3} & \dots & a_{pn_{rs}} \end{bmatrix}}_{E_H} \underbrace{\begin{bmatrix} H_1 \\ H_2 \\ \vdots \\ H_{n_{rs}} \end{bmatrix}}_{H} = 0.$$

Pressure drop equations with direct fan action

For the loops of the ventilation systems where the actuators are working, the Kirchhoff voltage law can be expressed as follows:

$$\sum_{j=1}^{n_{rs}} e_{Hij} H_j = -H_{Vi}, i = 1, ..., m, \tag{7}$$

or, equivalently

$$e_{Hm} H = -H_m, \tag{8}$$

where the values of e_{Hm} are obtained as

$$e_{Hm_{ij}} = \begin{cases} 1, & \text{if branch } \boldsymbol{j} \text{ is connected to the mesh } \boldsymbol{i} \text{ and airflow has the same direction of the loop} \\ -1, & \text{if branch } \boldsymbol{j} \text{ is connected to the mesh } \boldsymbol{i} \text{ and airflow has opposite direction of the loop} \\ 0, & \text{if branch } \boldsymbol{j} \text{ is not connected to the mesh } \boldsymbol{i}. \end{cases}$$

Nonlinear dynamic model of the ventilation network

The previous section introduced a static mathematical analysis of the variables involved in a ventilation network. However, a dynamic model is necessary to design control strategies. For a single branch, the airflow dynamics Sui *et al.* (2016) are described as follows:

$$\frac{dQ_j}{dt} + K_j R_j |Q_j| Q_j = K_j H_j, \tag{9}$$

where

Q_j: *Airflow of branch j*
R_j: *Aerodynamic resistance of branch j*
H_j: $P_{lj} - P_{lj0}$ *Pressure drop of branch j*
P_{lj}: *Absolute pressure at the end of branch j*
P_{lj0}: *absolute pressure at the beginning of branch j*
K_j: $S_j/\rho L_j$ *Inertial coefficient of branch j*
L_j: *Length of branch j*
S_j: *Cross section of branch j*
ρ: *Air density*

Parameter R_j can be obtained from the Atkinson equation McPherson (1993); Hartman *et al.* (1997):

$$R_j = \frac{\alpha_j L_j P_j}{S_j^3}, \tag{10}$$

with:

α_j: *Aerodynamic resistance constant of branch j*
P_j: *Perimeter of branch j*

Hu *et al.* (2003) propose a nonlinear generalization of ventilation systems in underground mining, which is expressed as

$$\frac{dQ}{dt} = A_v Q_D^2 R + B_v Q + C_v d, \tag{11}$$

$$H = Y_{RQ} Q_D^2 R + Y_Q Q + Y_d d, \tag{12}$$

with matrices $A_v, B_v, C_v, Y_{RQ}, Y_Q$, and Y_d of appropriate dimensions. Matrix A_v is defined as

$$A_v = -K(I - Y_{RQ}), B_v = K Y_Q, C_v = K Y_d. \tag{13}$$

The procedure to obtain the parameters of the dynamic model based on the static relations among the branches and nodes is presented in Sui *et al.* (2016) and is summarized as follows:

$$Y_{RQ} = \begin{bmatrix} S_{Ha}\zeta_{RQ} \\ \zeta_{RQ} \end{bmatrix}, \quad Y_Q = \begin{bmatrix} S_{Ha}\zeta_Q + S_Q \\ \zeta_Q \end{bmatrix},$$

$$Y_d = \begin{bmatrix} S_d + S_{Ha}\zeta_d \\ \zeta_d \end{bmatrix}, \quad S_{Ha} = -\begin{bmatrix} E_{Hc} \\ e_{Hmc} \end{bmatrix}^{-1} \begin{bmatrix} E_{Ha} \\ e_{Hma} \end{bmatrix},$$

$$S_Q = \begin{bmatrix} E_{Hc} \\ e_{Hmc} \end{bmatrix}^{-1} \begin{bmatrix} 0 \\ I \end{bmatrix} R_m e_{Qm}, \quad S_d = \begin{bmatrix} E_{Hc} \\ e_{Hmc} \end{bmatrix}^{-1} \begin{bmatrix} 0 \\ -I \end{bmatrix},$$

$$\zeta_{RQ} = [E_{Qc} K_c S_{Ha} + K_a]^{-1} E_Q K, \tag{14}$$

$$\zeta_Q = -[E_{Qc} K_c S_{Ha} + K_a]^{-1} E_{Qc} K_c S_Q, \tag{15}$$

$$\zeta_d = -[E_{Qc} K_c S_{Ha} + K_a]^{-1} E_{Qc} K_c S_d. \tag{16}$$

In Hu *et al.* (2003), the existence of $[E_{Qc} K_c S_{Ha} + K_a]^{-1}$ is demonstrated. Considering the dynamics in the fan branch, it is possible to write the following:

$$H_m = d - R_m Q_m, \tag{17}$$

where d is the pressure drop generated by the action of the fan, R_m is the coefficient of resistance in the fan branch, and Q_m is the airflow in the fan branch.

Reduced nonlinear model of the ventilation network

In order to simplify the control design, a reduced model is proposed Hu *et al.* (2003). Considering the dependence of the co-tree variables, it is possible to analyze only the state variables related to the links. The state variables are arranged in ascending order in the matrix Q_c, starting with the airflows that correspond to the links. Then, the matrix A_c, which has direct action with the links, is decomposed. The matrix A_{ca} relates the complementary flows of the network, thus completing the dynamics.

Thereupon, a reduced model using only the airflows of the links is proposed as

$$\dot{Q}_c = A_c Q_{cD}^2 R_c + A_{ca} Q_{aD}^2 R_a + B_c Q_c + C_c d, \tag{18}$$

$$H_c = \zeta_{RQc} Q_{cD}^2 R_c + \zeta_{RQa} Q_{aD}^2 (Q_c) R_a + \zeta_{Qc} Q_c + \zeta_d d, \tag{19}$$

where Q_c is the reduced state vector. This work considers the fan pressure drop d as the control input. The matrices of the system are defined as

$$A_c = -K_c + K_c S_{Ha} \zeta_{RQc}, \tag{20}$$

$$A_{ca} = K_c S_{Ha} \zeta_{RQa}, \tag{21}$$

$$B_c = K_c (S_{Ha} \zeta_{Qc} + Rm S_{Qc}, \tag{22}$$

$$C_c = K_c (S_d + S_{Ha} \zeta_d). \tag{23}$$

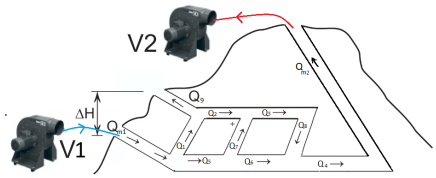

Figure 3. Physical view of the underground coal mine
Source: Authors

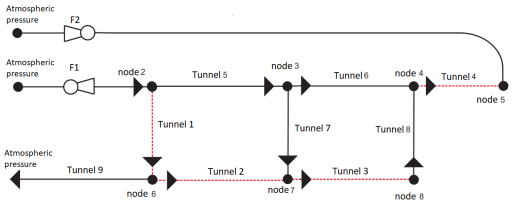

Figure 4. Schematic network diagram (tree and links)
Source: Authors

Application example

This section presents a case study of an underground coal mine in Colombia. A physical model of the mine is shown in Figure 3. The ventilation system consists of a couple of fans working as actuators, a forcing fan at the entrance of the mine (V_1), and an auxiliary extractor fan (V_2) strategically placed to improve the conditions of the working area. Usually, in small mining facilities, fans working with 440 V and a nominal power in the range of 10 to 30 HP are installed. The parameters in Table 1 are drawn from real data of the small-scale mine. The tunnel resistance is defined as $R = (\alpha_j * L_j * P_j / S_j^3)$, where α is the aerodynamic resistance constant, P is the perimeter of the tunnel, S is the cross-section of the tunnel, and L is the length of the tunnel.

A schematic diagram of the ventilation system is shown in Figure 4. In order to simplify the network analysis, the tree and co-tree must be identified. The tree of the network is indicated by the black solid line, and the links are represented by means of the red dashed line.

According to the network analysis for the system shown in Figure 4, the following elements can be defined

$$
\begin{array}{lll}
n_r & = 11 & \textit{Number of branches in the network} \\
n_{rs} & = 9 & \textit{Number of branches without fans in the network} \\
n_n & = 8 & \textit{Number of nodes} \\
l_1 & = 4 & \textit{Number of links} = n_r - (n_n - 1) \\
m & = 2 & \textit{Number of fans}
\end{array}
$$

Note that the branches forming the tree are V_1, V_2, *Tunnel* 5, *Tunnel* 6, *Tunnel* 7, *Tunnel* 8, and *Tunnel* 9. The links are formed by branches *Tunnel* 1, *Tunnel* 2, *Tunnel* 3, and *Tunnel* 4. The conservation equations for the flow in each node are defined as

$$
\begin{aligned}
-Q_{m1} + Q_1 + Q_5 &= 0, & -Q_4 + Q_{m2} &= 0, \\
-Q_5 + Q_6 + Q_7 &= 0, & -Q_1 + Q_2 + Q_9 &= 0, \\
-Q_6 - Q_8 + Q_4 &= 0, & -Q_7 - Q_2 + Q_3 &= 0, \\
 & & -Q_3 + Q_8 &= 0.
\end{aligned}
$$

The mesh equations can be written as

$$
\begin{aligned}
H_{m1} + H_1 + H_9 &= 0, \\
H_{m1} + H_5 + H_7 - H_2 + H_9 &= 0, \\
H_6 - H_8 - H_3 - H_7 &= 0, \\
H_{m1} + H_5 + H_6 + H_4 + H_{m2} &= 0.
\end{aligned}
$$

By reorganizing the equations in a structured matrix form, it is possible to write

$$
\underbrace{\begin{bmatrix} 0 & 1 & 0 & -1 & 1 & 0 & 0 & 0 & 0 \\ 0 & 0 & 1 & -1 & 0 & 1 & 0 & 0 & 0 \\ 0 & 1 & -1 & 0 & 0 & 0 & 1 & 0 & 0 \\ 0 & 0 & -1 & 0 & 0 & 0 & 0 & 1 & 0 \\ -1 & 1 & 0 & 0 & 0 & 0 & 0 & 0 & 1 \end{bmatrix}}_{E_Q} \underbrace{\begin{bmatrix} Q_1 \\ Q_2 \\ \vdots \\ Q_9 \end{bmatrix}}_{Q} = 0,
$$

$$
\underbrace{\begin{bmatrix} 1 & -1 & 0 & 1 & 0 & 0 & 0 & 0 & 0 \\ 0 & 0 & 0 & 1 & 0 & 0 & 0 & 0 & 0 \end{bmatrix}}_{e_{Qm}} \underbrace{\begin{bmatrix} Q_1 \\ Q_2 \\ \vdots \\ Q_9 \end{bmatrix}}_{Q} = \underbrace{\begin{bmatrix} Q_{m1} \\ Q_{m2} \end{bmatrix}}_{Q_{Gm}},
$$

$$
\underbrace{\begin{bmatrix} -1 & -1 & 0 & 0 & 1 & 0 & 1 & 0 & 0 \\ 0 & 0 & -1 & 0 & 0 & 1 & -1 & -1 & 0 \end{bmatrix}}_{E_H} \underbrace{\begin{bmatrix} H_1 \\ H_2 \\ \vdots \\ H_9 \end{bmatrix}}_{H} = 0,
$$

$$
\underbrace{\begin{bmatrix} 1 & 0 & 0 & 0 & 0 & 0 & 0 & 0 & 1 \\ -1 & 0 & 0 & 1 & 1 & 1 & 0 & 0 & -1 \end{bmatrix}}_{e_{Hm}} \underbrace{\begin{bmatrix} H_1 \\ H_2 \\ \vdots \\ H_9 \end{bmatrix}}_{H} = \underbrace{\begin{bmatrix} -H_{m1} \\ -H_{m2} \end{bmatrix}}_{H_{Gm}}.
$$

Considering the network's static analysis, a dynamic model can be found based on Equations (11) and (12). Matrices A_v, B_v, and C_v are obtained from Equation (13), which yields a non-linear system with nine state variables. The simulation parameters of the system are presented in Table 1.

Reduced model for small-scale mining

In order to simplify the analysis and control design, a reduced model is used. The states of the reduction are the airflows in the links, namely Q_1, Q_2, Q_3, and Q_4. The airflows Q_5, Q_6, Q_7 ,Q_8, and Q_9 can be expressed as a linear combination of the airflow in the links.

$$
\begin{aligned}
Q_5 &= Q_4 - Q_2, & Q_6 &= Q_4 - Q_3, & Q_8 &= Q_3, \\
Q_7 &= Q_3 - Q_2, & Q_9 &= Q_1 - Q_2.
\end{aligned}
$$

The reduced model is characterized via Equation (18)

$$
\dot{Q}_c = A_c Q_{cD}^2 R_c + A_{ca} Q_{aD}^2 R_a + B_c Q_c + C_c d, \qquad (24)
$$

$$
H_c = \zeta_{RQc} Q_{cD}^2 R_c + \zeta_{RQa} Q_{aD}^2 (Q_c) R_a + \zeta_{Qc} Q_c + \zeta_d d, \qquad (25)
$$

Table 1. Parameters of an underground coal mine

Tunnel	Resistance $[Ns^2/m^8]$	K $[Ns^2/m^4]$	Length $[m]$	operation point $[m^3/h]$
1	0,20	0,11	25	43,75
2	0,12	0,14	25	19,16
3	0,13	0,13	25	31,31
4	0,13	0,138	25	75,34
5	0,13	0,138	25	56,17
6	0,16	0,13	25	44,03
7	0,14	0,138	25	12,14
8	0,16	0,13	25	31,31
9	0,55	0,04	80	24,58

Source: Authors

where

$$A_c = \begin{bmatrix} -0,0546 & -0,0334 & -0,0118 & -0,0150 \\ -0,0334 & -0,0450 & -0,0159 & -0,0202 \\ -0,0118 & -0,0159 & -0,0418 & -0,0197 \\ -0,0150 & -0,0202 & -0,0197 & -0,0585 \end{bmatrix},$$

$$A_{ca} = \begin{bmatrix} 0,0184 & -0,0032 & 0,0216 & -0,0118 & -0,0212 \\ 0,0248 & -0,0043 & 0,0291 & -0,0159 & 0,0115 \\ -0,0038 & 0,0221 & -0,0259 & -0,0418 & 0,0041 \\ -0,0383 & -0,0388 & 0,0005 & -0,0197 & 0,0052 \end{bmatrix},$$

$$B_c = 0_{(4x4)}, \quad C_c = \begin{bmatrix} -0,0362 & -0,0150 \\ -0,0087 & -0,0202 \\ -0,0156 & -0,0197 \\ -0,0533 & -0,0585 \end{bmatrix},$$

where $R_{c(4x4)}$, $R_{a(4x5)}$. Figure 5 shows the behavior of the airflow at the operating point. A 15% variation in the signal applied to fans 1 and 2 is taken as input at $t = 800\ s$.

Controller design

An operation point given for a ventilation network with a constant input given by both fans is considered. Thus, by linearizing the nonlinear model, a linear state space representation is obtained:

$$\dot{x}(t) = Ax(t) + Bu(t), \tag{26}$$

$$Y(t) = Cx(t) + Du(t), \tag{27}$$

where the Jacobian matrices A, B, C, and D are obtained by applying the partial derivatives Egeland and Gravdahl (2002), evaluated at the point of operation as

$$A_{(4x4)} = \left.\frac{\partial f}{\partial x}\right|_{x_o(t),u_o(t)}, \qquad B_{(4x2)} = \left.\frac{\partial f}{\partial u}\right|_{x_o(t),u_o(t)},$$

$$C_{(4x4)} = \left.\frac{\partial h}{\partial x}\right|_{x_o(t),u_o(t)}, \qquad D_{(4x2)} = \left.\frac{\partial h}{\partial u}\right|_{x_o(t),u_o(t)}.$$

Then, the matrix values are

$$A = \begin{bmatrix} -0,0256 & 0,0014 & -0,0016 & -0,0012 \\ -0,0045 & -0,0164 & -0,0021 & -0,0015 \\ -0,0016 & -0,0007 & -0,0192 & -0,0022 \\ -0,0020 & 0,0053 & 0,0030 & -0,0371 \end{bmatrix},$$

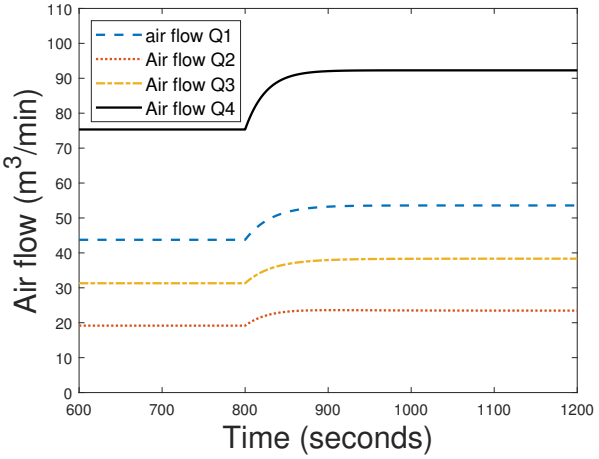

Figure 5. Airflow in the links (open loop)
Source: Authors

$$B = \begin{bmatrix} -0,0362 & -0,0150 \\ -0,0087 & -0,0202 \\ -0,0156 & -0,0197 \\ -0,0533 & -0,0585 \end{bmatrix}, \quad C^T = \begin{bmatrix} 0 \\ 0 \\ 0 \\ 1 \end{bmatrix}, \quad D = 0.$$

Given the limited number of sensors in the ventilation network, an observer-based controller is shown in Figure 6. The reduced set of airflow variables $Q_c(t)$ is considered as the state variables. The set of measured variables $Q_{meas}(t)$ is selected for the pair (A, C). Thus, with the estimated states $\hat{Q}_c$, an LQI (Linear-Quadratic-Integral) control is implemented. The aim is to compute an optimal state-feedback control law in the form

$$u(t) = F\hat{Q}_c(t) + K_i \int e(t)dt, \tag{28}$$

where $e(t) = Q_{ref} - Q_{meas}(t)$, with a constant set-point Q_{ref}. A constraint of the system is defined by the airflow through the work front, as it can not exceed the maximum and minimum limits allowed Kirk (1998), namely

$$Q_{i_{min}} \leq Q_i \leq Q_{i_{max}}. \tag{29}$$

The control signal must also be restricted, *i.e.*, the pressure drop generated by the fans must be limited, avoiding mechanical or electrical stresses in the fans:

$$U_{i_{min}} \leq U_i \leq U_{i_{max}}. \tag{30}$$

The objective of ventilation network optimization is to reduce energy consumption and to regulate airflow in the work front. Therefore, the cost function can be defined as

$$J(t) = \int_{t_0}^{t_f} \{U_i(t)^2 + Q_i(t)^2\} d(t) \tag{31}$$

For the issue of optimal control, the airflow of branch 1 will not be less than a minimum flow. Similarly, the function of cost is to minimize the energy applied to the ventilation system, and it is therefore necessary to find an admissible

control U* that causes the system to follow a permissible trajectory X* to minimize the cost function. The control law $u(t)$ for the ventilation system is defined as

$$u(t) = -Kx(t) - K_1 v(t) = -\begin{bmatrix} K & K_1 \end{bmatrix} \begin{bmatrix} x \\ v \end{bmatrix} (t), \qquad (32)$$

where $[K \quad K_1]$ are the constants of the controller, and $v(t)$ is the state variable of error. Based on Equation (32), the controller design problem focuses on solving the Riccati equation Kirk (1998), obtaining the values in the matrix K_T for

$$0 = -K_T A - A^T K_T - Q_o + K_T B R^{-1} B^T K_T, \qquad (33)$$

where $K_T = [K \quad K_1]$, $Q_o = 100 * I_{4x4}$ and $R = 0.5 * I_{2x2}$. The constants of the LQI controller are defined as

$$K = \begin{bmatrix} -29,5700 & 1,1614 & -2,7243 & -11,9784 \\ 9,3227 & -15,9746 & -10,0604 & -22,8246 \end{bmatrix},$$

$$K_1 = \begin{bmatrix} 0,6765 \\ -0,2059 \end{bmatrix}.$$

The algorithm for estimating the state vector $\hat{x}(t)$ is

$$\begin{array}{rcl} \frac{d}{dt}\hat{x} & = & A\hat{x}(t) + Bu(t) + L[y(t) - C\hat{x}(t)], \\ \hat{y}(t) & = & C\hat{x}(t), \end{array} \qquad (34)$$

and the gain L of the estimator is given by

$$L = \begin{bmatrix} 4,446 & 0,1925 & -0,2003 & -0,0616 \end{bmatrix}^T.$$

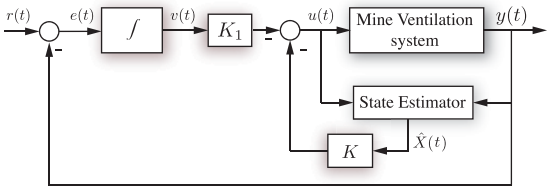

Figure 6. Observer-based LQI controller
Source: Authors

The dynamics of the nonlinear model and the controller were simulated in Matlab. The nonlinear model of the coal mine was implemented in an $s - function$, as shown in Figure 7. First, the system was set to its operation point, with $Q_1 = 43,75\ m^3/h$. At instant $t = 900\ s$, a change in the set point is required, so the airflow in the front work was adjusted to $Q_1 = 61,15\ m^3/s$. A couple of disturbances were introduced to the system at instants $t = 1\ 100\ s$ and $t = 1\ 150\ s$ in order to visualize the disturbance rejection provided by the integral term. The dotted line in the aforementioned Figure shows the response of the system while assuming the measurement of all the variables of the state vector $Q_c(t)$. The dashed line corresponds to the closed-loop behavior of the system considering the estimator-based controller proposed in Figure 6, with $Q_{meas}(t) = Q_1(t)$.

Figure 7 shows the comparison between the reference signal Q_1, the airflow measured by sensor 1 and the estimated value of Q_1. The objective of the control system is to keep the airflow at the reference level and reject disturbances. The characteristic closed-loop time for the proposed model is $1,5\ min$, an adequate time for a small-scale mine. In

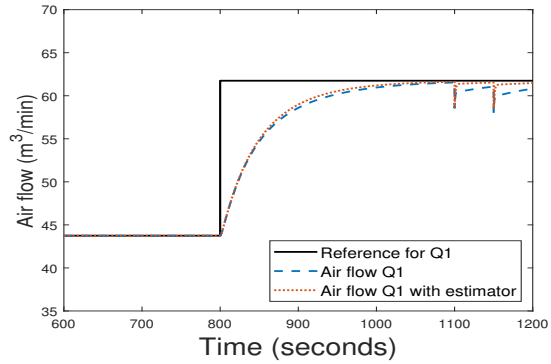

Figure 7. Controlled system output with reduced model
Source: Authors

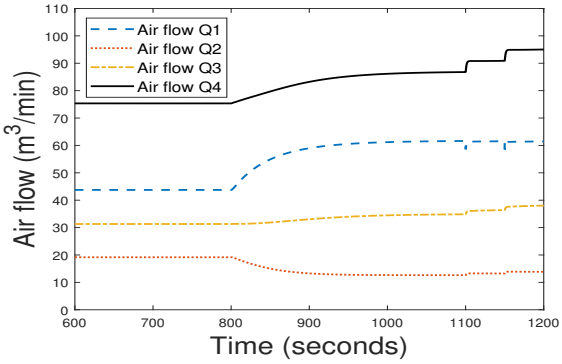

Figure 8. Airflows of the state variables with the estimator
Source: Authors

addition, the disturbance at $1\ 100\ s$ with a magnitude of 10% is attenuated by the controller in $7\ s$, showing the response speed of the closed loop system.

Figure 8 shows the behavior of the airflow in the four branches. In addition, the Figure shows how the airflow in branches 2, 3, and 4 is adjusted to ensure the airflow in branch 1 when there are disturbances at $t = 1\ 100\ s$. The dynamics of all the branches can also be observed; the fastest dynamic corresponds to branch 1, where the airflow for the control loop is measured.

Conclusions

A control strategy to regulate air flow in small-scale underground mine ventilation networks was designed in this work. In order to design a controller, a nonlinear model was obtained which has direct control of the airflow in each tunnel by varying the speeds of the fans available on the external surface of the mine. Based on this model, a linear quadratic controller with integral action and a state estimator was designed. The results were obtained from simulations of a typical condition of an underground coal mine using two fans: the first fan injects air into the mine, and the other one extracts it. The reduction of sensors and actuators helps reduce the implementation costs of underground coal mining. Future work in this field could include conducting an analysis to determine the minimum number of sensors and actuators in the different topologies of mine ventilation networks.

Acknowledgements

The authors gratefully acknowledge Universidad Pedagógica y Tecnológica de Colombia, Universidad del Valle, and the Colombian Ministry of Science (Minciencias) for supporting this research project, *i.e. Control strategies in small underground coal mining ventilation networks* (733/2015, department of Boyacá).

References

Danko, G. L. (2017). *Model Elements and Network Solutions of Heat, Mass and Momentum Transport Processes*. Springer International Publishing, http://dx.doi.org/10.1007/978-3-662-52931-7.

de Villiers, D. J., Mathews, M. J., Maré, P., Kleingeld, M., and Arndt, D. (2019). Evaluating the impact of auxiliary fan practices on localised subsurface ventilation. *International Journal of Mining Science and Technology*, 29(6):933–941, http://dx.doi.org/10.1016/j.ijmst.2019.02.008.

Egeland, O. and Gravdahl, J. T. (2002). *Modeling and Simulation for Automatic Control*.

Hartman, H., Mutmansky, J., Ramani, R., and Wang, Y. 1997. *Mine Ventilation and Air Conditioning*. John Wiley & Sons, INC., (3rd) edition.

Hu, Y., Koroleva, O. I., and Krstić, M. jul 2003. Nonlinear control of mine ventilation networks. *Systems & Control Letters*, 49(4):239–254, http://dx.doi.org/10.1016/S0167-6911(02)00336-5.

Jing, G., Cai, W., Zhang, X., Cui, C., Liu, H., and Wang, C. may 2020. An energy-saving control strategy for multi-zone demand controlled ventilation system with data-driven model and air balancing control. *Energy*, 199:117328, http://dx.doi.org/10.1016/j.energy.2020.117328.

Kirk, D. E. 1998. *Optimal control theory an introduction*. Dover publications, Mineola, New York.

Knights, P. and Scanlan, B. 2019. A study of mining fatalities and coal price variation. *International Journal of Mining Science and Technology*, 29(4):599–602, http://dx.doi.org/10.1016/j.ijmst.2019.06.016.

Kozielski, M., Sikora, M., and Wróbel, Ł. 2021. Data on methane concentration collected by underground coal mine sensors. *Data in Brief*, 39, http://dx.doi.org/10.1016/j.dib.2021.107457.

McPherson, M. J. 1993. *Subsurface Ventilation and Environmental Engineering*. Springer Netherlands, Dordrecht, http://dx.doi.org/10.1007/978-94-011-1550-6.

Nardo, M. and Yu, H. jul 2021. Intelligent Ventilation Systems in Mining Engineering: Is ZigBee WSN Technology the Best Choice? *Applied System Innovation*, 4(3):42, http://dx.doi.org/10.3390/asi4030042.

Pałaka, D., Paczesny, B., Gurdziel, M., and Wieloch, W. 2020. Industry 4.0 in development of new technologies for underground mining. *E3S Web of Conferences*, 174: 2–7, http://dx.doi.org/10.1051/e3sconf/202017401002.

Petrov, N. N., Shishkin, M., Dmitriev, V. M., and Shadrin, V. F. 1992. Modeling mine aerology problems. *Journal of Mining Science*, 28(2):185–191.

Raji, B., Tenpierik, M. J., Bokel, R., and van den Dobbelsteen, A. 2020. Natural summer ventilation strategies for energy-saving in high-rise buildings: a case study in the Netherlands. *International Journal of Ventilation*, 19(1):25–48, http://dx.doi.org/10.1080/14733315.2018.1524210.

Rasool, H., Rasool, A., Ikram, A. A., Rasool, U., Jamil, M., and Rasool, H. feb 2020. Compatibility of objective functions with simplex algorithm for controller tuning of HVDC system. *Ingenieria e Investigacion*, 39(3):34–43, http://dx.doi.org/10.15446/ing.investig.v39n3.70221.

Ren, C. and Cao, S.-J. jan 2020. Implementation and visualization of artificial intelligent ventilation control system using fast prediction models and limited monitoring data. *Sustainable Cities and Society*, 52(August 2019):101860, http://dx.doi.org/10.1016/j.scs.2019.101860.

Rodriguez-Diaz, O., Novella-Rodriguez, D. F., Witrant, E., and Franco-Mejia, E. jan 2021. Control strategies for ventilation networks in small-scale mines using an experimental benchmark. *Asian Journal of Control*, 23(1): 72–81, http://dx.doi.org/10.1002/asjc.2394.

Sui, J., Yang, L., and Hu, Y. aug 2016. Complex fluid network optimization and control integrative design based on nonlinear dynamic model. *Chaos, Solitons and Fractals*, 89: 20–26, http://dx.doi.org/10.1016/j.chaos.2015.09.009.

Summers, T. H. and Lygeros, J. 2014. *Optimal Sensor and Actuator Placement in Complex Dynamical Networks*, volume 47. IFAC, http://dx.doi.org/10.3182/20140824-6-ZA-1003.00226.

Tolmachev, S. T. 1966. Determining the air-flow directions in a ventilation network. *Soviet Mining Science*, 2:598–603.

Wang, K. and Du, F. 2020. Coal-gas compound dynamic disasters in China: A review. *Process Safety and Environmental Protection*, 133:1–17, http://dx.doi.org/10.1016/j.psep.2019.10.006.

Zhu, S., Jiang, Z., Zhou, K., Peng, G., and Yang, C. nov 2014. The characteristics of deformation and failure of coal seam floor due to mining in Xinmi coal field in China. *Bulletin of engineering geology and the environment*, 73(4):1151–1163, http://dx.doi.org/10.1007/s10064-014-0612-x.

Research Article/Electrical,Electronic and Telecommunications Engineering http://doi.org/10.15446/ing.investig.99251

Electric Vehicles and the Use of Demand Projection Models: A Systematic Mapping of Studies

Vehículos eléctricos y el uso de modelos de proyección de demanda: un mapeo sistemático de estudios

Dafne Lagos[1], Rodrigo Mancilla[2], Carolina Reinecke[3], and Paola Leal[4]

ABSTRACT

In today's world, electric vehicles have become a real solution to the problem of pollution caused by petrol and diesel-powered vehicles. However, incorporating them successfully into the global vehicle park poses new challenges. Some of these challenges have to do with meeting the electricity demand, providing the physical installations for charging, and the size and capacity of the electric grid required to deliver the necessary supply. Solving these new problems requires determining or projecting the electrical and/or physical requirements involved, but there is no single model or methodology to do this, nor any single document which summarizes the existing information. To address this situation, this work presents the result of a systematic mapping study that seeks to provide organized information about the (mathematical) models for the demand arising from electric vehicles, as well as to answer a series of questions posed for this research. The results obtained show that there is a wide variety of models used to determine demand requirements –of either physical or electrical elements– in which mathematical modelling and operations research tools are normally used. Other results indicate that demand models are mainly focused on the electrical requirements rather than on physical ones, and that, in most cases, the type of vehicle for which the demand is studied is not mentioned.

Keywords: electric vehicles, demand, models, systematic mapping

RESUMEN

En la actualidad, los vehículos eléctricos se han convertido en una alternativa real al problema de contaminación ocasionado por los vehículos a gasolina y diésel. Sin embargo, su incorporación exitosa al parque automotriz global implica nuevos desafíos. Algunos de estos desafíos tienen que ver con satisfacer la demanda de electricidad, suministrar las instalaciones físicas necesarias para la carga y el tamaño y capacidad de la red eléctrica para aportar el suministro requerido. Para resolver estos nuevos problemas, es necesario determinar o proyectar los requerimientos eléctricos y/o físicos implicados, pero no existe un único modelo o metodología para ello, como tampoco un único documento que resuma la información existente. En atención a esto, este documento presenta el resultado de un mapeo sistemático de estudios que busca entregar información organizada sobre los modelos (matemáticos) de demanda de vehículos eléctricos, como también dar respuesta a un conjunto de interrogantes planteadas para la investigación. Los resultados obtenidos muestran que existe una amplia variedad de modelos utilizados para determinar los requerimientos de demanda –ya sea de elementos físicos o eléctricos– donde normalmente se utilizan el modelamiento matemático y las herramientas de investigación de operaciones. Otros resultados indican que los modelos de demanda se centran principalmente en los requerimientos eléctricos por encima de los físicos, y que, en la mayoría de los casos, no se menciona el tipo de vehículo sobre el que se estudia la demanda.

Palabras clave: vehículos eléctricos, demanda, modelos, mapeo sistemático

Received: October 28th, 2021
Accepted: September 07th, 2022

Introduction

Today, pollution and climate change are recognized realities all over the world. The introduction of alternative vehicle technologies such as electric vehicles (EVs) is an efficient effort to reduce carbon and nitrogen oxides emissions (Akbari *et al*., 2018). Moreover, electric vehicles are regarded as sustainable transport solutions, unlike those with conventional combustion engines (Usman *et al*., 2020). Electric vehicles are therefore considered to be a clean, affordable means of transportation that will most likely replace conventional petrol/diesel vehicles (H. Wang *et al*., 2019).

The advantages of electric vehicles, which include reductions in greenhouse gases and other emissions, energy security, and fuel savings (Faridimehr *et al*., 2019), have led

[1] Industrial-civil engineer, Universidad de La Frontera, Chile. ScD in Industrial Engineering, Atlantic International University, United States. Affiliation: Professor, Universidad Católica de Temuco, Chile. E-mail: dlagos@uct.cl

[2] Industrial-civil engineer, Universidad Católica de Temuco, Chile. Bachelor's degree in Engineering Sciences, Universidad Católica de Temuco, Chile. Affiliation: Independent, Chile. E-mail: mancillavargas.rodrigo@gmail.com

[3] Industrial-Civil Engineering student, Universidad Católica de Temuco, Chile. Email: carolina.reinecke9@gmail.com

[4] Industrial-civil engineer, Universidad de La Frontera, Chile. Master's degree in Higher Education and University Pedagogy, Universidad Mayor, Chile. Affiliation: Vice-Dean of the School of Engineering, Universidad Católica de Temuco, Chile. E-mail: pleal@uct.cl

How to cite: Lagos, D., Mancilla, R., Reinecke, C., and Leal, P. (2023). Electric Vehicles and the Use of Demand Projection Models: A Systematic Mapping of Studies. *Ingeniería e Investigación, 43*(1), e99251. http://doi.org/10.15446/ing.investig.99251

governments to pro-mote EVs as a key measure to try to reduce greenhouse gas emissions (K. Huang *et al*., 2016). In 2017, the Chilean Energy Ministry set the target that 40% private vehicles should be electric by 2050 (Ministerio de Energía, 2017).

The demand for EVs has grown rapidly since 2010, influenced by renewable energy and socio-economic factors (X. Li *et al*., 2017), but also by government support, changes in the industry and private consumer demand (Cao *et al*., 2019), the price of EVs, their range, and the charging process and its associated infrastructure (Domínguez-Navarro *et al*., 2019).

Nevertheless, the social benefits of adopting EVs on a large scale cannot be achieved without the large-scale deployment of public charging stations (Faridimehr *et al*., 2019), since the existing network is insufficient. In other words, the small number of existing stations and their poorly chosen locations constitute a significant barrier for the propagation of EVs in many countries (Csiszár *et al*., 2019). Thus, the first step towards a wider adoption of electric vehicles is to establish the necessary charging infrastructure (H. Wang *et al*., 2019). However, this is not the only consideration, since the extensive penetration of EVs will threaten the stability of the electrical grid (Abdulaal *et al*., 2017). The generalized introduction of EVs and the deployment of renewable distributed generation on a large scale pose a major challenge to modern distribution systems (Ehsan and Yang, 2020). Furthermore, EVs introduce new charging demands that change the traditional patterns, while renewable energy sources (RES) are characterized by their highly variable generation patterns (de Quevedo *et al*., 2019).

All these factors imply that anticipating the use of future rapid charging stations, as well as the energy that they will demand, is critical information for organizations involved in planning the deployment of charging infrastructure for EVs (Bryden *et al*., 2018). At the same time, it is hard to decide on locations for charging stations due to the uncertainty of candidate sites and unidentified charging demands, which are subject to many variables (Ahn and Yeo, 2015).

It is therefore of great importance to obtain up-to-date information on charging demands in terms of both power and infra-structure, in order to support planning for the incorporation of EVs by governments, the private sector, and any other types of organization. The existing literature contains a number of scientific articles on this issue, but there is a lack of publications that systematize important knowledge of the mathematical models used to support decisions on charging requirements, which are also cross-linked with other important elements like vehicle types, study objects, *etc*. This research offers some answers to the questions raised above, together with a systematized presentation of the information currently available in articles and other documents.

Our methodology is one used mainly in the medical field, which has however been adapted to other areas: a *systematic mapping study* (Kitchenham *et al*., 2004).

The document is organized in sections as follows: Related works; Methodology; Results and discussion; Conclusions; and finally References.

Related works

The literature reports no works containing systematic mapping applied to the use of demand models associated with electric vehicles. Thanks to the versatility of the tool, however, and the broad scope of the field of EVs, some related works were found.

Systematic mapping study

The aim of a systematic mapping study is to organize and synthesize scattered information on a subject and present the relationship between two study variables in such a way that it can be quickly and easily understood. This tool can therefore be applied in a great variety of disciplines. One example from the healthcare area is a study by Saleemi *et al*. (2020) which uses systematic mapping to thoroughly analyze the available evidence on ubiquitous medical attention, in order to understand and evaluate the progress made in the field and identify the challenges that hinder further progress. Another example is a study by Drissi *et al*. (2020) which aims to provide a general description and structured comprehension of the literature on connected mental health (CMH). In a similar context, the research by Behmanesh *et al*. (2020) reports on the identification and classification of tele-orthopedic applications and services, together with a general description of trends in this field. Strictly in the field of technology and information, the following studies use systematic mapping: Khan *et al*. (2021), who try to identify, categorize, and present a complete general description of the approaches, techniques, and tools used in election predictions on Twitter; Rachad and Idri (2020), who aim to provide an overview of the use of machine learning (ML) techniques in the design and development of mobile applications; Jafari and Rasoolzadegan (2020), who explore security patterns as a means of encapsulating and communicating tested security solutions and introduce security into the development process. Moreover, Belmonte *et al*. (2019) present an overview of automatic tasks based on the concept of unmanned aerial vehicles (UAV); Zakari *et al*. (2019) present a study of software fault localization (SFL) in order to determine the general productivity of investigation, demography, and trends, as well as to classify existing techniques; Cravero *et al*. (2018) offer an overview of how IoT (Internet of Things) technologies and BigData can help oenologists to manage and optimize wine production, and how the components of the computer architectures used can be determined; Haghighatkhah *et al*. (2017) propose a classification and analysis of the literature related with software engineering in the motor car industry; and Gabriel *et al*. (2016) analyze the existing digital tools to support creativity in organizations. Other disciplines report the use of systematic mapping studies, such as geoconservation (Németh *et al*., 2021), legal ontologies (Rodrigues *et al*.,

2019), musical intervention carried out by nurses as part of research (Ciğerci *et al*., 2019), socio-technical congruence (Sierra *et al*., 2018), smart tourism (Celdrán-Bernabéu *et al*., 2018), and gamification in education (Dicheva *et al*., 2015), to name but a few.

When conducting a systematic mapping study, the relationship between two study variables is presented by a graph with circles, where circle size is proportional to the simultaneous occurrence frequency of both variables. Presenting the data in a graph makes an easy way to know and visually evaluate these relationships. Furthermore, conducting a systematic mapping study involves the creation of starting research questions that can be answered by the information obtained directly from observing the graph.

Reviews

With regard to the literature reviews about EVs, there are studies on: electric vehicle routing problems and their variants and algorithms (Qin *et al*., 2021); EV converters highlighting topology, features, components, operation, strengths, and weaknesses (Lipu *et al*., 2021); energy storage systems and balancing circuits (Habib *et al*., 2020); charging technologies and methods (Brenna *et al*., 2020); charge-discharge coordination between EVs and the power grid (Solanke *et al*., 2020); prospects of EVs in developing countries (Rajper and Albrecht, 2020); the performance of battery management and control systems for lithium ion batteries (Dileepan and Jayakumar, 2020); the technical development of EVs and emerging technologies (X. Sun *et al*., 2020); the integration of solar photovoltaic energy in various types of electric and hybrid vehicles (Waseem *et al*., 2019); the characterization of pure EVs, their energy sources, environmental impacts, energy management strategies, and the challenges they face (Z. Li *et al*., 2019); forms of charge planning, applying dynamic pricing (Limmer, 2019); analysis of the experiences of plug-in EV users (Meisel and Merfeld, 2018); the operating process of different types of EVs, batteries, and supercapacitor technologies (Ding *et al*., 2017); and theories, network modeling, solution algorithms, and applications (Jing *et al*., 2016), *etc*.

Methodology

This section presents some general conceptual elements, followed by the activities carried out in the systematic mapping study.

Use of mathematical models

The use of mathematical models is fundamental for generating information for decision-making in the context of EV incorporation planning. Specifically, these models are useful for designing charging stations (Mehrjerdi and Hemmati, 2019), determining the number of charging stations (Kim and Kim, 2021), determining the charging time and/or the amount of charge involved (Cheon and Kang, 2017), and determining the flow that charging requires from transmission and distribution systems (Bhat *et al*., 2017), as well as for the robust operation of distribution networks (Wei *et al*., 2017), *etc*.

Depending on the purpose for which the model is used, it may include spatial and location elements (de Quevedo *et al*., 2019); uncertainty in demand, consumption, or any other variable (Hafez and Bhattacharya, 2018b); the number of charging stations and population densities (X. Li *et al*., 2017); space-time parameters (Arias *et al*., 2017); the spatial distribution of traffic flows (Xiang *et al*., 2016); economic parameters such as operating costs, investment, connection costs, the total cost of losses, *etc*. (Liao and Lu, 2015; Simorgh *et al*., 2018); and the state of a vehicle, the state of battery charge (SOC), and distance to the destination (Kim and Kim, 2021), to name only a few.

Activities carried out in the systematic mapping

Research Questions. *The following research questions (RQ) were defined in accordance with the proposed aim of this study and the recommendations made by Kitchenham and Charters (2007).*

RQ-1: What is the use given to demand projection in the study (consumable, focus)? *RQ-2:* What are the requirements to enable the demand to be constructed (physical elements, electrical elements, mixed)? *RQ-3:* What type of vehicle use is considered in studying the demand (public, private, mixed)? *RQ-4:* What is the context of the research (applied or theoretical)? *RQ-5:* How is the type of (mathematical) model used in the demand projection (or study) defined?

Data sources and search. To answer the research questions, data were collected from the Web of Science (WoS) and Scopus digital databases, which are available online. The search for articles in these databases used Boolean expressions such as "Or" and "And", with the following key words (in English): "Electric car", "Electric vehicle", "Demand", "Charging station" (as well as their plurals, as appropriate), which were defined from the research object. The advanced search option was used in order to obtain articles which contained the search terms in the title and/or keywords. The search was limited to the period between 2015 and May 2021. The result was a total of 1 245 articles, 472 in WoS and 773 in Scopus.

Inclusion and exclusion criteria. A preliminary selection was made of the 1 245 articles found, which was based on the following set of criteria:

First, all articles were included which were written in Spanish or English and came from journals, conferences, and congresses in which mathematical demand models were developed, describing physical and/or electrical requirements associated with the different types of electric cars.

Articles with fewer than three citations (Agostino *et al.*, 2020) and referring to electric vehicles other than cars or buses (*e.g.* drones or electric bicycles) were excluded. Articles which did not present a mathematical demand model were excluded, as well as those that contained only mean data or took probability distributions to obtain the median value and its variance, which were used as final data in order to reflect demand without using an explicit mathematical model. These criteria were applied to the abstracts of all articles. If the abstract did not provide sufficient information to make a decision, the conclusions and general content of the document were reviewed in greater detail. After applying the inclusion and exclusion criteria to the 1 245 articles, only 50 articles remained, in which the particular demand models were studied, and answers to the research questions were sought.

Classification elements. Once the relevant publications had been selected, a set of classifications was defined based on the study object, namely (i) *the use of the demand*, or the identification of the purpose for which the demand model was constructed and used. The following potential uses were included: a) consumable, where information on the demand was used as information for a subsequent purpose within the study; and b) focus, where the construction of the demand model was the final object of the study. (ii) *Requirements of the demand*: The elements for which the demand was developed were classified into: a) physical elements associated with the number of stations, charging points, infrastructure conditions, *etc.*; b) electrical elements, considering the amount of energy, its power, voltage, supply characteristics, *etc.*; and c) mixed, *i.e.*, whether the model allowed information to be derived from both the physical and electrical elements. (iii) *Type of vehicle*: This element classified the type of vehicle included in the study, namely a) public, when the vehicle was available for use by the general public, including taxis, buses, van services, *etc.*; b) private, when the vehicle was available for private use, including private vehicles and Uber, limousines, and similar services; c) mixed, for both public and private use; and d) unreported, when the article provided no information for classification. (iv) *Research area*: The purpose of this definition was to establish the context in which the demand model was applied. The options for this classification were: a) application, b) theoretical, or c) unreported.

Systematic mapping. Based on the above classifications and the study of the articles, the relationship between different elements was graphically depicted on the XY plane. The size of each circle in the graph is proportional to the frequency of the occurrence in conjunction of the X and Y variables defined on the axes. Thus, Figure 1 shows the interaction between the research context (Y axis) and the use of the demand and is requirements (X axis).

Figure 1 shows that the highest frequencies are associated with: (i) the theoretical content, when the demand information is used as a consumable, and (ii) with the theoretical content, when the demand requirements are electrical.

Figure 2 shows the link between the use of the demand (Y axis) and the type of vehicle and the demand requirements (X axis).

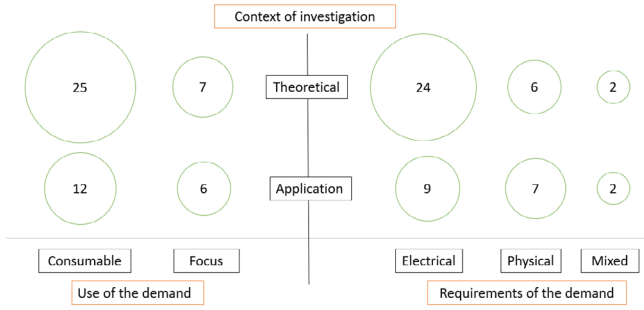

Figure 1. Systematic mapping according to the research context, the use of the demand, and the demand requirements
Source: Authors

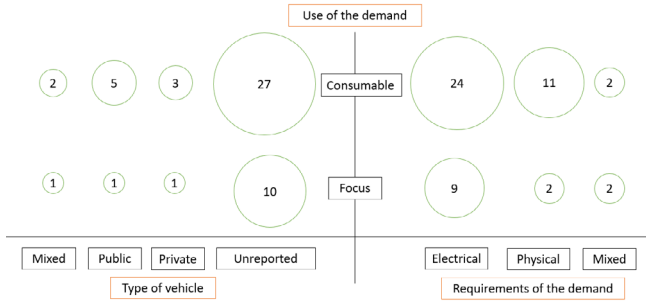

Figure 2. Systematic mapping according to the use of the demand, the type of vehicle, and the demand requirements
Source: Authors

Figure 2 clearly shows that the combinations occurring with the greatest frequency are (i) a consumable use of the demand with a lack of information on the type of vehicle, and (ii) a consumable use of the demand identified for electrical demand requirements.

Results and discussion

The answers to the research questions obtained by analyzing the articles are given below:

For RQ-1, it was found that 74% of the reviewed articles used the demand model as a consumable for the construction of further information. For RQ-2, the main requirements for the construction of the demand were associated with electrical elements, (66%). However, it should be noted that 8% of the articles used a model that provided data on both electrical and physical requirements. The type of use of the vehicle in the demand study, *i.e.*, the subject of RQ-3, was not clearly identified in most cases (74%). Some articles explicitly mentioned cars in shared use, fleets of taxis, and applications for buses. The results for RQ-4, *i.e.*, the research area, show a clear tendency towards the theoretical field (64%). However, when the research area is compared to the different demand requirements, it is found that, for articles addressing physical demand requirements, the application field (7 cases) predominates over the theoretical

one (6 cases). Finally, as for the results for RQ-5 (*i.e.*, the type of (mathematical) model used for demand projection) were very diverse. Table 1 is a summarized list of authors, articles, and the various models applied.

Table 1. Demand models

Demand model	Author(s)
Markov chains (regular, hidden)	(Ehsan and Yang, 2020); (N. Chen *et al.*, 2018); (Arias *et al.*, 2017); (Abdulaal *et al.*, 2017)
Markov chains and stochastic scenario-based programming	(Z. Wang *et al.*, 2020)
Queueing model	(Meng *et al.*, 2020); (Hafez and Bhattacharya, 2018b); (Ou *et al.*, 2015)
Queueing model and neural networks	(Hafez and Bhattacharya, 2018a)
Simulation models	(Dai *et al.*, 2019); (Iacobucci *et al.*, 2018); (M. Mohamed *et al.*, 2017)
Non-linear models (integer numbers, mixed integers)	(Gan *et al.*, 2020); (A. A. S. Mohamed *et al.*, 2020)
Non-linear model of maximum coverage and heuristics	(Gao *et al.*, 2020)
Heuristic algorithm (closest neighbor, genetic algorithm)	(Akbari *et al.*, 2018); (Majidpour *et al.*, 2015)
Genetic algorithm and profit optimization	(Y. Huang and Kockelman, 2020)
Monte Carlo method	(Domínguez-Navarro *et al.*, 2019); (Ahmed *et al.*, 2018)
Stochastic programming (regular – dynamic)	(Mehrjerdi and Hemmati, 2019); (Liao and Lu, 2015)
Linear programming (mixed integers, dynamic)	(Liu *et al.*, 2018); (Q. Chen *et al.*, 2017)
Traffic assignment model	(X. Wang *et al.*, 2019); (Wei *et al.*, 2017)
Multiplicatively weighted Voronoi diagram	(Lee *et al.*, 2019)
Polygon overlay method	(K. Huang *et al.*, 2016)
Temporary SoC modeling	(S. Sun *et al.*, 2018)
Cost based model	(Xiang *et al.*, 2016)
Multi-objective optimization	(Mozafar *et al.*, 2017)
Space-time model	(Z. Sun *et al.*, 2017)
Modified capacitated flow location model based on sub-paths	(H. Zhang *et al.*, 2018)
Automatic learning	(Almaghrebi *et al.*, 2020)
Vector regression support method	(Lan *et al.*, 2021)
Nguyen-Dupius network	(Yang *et al.*, 2020)
Time series	(Kim and Kim, 2021)
Independent models (names not specified)	(Xu and Meng, 2020); (H. Zhang *et al.*, 2020); (H. Wang *et al.*, 2019); (de Quevedo *et al.*, 2019); (Xiong *et al.*, 2018); (Y. Wang *et al.*, 2018); (Bryden *et al.*, 2018); (Simorgh *et al.*, 2018); (Yi *et al.*, 2018); (Kisacikoglu *et al.*, 2018); (Bhat *et al.*, 2017); (Bhat *et al.*, 2017); (Ahn and Yeo, 2015)

Source: Authors

This Table shows the remarkable and wide variety of methodologies designed to establish the demands associated with electric vehicles. Mathematical modeling and operations research tools play a leading role. An interesting aspect is the use of queueing theory as a mathematical theory of the stochastic service system (L. Li *et al.*, 2016), which refers to queue analysis when a client comes to a service station and has to queue before being served (Hamdan *et al.*, 2017). The tool is applied to provide an answer regarding the efficient number of parameters or charging points needed to supply energy to EVs. Different stochastic systems may be used to calculate this number, such as the one that treats the arrival of the vehicles as a non-homogeneous Poisson process while modeling the serving time based on the detailed characteristics of the battery (Hafez and Bhattacharya, 2018b). Other cases are defined with a compound M/G/∞ queueing model (Ou *et al.*, 2015). In parallel, and in the same field of operations research, Markov models are also used in several cases, *e.g.*, to determine the forecast power demand for charging EVs at fast charging stations located in urban areas (Arias *et al.*, 2017), or to estimate the energy states among a group of charging stations (Chen *et al.*, 2018).

An interesting finding outside the parameters indicated for this study emerged while reviewing the abstracts: the object of this investigation was to study the demand for EVs, particularly physical or electrical requirements; however, many publications do not mention these elements, but refer to the concept of the response to demand and charging patterns. These are signs of progress being made in the most recent needs regarding EVs, where it is important to have data and models with which to describe how vehicle users follow their charging programs, both as a function of the time they devote to charging and the time of day in which they do so. It is also relevant to study how users' charging behavior influences supply systems and the power grid. Some examples of this situation are found in the works by Kamruzzaman and Benidris (2020), A. A. S. Mohamed *et al.* (2020), P. Wang *et al.* (2020), Yan *et al.* (2020), M. Zhang *et al.* (2020), and Zhou *et al.* (2020).

Conclusions

The results of the systematic mapping study show a wide variety of demand models for electric vehicles., among which mathematical programming and operations research tools such as Markov chains and queueing models are the most frequently used.

Demand models are frequently used as a research consumable in the reviewed articles to establish electrical over physical ones. Most articles did not provide information on the type of vehicle, suggesting that this was not relevant for their research purposes. Finally, most of the reviewed articles were associated with the theoretical field rather than the practical one.

References

Abdulaal, A., Cintuglu, M. H., Asfour, S., and Mohammed, O. A. (2017). Solving the multivariant EV routing problem incorporating V2G and G2V options. *IEEE Transactions on Transportation Electrification*, *3*(1), 238-248. https://doi.org/10.1109/TTE.2016.2614385

Agostino, Í. R. S., Ristow, C., Frazzon, E. M., and Taboada Rodriguez, C. M. (2020). Perspectives on the application of Internet of Things in logistics. In M. Freitag, H.-D. Haasis, and J. Pannek (Eds.), *Lecture Notes in Logistics* (pp. 387-397). Springer. https://doi.org/10.1007/978-3-030-44783-0_37

Ahmed, H. M. A., Eltantawy, A. B., and Salama, M. M. A. (2018). A planning approach for the network configuration of AC-DC hybrid distribution systems. *IEEE Transactions on Smart Grid*, *9*(3), 2203-2213. https://doi.org/10.1109/TSG.2016.2608508

Ahn, Y., and Yeo, H. (2015). An analytical planning model to estimate the optimal density of charging stations for electric vehicles. *PLoS One*, *10*(11), 0141307. https://doi.org/10.1371/journal.pone.0141307

Akbari, M., Brenna, M., and Longo, M. (2018). Optimal locating of electric vehicle charging stations by application of Genetic Algorithm. *Sustainability*, *10*(4), 1076. https://doi.org/10.3390/su10041076

Almaghrebi, A., Aljuheshi, F., Rafaie, M., James, K., and Alahmad, M. (2020). Data-driven charging demand prediction at public charging stations using supervised machine learning regression methods. *Energies*, *13*(16), 4231. https://doi.org/10.3390/en13164231

Arias, M. B., Kim, M., and Bae, S. (2017). Prediction of electric vehicle charging-power demand in realistic urban traffic networks. *Applied Energy*, *195*, 738-753. https://doi.org/10.1016/j.apenergy.2017.02.021

Behmanesh, A., Sadoughi, F., Mazhar, F. N., Joghataei, M. T., and Yazdani, S. (2020). Tele-orthopaedics: A systematic mapping study. *Journal of Telemedicine and Telecare, 28*(1), 3-23. https://doi.org/10.1177/1357633X20919308

Belmonte, L. M., Morales, R., and Fernández-Caballero, A. (2019). Computer vision in autonomous unmanned aerial vehicles – A systematic mapping study. *Applied Sciences*, *9*(15), 3196. https://doi.org/10.3390/app9153196

Bhat, N. G., Prusty, B. R., and Jena, D. (2017). Cumulant-based correlated probabilistic load flow considering photovoltaic generation and electric vehicle charging demand. *Frontiers in Energy*, *11*(2), 184-196. https://doi.org/10.1007/s11708-017-0465-7

Brenna, M., Foiadelli, F., Leone, C., and Longo, M. (2020). Electric vehicles charging technology review and optimal size estimation. *Journal of Electrical Engineering and Technology*, *15*(6), 2539-2552. https://doi.org/10.1007/s42835-020-00547-x

Bryden, T. S., Hilton, G., Cruden, A., and Holton, T. (2018). Electric vehicle fast charging station usage and power requirements. *Energy*, *152*, 322-332. https://doi.org/10.1016/j.energy.2018.03.149

Cao, Y., Kaiwartya, O., Zhuang, Y., Ahmad, N., Sun, Y., and Lloret, J. (2019). A decentralized deadline-driven electric vehicle charging recommendation. *IEEE Systems Journal*, *13*(3), 3410-3421. https://doi.org/10.1109/JSYST.2018.2851140

Celdrán-Bernabéu, M. A., Mazón, J.-N., Ivars-Baidal, J. A., and Vera-Rebollo, J. F. (2018). Smart tourism. Un estudio de mapeo sistemático. *Cuadernos de Turismo*, *41*, 326971. https://doi.org/10.6018/turismo.41.326971

Chen, N., Ma, J., Wang, M., and Shen, X. (2018). Two-tier energy compensation framework based on mobile vehicular electric storage. *IEEE Transactions on Vehicular Technology*, *67*(12), 11719-11732. https://doi.org/10.1109/TVT.2018.2874046

Chen, Q., Wang, F., Hodge, B.-M., Zhang, J., Li, Z., Shafie-Khah, M., and Catalao, J. P. S. (2017). Dynamic price vector formation model-based automatic demand response strategy for PV-assisted EV charging stations. *IEEE Transactions on Smart Grid*, *8*(6), 2903-2915. https://doi.org/10.1109/TSG.2017.2693121

Cheon, S., and Kang, S. J. (2017). An electric power consumption analysis system for the installation of electric vehicle charging stations. *Energies*, *10*(10), 1534. https://doi.org/10.3390/en10101534

Ciğerci, Y., Kısacık, Ö. G., Özyürek, P., and Çevik, C. (2019). Nursing music intervention: A systematic mapping study. *Complementary Therapies in Clinical Practice*, *35*, 109-120. https://doi.org/10.1016/j.ctcp.2019.02.007

Cravero, A., Lagos, D., and Espinosa, R. (2018). Big data/IoT use in wine production: A systematic mapping study. *IEEE Latin America Transactions*, *16*(5), 1476-1484. https://doi.org/10.1109/TLA.2018.8408444

Csiszár, C., Csonka, B., Földes, D., Wirth, E., and Lovas, T. (2019). Urban public charging station locating method for electric vehicles based on land use approach. *Journal of Transport Geography*, *74*, 173-180. https://doi.org/10.1016/j.jtrangeo.2018.11.016

Dai, Q., Liu, J., and Wei, Q. (2019). Optimal photovoltaic/battery energy storage/electric vehicle charging station design based onmulti-agent particle swarm optimization algorithm. *Sustainability*, *11*(7), 1973. https://doi.org/10.3390/su11071973

de Quevedo, P. M., Muñoz-Delgado, G., and Contreras, J. (2019). Impact of electric vehicles on the expansion planning of distribution systems considering renewable energy, storage, and charging stations. *IEEE Transactions on Smart Grid*, *10*(1), 794-804. https://doi.org/10.1109/TSG.2017.2752303

Dicheva, D., Dichev, C., Agre, G., and Angelova, G. (2015). Gamification in education: A systematic mapping study. *Educational Technology and Society*, *18*(3), 75-88.

Dileepan, V. M., and Jayakumar, J. (2020). Analysis of performance improvement in energy storage system for electric vehicles: A review. *International Journal of Electric and Hybrid Vehicles*, *12*(4), 315-348. https://doi.org/10.1504/IJEHV.2020.113077

Ding, N., Prasad, K., and Lie, T. T. (2017). The electric vehicle: A review. *International Journal of Electric and Hybrid Vehicles*, *9*(1), 49-66. https://doi.org/10.1504/IJEHV.2017.082816

Domínguez-Navarro, J. A., Dufo-López, R., Yusta-Loyo, J. M., Artal-Sevil, J. S., and Bernal-Agustín, J. L. (2019). Design of an electric vehicle fast-charging station with integration of renewable energy and storage systems. *International Journal of Electrical Power and Energy Systems*, *105*, 46-58. https://doi.org/10.1016/j.ijepes.2018.08.001

Drissi, N., Ouhbi, S., Idrissi, M. A. J., Fernandez-Luque, L., and Ghogho, M. (2020). Connected mental health: Systematic mapping study. *Journal of Medical Internet Research*, *22*(8), e19950. https://doi.org/10.2196/19950

Ehsan, A., and Yang, Q. (2020). Active distribution system reinforcement planning with EV charging stations – Part I: Uncertainty modeling and problem formulation. *IEEE Transactions on Sustainable Energy*, *11*(2), 970-978. https://doi.org/10.1109/TSTE.2019.2915338

Faridimehr, S., Venkatachalam, S., and Chinnam, R. B. (2019). A stochastic programming approach for electric vehicle charging network design. *IEEE Transactions on Intelligent Transportation Systems*, *20*(5), 1870-1882. https://doi.org/10.1109/TITS.2018.2841391

Gabriel, A., Monticolo, D., Camargo, M., and Bourgault, M. (2016). Creativity support systems: A systematic mapping study. *Thinking Skills and Creativity*, *21*, 109-122. https://doi.org/10.1016/j.tsc.2016.05.009

Gan, X., Zhang, H., Hang, G., Qin, Z., and Jin, H. (2020). Fast-charging station deployment considering elastic demand. *IEEE Transactions on Transportation Electrification*, *6*(1), 158-169. https://doi.org/10.1109/TTE.2020.2964141

Gao, H., Liu, K., Peng, X., and Li, C. (2020). Optimal location of fast charging stations for mixed traffic of electric vehicles and gasoline vehicles subject to elastic demands. *Energies*, *13*(8), 1964. https://doi.org/10.3390/en13081964

Habib, A. K. M. A., Hasan, M. K., Mahmud, M., Motakabber, S. M. A., Ibrahimya, M. I., and Islam, S. (2020). A review: Energy storage system and balancing circuits for electric vehicle application. *IET Power Electronics, 14*(1), 1-13. https://doi.org/10.1049/pel2.12013

Hafez, O., and Bhattacharya, K. (2018a). Integrating EV charging stations as smart loads for demand response provisions in distribution systems. *IEEE Transactions on Smart Grid*, *9*(2), 1096-1106. https://doi.org/10.1109/TSG.2016.2576902

Hafez, O., and Bhattacharya, K. (2018b). Queuing analysis based PEV load modeling considering battery charging behavior and their impact on distribution system operation. *IEEE Transactions on Smart Grid*, *9*(1), 261-273. https://doi.org/10.1109/TSG.2016.2550219

Haghighatkhah, A., Banijamali, A., Pakanen, O.-P., Oivo, M., and Kuvaja, P. (2017). Automotive software engineering: A systematic mapping study. *Journal of Systems and Software*, *128*, 25-55. https://doi.org/10.1016/j.jss.2017.03.005

Hamdan, A. R., Ishak, R., and Usop, M. F. (2017). Effective school cooperative-mart queuing system. *Malaysian Journal of Fundamental and Applied Sciences*, *13*(SI), 412-415. https://doi.org/10.11113/mjfas.v13n4-1.859

Huang, K., Kanaroglou, P., and Zhang, X. (2016). The design of electric vehicle charging network. *Transportation Research Part D: Transport and Environment*, *49*, 1-17. https://doi.org/10.1016/j.trd.2016.08.028

Huang, Y., and Kockelman, K. M. (2020). Electric vehicle charging station locations: Elastic demand, station congestion, and network equilibrium. *Transportation Research Part D-Transport and Environment*, *78*, 102179. https://doi.org/10.1016/j.trd.2019.11.008

Iacobucci, R., McLellan, B., and Tezuka, T. (2018). Modeling shared autonomous electric vehicles: Potential for transport and power grid integration. *Energy*, *158*, 148-163. https://doi.org/10.1016/j.energy.2018.06.024

Jafari, A. J., and Rasoolzadegan, A. (2020). Security patterns: A systematic mapping study. *Journal of Computer Languages*, *56*, 100938. https://doi.org/10.1016/j.cola.2019.100938

Jing, W., Yan, Y., Kim, I., and Sarvi, M. (2016). Electric vehicles: A review of network modelling and future research needs. *Advances in Mechanical Engineering*, *8*(1), 1-8. https://doi.org/10.1177/1687814015627981

Kamruzzaman, M. D., and Benidris, M. (2020). A reliability-constrained demand response-based method to increase the hosting capacity of power systems to electric vehicles. *International Journal Of Electrical Power and Energy Systems*, *121*, 106046. https://doi.org/10.1016/j.ijepes.2020.106046

Khan, A., Zhang, H., Boudjellal, N., Ahmad, A., Shang, J., Dai, L., and Hayat, B. (2021). Election prediction on Twitter: A systematic mapping study. *Complexity*, *2021*, 5565434. https://doi.org/10.1155/2021/5565434

Kim, Y., and Kim, S. (2021). Forecasting charging demand of electric vehicles using time-series models. *Energies*, *14*(5), 1487. https://doi.org/10.3390/en14051487

Kisacikoglu, M. C., Erden, F., and Erdogan, N. (2018). Distributed control of PEV charging based on energy demand forecast. *IEEE Transactions on Industrial Informatics*, *14*(1), 332-341. https://doi.org/10.1109/TII.2017.2705075

Kitchenham, B., Dybå, T., and Jørgensen, M. (2004). Evidence-based software engineering. In *Proceedings - International Conference on Software Engineering, 26*, 273-281.

Kitchenham, B., and Charters, S. (2007). *Guidelines for performing systematic literature reviews in software engineering*. https://www.researchgate.net/publication/302924724_Guidelines_for_performing_Systematic_Literature_Reviews_in_Software_Engineering

Lan, T., Jermsittiparsert, K., Alrashood, S. T., Rezaei, M., Al-Ghussain, L., and Mohamed, M. A. (2021). An advanced machine learning based energy management of renewable microgrids considering hybrid electric vehicles' charging demand. *Energies*, *14*(3), 0569. https://doi.org/10.3390/en14030569

Lee, W., Schober, R., and Wong, V. W. S. (2019). An analysis of price competition in heterogeneous electric vehicle charging stations. *IEEE Transactions on Smart Grid*, *10*(4), 3990-4002. https://doi.org/10.1109/TSG.2018.2847414

Li, L., Liu, F., Long, G., Zhao, H., and Mei, Y. (2016). Performance analysis and optimal allocation of layered defense M/M/N queueing systems. *Mathematical Problems in Engineering*, *2016*, 5915918. https://doi.org/10.1155/2016/5915918

Li, X., Chen, P., and Wang, X. (2017). Impacts of renewables and socioeconomic factors on electric vehicle demands - Panel data studies across 14 countries. *Energy Policy*, *109*, 473-478. https://doi.org/10.1016/j.enpol.2017.07.021

Li, Z., Khajepour, A., and Song, J. (2019). A comprehensive review of the key technologies for pure electric vehicles. *Energy*, *182*, 824-839. https://doi.org/10.1016/j.energy.2019.06.077

Liao, Y.-T., and Lu, C.-N. (2015). Dispatch of EV charging station energy resources for sustainable mobility. *IEEE Transactions on Transportation Electrification*, *1*(1), 86-93. https://doi.org/10.1109/TTE.2015.2430287

Limmer, S. (2019). Dynamic pricing for electric vehicle charging – A literature review. *Energies*, *12*(18), 3574. https://doi.org/10.3390/en12183574

Lipu, M. S. H., Faisal, M., Ansari, S., Hannan, M. A., Karim, T. F., Ayob, A., Hussain, A., Sazal Miah, M., and Saad, M. H. M. (2021). Review of electric vehicle converter configurations, control schemes and optimizations: Challenges and suggestions. *Electronics*, *10*(4), 477. https://doi.org/10.3390/electronics10040477

Liu, Z., Song, Z., and He, Y. (2018). Planning of fast-charging stations for a battery electric bus system under energy consumption uncertainty. *Transportation Research Record*, *2672*(8), 96-107. https://doi.org/10.1177/0361198118772953

Majidpour, M., Qiu, C., Chu, P., Gadh, R., and Pota, H. R. (2015). Fast prediction for sparse time series: Demand forecast of EV charging stations for cell phone applications. *IEEE Transactions On Industrial Informatics*, *11*(1), 242-250. https://doi.org/10.1109/TII.2014.2374993

Mehrjerdi, H., and Hemmati, R. (2019). Electric vehicle charging station with multilevel charging infrastructure and hybrid solar-battery-diesel generation incorporating comfort of drivers. *Journal of Energy Storage*, *26*, 100924. https://doi.org/10.1016/j.est.2019.100924

Meisel, S., and Merfeld, T. (2018). Economic incentives for the adoption of electric vehicles: A classification and review of e-vehicle services. *Transportation Research Part D: Transport and Environment*, *65*, 264-287. https://doi.org/10.1016/j.trd.2018.08.014

Meng, X., Zhang, W., Bao, Y., Yan, Y., Yuan, R., Chen, Z., and Li, J. (2020). Sequential construction planning of electric taxi charging stations considering the development of charging demand. *Journal of Cleaner Production*, *259*, 120794. https://doi.org/10.1016/j.jclepro.2020.120794

Ministerio de energía (2017). *Estrategia Nacional de Electromovilidad*. http://www.minenergia.cl/archivos_bajar/2018/electromovilidad/estrategia_electromovilidad-27dic.pdf

Mohamed, A. A. S., Zhu, L., Meintz, A., and Wood, E. (2020). Planning optimization for inductively charged on-demand automated electric shuttles project at Greenville, South Carolina. *IEEE Transactions on Industry Applications*, *56*(2), 1010-1020. https://doi.org/10.1109/TIA.2019.2958566

Mohamed, M., Farag, H., El-Taweel, N., and Ferguson, M. (2017). Simulation of electric buses on a full transit network: Operational feasibility and grid impact analysis. *Electric Power Systems Research*, *142*, 163-175. https://doi.org/10.1016/j.epsr.2016.09.032

Mozafar, M. R., Moradi, M. H., and Amini, M. H. (2017). A simultaneous approach for optimal allocation of renewable energy sources and electric vehicle charging stations in smart grids based on improved GAPSO algorithm. *Sustainable Cities and Society*, *32*, 627-637. https://doi.org/10.1016/j.scs.2017.05.007

Németh, B., Németh, K., Procter, J. N., and Farrelly, T. (2021). Geoheritage conservation: Systematic mapping study for conceptual synthesis. *Geoheritage*, *13*, 45. https://doi.org/10.1007/s12371-021-00561-z

Ou, C.-H., Liang, H., and Zhuang, W. (2015). Investigating wireless charging and mobility of electric vehicles on electricity market. *IEEE Transactions on Industrial Electronics*, *62*(5), 3123-3133. https://doi.org/10.1109/TIE.2014.2376913

Qin, H., Su, X., Ren, T., and Luo, Z. (2021). A review on the electric vehicle routing problems: Variants and algorithms. *Frontiers of Engineering Management*, *8*(3), 370-389. https://doi.org/10.1007/s42524-021-0157-1

Rachad, T., and Idri, A. (2020). Intelligent mobile applications: A systematic mapping study. *Mobile Information Systems*, *2020*, 6715363. https://doi.org/10.1155/2020/6715363

Rajper, S. Z., and Albrecht, J. (2020). Prospects of electric vehicles in the developing countries: A literature review. *Sustainability*, *12*(5), 1906. https://doi.org/10.3390/su12051906

Rodrigues, C. M. D. O., Freitas, F. L. G. D., Barreiros, E. F. S., Azevedo, R. R. D., and de Almeida Filho, A. T. (2019). Legal ontologies over time: A systematic mapping study. *Expert Systems with Applications*, *130*, 12-30. https://doi.org/10.1016/j.eswa.2019.04.009

Saleemi, M., Anjum, M., and Rehman, M. (2020). Ubiquitous healthcare: A systematic mapping study. *Journal of Ambient Intelligence and Humanized Computing*, *2020*, 02513. https://doi.org/10.1007/s12652-020-02513-x

Sierra, J. M., Vizcaíno, A., Genero, M., and Piattini, M. (2018). A systematic mapping study about socio-technical congruence. *Information and Software Technology*, *94*, 111-129. https://doi.org/10.1016/j.infsof.2017.10.004

Simorgh, H., Doagou-Mojarrad, H., Razmi, H., and Gharehpetian, G. B. (2018). Cost-based optimal siting and sizing of electric vehicle charging stations considering demand response programmes. *IET Generation, Transmission and Distribution*, *12*(8), 1712-1720. https://doi.org/10.1049/iet-gtd.2017.1663

Solanke, T. U., Ramachandaramurthy, V. K., Yong, J. Y., Pasupuleti, J., Kasinathan, P., and Rajagopalan, A. (2020). A review of strategic charging-discharging control of grid-connected electric vehicles. *Journal of Energy Storage*, *28*, 101193. https://doi.org/10.1016/j.est.2020.101193

Sun, S., Yang, Q., and Yan, W. (2018). Hierarchical optimal planning approach for plug-in electric vehicle fast charging stations based on temporal-SoC charging demand characterisation. *IET Generation, Transmission and Distribution*, *12*(20), 4388-4395. https://doi.org/10.1049/iet-gtd.2017.1894

Sun, X., Li, Z., Wang, X., and Li, C. (2020). Technology development of electric vehicles: A review. *Energies*, *13*(1), 90. https://doi.org/10.3390/en13010090

Sun, Z., Zhou, X., Du, J., and Liu, X. (2017). When traffic flow meets power flow: On charging station deployment with budget constraints. *IEEE Transactions on Vehicular Technology*, *66*(4), 2915-2926. https://doi.org/10.1109/TVT.2016.2593712

Usman, M., Knapen, L., Yasar, A.-U.-H., Bellemans, T., Janssens, D., and Wets, G. (2020). Optimal recharging framework and simulation for electric vehicle fleet. *Future Generation Computer Systems*, *107*, 745-757. https://doi.org/10.1016/j.future.2017.04.037

Wang, H., Zhao, D., Meng, Q., Ong, G. P., and Lee, D.-H. (2019). A four-step method for electric-vehicle charging facility deployment in a dense city: An empirical study in Singapore. *Transportation Research Part A: Policy and Practice*, *119*, 224-237. https://doi.org/10.1016/j.tra.2018.11.012

Wang, P., Wang, D., Zhu, C., Yang, Y., Abdullah, H. M., and Mohamed, M. A. (2020). Stochastic management of hybrid AC/DC microgrids considering electric vehicles charging demands. *Energy Reports*, *6*, 1338-1352. https://doi.org/10.1016/j.egyr.2020.05.019

Wang, X., Shahidehpour, M., Jiang, C., and Li, Z. (2019). Coordinated planning strategy for electric vehicle charging stations and coupled traffic-electric networks. *IEEE Transactions on Power Systems*, *34*(1), 268-279. https://doi.org/10.1109/TPWRS.2018.2867176

Wang, Y., Shi, J., Wang, R., Liu, Z., and Wang, L. (2018). Siting and sizing of fast charging stations in highway network with budget constraint. *Applied Energy*, *228*, 1255-1271. https://doi.org/10.1016/j.apenergy.2018.07.025

Wang, Z., Jochem, P., and Fichtner, W. (2020). A scenario-based stochastic optimization model for charging scheduling of electric vehicles under uncertainties of vehicle availability and charging demand. *Journal of Cleaner Production*, *254*, 119886. https://doi.org/10.1016/j.jclepro.2019.119886

Waseem, M., Sherwani, A. F., and Suhaib, M. (2019). Integration of solar energy in electrical, hybrid, autonomous vehicles: a technological review. *SN Applied Sciences*, *1*, 1459. https://doi.org/10.1007/s42452-019-1458-4

Wei, W., Mei, S., Wu, L., Wang, J., and Fang, Y. (2017). Robust operation of distribution networks coupled with urban transportation infrastructures. *IEEE Transactions on Power Systems*, *32*(3), 2118-2130. https://doi.org/10.1109/TPWRS.2016.2595523

Xiang, Y., Liu, J., Li, R., Li, F., Gu, C., and Tang, S. (2016). Economic planning of electric vehicle charging stations considering traffic constraints and load profile templates. *Applied Energy*, *178*, 647-659. https://doi.org/10.1016/j.apenergy.2016.06.021

Xiong, Y., Wang, B., Chu, C.-C., and Gadh, R. (2018). Vehicle grid integration for demand response with mixture user model and decentralized optimization. *Applied Energy*, *231*, 481-493. https://doi.org/10.1016/j.apenergy.2018.09.139

Xu, M., and Meng, Q. (2020). Optimal deployment of charging stations considering path deviation and nonlinear elastic demand. *Transportation Research Part B: Methodological*, *135*, 120-142. https://doi.org/10.1016/j.trb.2020.03.001

Yan, H., Ma, R., Liu, Z., Zhu, X., and Wei, Z. (2020). Multi-time scale stochastic optimal dispatch of electric vehicle charging station considering demand response [计及需求响应的电动汽车充电站多时间尺度随机优化调度]. *Dianli Xitong Baohu Yu Kongzhi/Power System Protection and Control*, *48*(10), 71-80. https://doi.org/10.19783/j.cnki.pspc.190768

Yang, J., Wu, F., Yan, J., Lin, Y., Zhan, X., Chen, L., Liao, S., Xu, J., and Sun, Y. (2020). Charging demand analysis framework for electric vehicles considering the bounded rationality behavior of users. *International Journal of Electrical Power and Energy Systems*, *119*, 105952. https://doi.org/10.1016/j.ijepes.2020.105952

Yi, Z., Smart, J., and Shirk, M. (2018). Energy impact evaluation for eco-routing and charging of autonomous electric vehicle fleet: Ambient temperature consideration. *Transportation Research Part C: Emerging Technologies*, *89*, 344-363. https://doi.org/10.1016/j.trc.2018.02.018

Zakari, A., Lee, S. P., Alam, K. A., and Ahmad, R. (2019). Software fault localisation: A systematic mapping study. *IET Software*, *13*(1), 60-74. https://doi.org/10.1049/iet-sen.2018.5137

Zhang, H., Moura, S. J., Hu, Z., Qi, W., and Song, Y. (2018). A second-order cone programming model for planning PEV fast-charging stations. *IEEE Transactions on Power Systems*, *33*(3), 2763-2777. https://doi.org/10.1109/TPWRS.2017.2754940

Zhang, H., Sheppard, C. J. R., Lipman, T. E., Zeng, T., and Moura, S. J. (2020). Charging infrastructure demands of shared-use autonomous electric vehicles in urban areas. *Transportation Research Part D-Transport and Environment*, *78*, 102210. https://doi.org/10.1016/j.trd.2019.102210

Zhang, M., Cai, Y., Yang, X., and Li, L. (2020). Charging demand distribution analysis method of household electric vehicles considering users' charging difference [考虑用户充电差异性的家用电动汽车充电需求分布分析方法]. *Dianli Zidonghua Shebei/Electric Power Automation Equipment*, *40*(2), 154-161. https://doi.org/10.16081/j.epae.202002003

Zhou, K., Cheng, L., Wen, L., Lu, X., and Ding, T. (2020). A coordinated charging scheduling method for electric vehicles considering different charging demands. *Energy*, *213*, 118882. https://doi.org/10.1016/j.energy.2020.118882

Research Article/Electrical, Electronic, and Telecommunications Engineering https://doi.org/10.15446/ing.investig.94695

Radiofrequency Absorbance as a Novel Concentration Indicator in Sucrose Aqueous Solutions

La absorción de radiofrecuencia como nuevo indicador de la concentración en soluciones acuosas de sacarosa

Javier Coronel-Gaviro [1], Virginia Yagüe-Jiménez [2], and José L. Blanco-Murillo [3]

ABSTRACT

Microwave-based methods have been used for years to monitor processes, tests, and substance mixtures. Solutions must preserve sample integrity and avoid time-consuming procedures to scale inline industrial applications and promote on-field tests. Today, testing procedures use portable, cost-effective devices operating on wide frequency ranges to perform low-power, wide-band microwave dielectric spectroscopy. This paper describes a proof of concept using SDR technology to match all these requirements. A prototype was tested for measuring sucrose-in-water solutions at different concentrations, which resulted in a novel concentration indicator based on radiofrequency absorbance. This application is critical for in-line monitoring and on-field testing in the food and beverage industries. The proposed method delivered robust, replicable, and reliable results. High levels of significance (> 99%) were achieved in statistical tests in the frequency range of 4 125 to 4 410 MHz. The indicator was shown to be sensitive to concentrations below those reported in the literature and could be easily integrated into non-destructive early chemical evaluation for food quality and production monitoring or into on-field testing devices, to name some applications.

Keywords: radiofrequency, absorbance spectra, software defined radio, aqueous solutions

RESUMEN

Los métodos basados en microondas se han utilizado durante años para monitorizar procesos, pruebas y mezclas de sustancias. Estas soluciones buscan preservar la integridad de las muestras y evitar procedimientos lentos para escalar aplicaciones industriales en línea y promover pruebas en campo. Actualmente, los procedimientos de prueba emplean dispositivos portátiles y económicos que operan en amplios rangos de frecuencia para realizar espectroscopia dieléctrica de microondas de baja potencia y banda ancha. Este artículo describe una prueba de concepto que emplea la tecnología SDR para cumplir con todos estos requisitos. Se evaluó un prototipo para la medición de soluciones de sacarosa en agua a diferentes concentraciones, lo cual derivó en un nuevo indicador de concentración basado en la absorbancia por radiofrecuencia. Esta aplicación es crucial para la monitorización en línea y la realización de pruebas en campo en la industria alimentaria y de bebidas. El método propuesto aportó resultados robustos, replicables y confiables. Se alcanzaron altos niveles de significancia (> 99 %) en las pruebas estadísticas en el rango de 4 125 a 4 410 MHz. Este indicador demostró ser sensible a concentraciones inferiores a las reportadas en la literatura y podría integrarse fácilmente en la evaluación química temprana no destructiva de la calidad de los alimentos y el control de la producción, o incluso en dispositivos de prueba en campo, por nombrar algunas aplicaciones.

Palabras clave: radiofrecuencia, espectro de absorción, radio definida por software, soluciones acuosas

Received: March 26th, 2021
Accepted: June 10th, 2022

Introduction

Radiofrequency absorbance quantifies the physical and chemical properties of samples from controlled measurements of the perturbed electromagnetic (EM) field (Wlodarczak, 2017). These methods are increasingly being used for monitoring, testing, and quantifying productive processes in different industries (Xia *et al.*, 2019; Lu *et al.*, 2019; Pu *et al.*, 2020). Industrial applications tend to avoid high-energy fields that compromise sample integrity (El-Mesery *et al.*, 2019) while aiming for portable, cost-effective technologies that mitigate time-consuming processes (Lindon et al., 2017).

Characterizing EM properties is an ongoing task that has drawn considerable attention. Most of the work is aimed at estimating complex permittivity (ϵ) (Bindu *et al.*, 2006; Kaatze, 2013; Wlodarczak, 2017) as a way to describe the differences and characteristic patterns. This quantifies the measurable impact on field displacement ($\bar{D}$) of an electric field ($\bar{E}$) in the presence of intrinsic polarity ($\bar{P}$):

$$\bar{D}(r,\phi,\theta,f) = \epsilon(r,\phi,\theta,f) \cdot \bar{E}(r,\phi,\theta,f) + \bar{P}(r,\phi,\theta,f) \quad (1)$$

[1] Computer engineer, Universidad Nacional de Educación a Distancia, Spain. MSc in Medical Physics, Universidad Nacional de Educación a Distancia, Spain. PhD in Communications Technologies and Systems, Universidad Politécnica de Madrid, Spain. Affiliation: Postdoctoral researcher, Universidad Politécnica de Madrid, Spain. E-mail: j.coronel@alumnos.upm.es

[2] Telecommunications engineer, Universidad Politécnica de Madrid, Spain. PhD in Electrical Engineering, Universidad Politécnica de Madrid, Spain. Affiliation: Postdoctoral researcher, Universidad Politécnica de Madrid, Spain. E-mail: virginia.yague@upm.es

[3] Telecommunications engineer, Universidad Politécnica de Madrid, Spain. PhD Electrical Engineering, Universidad Politécnica de Madrid, Spain. Affiliation: Associate professor, Information Processing and Telecommunciations Center, Universidad Politécnica de Madrid, Spain. E-mail:jl.blanco@upm.es

How to cite: Coronel-Gaviro, J., ague-Jiménez, V., and Blanco-Murillo J. (2023). Radiofrequency Absorbance as a Novel Concentration Indicator in Sucrose Aqueous Solutions. *Ingeniería e Investigaci ón, 43*(1), e94695. https://doi.org/10.15446/ing.investig.94695

There is a similar equation for magnetic permeability (μ), which relates the magnetic field ($\bar{H}$) and the magnetic flux density ($\bar{B}$), but requires higher power. Maxwell's equations connect these fields with geometries and interfaces *etc.*, and provide the means to derive different techniques that serve multiple applications (Choi and Kim, 2009; Brovoll *et al.*, 2014; Naishadham *et al.*, 2016).

The coefficient $\epsilon = \epsilon_r \epsilon_0$, with ϵ_r being the relative media-specific permittivity, describes how the traversing field is attenuated and delayed at different frequencies depending on the material, the state of the matter, the geometry (Kaatze, 2013), or the transmitted power level, according to (Agilent Technologies, Inc., 2006; Heileman *et al.*, 2013):

- *Temperature*: it affects atomic but mostly subatomic mobility, microstructures, and state (*e.g.*, solid);
- *Mechanical properties, viscosity, etc.*: macroscopic properties are ultimately related to existing molecular and atomic structures, interactions, and bonds;
- *Electro-static* and *electro-dynamic properties* are affected due to bonds and interactions at a chemical level, polarity, size, weight, and structure of molecules, radicals, or ions.

Therefore, changes and differences in the media at the molecular, atomic, and subatomic levels produce characteristic responses in the EM field at different levels and bands.

Depending on the specific method and the excited bands, one can evaluate the presence of different substances, estimate the geometry of the underlying structures (at molecular and microscopic levels) or collect evidence on the inner state of matter (*e.g.*, temperature) (Meng, Wu, and Gray, 2018). Although complex interactions still pose a challenge, there is certainly room for improvement with respect to instruments, setups, and indicators for field tests.

Different frequency ranges have been inspected. The visible spectrum can be used for nondestructive spectrophotometry or destructive spectrometry. Adjacent bands, such as UV or IR, have gained attention and are now standard (Becker *et al.*, 2020). High energy bands (*e.g.*, X-ray and above) were initially used for internal structure inspection and diagnosis (Maier *et al.*, 2018; Torres Castellanos and Rodríguez-Torres, 2019). In recent decades, spectrometry has reached these bands (Lindon *et al.*, 2017), and dielectric spectrometry has gained attention (Pirola *et al.*, 2007; Agilent Technologies, Inc., 2006) regarding the characterization of the physical properties of substances (Konings *et al.*, 2019) or complex interactions (Yao *et al.*, 2022).

Nondestructive dielectric characterization using radiofrequency measurements requires sensitive instrumentation and subtle perturbations. It has been introduced to evaluate highly conductive substances (Liu and Brady, 1996; Periasamy and Ravi, 2020) and more challenging nonconductive aqueous solutions such as sucrose in water (Gennarelli *et al.*, 2013; Harnsoongnoen and Wanthong, 2017, 2016), where differences in the properties and sizes of the polarity of the molecules (Figure 1) cause distinct and less prominent effects.

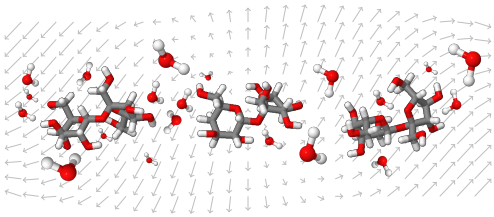

Figure 1. Schematic of sucrose-in-water solution. One may identify both sucrose and pure water molecules under an externally induced EM field (gray). Molecules, ions, and radicals change their locations and orientations as the EM field is perturbed.
Source: Authors

The detection of sucrose concentration is critical for the food and beverage industries to adjust the sweetness of the final product (Harnsoongnoen and Wanthong, 2016), as well as for the improvement and monitoring of crops (Kennedy *et al.*, 2007). The continuous request for non-intrusive, portable, non-contact, and easy ways of measuring has received limited attention. Gennarelli et al. (2013) use a resonant cavity and a 6 MHz bandwidth to measure sugar/water concentrations starting at 500% wt in steps of 5 Kg/L. In (Harnsoongnoen and Wanthong, 2016, 2017), the authors used coplanar open waveguides, achieving a 1 GHz and 600 MHz bandwidth, respectively, reporting on 20% wt mixes in steps of 0,2 g/mL, and from 4% in steps of 4 g/mL.

This paper aims to present a novel method for radiofrequency absorbance evaluation that provides a novel concentration indicator. It uses non-contact, portable, low-cost, and wideband microwave Software-Defined Radio (SDR) technology to compute amplitude and phase contributions. It avoids costly, time-consuming procedures and provides reliable measurements. This work tested it on sucrose-in-water solutions, but it could be used on other aqueous solutions.

Materials and methods

For our experiments, sugar was mixed in water at concentrations of 0, 5, 10, 15, 20, and 25% in weight and measured under normal conditions to ensure repeatability and mitigate spurious temperature effects. These values were selected to validate the proposed method and its sensibility in a challenging scenario, expecting systematic increases in absorbance levels as the solute concentration increases.

The prepared samples were placed within our SDR-based free space setup, as shown in Figures 2 and 3, halfway between the antennas (inside the white recipient). The placement was maintained throughout the experiment to avoid spurious effects. EM field perturbations were induced and measurements were taken with a commercial Ettus Research™ B210 board (a National Instruments Company, 4600 Patrick Henry Drive, Santa Clara, CA, USA) on a procedure specifically devised for the tests described hereafter.

SDR technology was initially developed as a cost-effective solution for end-to-end amateur communications (Pawlan, 2015; Nesimoglu, 2010). The boards were designed to facilitate signal transmission and reception, incorporating

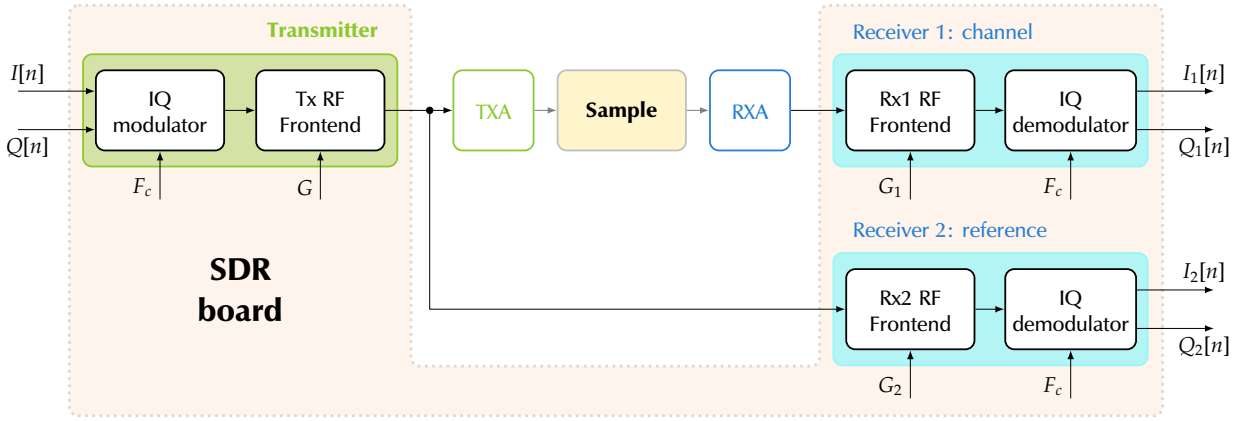

Figure 2. Block diagram describing the proposed SDR configuration. It involves a single transmitter (TX) and a pair of synchronized receivers (RX_1, RX_2). The outputs for the test sample (top) and the reference (bottom) pathways are to the right. TXA and RXA stand for the antennas connected to the transmitter and receiver, respectively. The resulting outputs $\{I_1, Q_1, I_2, Q_2\}$ are compared afterwards with the corresponding input (I, Q). F_c and $\{G, G_1, G_2\}$ are the carrier frequency and the gains assigned to transmitter and receivers amplifiers.
Source: Authors

configurable amplification and carrier recovery, *etc.* (Li, 2014).

An SDR board was used to produce (generate, modulate, and transmit) and recover (receive, demodulate, and digitize) a pre-specified signal perturbing the EM field. Rather than looking at communication capabilities, degradation patterns induced in the recovered signals were traced to successfully connect observed patterns with traversed media properties (in this case, sample concentration levels).

Figure 2 shows the block diagram of the proposed setup. Conveniently selecting $I[n]$ and $Q[n]$ input sequences (left) while varying carrier frequency (F_c) and adapting gain levels in (G, G_1, and G_2), we expected to produce controlled, time- and energy-bounded, frequency modulated pulses. The corresponding measures were used at the receiver antenna (RXA, $I_1[n]$ and $Q_1[n]$, top) and the reference line ($I_2[n]$ and $Q_2[n]$, bottom) to assess absorbance levels.

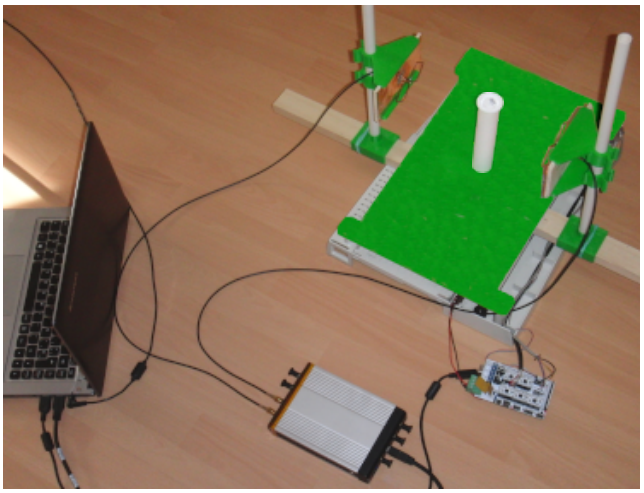

Figure 3. Setup used for the experiment. The enclosed SDR board is shown in the lower part, and the antennas and the specimen are at the top right corner. The laptop controls the board and stores the recordings.
Source: Authors

Radiofrequency absorbance assessment

The proposed method assumes a linear behavior. The input to the transmitter antenna (TXA) should match the following Equation:

$$x_{\mathrm{TX}}(t) = G \cdot A \cdot [I(t)\cos(2\pi F_c t) + Q(t)\sin(2\pi F_c t)] \qquad (2)$$

while a linear channel would produce an output behind the receiver antenna (RXA) that follows

$$x_{\mathrm{RX1}}(t) = (h * x_{\mathrm{TX}})(t) = (h_{\mathrm{RXA}} * h_{\mathrm{chan}} * h_{\mathrm{TXA}} * x_{\mathrm{TX}})(t) \qquad (3)$$

The operator $*$ stands for the linear convolution, and $h(t)$ represents the combined response of the channel (h_{chan}) and antennas (h_{RXA}, h_{TXA}). Whenever the transmitted signal is a modulated pulse (sweep), the received signal may be reformulated as

$$x_{\mathrm{RX}}(t) = H(f_i(t)) \cdot x_{\mathrm{TX}}(t - \tau(f_i(t))) + \eta(t) \qquad (4)$$

with $f_i(t)$ being the exciting frequency at t; H and τ the amplitude and phase responses, respectively; and $\eta(t)$ a noise term.

Network analyzers use this model to derive channel-specific parameters. For an SDR, one must work on the input and output sequences to address the major technological drawbacks before deriving the model parameters. Readers may refer to (Blanco-Murillo *et al.*, 2017, 2022) for details on the use and processing of frequency-modulated chirps, specifically in the characterization of EM response along a transmission scheme.

After traversing the channel branch (top) and considering the SDR scheme, the IQ demodulation of a pulse produces the following outputs:

$$\begin{aligned} I_{\mathrm{RX}}(t) &= K_{\mathrm{RX}} GA/2\,[I(t-\tau_{\mathrm{RX}})\cos\theta + Q(t-\tau_{\mathrm{RX}})\sin\theta] \\ Q_{\mathrm{RX}}(t) &= K_{\mathrm{RX}} GA/2\,[I(t-\tau_{\mathrm{RX}})\sin\theta + Q(t-\tau_{\mathrm{RX}})\cos\theta] \end{aligned} \qquad (5)$$

with $K_1 = G_1 \cdot H(t)$, $K_2 = G_2 \cdot B$, $\tau_1 = \tau$, and $\tau_2 = \tau_0$ for outputs corresponding to the channel (RX = 1) and the reference (RX = 2). θ represents a deviation term in the received signal due to uncertainty in the IQ demodulation

process, B is the attenuation corresponding to this channel and τ_0 is the reference delay. Noise terms have been removed for the sake of simplicity. Ideally, we may achieve $\theta = 0$ and perfect synchronization, but it is not precisely zero due to local oscillators. However, our objective is to estimate the channel-characteristic attenuation $H(f)$ (dB), and phase $\phi(f)$ (rad) along the inspected bandwidth. The wider the inspected frequency band, the more information we have to characterize the samples and underlying processes.

Frequency-modulated (FM) pulses were used on the aforementioned IQ modulator (transmitter) and demodulators (receivers) from digital sequences.

$$I[n] = \sin(\phi[n]), \qquad Q[n] = \cos(\phi[n]) \tag{6}$$

One must select a suitable phase sequence $\phi[n]$ that corresponds to some frequency profile. The simplest one consists of a monotone. Alternatively, one may choose a linear or exponential sweep. Constant frequency is mainly affected by noise and distortion in the band, whereas exponential sweeps display convenient properties for modeling broadband channels, as discussed in (Blanco-Murillo and Yagüe-Jiménez, 2017). Linear sweeps present an excellent trade-off for linear processes and a simple formulation:

$$\phi[n] = 2\pi \underbrace{\left(f_0 + \left[\frac{f_1 - f_0}{N}\right] n\right)}_{f_i} \frac{n}{F_s} + \phi_0, \quad 0 \le n \le N \tag{7}$$

where $f_0 \le f_i \le f_1$, F_s is the sampling frequency, N is the sequence length (in samples), and ϕ_0 is the initial phase. For our experiments, the parameters were set to $f_0 = 0,5\,\text{MHz}$, $f_1 = 15\,\text{MHz}$, and $F_s = 30\,\text{MHz}$. By varying the carrier frequency, $1,8\,\text{GHz} \le F_c \le 5,0\,\text{GHz}$, one may excite all frequencies to be inspected, $f = F_c + f_i$. An 8 MHz overlap between consecutive bands was established to ensure phase continuity. The normalized amplitude was set to $A = 0,7$ in order to avoid saturation. Amplifier gains were set to $G = 30\,\text{dB}$, $G_1 = 55\,\text{dB}$, and $G_2 = 40\,\text{dB}$, and the reference channel attenuator introduced $B = 6\,\text{dB}$ losses.

In assessing the EM response based on the collected measurements and Equation (5), the amplitude and angle (phase) from the in-phase ($I_k[n]$) and quadrature ($Q_k[n]$) components were studied according to the following:

$$\Lambda_k[n] = \sqrt{I_k^2[n] + Q_k^2[n]}, \quad \Theta_k[n] = \tan^{-1}\left(Q_k[n]/I_k[n]\right) \tag{8}$$

From these, the following is obtained:

$$\begin{aligned} \Lambda_1[n] &= G_1 H[n] GA/2 \cdot \Psi(n,\tau,\theta) \\ \Lambda_2[n] &= G_2 BGA/2 \cdot \Psi(n,\tau_0,\theta) \\ \Theta_1[n] &= \tan^{-1}\left(\Psi_Q(n,\tau,\theta)/\Psi_I(n,\tau,\theta)\right) \\ \Theta_2[n] &= \tan^{-1}\left(\Psi_Q(n,\tau_0,\theta)/\Psi_I(n,\tau_0,\theta)\right) \end{aligned} \tag{9}$$

with $\Psi^2(n,\tau_k,\theta) = \Psi_I^2(n,\tau_k,\theta) + \Psi_Q^2(n,\tau_k,\theta)$ and

$$\begin{aligned} \Psi_I(n,\tau_k,\theta) &= I(n/F_s - \tau_k)\sin\theta + Q(n/Fs - \tau_k)\cos\theta \\ \Psi_Q(n,\tau_k,\theta) &= I(n/F_s - \tau_k)\cos\theta + Q(n/Fs - \tau_k)\sin\theta \\ \Psi_Q/\Psi_I\,(n,\tau_k,\theta) &= \tan(\phi[n] - \phi(\tau_k) + \theta) \end{aligned} \tag{10}$$

Assuming that the reference line measurements are consistent and synchronized, one may compute the absorbance levels of a given sample by subtracting these values from those from measurements collected with no sample:

$$\begin{aligned} \textit{Phase delay}: \quad \Delta\phi_k &= \phi(f) - \phi(\tau_0) \quad \text{(rad)} \\ \textit{Magnitude}: \quad |\text{Ab}|_k &= G_1 H(f)/G_2 B \quad \text{(dB)} \end{aligned} \tag{11}$$

The Equations above describe absorbance level computation from a single measurement. Regarding the calibration and secure usage of this technology, the SDR-based setup must ensure that

1. the generated carrier frequency F_c matches the specified value (*i.e.*, negligible deviations are expected);
2. the transmission power is low enough not to cause damage (*i.e.*, using non-ionizing, hazardless radiation); and
3. carrier generation does not introduce significant spurious terms along the inspected bandwidth (*i.e.*, spurious radiation does not spoil our measurements).

In other words, (i) the difference between expected frequency and carrier frequency must be negligible, (ii) the power level needs to be measured before experimentation and be significantly below a given threshold, and (iii) the ratio between the primary frequency content (the expected signal) and other second-order terms (noise, distortion, *etc.*) must be above a given threshold. All this was checked before the test was conducted, while autocalibration of the SDR device was ensured (Coronel-Gaviro *et al.*, 2020).

The complete testing methodology requires that the entire inspection bandwidth is covered, as follows:

1. Set the SDR configuration parameters.
2. Record $\{I_1, Q_1, I_2, Q_2\}$ with no sample between the antennas. Compute the reference estimates for $H(f)$ and $\Delta\phi(f)$ (Equation (11)).
3. Place the sample between the antennas and repeat steps 1 and 2. Compute the channel estimates for $H(f)$ and $\Delta\phi(f)$ (Equation (11)).
4. Subtract measurements from the estimated attenuation levels on the channel and reference to compute the absorbance magnitude (in dB).
5. Subtract measurements from the estimated phases on the channel and reference in order to compute the absorbance phase (in radians).

To improve the signal-to-noise ratios of the collected measurements, this procedure should be repeated M times. The carrier frequency can be tuned rapidly (less than 1 s), and the duration of the signal (1 ms) is negligible compared to the setup time. A 5 MHz step over the $1,8\,\text{GHz} \le F_c \le 5\,\text{GHz}$ range (640 steps) took approximately 2 minutes to collect $M = 5$ repetitions of a complete set of measures on a single sample. The setup was validated in (Coronel-Gaviro *et al.*, 2020).

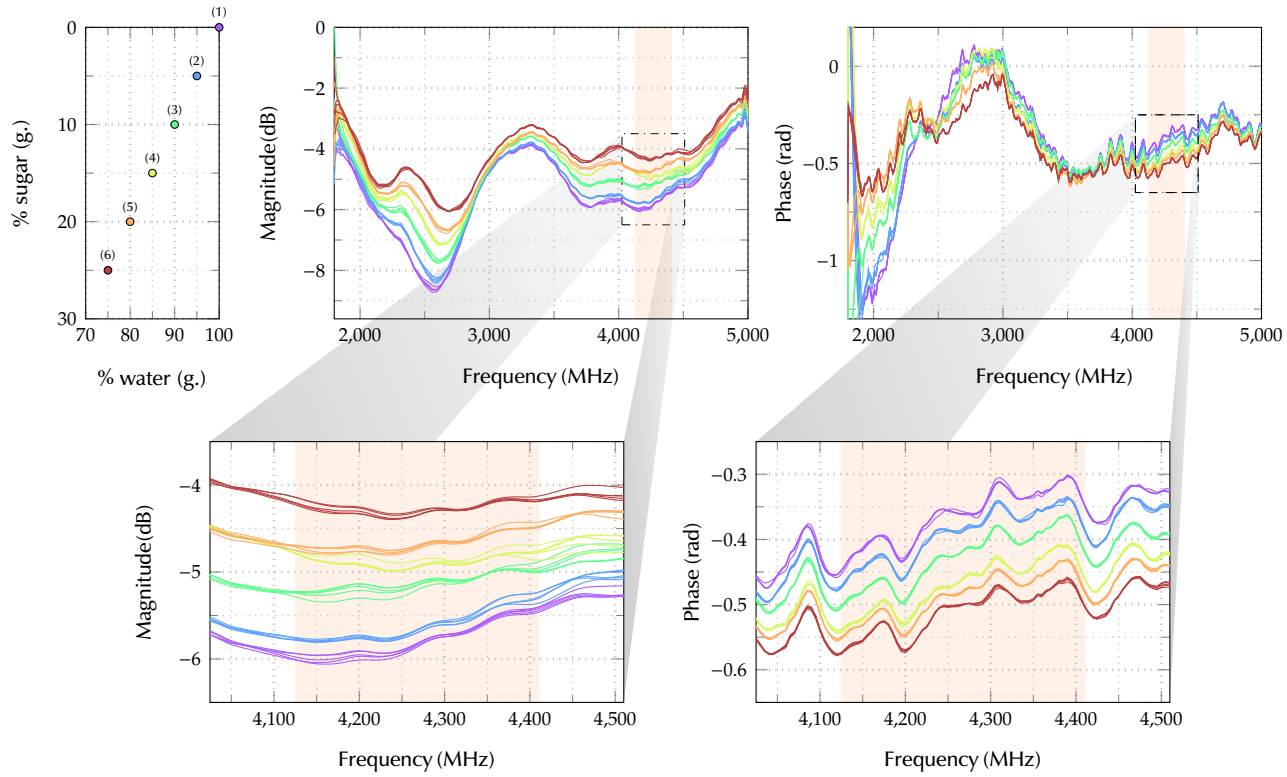

Figure 4. Magnitude and phase results for different sucrose-in-water solutions. A schematic legend is included which shows the concentration levels reported (upper left). At the center and on the right (upper and lower) are the magnitude and phase responses.
Source: Authors

Statistical tests were conducted to evaluate the significance of the computed radiofrequency absorbance levels (amplitude and phase) across the reported concentration levels and along the inspected bandwidth. On the one hand, the Kruskal-Wallis nonparametric test quantified the significance of the observed differences in concentration levels. On the other hand, the Jonckheere-Terpstra test was introduced to evaluate the significance of the levels' ordering (increased absorbance levels should match increased concentrations).

The proposed concentration indicator is the average radiofrequency absorbance for the amplitude and phase values.

Results

Figure 4 shows the magnitude and phase of the absorbances computed in $1,8\,\text{GHz} \leq F_c \leq 5\,\text{GHz}$. Zoomed versions are shown at the bottom.

Magnitude levels vary greatly with concentration throughout the inspected bandwidth, while phase trends are more intricate. The characteristic and systematic patterns identified are consistent with the results reported in the aforementioned literature.

The observed trends could exhibit different significance levels at the multiple frequencies inspected. The results for the statistical tests on both magnitude and phase curves are depicted in Figure 5. One may observe that:

1. The Kruskal-Wallis test achieved $p \leq 10^{-4}$ (99,99% significance).
2. The Jonckheere-Terpstra test identified frequency bands displaying $p \leq 10^{-9}$ on magnitude and phase.
3. The colored regions in Figures 5a and 5b mark the best suited band (high significance) for both tests.

The 4 125 to 4 410 MHz band showed very high significance levels in terms of magnitude and phase for both tests in prepared sucrose-in-water solutions. This band is also marked in Figure 4. It differs from the one identified by Coronel-Gaviro *et al.* (2020) for the detection and quantification of honey fraud (2 150 to 3 250 MHz). However, the authors reported on honey samples and only addressed magnitude levels.

Finally, the proposed concentration indicator was calculated, averaging the calculated absorbance levels in amplitude and phase for the most representative selected bandwidth (4 125 to 4 410 MHz). We used a polar visualization of the computed frequency-dependent complex absorbance $\text{Ab}(f)$ (magnitude and phase in Equation (11):

$$\text{Ab}(f) = \Big(|\text{Ab}|(f), \Delta\phi(f)\Big) \tag{12}$$

This indicator can be easily represented as a complex phasor on a polar coordinate chart, with magnitude (attenuation) providing the distance to the center (radius) and angle (in grades) matching the phase (previously expressed in

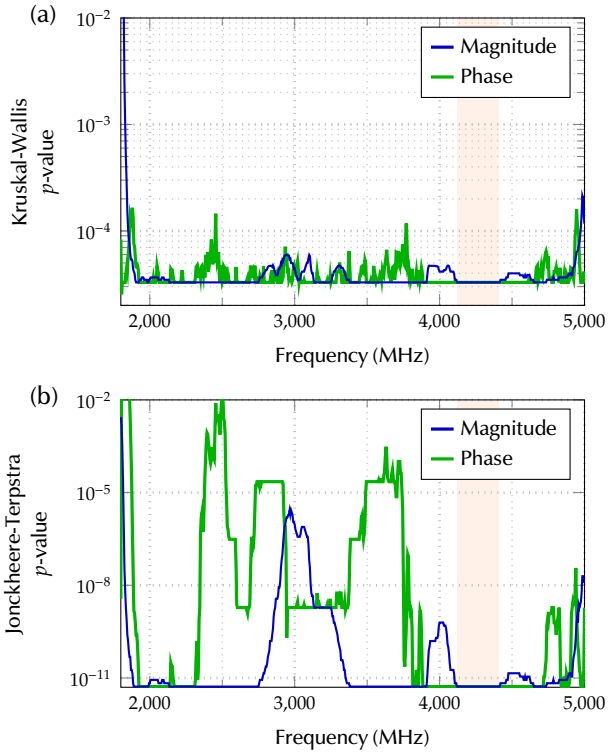

Figure 5. Significance levels (p-values) for the Kruskal-Wallis and the Jonckheere-Terpstra tests on the magnitude and phase levels along the inspected frequency range.
Source: Authors

radians). Thus, an attenuation of 0 dB represents a non-attenuated field, while a decreasing angle (less than 360°) is expected as the group delay increases.

Figure 6 shows the phasors computed in the selected bandwidth for all samples at different concentration levels. The Figure includes a) all absorbance levels and b) the computed concentration indicator corresponding to the averaged values. The larger the concentration of sugar, the further out and lower the indicator.

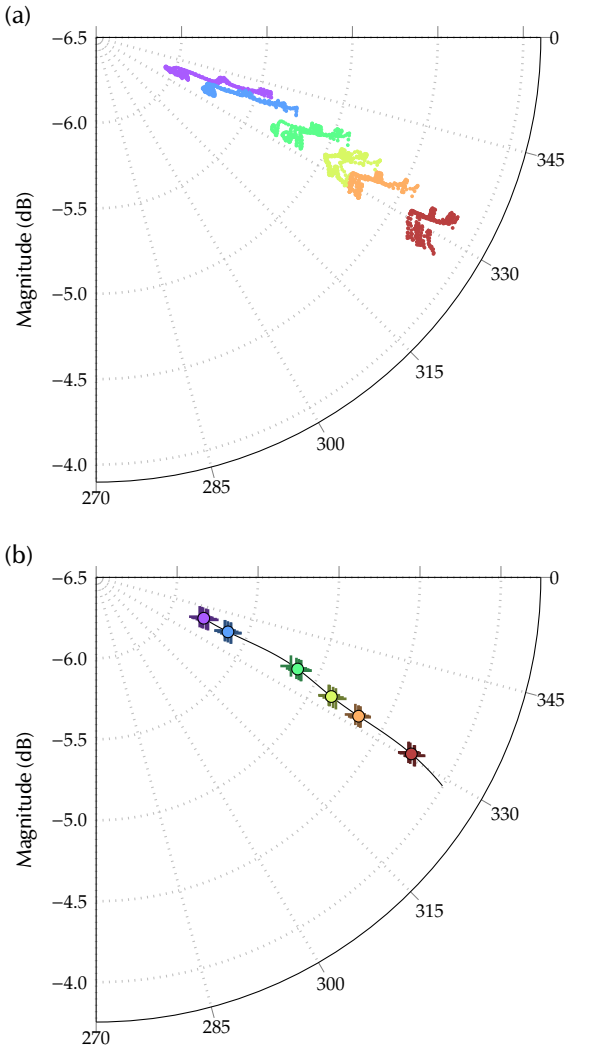

Figure 6. Concentration indicator levels. Colors represent sample concentrations. a) Includes all values on the representative bandwidth for all measured samples, and b) depicts the final values for the indicator (all samples), for the M repetitions (crosses), and for the averaged values in all repeated measures (circles). A trend curve for sucrose concentration has been computed and plotted in black.
Source: Authors

Conclusions

This work presented the basis for a novel noncontact method to evaluate concentration levels using SDR-based low power radio frequency absorbance analysis while computing a reliable concentration indicator. The indicator was derived from the calculated absorbance levels and successfully evaluated the significance of the reported results at different concentration levels in sucrose-in-water solutions.

Compared to previous studies on sucrose in water (Gennarelli *et al.*, 2013; Guariti *et al.*, 2013; Harnsoongnoen and Wanthong, 2016, 2017), the proposed methodology obtained statistically significant results at lower concentrations. The technology is affordable and could be used for on-field tests, but it can still cover a wider frequency range during inspection. It could be introduced for food processing industries, such as beverage production, as well as integrated for inline sensing. It can also be used for on-field measurements, as well as in other aqueous solutions, since the device is portable and noncontact.

Considering on-field measurement and inline monitoring, (i) the measuring temperature, (ii) defective materials (*e.g.*, sample containers), or (iii) spurious electrical conditions may impact EM measures, automatically affecting the performance of the proposed indicator, which is why further analysis is required.

Future work may be dedicated to delving into these aspects, as well as developing a solution for the quantification of the concentration level (Ballin and Laursen, 2019) and generalizing it to other types of aqueous solutions. Quantification may require linearization techniques, as shown by the results obtained for the proposed indicator. Addressing aqueous solutions requires a larger number of samples and more complex mixtures. Although the significance levels obtained (Kruskal-Wallis 99, 99%, Jonckheere-Terpstra $p \leq 10^{-9}$) favor our hypothesis, several spurious effects need to be addressed. These include measuring the impact of temperature and EM distortions on absorbance measures and testing for the required EM compatibility compliance.

Acknowledgements

The activities described in this contribution were partially funded by the European Union's Horizon 2020 Research and Innovation Programme under grant agreement No. 101003750, the Ministry of Economy and Competitiveness of Spain under grant PID2021-128469OB-I00, and the UPM Research Programme.

Author contributions

Author 1 built and programmed the device (HW and SW), collected the data, did the background research, and wrote the original draft. *Author 2* conceptualized the tests, defined the methodology, supervised the experiments, and the data collection process; she also prepared the manuscript including visuals review and editing. *Author 3* participated in the conceptualization of the work, supervised the research, led the formal analysis of the application addressed, wrote specific sections of the manuscript, reviewed the writing, validated results, and provided critical feedback. All authors contributed to the writing of the manuscript.

References

Agilent Technologies, Inc. (2006). *Basics of measuring the dielectric properties of materials*. Agilent Technologies: Santa Clara, CA, USA. (Application Note 5989-2589EN)

Ballin, N. Z., and Laursen, K. H. (2019). To target or not to target? definitions and nomenclature for targeted versus non-targeted analytical food authentication. *Trends in Food Science and Technology*, *86*, 537-543. https://doi.org/10.1016/j.tifs.2018.09.025

Becker, F., Schwabig, C., Krause, J., Leuchs, S., Krebs, C., Gruna, R., Kuter, A., Langle, T., Nuessler, D., and Beyerer, J. (2020). From visual spectrum to millimeter wave: A broad spectrum of solutions for food inspection. *IEEE Antennas and Propagation Magazine*, *62*(5), 55-63. https://doi.org/10.1109/MAP.2020.3003225

Bindu, G., Lonappan, A., Thomas, V., Aanandan, C. K., and Mathew, K. T. (2006). Dielectric studies of corn syrup for applications in microwave breast imaging. *Prog. Electromagn. Res.*, *59*, 175–186. https://doi.org/10.2528/PIER05072801

Blanco-Murillo, J.L., Yagüe-Jiménez, V., Coronel-Gaviro, J., and Casajús Quirós, F. (2022). A model-informed, single-input method for amplifiers assessment from pruned Volterra kernels collapsed projection. *Measurement*, *193*, 110856. https://doi.org/10.1016/j.measurement.2022.110856

Blanco-Murillo, J. L., and Yagüe-Jim'enez, V. (2017) A Method for informed selection of memory-length and nonlinearity-order parameters in Volterra–Wiener systems from exponential sweep excitations. *Multidimensional Systems and Signal Processing*, *29*, 1861–1893. https://doi.org/10.1007/s11045-017-0535

Blanco-Murillo, J.L., Yagüe-Jim'enez, V., and Casaj 'us-Quir'os F. J. (2017). Assessment of nonlinearities for precision DACs. *IEEE Transactions on Instrumentation and Measurement*, *66*(11), 2852–2857. https://doi.org/10.1109/TIM.2017.2734019

Brovoll, S., Berger, T., Paichard, Y., Aardal, Ã., Lande, T. S., and Hamran, S. (2014). Time-lapse imaging of human heart motion with switched array UWB radar. *IEEE Transactions on Biomedical Circuits and Systems*, 8(5), 704–715. https://doi.org/10.1109/TBCAS.2014.2359995

Choi, J. H., and Kim, D. K. (2009). A remote compact sensor for the real-time monitoring of human heartbeat and respiration rate. *IEEE Transactions on Biomedical Circuits and Systems*, *3*(3), 181–188. https://doi.org/10.1109/TBCAS.2009.2019628

Coronel-Gaviro, J., Yagüe-Jiménez, V., and Blanco-Murillo, J. (2020). Nonintrusive Honey Fraud Detection and Quantification based on Differential Radiofrequency Absorbance Analysis. *Journal of Food Engineering*, 110448. https://doi.org/10.1016/j.jfoodeng.2020.110448

El-Mesery, H. S., Mao, H., and Abomohra, A. E.-F. (2019). Applications of non-destructive technologies for agricultural and food products quality inspection. *Sensors*, *19*(4), 846. https://doi.org/10.3390/s19040846

Gennarelli, G., Romeo, S., Scarfi, M. R., and Soldovieri, F. (2013, May). A Microwave Resonant Sensor for Concentration Measurements of Liquid Solutions. *IEEE Sensors Journal*, *13*(5), 1857–1864. https://doi.org/10.1109/JSEN.2013.2244035

Guariti, G., Hofmann, M., Weigel, R., Fischer, G., and Kissinger, D. (2013). Determination of sugar concentration in aqueous solutions using ultra-wideband microwave impedance spectroscopy [Conference presentation]. In *2013 IEEE MTT-S International Microwave Symposium Digest (MTT)* Seattle, WA, USA. https://doi.org/10.1109/MWSYM.2013.6697563

Harnsoongnoen, S., and Wanthong, A. (2016). Coplanar waveguides loaded with a split ring resonator-based microwave sensor for aqueous sucrose solutions. *Measurement Science and Technology*, *27*(1), 015103. https://doi.org/10.1088/0957-0233/27/1/015103

Harnsoongnoen, S., and Wanthong, A. (2017). Real-time monitoring of sucrose, sorbitol, D-glucose, and D-fructose concentration by electromagnetic sensing. *Food Chemistry*, *232*, 566–570. https://doi.org/10.1016/j.foodchem.2017.04.054

Heileman, K., Daoud, J., and Tabrizian, M. (2013) Dielectric spectroscopy as a viable biosensing tool for cell and tissue characterization and analysis. *Biosensors and Bioelectronics*, *49*, 348–359. https://doi.org/10.1016/j.bios.2013.04.017

Kaatze, U. (2013). Measuring the dielectric properties of materials. ninety-year development from low-frequency techniques to broadband spectroscopy and high-frequency imaging. *Measurement Science and Technology*, *24*(1), 012005. https://doi.org/10.1088/0957-0233/24/1/012005

Kennedy, J. F., Pimentel, M. d. C. B., Melo, E. H., and Lima-Filho, J. L. (2007). Sucrose biosensor as an alternative tool for sugarcane field samples. *Journal of the Science of Food and Agriculture*, *87*(12), 2266–2271. https://doi.org/10.1002/jsfa.2982

Konings, A. G., Rao, K., and Steele-Dunne, S. C. (2019, .) Macro to micro: microwave remote sensing of plant water content for physiology and ecology. *New Phytologist*, *223*(3), 1166–1172. https://doi.org/10.1111/nph.15808

Li, Y. (2014). *In-phase and quadrature imbalance: modeling, estimation, and compensation*. Springer.

Lindon, J. C., Tranter, G. E., and Koppenaal, D. W. (Eds.). (2017). *Encyclopedia of spectroscopy and spectrometry*. Elsevier.

Liu, Q., and Brady, J. (1996). Anisotropic solvent structuring in aqueous sugar solutions. *Journal of the American Chemical Society*, *118*(49), 12276–12286. https://doi.org/10.1021/ja962108d

Lu, M., Xie, Y., Zhu, W., Peyton, A., and Yin, W. (2019). Determination of the magnetic permeability, electrical conductivity, and thickness of ferrite metallic plates using a multifrequency electromagnetic sensing system. *IEEE Transactions on Industrial Informatics*, *15*(7), 4111-4119. https://doi.org/10.1109/TII.2018.2885406

Maier, A., Steidl, S., Christlein, V., and Hornegger, J. (Eds.). (2018). *Medical imaging systems: an introductory guide* (No. 11111). Cham: Springer Open.

Meng, Z., Wu, Z., and Gray, J. (2018). Microwave sensor technologies for food evaluation and analysis: Methods, challenges and solutions. *Transactions of the Institute of Measurement and Control*, *40*(12), 3433–3448. https://doi.org/10.1177/0142331217721968

Naishadham, K., Piou, J. E., Ren, L., and Fathy, A. E. (2016). Estimation of cardiopulmonary parameters from ultra-wideband radar measurements using the state space method. *IEEE Transactions on Biomedical Circuits and Systems*, *10*(6), 1037–1046. https://doi.org/10.1109/TBCAS.2015.2510652

Nesimoglu, T. (2010). A review of Software Defined Radio enabling technologies. In IEEE (Eds.), *2010 10th Mediterranean Microwave Symposium* (pp. 87–90). IEEE. https://doi.org/10.1109/MMW.2010.5605145

Pawlan, J. (2015). An introduction to Software Defined *Radio [Conference presentation]. In 2015 IEEE International Conference on Microwaves, Communications, Antennas and Electronic Systems (COMCAS), Tel Aviv, Israel*. https://doi.org/10.1109/COMCAS.2015.7360430

Periasamy, S., and Ravi, K. P. (2020). A novel approach to quantify soil salinity by simulating the dielectric loss of SAR in three-dimensional density space. *Remote Sensing of Environment*, *251*, 112059. https://doi.org/10.1016/j.rse.2020.112059

Pirola, M., Teppati, V., and Camarchia, V. (2007) Microwave measurements Part i: Linear Measurements. *IEEE Instrumentation and Measurement Magazine*, *10*(2), 14–19. https://doi.org/10.1109/MIM.2007.364959

Pu, Y.-Y., O'Donnell, C., Tobin, J. T., and O'Shea, N. (2020). Review of near-infrared spectroscopy as a process analytical technology for real-time product monitoring in dairy processing. *International Dairy Journal*, *103*, 104623. https://doi.org/10.1016/j.idairyj.2019.104623

Torres Castellanos, N., and Rodríguez-Torres, S. D. (2019, May). Evaluation of internal curing effects on concrete. *Ingeniería e Investigación*, *39*(2), 37–45. https://doi.org/10.15446/ing.investig.v39n2.76505

Wlodarczak, G. (2017). Microwave and radiowave spectroscopy, applications. In J. C. Lindon, G. E. Tranter, and D. W. Koppenaal (Eds.), *Encyclopedia of spectroscopy and spectrometry* (pp. 803–812). Elsevier. https://doi.org/10.1016/B978-0-12-409547-2.11270-3

Xia, Y., Xu, Y., Li, J., Zhang, C., and Fan, S. (2019). Recent advances in emerging techniques for non-destructive detection of seed viability: A review. *Artificial Intelligence in Agriculture*, *1*, 35-47. https://doi.org/10.1016/j.aiia.2019.05.001

Yao, H.-Y., Wang, Y.-C., and Chang, T.-H. (2022) Investigation of dielectric spectrums, relaxation processes, and intermolecular interactions of primary alcohols, carboxylic acids, and their binary mixtures. *Journal of Molecular Liquids*, *353*, 118755. https://doi.org/10.1016/j.molliq.2022.118755

Research Article/Mechanical Engineering, Mechatronics, and Materials Science http://doi.org/10.15446/ing.investig.93635

Inverse Hall-Petch Behavior in Nanocrystalline Aluminum Using Molecular Dynamics

Estudio del comportamiento inverso de Hall-Petch en aluminio nanocristalino usando dinámica molecular

Alexandre M. Barboza [1], Luis C. R. Aliaga [2], and Ivan N. Bastos [3]

ABSTRACT

This work investigates the mechanical behavior of nanocrystalline aluminum, with special focus on deformation mechanisms, using molecular dynamics simulations with an interatomic potential parameterized by the authors. To this end, four nanocrystalline samples with grain sizes ranging from 8,2 to 14,2 nm were constructed, each with a volume of 15 x 15 x 20 nm^3. As expected, the data from the tensile tests at a strain rate of 1,0 x 10^9 s^{-1} showed an inverse Hall-Petch relationship. The work hardening behavior revealed no significant gain in mechanical strength. The dislocation analysis indicated that perfect dislocation density decreases during tensile testing, while the Shockley partials increase. Grain boundary-mediated plasticity was evidenced with atomic diffusion along grain boundaries, as well as by grain rotation. Thus, it is concluded that the conventional plastic deformation mechanisms of metals are not preponderant for nanocrystalline aluminum.

Keywords: molecular dynamics, Hall-Petch, mechanical behavior, nanocrystalline aluminum

ABSTRACT

En este trabajo se evalúa el comportamiento mecánico del aluminio nanocristalino, con especial atención a los mecanismos de deformación, utilizando simulaciones de dinámica molecular mediante un potencial interatómico parametrizado por los autores. Para este fin, se construyeron cuatro muestras nanocristalinas con tamaños de grano que oscilaban entre 8,2 y 14,2 nm, cada una con un volumen de 15 x 15 x 20 nm^3. Como se esperaba, los datos de los ensayos de tracción con tasa de deformación de 1,0 x 10^9 s^{-1} mostraron una clara relación inversa de Hall-Petch. El comportamiento de endurecimiento por trabajo mecánico no reveló una ganancia significativa de resistencia mecánica. El análisis de las dislocaciones indicó que las dislocaciones perfectas disminuyen durante los ensayos de tracción, mientras que los parciales de Shockley aumentan. Se evidenció la plasticidad del material con la difusión atómica a lo largo de los límites de grano, así como por la rotación de los granos. De este modo, se concluye que los mecanismos convencionales de deformación plástica de los metales convencionales no son preponderantes para el aluminio nanocristalino.

Palabras clave: dinámica molecular, Hall-Petch, comportamiento mecánico, aluminio nanocristalino

Received: February 15th, 2021
Accepted: June 3rd, 2022

Introduction

Nanocrystalline (NC) metallic materials are a particular case of polycrystalline materials, as their grain size is smaller than 100 nm (Naik and Walley, 2020). These grains have a well-defined atomic arrangement (*i.e.*, body-centered cubic, face-centered cubic, *etc.*) and a large volume fraction of grain boundaries (GBs), which are places of major atomic disorder (Pande and Cooper, 2009). Nanocrystalline materials exhibit interesting mechanical characteristics for various types of applications, as they have, for instance, higher mechanical strength when compared to crystalline alloys of the same chemical composition containing larger grains (Hasan *et al.*, 2020). The relationship between grain size and mechanical strength is given by the Hall-Petch (HP) equation, which can be expressed as follows (Schneider and Laplanche, 2021):

$$\sigma_y = \sigma_0 + k_l d_{GB}^{-1/2} \quad (1)$$

where σ_y is the yield stress, σ_0 and k_l are constants that dependent on the material, and d_{GB} is the average grain size.

The physical explanation of the HP relationship is based on the pile-up model (Baracaldo *et al.*, 2011). Dislocations can usually slip inside a crystal if enough stress is provided and accumulate (pile-up) at some obstacles such as GBs, impurity atoms, second phase precipitates, or other dislocations (Meyers *et al.*, 2006). While the obstacles anchor the dislocations, the plastic deformation is prevented from progressing. However, for every accumulated dislocation, more stress is concentrated at the tip of the pile-up. At some point, the accumulated stress will be such that the obstacle will no longer hold the dislocation pile-up. Consequently, the dislocations will overtake the

[1]Mechanical engineer, Universidade do Estado do Rio de Janeiro (UERJ), Brazil. PhD in Computational Modelling, UERJ, Brazil. Affiliation: Researcher, UERJ, Brazil. E-mail: abarboza@iprj.uerj.br
[2]Bachelor of Physics, Universidad Nacional de Trujillo, Peru. MSc in Physics, Universidade Federal de São Carlos (UFSCAR), Brazil. PhD in Materials Science and Engineering, UFSCAR, Brazil. Affiliation: Professor, UERJ, Brazil. E-mail: aliaga@iprj.uerj.br
[3]Metallurgical engineer, Universidade Federal do Rio de Janeiro (UFRJ), Brazil. MSc in Metallurgical and Materials Engineering, UFRJ, Brazil. PhD in Metallurgical and Materials Engineering, UFRJ, Brazil. Affiliation: Professor, UERJ, Brazil. E-mail: inbastos@iprj.uerj.br

How to cite: Barboza, A. M., Aliaga, L. C. R, and Bastos, I. N. (2022). Inverse Hall-Petch behavior in nanocrystalline aluminum using molecular dynamics. *Ingeniería e Investigación, 43*(1), e93635. DOI: http://doi.org/10.15446/ing.investig.93635

obstacles, continuing with plastic deformation on adjacent grains. Considering the pile-up model, Equation (1), and the fact that NC materials possess an extremely high-volume fraction of GBs, it is clear that they will present enhanced mechanical strength compared to conventional materials.

The HP relationship was believed to be valid for smaller and smaller grains, thus yielding increasingly resistant materials. However, when technology allowed grains to be refined to sizes below a few dozens of nanometers, it was made clear that this relationship was no longer valid. Several studies reported that the yield stress deviates from the HP relationship below a critical grain size, or that even an inverse (or negative) HP relationship is observed (Naik and Walley, 2020; Hu *et al.*, 2017). Figure 1 shows the schematic representation of both regimes: for large grains (conventional HP) and nanograins (inverse HP). The mechanisms by which the inverse HP relationship occurs are not yet well understood.

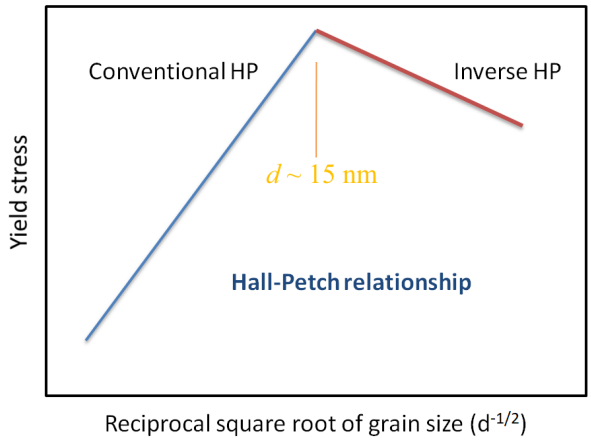

Figure 1. Schematic representation of yield stress dependence on grain size
Source: Authors

The difficulty in manufacturing experimental flaw-free NC samples associated with the progress of computational technology has created an excellent opportunity to study this class of materials by means of computational materials science. By definition, computational materials science involves the computer-based tools employed in modeling and simulation to better understand and predict a material's behavior (Lesar, 2013). It can be used to study alloys (Barboza *et al.*, 2020), glass-forming ability (Aliaga, Lima, *et al.*, 2019; Aliaga, Schimidt, *et al.*, 2018), ceramics and polymers (Tjong, 2013), biocomposites (Kashan and Ali, 2019), and many more systems. Furthermore, computational materials science allows studying phenomena and properties that would be too complex to be tested experimentally due to high pressures/temperatures, deformation rates, heating/cooling rates, or any other physical variable that exceeds the technological capability for actual execution. A computational method often used to study NC materials' behavior is molecular dynamics (MD) simulations.

Molecular dynamics is a simulation method used to study the motion of atoms and molecules by applying classical mechanics (Afkham *et al.*, 2017). The force acting on an atom i, in a system composed of N atoms, can be described as follows (Lee, 2012; Tschopp *et al.*, 2008):

$$\vec{F}_i = m_i\vec{a}_I = m_i\frac{d\vec{v}_i}{dt} = m_i\frac{d^2\vec{r}_i}{dt^2} = -\frac{dU(\vec{r}_N)}{d\vec{r}_i} \quad (2)$$

where m_i, $\vec{a}_i$, $\vec{v}_i$, $\vec{r}_i$, and $U(\vec{r}_N)$ are the atomic mass, acceleration vector, velocity vector, position vector, and interatomic potential, respectively. It can be seen in Equation (2) that the force acting on an atom can be obtained from the interatomic potential, which is a function of the position of all atoms. In theory, it would be enough to integrate Equation (2) in order to obtain the velocity and position. However, this results in the classical physical N-body problem, which does not have an analytical solution. Thus, MD simulations employ numerical methods such as the velocity Verlet algorithm (Pal and Ray, 2020).

To reduce the computational cost, the MD considers the atom as a rigid sphere, neglecting the interaction of electrons (Lee, 2012). This technique drastically reduces the complexity of the simulation and thereby its runtime. There is, however, a negative consequence: the interatomic potentials need to be empirically generated, either by fitting certain functions with experimental information or with calculated data from first-principles methods (Lee, 2012). In general, a simulation using MD can be summarized in the following steps:

- Given the initial positions, velocities, and interatomic potential of the atoms, the interaction forces are calculated.
- With the force information, positions are advanced in time by a small interval called *timestep*, which results in new positions, velocities, and forces.
- This new information is then used as input for a new iteration, repeating the previous steps until an equilibrium state is reached.

Various data are stored for each timestep, such as energy, atomic positions, forces, pressure, and temperature. The stored values vary according to the need of each study. The properties that can be calculated with these data are diverse: coefficient of expansion, melting point, thermal conductivity, mechanical/structural properties, among others.

Compared to other methods, such as the first-principles, MD is faster and can handle larger systems. However, one significant disadvantage is its spatial and temporal scale, which is limited to the *nano* range. Moreover, information regarding magnetic properties can not be obtained.

The essence of an MD simulation lies in the interatomic potential, which informs how the forces acting on each atom are calculated. Although there are several interatomic potentials available in the literature for Al, this study used an Embedded Atom Method (EAM) potential parameterized by ourselves via the RAMPAGE technique (Ward *et al.*, 2012). In fact, this potential was initially created to study an Al-Ti-Ni alloy (Barboza *et al.*, 2020). Regarding pure Al, the used potential is capable of reproduce its lattice constant, elastic constants, and cohesive energy. More details regarding the parameterization methodology can be seen in Barboza *et al.* (2020). The key idea of the EAM potential is based on the principle that the system's total energy results from the contribution of the pair potential energy between atoms (the

result of interaction forces), and a term that depends on the local density at the point where each atom is located (Jang *et al.*, 2021). Therefore, by using the EAM formalism, the atom's energy, U_i, can be represented as follows (Saidi *et al.*, 2017):

$$U_i = \frac{1}{2}\sum_{j\neq i}\phi_{ij}(r_{ij}) + F_i(\mu_i) \tag{3a}$$

$$\mu_i = \sum_{j\neq i} f_i(r_{ij}) \tag{3b}$$

where $\phi_{ij}(r_{ij})$ is the interaction function of atomic pairs, $F_i(\mu_i)$ is the energy of embedded atoms concerning the electronic density μ_i, r_{ij} is the scalar distance between two atoms i and j, and $f_i(r_{ij})$ is the partial contribution of electronic densities.

It is important to note that, while computational tools are of great value, one should investigate the differences between simulation and experimental results. Experiments that would take hundreds of thousands of seconds are modeled in a few nanoseconds. This discrepancy may exclude some time-dependent phenomena, thus leading to erroneous results. For this reason, it is essential to evaluate the effectiveness of a given computational tool, comparing it with known phenomena obtained from real tests whenever possible.

Nanocrystalline Al has been extensively studied via computational approaches, such as the recent work by Xu and Dávila (2017). However, the vast majority of these works vary the number of atoms and, consequently, the volume of the samples in order to reduce the computational cost, which may negative impact the results.

In this context, this work investigates the mechanical behavior and mechanisms responsible for the plasticity of NC Al by molecular dynamics using all samples with the same volume and number of atoms. Thus, the parameter that varies in our case is the number of grains in each sample. In addition, the interatomic potential used is another novel approach, as it has never been applied to study this metal.

Methodology

The simulations were performed using the Large Scale Atomic/Molecular Massively Parallel Simulator (LAMMPS) code (Plimpton, 1995). As the name suggests, LAMMPS is based on the concept of parallel computing to optimize the processing power. In addition to processors, it also has implementation packages that allow the Graphics Processing Unit (GPU) to run in parallel with the processors, increasing the processing power; this work made use of the GPU package. The NC aluminum samples were initially generated from different seeds with random locations and crystallography directions using a region of 15 × 15 × 20 nm^3 and 271 708 atoms by means of the Atomsk software (Hirel, 2015). In total, four NC samples with different quantities of grains were generated. The average grain sizes were 14,2, 11,9, 9,4, and 8,2 nm for samples with 3, 5, 10, and 15 grains, respectively. The samples were initially relaxed at 300 K, maintaining the external pressure in all directions at 0 Pa with periodic boundary conditions. Subsequently, the samples were loaded into LAMMPS for the uniaxial tensile test performed at a strain rate of 1,0 x 10^9 s^{-1} along the z-axis.

After the tensile test, the 10- and 15-grain samples were chosen to perform a work hardening study, as they have the smallest average grain size and, therefore, the grain boundary effect is enhanced. The work hardening study was performed by loading the samples to a deformation level of 0,06 (beyond the elastic deformation), unloading, and loading one last time. The work hardening was performed under the same temperature and strain rate used in the tensile test.

Results and discussion

Grain morphology in the considered volume is shown in Figure 2, and the distribution of grain volumes for each NC sample is depicted in Figure 3. Since the total volume of the samples is constant (4 500 nm^3), the histogram shows that samples with fewer grains occupy a larger individual grain volume.

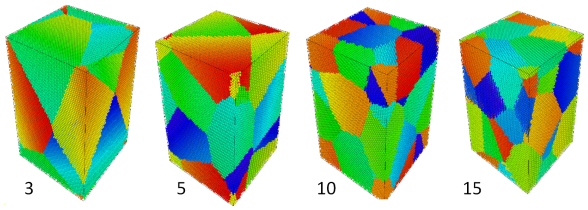

Figure 2. Depiction of Al NC samples. From left to right: samples with 3, 5, 10, and 15 nanograins. The colors are to aid the identification of the grains.
Source: Authors

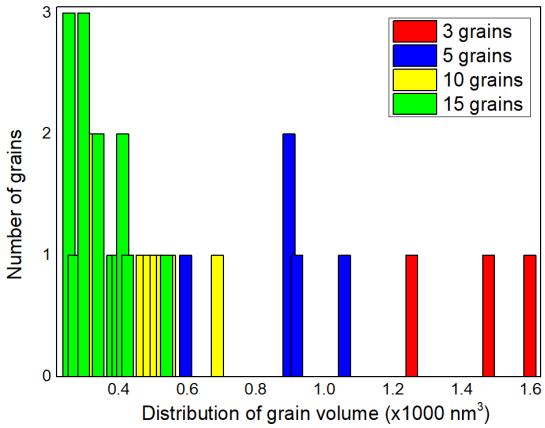

Figure 3. Grain volume distribution of the NC samples
Source: Authors

Figure 4 shows the three-grain sample before and after the tensile test. An increase in length along the z-axis and a relatively small decrease in x- and y-directions are observed, as is expected in this type of test. Plastic deformation occurs homogeneously without variation in the total volume.

The simulated stress-strain curves are shown in Figure 5. For all generated nanocrystals, the grain sizes are much smaller than 100 nm. Thus, the inverse HP behavior is expected. The sample with 15 grains (smallest grain size) shows the lowest mechanical resistance. In contrast, the sample with three grains (largest grain size) exhibits the highest strength, with the five- and ten-grain samples presenting intermediate

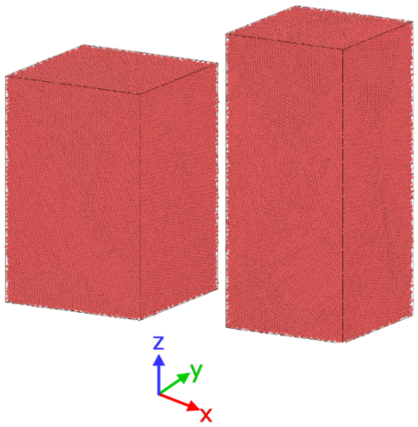

Figure 4. The three-grain NC sample before (left) and after (right) uniaxial tensile testing
Source: Authors

stress values and obeying the inverse HP relationship. It is important to note that the mechanical strength of NC Al is higher when compared to conventional coarse-grained systems, in agreement with other studies (Xu and Dávila, 2017).

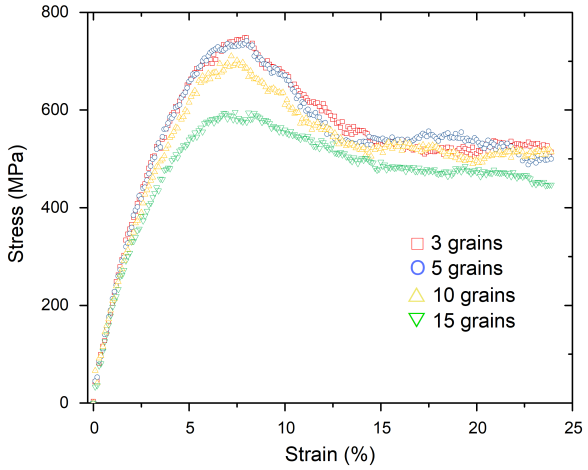

Figure 5. Stress-strain curves of nanocrystalline samples
Source: Authors

The similar mechanical behavior between the three- and five-grain samples is because they are close to the transition from a conventional to an inverse HP relationship. This transition does not occur abruptly; a parabolic trend is expected, as computationally reported for Cu (Weng and Barai, 2009), and experimentally for 0,6%C steel (Baracaldo *et al.*, 2011). Thus, for materials with grain sizes close to the parabola vertex, the difference between their stress values is small compared to materials with grain sizes far from the vertex. For this reason, the difference between the stress values for the five- and ten-grain samples was not pronounced.

Experimental tensile testing of samples with grain sizes ranging from micrometer to nanometer for Al with at least 99% purity can be found elsewhere (Tsuji *et al.*, 2002; Choi *et al.*, 2009). Figure 6 presents the combination of these data with the results of this MD work. The ultimate tensile strength was used in Figure 6 instead of yield stress in order to ease the visualization of HP regimes.

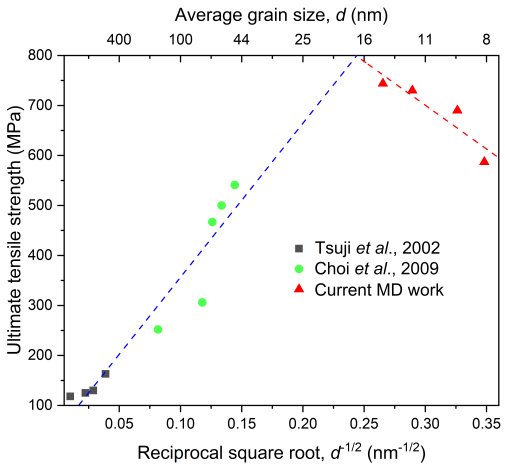

Figure 6. Tensile strength versus the reciprocal square root of the grain size: black squares and green circles represent experimental values reported in literature, whereas red triangles denote simulated results found in this work. The blue and red dashed lines are the linear fit of the corresponding HP behaviors.
Source: Authors

The pattern in Figure 6 resembles the expected behavior of the schematic representation of Figure 1. Moreover, the fitted intersection corresponds to a grain size of approximately 17 nm. Even though it is within the expected grain size transition value from conventional to inverse HP relationship for metals, the 17 nm value might be even smaller in practice. This assumption is based on two reasons: (i) the fitting curves of Figure 6 were extrapolated to cover the full axis range, jeopardizing the results, especially for grain sizes below 50 nm due to the dearth of reliable experimental data; (ii) although it is not shown in Figure 1, a reduction in the conventional HP relationship slope is expected at grain sizes below 100 nm, thus changing its direction. Unfortunately, to reach a grain size of 17 nm, it would be necessary to decrease the number of grains even further, which is impractical in our case, since the sample with largest grain size only has three grains. A decrease in this quantity of grain would place the samples closer to a single crystal than to a polycrystalline structure. Thus, the only way to verify if this grain size value indeed marks an HP regime transition for the NC Al while applying the same methodology of this work would be to reconstruct all samples using larger volumes, which is in intended to be done in future works.

The reasons why the inverse HP relationship occurs are still under debate, but there are indications that the conventional dislocation slip mechanisms are not fully functional at the *nano* scale (Fan *et al.*, 2005; Pande and Cooper, 2009). Instead, GB-mediated mechanisms should dominate the plastic deformation of NC materials (Fan *et al.*, 2005), such as grain boundary sliding and room-temperature Coble creep (Ovid'ko and Shinerman, 2013), *i.e.*, diffusion of atoms along the GBs. To evaluate if the dislocation mechanism persists for NC Al, the work hardening behavior of the 15 and 10-grain samples was investigated. It is well-known that the work hardening phenomenon occurs, basically, by the generation and interaction of the dislocation stress fields. Thus, it is expected that NC samples would not exhibit strain hardening, since the reduced grain sizes would hinder or even inhibit the generation of dislocations. Figure

7 shows the stress-strain curves before and after the work hardening of the 15-grain sample. The 10-grain sample had a similar behavior and was not exhibited.

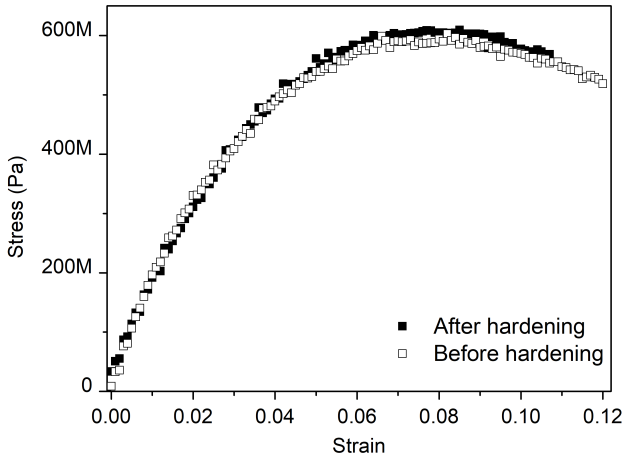

Figure 7. Tensile test after work hardening of the 15-grain sample
Source: Authors

The results reported in Figure 7 confirm the expectation that no significant increase in strength should be observed after strain hardening for NC systems. Therefore, for the conditions applied in this work, dislocations are not responsible for the plastic deformation. However, a diffusion mechanism along GBs (Coble creep) was evidenced, as shown in Figure 8 for the 15-grain sample: grain boundaries are well defined before loading, but after a strain of 0,06, it is possible to observe some atoms migrating along the neighboring grains due to diffusion. Furthermore, the grains are rotated from their original position.

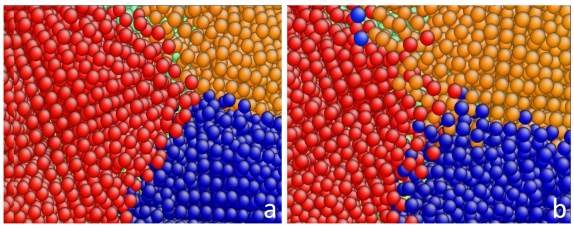

Figure 8. A triple junction in the 15-grain sample: (a) Grain boundaries before the tensile test and (b) after a strain of 0,06. Note the small displacement of atoms along GBs
Source: Authors

To investigate the dislocation dynamics, the dislocation extraction algorithm was used, as implemented in the Ovito software (Stukowski, 2010), which has the function of quantifying the dislocation density for different strains values. Figure 9 shows the dislocation segments for the three-grain sample at strain values of 0,00 and 0,10. Frank and Stair-Rod dislocations are present, but their quantities are negligible in comparison with Shockley partials.

Perfect dislocations are present in a small amounts at the beginning of deformation, and they decrease linearly with the strain. However, Shockley partials grow exponentially, as shown in Figure 10 for the sample with three grains as an example. All the other samples follow this same trend. The parameter ρ is the dislocation density at a given strain, while ρ_0 denotes the initial dislocation density, and the dislocation ratio (normalized dislocation density) is expressed as ρ/ρ_0.

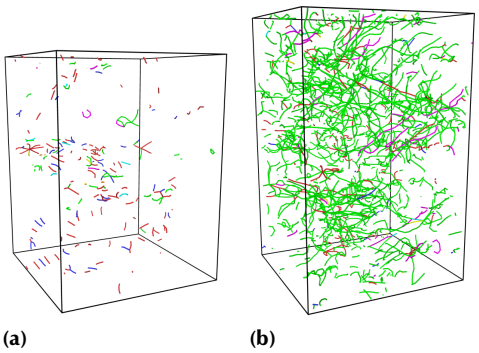

Figure 9. Dislocation evolution of the three-grain sample at strain levels of (a) 0,00 and (b) 0,10. The colors green, strong blue, light blue, purple, and red represent Shockley, perfect, Frank, Stair-Rod, and non-identified dislocations, respectively. Atoms were removed to ease the visualization of the dislocation segments.
Source: Authors

The decreasing of perfect dislocation density is expected, as new perfect dislocations are not possible because of the inhibited Frank-Read source. Moreover, the already existing perfect dislocations are dissociated into two Shockley partials or absorbed by the GBs; both processes reduce its density. The increase in Shockley partials indicates the formation of stacking faults and twinning structures. These results are similar to those obtained for NC Ni (Barboza *et al.*, 2021) and an $Al_{85}Ti_{15}Ni_5$ alloy (Barboza *et al.*, 2020). Finally, the increase in partial dislocations for NC Al was also reported in Xu and Dávila (2017), demonstrating that the interatomic potential applied in this work is capable of reproducing such phenomenon.

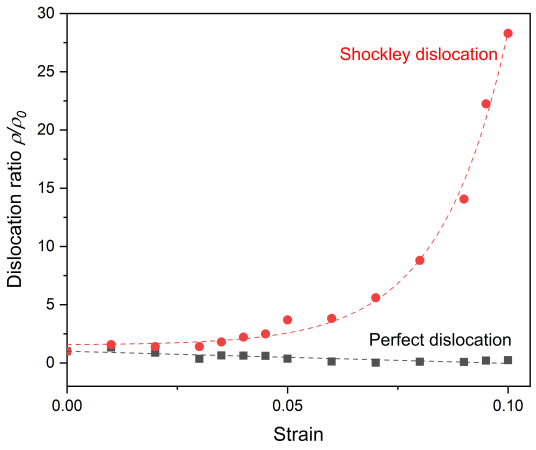

Figure 10. Dislocation ratio (normalized dislocation density) for different strain values of the three-grain sample. The red and black dashed lines are the exponential and linear fit, respectively.
Source: Authors

Conclusions

Molecular dynamics simulations were employed with a novel interatomic potential for Al in order to investigate its mechanical properties and behavior. The tensile testing results clearly showed an inverse Hall-Petch relationship. The grain size transition from the conventional to the inverse Hall-Petch relationship was calculated to be around 17 nm by fitting pertinent data. No work hardening was

observed for the 10- and 15-grain samples. An increase in partial dislocations was observed, but its contribution to the total deformation was limited. For instance, a strain of 0,10 causes a relatively small increase in dislocation density of just one order of magnitude. Coble creep atomic diffusion and grain rotation were evidenced, demonstrating that the conventional slip mechanisms are not predominant for grains in the nanosize. Therefore, further studies are required to better understand these two crucial deformation mechanisms in nanocrystalline materials.

Acknowledgements

This work was financially supported by Fundação de Amparo à Pesquisa do Estado do Rio de Janeiro (FAPERJ) and Conselho Nacional de Desenvolvimento Científico e Tecnológico (CNPq). This study was financed in part by the Coordenação de Aperfeiçoamento de Pessoal de Nível Superior — Brasil (CAPES) — Finance Code 001.

References

Afkham, Y., Bahramyan, M., Mousavian, R. T., and Brabazon, D. (2017). Tensile properties of AlCrCoFeCuNi glassy alloys: A molecular dynamics simulation study. *Materials Science and Engineering A, 698*, 143-151. https://doi.org/10.1016/j.msea.2017.05.057

Aliaga, L. C. R., Lima, L. V. P. C., Domingues, G. M. B., Bastos, I. N., and Evangelakis, G. A. (2019). Experimental and molecular dynamics simulation study on the glass formation of CuZrAl alloys. *Materials Research Express, 6*, 045202. https://doi.org/10.1088/2053-1591/aaf97e

Aliaga, L. C. R., Schimidt, C. S., Lima, L. V. P. C., Bastos, I. N., and Botta, W. J. (2018). Study of glass forming on Cu60.0Zr32.5Ti7.5 alloy by molecular dynamics simulation. *Materials Research, 21*(2), e20170555. https://doi.org/10.1590/1980-5373-MR-2017-0555

Baracaldo, R. R., Marrero, J. M. C, and Páramo, A. B. (2011). Studying the Hall-Petch effect regarding sub-micrometer steel (0.6%C). *Ingeniería e Investigación, 31*(3), 112-120. https://doi.org/10.15446/ing.investig.v31n3.26398

Barboza, A. M., Bastos, I. N., and Aliaga, L. C. R. (2020). Molecular dynamics simulations of the mechanical behavior of nanostructured and amorphous $Al_{80}Ti_{15}Ni_5$ alloy. *Revista Facultad de Ingeniería, 103*, 20-33. https://doi.org/10.17533/udea.redin.20201009

Barboza, A. M., Bastos, I. N., and Aliaga, L. C. R. (2021). Nanograin size effects on deformation mechanisms and mechanical properties of nickel: A molecular dynamics study. *Materials Express, 11*(11), 1841-1855. https://doi.org/10.1166/mex.2021.2091

Choi, H. J., Lee, S. W., Park, J. S., and Bae, D. H. (2009). Positive deviation from a Hall-Petch relation in nanocrystalline aluminum. *Materials Transactions, 50*, 640-643. https://doi.org/10.2320/matertrans.MRA2008343

Fan, G.J., Choo, H., Liaw, P. K., and Lavernia, E. J. (2005). A model for the inverse Hall-Petch relation of nanocrystalline materials. *Materials Science and Engineering A, 409*, 243-248. https://doi.org/10.1016/j.msea.2005.06.073

Hasan, M. S., Lee, R., and Xu, W. (2020). Deformation nanomechanics and dislocation quantification at the atomic scale in nanocrystalline magnesium. *Journal of Magnesium and Alloys, 8*, 1296-1303. https://doi.org/10.1016/j.jma.2020.08.014

Hirel, P. (2015). Atomsk: A tool for manipulating and converting atomic data files. *Computer Physics Communications, 197*, 212-219. https://doi.org/10.1016/j.cpc.2015.07.012

Hu, J., Shi, Y. N., Sauvage, X., Sha, G., and Lu, K. (2017). Grain boundary stability governs hardening and softening in extremely fine nanograined metals. *Science, 355*, 1292-1296. https://doi.org/10.1126/science.aal5166

Jang, H.-S., Seol, D., and Lee, B.-J. (2021). Modified embedded-atom method interatomic potentials for Mg-Al-Ca and Mg-Al-Zn ternary systems. *Journal of Magnesium and Alloys, 9*, 317-335. https://doi.org/10.1016/j.jma.2020.09.006

Kashan, J. S., and Ali, S. M. (2019). Modeling and simulation for mechanical behavior of modified biocomposite for scaffold application. *Ingeniería e Investigación, 39*, 63-75. https://doi.org/10.15446/ing.investig.v39n1.73638

Lee, J.G. (2012). *Computational materials science: An introduction*. Taylor & Francis Group.

Lesar, R. (2013). *Introduction to computational materials science—Fundamentals to applications*. Cambridge University Press.

Meyers, M. A., Mishra, A., and Benson, D.J. (2006). Mechanical properties of nanocrystalline materials. *Progress in Materials Science, 51*, 427-556. https://doi.org/10.1016/j.pmatsci.2005.08.003

Naik, S. N. and Walley, S. M. (2020). The Hall-Petch and inverse Hall-Petch relations and the hardness of nanocrystalline metals. *Journal of Materials Science, 55*, 2661-2681. https://doi.org/10.1007/s10853-019-04160-w

Ovid'ko, I. A., and Shinerman, A. G. (2013). Kinects of grain boundary sliding and rotational deformation in nanocrystalline materials. *Reviews on Advanced Materials Science, 35*, 48-58. https://www.ipme.ru/e-journals/RAMS/no_13513/04_13513_ovidko.pdf

Pal, S., and Ray, B. C. (2020). *Molecular dynamics simulation of nanostructured materials: An understanding of mechanical behavior*. CRC Press.

Pande, C. S., and Cooper, K. P. (2009). Nanomechanics of Hall-Petch relationship in nanocrystalline materials. *Progress in Materials Science, 54*, 689-706. https://doi.org/10.1016/j.pmatsci.2009.03.008

Plimpton, S. (1995). Fast parallel algorithms for short-range molecular dynamics. *Journal of Computational Physics, 117*, 1-19. https://doi.org/10.1006/jcph.1995.1039

Saidi, P., Dai, C., Power, T., Yao, Z., and Daymond, M. R. (2017). An embedded atom method interatomic potential for the zirconium-iron system. *Computational Materials Science, 133*, 6-13. https://doi.org/10.1016/j.commatsci.2017.02.028

Schneider, M., and Laplanche, G. (2021). Effects of temperature on mechanical properties and deformation mechanisms of the equiatomic CrFeNi medium-entropy alloy. *Acta Materialia, 204*, 116470. https://doi.org/10.1016/j.actamat.2020.11.012

Stukowski, A. (2010). Visualization and analysis of atomistic simulation data with OVITO - The Open Visualization Tool.*Modelling and Simulation in Materials Science and Engineering, 18*, 015012. https://doi.org/10.1088/0965-0393/18/1/015012

Tjong, S.-C. (2013). *Nanocrystalline materials: Their synthesis-structure-property relationships and applications* (2nd ed.), Elsevier.

Tschopp, M. A., Spearot, D. E., and McDowell., D. L. (2008). Influence of grain boundary structure on dislocation nucleation in FCC metals. *Dislocations in Solids, 14*, 46-139. https://doi.org/10.1016/S1572-4859(07)00002-2

Tsuji, N., Ito, Y., Saito, Y., and Minamino, Y. (2002). Strength and ductility of ultrafine grained aluminum and iron produced by ARB and annealing. *Scripta Materialia, 47*, 893-899. https://doi.org/10.1016/S1359-6462(02)00282-8

Xu, W., and Dávila, L. P. (2017). Tensile nanomechanics and the Hall-Petch effect in nanocrystalline aluminium. *Materials Science & Engineering A, 710*, 413-418. https://doi.org/10.1016/j.msea.2017.10.021

Ward, L., Agrawal, A., Flores, K. M., and Windl, W. (2012). Rapid production of accurate embedded-atom method potentials for metal alloys. *arXiv*. https://doi.org/10.48550/arXiv.1209.0619

Weng, G. J., and Barai, P. (2009). Mechanics of very fine-grained nanocrystalline materials with contributions from grain interior, GB zone, and grain-boundary sliding. *International Journal of Plasticity*, 25, 2410-2434. https://doi.org/10.1016/j.ijplas.2009.04.001

Research Article/Mechanical Engineering, Mechatronics, and Materials Science http:// doi.org/10.15446/ing.investig.95364

Aqueous Recovery of Zinc and Lead from Coal Fly Ashes of a Colombian Thermoelectric Plant

Recuperación acuosa de zinc y plomo a partir de cenizas volantes de carbón de una planta termoeléctrica colombiana

Johana Borda[1], Claudia González[2], and Robinson Torres[3]

ABSTRACT

A hydrometallurgical treatment under ambient conditions was proposed in order to eliminate and recover the lead and zinc contained in a sample of thermal coal fly ash used to produce energy. By using leaching solutions with conventional inorganic acids (HCl, HNO3, and H2SO4), ferric chloride, and sodium citrate, more than 90% zinc and approximately 40% lead were obtained. The most favorable leaching conditions were set at 0,5 M, with a pH value of 8 for citrate. Two leaching stages were necessary to optimize metal recovery: the first with nitric acid for zinc extraction and the second one with citrate for the lead. The sulfur phases of the metals limited a complete metal extraction.

Keywords: fly ash, leaching, HNO3, sodium citrate, zinc, lead

RESUMEN

Se propuso un tratamiento hidrometalúrgico en condiciones ambientales para eliminar y recuperar el plomo y zinc contenidos en una muestra de cenizas volantes de carbón térmico que se utiliza para producir energía. Mediante el uso de soluciones de lixiviación con ácidos inorgánicos convencionales (HCl, HNO3 y H2SO4), cloruro férrico y citrato de sodio, se obtuvo más del 90 % de zinc y aproximadamente el 40 % de plomo. Las condiciones de lixiviación más favorables se establecieron en 0,5 M y un valor pH de 8 para el citrato. Fueron necesarias dos etapas de lixiviación para optimizar la recuperación de metales: la primera con ácido nítrico para la extracción de zinc y la segunda con citrato para el plomo. Las fases de azufre de los metales limitaron una completa extracción de metales.

Palabras clave: cenizas volantes, lixiviación, HNO3, citrato de sodio, zinc, plomo

Received: April 28th, 2021
Accepted: July 18th, 2022

Introduction

The production of electrical energy around the world is mainly related to the consumption of fossil fuels. Colombia, for example, is a country that depends to a great extent on the energy generated in thermoelectric plants. However, despite the fact that, over the years, efforts have been invested in the construction of power plants based on alternative energies, replacing the conventional coal routes has not yet been possible (Henao and Dyner, 2020). Additionally, situations such as those undergone by megaprojects such as Hidroituango (which, due to failures during the construction phase, is likely not to be completed) threaten the future security of Colombia's energy supply. Due to the above, and because Colombia has large coal reserves, the country continues to generate a good part of its electrical energy from this fossil fuel (Henao and Dyner, 2020; Vinascoa *et al*., 2014).

Most generation plants use pulverized coal for their production. However, some solid waste such as fly ash (FA), bottom ash (BA), boiler slag (BS), and flue gas desulfurization residues (FGD or synthetic gypsum) are discharged in large amounts when burning coal for energy. These residues pose a potential risk to the environment if they are not treated or disposed of properly (Fytianos *et al*., 1998). Currently, fly ash (hereinafter FA) is the most abundant among the coal combustion products (Punshon *et al*., 2003). It is composed of fine particles that remain suspended in the airstream. FA makes up about 80% of the total ash produced in the aforementioned process; the remaining 20% is made up of the BA that fall and vitrify at the bottom of the furnace and is characterized

[1] Ingeniero metalúrgico, Magíster en Metalurgia y Ciencia de los Materiales. Universidad Pedagógica y Tecnológica de Colombia. Facultad de Ingeniería. Escuela de Ingeniería Metalúrgica. Email: angelajohana.borda@uptc.edu.co

[2] Estudiante de Ingeniería Metalúrgica. Universidad Pedagógica y Tecnológica de Colombia. Facultad de Ingeniería. Escuela de Ingeniería Metalúrgica. Email: claudia.gonzalez03@uptc.edu.co.

[3] Ingeniero metalúrgico, PhD en Ingeniería Química. Profesor Universidad Pedagógica y Tecnológica de Colombia. Facultad de Ingeniería. Escuela de Ingeniería Metalúrgica. Email: robinson.torres@uptc.edu.co.

How to cite: Borda, J., González, C., and Torres, R. (2023). Aqueous recovery of zinc and lead from coal fly ashes of a Colombian thermoelectric plant. *Ingeniería e Investigación, 43*(1), e95364. http:// doi.org/10.15446/ing.investig.95364

by a coarser granulometry compared to FA (Asokan *et al*., 2015; Menéndez, *et al*., 2013; Siddique, 2010). Ashes can damage the environment and human health due to their heterogeneous composition, size, and physical and chemical properties (Jaramillo-Nieves *et al*., 2020; Wang *et al*., 2020). FA is susceptible to mixing with the environment due to its fine granulometry. Every year, coal-fired power plants produce between 600 and 800 million tons of FA around the world (Jayaranjan *et al*., 2014), out of which approximately 48% are recycled (Sushil and Batra, 2006). Some power generation plants choose to dispose of the FA in mounds and landfills, ignoring the harmful effects that this could cause: research has shown that landfill ash disposal activities are environmentally unsafe in the long term (Danker *et al*., 2011). The main dangers associated with FA arise from trace metals, metalloids, and potentially toxic concentrations with toxic effects on biota (Jackson *et al*., 2001). It is common to find traces of heavy metals (Cd, Cr, Zn, Pb) that can be leached into the water (Menéndez *et al*., 2013). Once dissolved, these spread to nearby lands, generating soil and water contamination. Additionally, they interfere with treatment and recycling methods on which several authors have been working (Lv *et al*., 2022). In soil improvement, for example, the physicochemical properties of FA and its alkaline nature make it a potential soil amendment, improving soil conditions and controlling its acidity. However, ashes represent a risk of contamination for the soil, plants, and groundwater due to its content of heavy metals (Pandey and Singh, 2010; Ram *et al*., 2006; Yao *et al*., 2015). In other treatment routes such as the manufacturing of cement mortars (Pedraza *et al*., 2015; Valderrama *et al*., 2011) and the production of geopolymers and hybrid materials (Chindaprasirt *et al*., 2014; Rivera *et al*., 2014; Martínez-López *et al*., 2015), their incorporation into ceramic pastes (Erol *et al*., 2008; Peng, 2004; Kockal, 2012), zeolite synthesis (Querol *et al*., 2002; Shigemoto and Hayshi, 1993; Murayama *et al*., 2002), and wastewater treatment can also cause interference due to contamination (Wang *et al*., 2020; Awoyemi *et al*., 2009; Dere Ozdemir and Piskin 2017; Tang *et al*., 2019; Wang *et al*., 2017). Although these elements are present in a relatively small fraction, they are of special interest due to their accumulation, long life, and high toxicity. Therefore, estimating their leaching potential is important to assess the possible environmental impacts associated with the reuse and disposal of FA (Fytianos *et al*., 1998)

Since the metal/metalloid ions contained in FA are not tightly bound, all of its heavy metals are susceptible to leaching to varying degrees. The aqueous phase extraction of these metals has been modestly studied, showing that AF leaching depends on several factors such as leaching time, temperature, pH of the medium, solid-liquid ratio, and FA source (Das *et al*., 2021).

However, FA leaching has been studied mainly for the recovery of trace metals from soft organic soils stabilized with this residue (Sauer *et al*., 2012; Das *et al*., 2021), as well as for the removal of impurities such as CaO and Fe_2O_3 with hydrochloric acid solutions at 80 °C under a liquid-solid ratio of 4,0 in 6,0 mol/L of acid (Lv *et al*., 2022).

Therefore, this study proposes an alternative for metallurgical use which allows for the valorization of this type of waste. This research analyzes the extraction of two of the heavy metals with the highest presence in the composition of an FA sample (Zn and Pb), through a process of agitation leaching. The experiments were carried out under ambient conditions, using three conventional inorganic acids (HCl, HNO_3, and H_2SO_4), a salt ($FeCl_3$), and a carboxylic agent (sodium citrate). This treatment aims to obtain a liquor rich in Zn and Pb for the subsequent recovery of metals through electro-recovery processes. On the other hand, a leached solid free of heavy metals is left to be applied as a secondary material.

Materials and methods

Materials

The FA sample used for the leaching experiments was obtained from a Colombian thermal power plant that uses mixtures of bituminous coal for its operation. The specific location, date of generation of the ashes, and their storage characteristics were not provided by the company.

Methods

Leaching methods and reactives: To carry out the leaching tests, conventional inorganic reagents were used, such as sulfuric acid (H_2SO_4), hydrochloric (HCl), and nitric acid (HNO_3), as well as other alternatives such as ferric chloride ($FeCl_3$) and sodium citrate ($Na_3C_6H_5O_7.2H_2O$) at a concentration of 0,5 M. All solutions were prepared with JT Baker and Milli-Q deionized water. In some tests, it was necessary to modify the concentration of the solutions in order to determine its effect on the dissolution of the studied metals. The extraction process was carried out via stirring leaching (500 rpm), using mechanical stirrers without baffles (Model 50006-03, Cole-Parmer) with paddle-type propellers. An S/L ratio of 50 g of FA per liter of solution was used for 3 hours, at room temperature and pressure (1 022 bar; 17 °C). In citrate solutions, the pH was adjusted with the addition of sodium hydroxide (NaOH) and HNO_3. The potential was monitored using a saturated Ag/AgCl reference electrode (Oakton pH ORP 700 Benchtop Meter). Subsequently, the values were adjusted to the standard hydrogen electrode (SHE) for the corresponding thermodynamic analyses. Predominant area diagrams were elaborated using the MEDUSA software (Eriksson, 1979; Puigdomenech, 2004). The thermodynamic data of the metallic species in solution were contrasted with the NIST 46 database (NIST, 2004). The metal contents of the solutions were determined by microwave plasma atomic emission spectrophotometry (Agilent MP-AES), using the indications and calibration standards recommended by the manufacturer.

Sample characterization: The FA sample was chemically and mineralogically characterized. The chemical composition was determined by digestion with *aqua regia* (HCl: HNO_3, 3:1). The results showed that iron was the most present element in the study sample (Table 1).

Table 1. Elemental composition of the FA sample

Element	Content (%)
Fe	20,62
Pb	0,414
Zn	0,314
Cu	0,08
Cr	0,02
Ni	0,01

Source: Authors

On the other hand, the content of trace elements such as Zn and Pb is due to their association with the inorganic fraction of coal, which, during its combustion process, vaporizes, condenses, and finally concentrates in fine ash particles in the form of oxides.

Mineralogical characterization was performed via X-ray diffraction (Panalytical X'pert Pro), using Bragg-Brentano geometry with a cobalt cathode. The ICDD database (International Center for Diffraction Data) made it possible to contrast the peaks shown in the diffraction pattern (Figure 1), which indicated that the FA was mainly composed of silica (SiO_2) and alumina (Al_2O_3). The presence of these two was expected due to the dehydration suffered by kaolin in the coal combustion process. The iron content of the sample (Table 1) comes from both the pyrite (FeS_2) inherent in the formation of the fuel and the iron oxide (Fe_2O_3), a product of the little oxidation of this sulfide during the combustion process:

$$2FeS_2 + 5{,}5\ O_2 \rightarrow 4SO_2 + Fe_2O_3 \quad (1)$$

Both the considerable presence of species such as SiO_2 and Al_2O_3 and the absence of CaO in the FA sample indicate its silico-aluminous classification (F) (ASTM International, 2014), as well as the fact that the concentration of its relatively inert crystalline components is in a slow reaction phase, rich in iron and silica (Santaella, 2001).

Zn and Pb oxides are found in low concentrations, so they cannot be identified in the spectrum. However, it is possible to know its presence in FA due to its formation process:

$$ZnS + 1{,}5\ O_2 \rightarrow SO_2 + ZnO \quad (2)$$

$$PbS + 1{,}5\ O_2 \rightarrow SO_2 + PbO \quad (3)$$

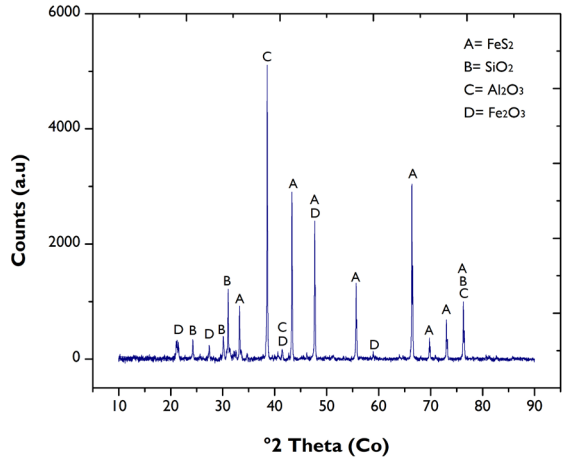

Figure 1. Raw FA diffraction pattern
Source: Authors

Thermodynamic considerations

It was necessary to conduct a thermodynamic analysis for the carboxylic agent to identify the pH and potential conditions of the soluble and metallic species. The information provided by the prevalence diagrams indicates that, for Pb, at pH values 1 to 9, the formation of soluble species with potentials greater than -200 mV is favored. Under more alkaline conditions, the species formed are in a solid state. Zn, for its part, shows independence from the potential for species formation, while the favorable pH is within a range from 1 to 11. This can be seen in Figure 2.

The above shows the citrate leaching ability of FA heavy metals across a wide pH range. Thus, three different values of pH were tested (4, 8, and 10) in order to determine their effect on the extraction of the metals of interest.

Results and discussion

Leaching tests

Leaching using HCl, HNO_3, $FeCl_3$ and H_2SO_4: In hydrometallurgy, the capabilities of inorganic acids to chemically attack metallic elements is well known. Similarly, it has been reported that salts such as $FeCl_3$ are favorable for eliminating heavy metals such as Zn and Pb (Guo *et al.*, 2016). Figure 3 shows the performance of HCl, HNO_3, H_2SO_4, and $FeCl_3$ in metals extraction. Regarding Zn dissolution, it is evident that acidic media provide an adequate amount of hydronium ions, which is favorable for metal dissolution. However, the dissolution kinetics are different for the reagents tested. For the three acids, a greater rate of leaching was observed in the first hour, during which between 80 to 85% of Zn was recovered. The extraction with HCl and H_2SO_4 showed an asymptotic

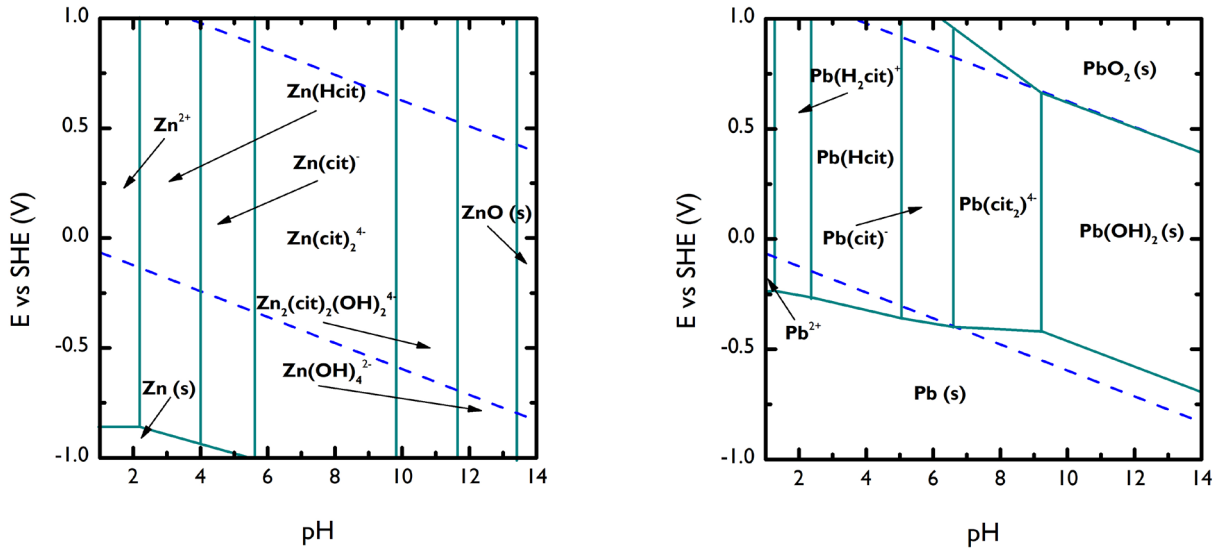

Figure 2. Predominance diagrams for Zn (a) and Pb (b) in the presence of 0,5 M citrate. Designed with the MEDUSA software.
Source: Authors

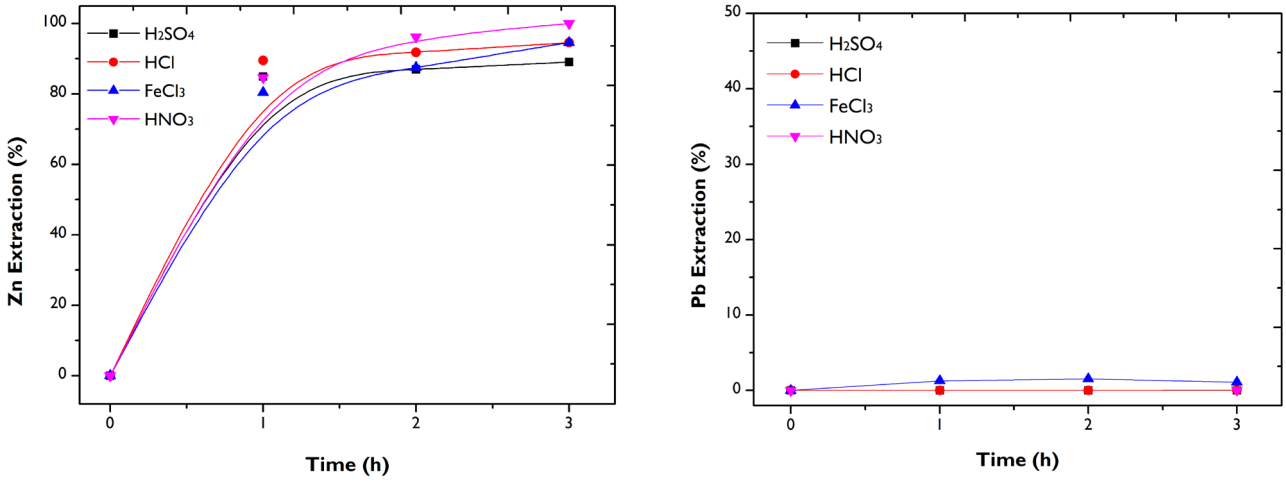

Figure 3. Leaching of Zn and Pb from FA. Conditions: HCl, HNO_3, $FeCl_3$, and H_2SO_4 – 0,5 M; 500 rpm; 50g/L.
Source: Authors

behavior, while HNO_3 exhibited a progressive metals extraction of up to 98%. This can be attributed to the fact that, in the Zn-HCl and Zn-H_2SO_4 systems, the acid is quickly consumed, thus requiring a higher concentration of the solution to improve recovery.

On the other hand, the acidity of the chloride medium (pH 2,6) also allowed for a progressive recovery of the metal. However, after three hours, HNO_3 was the one that achieved the best extraction of the non-ferrous metal. Due to the high presence of FeS_2 in FA, the chemical systems of the three inorganic reagents have a lower lead leaching capacity. The presence of sulfur in the acidic medium gives way to the formation of solid-state sulfate species, which leads to the inhibition of the dissolution of the metal.

Pb chlorides resulting from leaching with $FeCl_3$ are of low solubility, and their dissolution takes place at temperatures equal to or greater than 100 °C (Aguilar-Pérez *et al*., 1997). The low extraction of Pb with these agents is interesting, as it implies selectivity in leaching. Subsequent treatments can be proposed to detoxify the leached solid while obtaining a liquor rich in Zn.

Leaching using sodium-citrate

pH effect.: The influence of pH on the extraction of the metals of interest in the citrate solution was evaluated (Figure 4). With oxidation potentials in ranges from 400 to 600 mV that were recorded by the leaching tests, it was found that the dissolution of metals is independent of pH values.

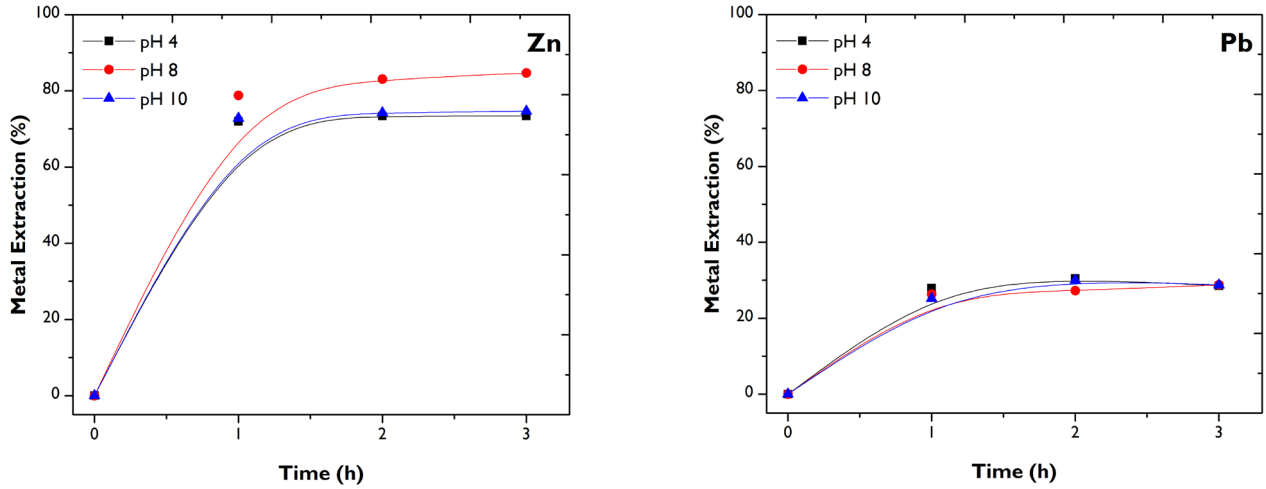

Figure 4. pH effect on the extraction of metals from FA. Conditions: citrate 0,5 M; 500 rpm; 50g/L.
Source: Authors

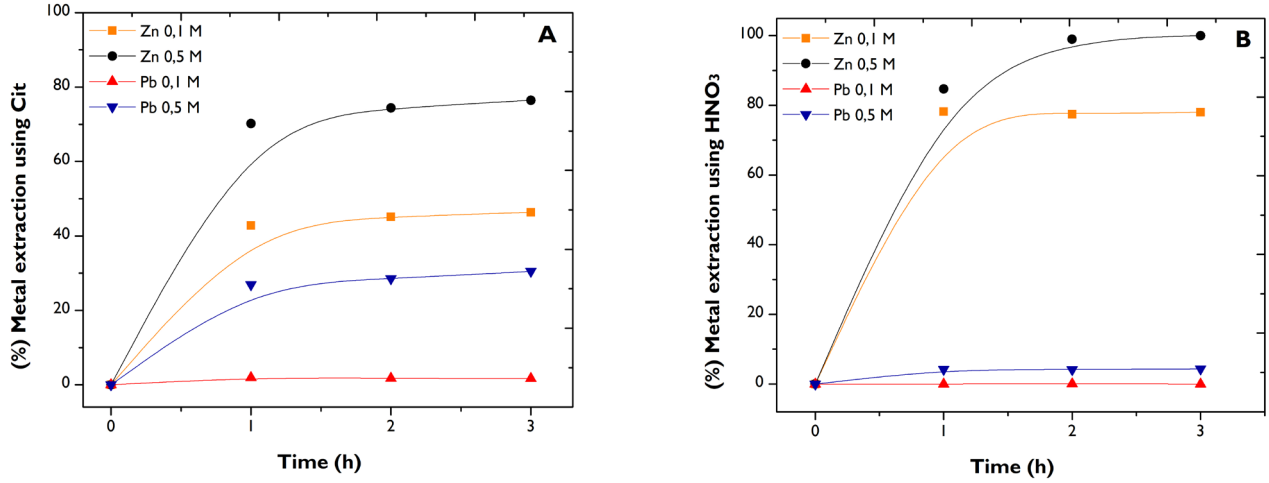

Figure 5. Effect of citrate (a) and HNO_3 (b) concentration. Conditions: 500 rpm; 50g/L.
Source: Authors

Likewise, it was observed that Pb is leached in the same way in the three media (acid, basic, or neutral). This characteristic creates the need for adequate FA treatment in order to avoid possible toxic effects on the environment caused by this heavy metal. Regarding Zn, tests at pH 8 indicate a slight improvement in metal dissolution, albeit only 6%. Due to economic and environmental factors, it is advisable to work under neutral conditions. Thus, a pH value of 8,0 was selected to continue the study.

Metal dissolution: The graphs indicate that the extraction of Zn and Pb combine the dissolution of two phases: the first corresponds to the spontaneous leaching of the oxides ZnO and PbO, while the second represents the slow dissolution of the sulfides inherent to coal, which fail to oxidize in the fuel combustion stage. For this reason, both Pb-Cit and Zn-Cit systems exhibit rapid dissolution kinetics, achieving beneficial extractions within the first hour. After this time, metal recovery becomes too slow (more for Zn at pH 4 and 10). Sulfide leaching is more complex due to both their refractory nature and the formation of a passivating layer during the process (Santaella, 2001; Borda and Torres, 2022). Research has shown that it is possible to dissolve divalent Zn and Pb ions with citrate when these are associated with sulfides. However, additional time is necessary to obtain a better dissolution of the metals (Torres and Lapidus, 2020), as well as a higher molar concentration of citrate and the presence of hydrogen peroxide (Zárate *et al.*, 2015). However, it has been shown that, in processes that combine the dissolution of two phases (in this study: oxides and sulfides), overall leaching kinetics can be affected (Borda *et al.*, 2022).

Effect of citrate and HNO_3 concentration

The degree of dissolution of metals was studied based on the variation of citrate and HNO_3 concentrations from 0,5 to 0,1 M. The influence of the reagents' molarity was different for both systems (Figure 5).

Although a greater metallic extraction was obtained when using the highest molarity of the agents, this occurred in different amounts and more noticeably in citrate. However, even though the reactions proceeded with an apparently concentration-dependent speed, the variation in the amount of species formed was not directly proportional to the agent's concentration, which is evidenced by the 28 and 26% increase in extraction with citrate and 17 and 4,3% with HNO_3 for Zn and Pb, respectively. Although the metal recovery increases, it is not proportional to the increase in the molarity of the reactants.

The presence of leaching agents was higher than the available Zn^{2+} and Pb^{2+} ions. The concentration of the agents did not change appreciably over time, attributing a pseudo-first order to the chemical reactions taking place. Thus, the leaching kinetics did not reveal any dependence of rate concerning the concentration of citrate and HNO_3 (Levenspiel, 1999; Smith, 1981).

Efficiency of Zn and Pb dissolution from solid leached with HNO_3

HNO_3 at 0,5 M achieved the highest Zn extraction (98%) compared to citrate under the same conditions (Figure 5). Note that the low dissolution of Pb is advantageous, as the selectivity towards Zn in the process facilitates its subsequent recovery. Leaching was required to detoxify the leached solid by removing the Pb from the residue. To this effect, the solution was filtered after three hours in order to subject the solid to a second leaching, this time using a fresh solution of sodium citrate with the initially established conditions (pH 8, 0,5 M).

The results show that the post-treatment reaches a 40% elimination of the Pb from the leached FA. As explained above, under these conditions, citrate can form soluble complexes only with the Pb ions present in oxide form. However, after previously extracting the Zn from the FA sample, the amount of reagent available to react with Pb sulfide compounds increases, which is reflected on a 10% improvement in metal removal in comparison with direct citrate leaching (Table 2).

Table 2. Efficiency of Zn and Pb dissolution from leached solid. Conditions: Leaching I with HNO_3; Leaching II with citrate; 500 rpm; 30 g/L; 3 h.

	Leaching I	Leaching II
Zn (%)	98	98
Pb (%)	0,04	39,45

Source: Authors

Iron extraction

The results of the chemical digestion revealed that the iron content in the study sample was 20,6%. Its presence in the FA sample is high compared to the percentage of trace elements such as Zn and Pb (Table 1). However, its extraction is not relevant in this study, as it is not considered as a contaminating or interfering element in the mechanical properties of the secondary material after FA treatment (Yao *et al.*, 2015). The main issue with the extraction of iron lies the difficulty of its electrodeposition (Torres and Lapidus, 2017). Thus, in order to avoid drawbacks in the electrolytic recovery of Zn, it is preferable to minimize iron extraction.

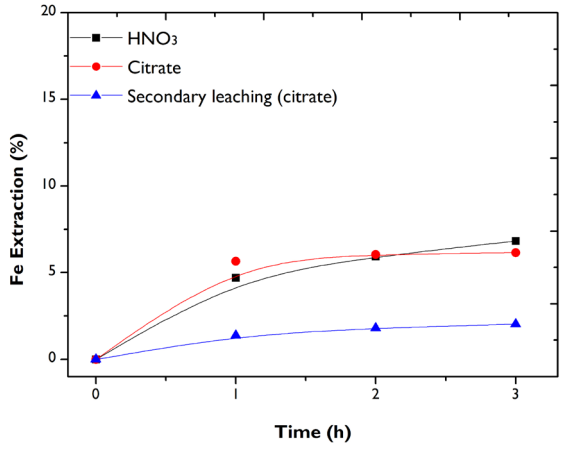

Figure 6. Iron leaching using citrate solutions (direct and secondary) and HNO_3
Source: Authors

Figure 6 shows the low dissolution of iron in the direct leaching with HNO_3 and citrate, as well as the secondary leaching from the solid leached. The extracted metal content can come from the two iron phases present in FA: an easy to leach Fe_2O_3 and a somewhat more complex Fe_2S (Figure 1). The fast iron extraction in the first hour is attributed to the dissolution of the oxide in the solutions, and, while the citrate leaching stops, HNO_3 continues with very slow kinetics due to the dissolution of the sulfide species.

Conclusions

A method was presented to recover some heavy metals from thermal coal fly ash by a hydrometallurgical route under ambient conditions. Due to their characteristics, these metals can be potentially dangerous for the environment and extremely harmful for living beings. The results showed that inorganic acids and ferric chloride are more efficient for extracting Zn, as they achieve more than 90% recovery when compared to citrate. Their inefficiency in Pb recovery allows selective leaching of Zn. Two leaching stages are necessary to clean the residue: the first with HNO_3 for Zn extraction and a subsequent one with citrate for Pb. It was shown that the dissolution of the oxide phases is fast, while that achieved by the sulfide phases is too slow and null in some cases.

This method achieves the removal of the Pb and Zn contained in the FA, yielding a residual product with non-toxic characteristics, which can be used as a secondary material.

Acknowledgements

The authors are grateful for the support received from the VIE-SGI project in order to carry out this research, as well as for the support offered by Grupo Metalurgia No Ferrosa [Non-ferrous metallurgy group] of Universidad Pedagógica y Tecnológica de Colombia.

References

Aguilar-Pérez, G., González-Aguirre, M., and Morales-Pérez, A. A. (1997). *Lixiviación de galena con cloruro férrico para la obtención de plomo*. Universidad Autónoma Metropolitana de México. http://148.206.53.233/tesiuami/UAM5165.pdf

Asokan, P., Saxena, M., and Asolekar, S. R. (2005). Coal combustion residues – Environmental implications and recycling potentials. *Resources, Conservation and Recycling, 43*(3), 239-262. https://doi.org/10.1016/j.resconrec.2004.06.003

ASTM International (2012). *ASTM C 618. 2012: Standard specification for coal fly ash and raw or calcined natural pozzolan for use in concrete*. ASTM International. https://doi.org/10.1520/C0618

Awoyemi, O. M., Adeleke, E. O., and Dzantor, E. K. (2019). Arbuscular mycorrhizal fungi and exogenous glutathione mitigate coal fly ash (CFA)-induced phytotoxicity in CFA-contaminated soil. *Journal of Environmental Management, 237*, 449-456. https://doi.org/10.1016/j.jenvman.2019.02.103

Borda, J., and Torres, R. (2022). Recycling of zinc and lead from electric arc furnace dust by selective leaching with EDTA. *Canadian Metallurgical Quarterly, 61*(4), 464-474. https://doi.org/10.1080/00084433.2022.2046902

Borda, J., Torres, R., and Lapidus, G. (2022). Selective leaching of zinc and lead from electric arc furnace dust using citrate and H2SO4 solutions. A kinetic perspective. *Revista Mexicana De Ingeniería Química, 21*(1), Cat2606. https://doi.org/10.24275/rmiq/cat2606

Chindaprasirt, P., de Silva, P., and Hanjitsuwan, S. (2014). Effect of high-speed mixing on properties of high calcium fly ash geopolymer paste. *Arabian Journal for Science and Engineering, 39*(8), 6001-6007. https://doi.org/10.1007/s13369-014-1217-1

Danker, R., Adriano, D.C., Barton, C., and Punshon, T. (2001). *Revegetation of a coal fly ash - reject landfill* [Conference presentation]. 6th International Conference on the Biogeochemistry of Trace Elements (ICOBTE), Guelph, Canada.

Das, S. K., Dan, A. K., Behera, U., Tripathi, A. K., Behari, M., Das, D., and Parhi, P. K. (2021). A novel approach on leaching study for removal of toxic elements from thermal power plant-based fly ash using natural bio-surfactant. *Case Studies in Chemical and Environmental Engineering, 4*, 100156. https://doi.org/10.1016/j.cscee.2021.100156

Dere Ozdemir, O., and Piskin, S. (2017). A novel synthesis method of zeolite X from coal fly ash: Alkaline fusion followed by ultrasonic-assisted synthesis method. *Waste and Biomass Valorization, 10*, 143-154. https://doi.org/10.1007/s12649-017-0050-7

Eriksson, G. (1979). An algorithm for the computation of aqueous multicomponent, multiphase equilibria. *Analytica Chimica Acta, 112*(4), 375-383. https://doi.org/10.1016/S0003-2670(01)85035-2

Erol, M., Küçükbayrak, S., and Ersoy-Meriçboyu, A. (2008). *Characterization of sintered coal fly ashes. Fuel, 87*(7), 1334-1340. https://doi.org/10.1016/j.fuel.2007.07.002

Fytianos, K., Tsaniklidi,B., and Voudrias. E. (1998). Leachability of heavy metals in Greek fly ash from coal combustion. *Environment International, 24*(4), 477-486. https://doi.org/10.1016/S0160-4120(98)00027-0

Guo, X., Wei, Z., Wu, Q., Li, C., Qian, T., and Zheng, W. (2016). Effect of soil washing with only chelators or combining with ferric chloride on soil heavy metal removal and phytoavailability: Field experiments. *Chemosphere, 147*, 412-419. https://doi.org/10.1016/j.chemosphere.2015.12

Menéndez, E., Álvaro, E. M., Argiz, C., Parra, J. L., and Moragues, A. (2013). Characterization of bottom ashes from coal pulverized power plants to determine their potential use feasibility. *Boletín de la Sociedad Española de Cerámica y Vidrio*, *52*(6), 296-304. https://doi.org/10.3989/cyv.372013

Henao, F., and Dyner, I. (2020). Renewables in the optimal expansion of Colombian power considering the Hidroituango crisis. *Renewable Energy 158*, 612-627. https://doi.org/10.1016/j.renene.2020.05.055

Jackson, B., Shaw-Allen, P., Mills, G., Hopkins, W., and Jagoe, C. (2001). *Trace element-protein interactions in fish from a fly ash settling basin. A study using size exclusion chromatography coupled to ICP-MS* [Conference presentation]. 6th International Conference on the Biogeochemistry of Trace Elements, Guelph, Canada.

Jaramillo-Nieves, L. J., Elyseu, F., Goulart, S., de Souza Pereira, M., Valvassori, E. Z., and Bernardin, A. M. (2020). Use of fly and bottom ashes from a thermoelectrical plant in the synthesis of geopolymers: Evaluation of reaction efficiency. *Energy Geoscience, 2*(2), 167-173. https://doi.org/10.1016/j.engeos.2020.09.004

Jayaranjan, M. L. D., van Hullebusch, E. D., and Annachhatre, A. P. (2014). Reuse options for coal fired power plant bottom ash and fly ash. *Reviews in Environmental Science and Bio/Technology, 13*(4), 467-486. http://doi.org/10.1007/s11157-014-9336-4

Kockal, N. U. (2012). Utilisation of different types of coal fly ash in the production of ceramic tiles. *Boletín de la Sociedad Española de Cerámica y Vidrio*, *51*(5), 297-304. https://doi.org/10.3989/cyv.412012

Levenspiel, O. (1999). *Chemical reaction engineering* (3rd ed). John Wiley & Sons.

Lv, Z., Pan, X., Geng, X., and Yu, H. (2022). Synergistic removal of calcium and iron impurities from calcium-rich and high-alumina fly ash by acid leaching control. *Journal of Environmental Chemical Engineering, 10*(2), 107268. https://doi.org/10.1016/j.jece.2022.107268

Martínez-López, C., Mejía-Arcila, J., Torres-Agredo, J., and Mejía de Gutiérrez, R. (2015). Evaluation of the toxicity characteristics of two industrial wastes valorized by geopolymerization process. *Dyna, 82*(190), 74-81. https://doi.org/10.15446/dyna.v82n190.43136

Murayama, N., Yamamoto, H., and Shibata, J. (2002). Mechanism of zeolite synthesis from coal fly ash by alkali hydrothermal reaction. *International Journal of Mineral Processing, 64*(1), 1-17. https://doi.org/10.1016/s0301-7516(01)00046-1

NIST (2004). *Critically selected stability constants of metal complexes*. NIST Standard Reference Database.

Pandey, V. C., and Singh, N. (2010). Impact of fly ash incorporation in soil systems. *Agriculture, Ecosystems and Environment, 136*(1-2), 16-27. https://doi.org/10.1016/j.agee.2009.11.013

Peng, F., Liang, K. M., Hu, A. M., and Shao, H. (2004). Nano-crystal glass-ceramics obtained by crystallization of vitrified coal fly ash. *Fuel, 83*, 1973-1977. https://doi.org/10.1016/j.fuel.2004.04.008

Pedraza, S., Pineda, Y., and Gutiérrez, O. (2015). Influence of the unburned residues in fly ash additives on the mechanical properties of cement mortars. *Procedia Materials Science, 9,* 496-503. https://doi.org/10.1016/j.mspro.2015.05.022

Puigdomenech, I. (2004). *Make equilibrium diagrams using sophisticated algorithms* (*MEDUSA*). Inorganic Chemistry, Royal Institute of technology.

Punshon, T., Seaman,J. C., and Sajwan, K. S. (2003). The production and use of coal combustion products. In K. S Sajwan, A. K. Alva, and R. F. Keefer (Eds.), *Chemistry of Trace Elements in Fly Ash* (pp. 1-11). Springer. https://doi.org/10.1007/978-1-4757-4757-7_1

Querol, X., Moreno, N., Umaña, J., Alastuey, A., Hernández, E., López-Soler, A., and Plana, F. (2002). Synthesis of zeolites from coal fly ash: An overview. *International Journal of Coal Geology, 50*(1-4), 413-423. https://doi.org/10.1016/s0166-5162(02)00124-6

Ram, L. C., Srivastava, N. K., Tripathi, R. C., Jha, S. K., Sinha, A. K., Singh, G., and Manoharan, V. (2006). Management of mine spoil for crop productivity with lignite fly ash and biological amendments. *Journal of Environmental Management, 79*(2), 173-187. https://doi.org/10.1016/j.jenvman.2005.06.008

Ram, L. C., Srivastava, N. K., Jha, S. K., Sinha, A. K., Masto, R. E., and Selvi, V. A. (2007). Management of lignite fly ash for improving soil fertility and crop productivity. *Environmental Management, 40*(3), 438-452. https://doi.org/10.1007/s00267-006-0126-9

Rivera, J. F., Mejía, J. M., Mejía de Gutiérrez, R., and Gordillo, M. (2014). Hybrid cement based on the alkali activation of by-products of coal. *Revista de la Construcción, 13*(2), 31-39. https://doi.org/10.4067/s0718-915x2014000200004

Santaella, L. E. (2001). Caracterización física química y mineralógica de las cenizas volantes. *Ciencia e Ingeniería Neogranadina, 10*, 47-62. https://www.redalyc.org/articulo.oa?id=91101007

Sauer, J. J., Benson, C. H., Aydilek, A. H., and Edil, T. B. (2012). Trace elements leaching from organic soils stabilized with high carbon fly ash. *Journal of Geotechnical and Geoenvironmental Engineering, 138*(8), 968-980, https://doi.org/10.1061/(asce)gt.1943-5606.0000653

Shigemoto, N., Hayashi, H., and Miyaura, K. (1993). Selective formation of Na-X zeolite from coal fly ash by fusion with sodium hydroxide prior to hydrothermal reaction. *Journal of Materials Science, 28*(17), 4781-4786. https://doi.org/10.1007/bf00414272

Siddique, R. (2010). Utilization of coal combustion by-products in sustainable construction materials. *Resources, Conservation and Recycling, 54*(12), 1060-1066. https://doi.org/10.1016/j.resconrec.2010.06.011

Smith, J. M. 1981. *Chemical engineering kinetics* (3rd ed.). McGraw Hill.

Sushil, S., and Batra, V. S. (2006). Analysis of fly ash heavy metal content and disposal in three thermal power plants in India. *Fuel, 85*(17-18), 2676-2679. https://doi.org/10.1016/j.fuel.2006.04.031

Tang, M., Zhou, C., Pan, J., Zhang, N., Liu, C., Cao, S., Hu, t., and Ji, W. (2019). Study on extraction of rare earth elements from coal fly ash through alkali fusion – Acid leaching. *Minerals Engineering, 136*, 36-42. https://doi.org/10.1016/j.mineng.2019.01.027

Torres, R., and Lapidus, G. T. (2017). Closed circuit recovery of copper, lead and iron from electronic waste with citrate solutions. *Waste Management, 60*, 561-568. https://doi.org/10.1016/j.wasman.2016.12.001

Torres, R., and Lapidus, G. T. (2020). Base metal citrate pretreatment of complex ores to improve gold and silver leaching with thiourea. *Hydrometallurgy, 197*, 105461. https://doi.org/10.1016/j.hydromet.2020.105461

Valderrama, C. P., Torres-Agredo, J., and Mejía de Gutiérrez, R. (2011). A high unburned carbon fly ash concrete's performance characteristics . *Ingeniería e Investigación, 31*(1), 39-46. https://repositorio.unal.edu.co/handle/unal/33469

Vinasco, G., Tejada, D., da Silva, E. F., and Rider, M. J. (2014). Transmission network expansion planning for the Colombian electrical system: Connecting the Ituango hydroelectric power plant. *Electric Power Systems Research, 110*, 94-103. https://doi.org/10.1016/j.epsr.2013.12.016

Wang, N., Chen, J., Zhao, Q., and Xu, H. (2017). Study on preparation conditions of coal fly ash catalyst and catalytic mechanism in a heterogeneous Fenton-like process. *RSC Advances, 7*(83), 52524-52532. https://doi.org/10.1039/c7ra09925h

Wang, N., Sun, X., Zhao, Q., Yang, Y., and Wang, P. (2020). Leachability and adverse effects of coal fly ash: A review. *Journal of Hazardous Materials, 396*, 122725. https://doi.org/10.1016/j.jhazmat.2020.122725

Yao, Z. T., Ji, K. S., Sarker, P. K., Tang, J. H., Ge, L. Q., Xia, M. S., and Xi, Y. Q. (2015). A comprehensive review on the applications of coal fly ash. *Earth-Science Reviews. 141*, 105-121. https://doi.org/10.1016/j.earscirev.2014.11.016

Zárate-Gutiérrez, R., Gregorio-Vázquez, L., and Lapidus, G. T. (2015). Selective leaching of lead from a lead-silver-zinc concentrate with hydrogen peroxide in citrate solutions. *Canadian Metallurgical Quarterly, 54*(3), 305-309. https://doi.org/10.1179/1879139515Y.0000000020

Research Article / Mechanical Engineering, Mechatronics, and Materials Science https://doi.org/10.15446/ing.investig.93876

Development of a New Method for Synthesizing HITEC Salt-Based Alumina Nanofluids

Desarrollo de un nuevo método de síntesis de nanofluidos de alúmina a base de sal HITEC

Marllory Isaza-Ruiz[1], and Francisco Bolívar-Osorio[2]

ABSTRACT

This study presents a new two-step method to synthesize molten salt-based nanofluids by replacing water with butanol and using an Emax high-energy mill to ensure good stability and homogeneity. Commercial HITEC molten salt was selected as the base fluid, and alumina nanoparticles (nominal size of 5,1 nm) were used as an additive in three different proportions: 0,5, 1,0, and 1,5 wt.%. The specific heat capacity was evaluated through two different methods: differential scanning calorimetry (DSC) and modulated differential scanning calorimetry (MDSC). According to the evaluation by MDSC, an increment of up to 4,27% in the specific heat capacity was achieved with 1,0 wt.% of alumina nanoparticles in comparison with the raw salt, without affecting the melting point and thermal stability of the salt. This behavior may be related to the good distribution of the nanoparticles in the salt. However, no significant improvement in the specific heat capacity of the nanofluid was observed when the standard DSC method was applied. This behavior may be due to the different sensitivities of the two methods to small changes in the sample, with MDSC being the more sensitive technique, as it establishes the contribution of the two phases that make up the nanofluid: the molten salt as the base fluid and the solid nanoparticles. Similarly, the heating rate used in each of the techniques can influence the sensitivity with regard to determining changes in nanofluids.

Keywords: DSC, MDSC, molten salt-based nanofluids, specific heat capacity

RESUMEN

Este estudio presenta un nuevo método de dos pasos para sintetizar nanofluidos a base de sales fundidas reemplazando el agua por butanol y utilizando un molino de alta energía Emax para garantizar una buena estabilidad y homogeneidad. Se seleccionó la sal fundida comercial HITEC como fluido base y se utilizaron nanopartículas de alúmina (tamaño nominal de 5,1 nm) como aditivo en tres proporciones diferentes: 0,5, 1,0 y 1,5 % en peso. La capacidad calorífica específica se evaluó mediante dos métodos diferentes: calorimetría diferencial de barrido (DSC) y calorimetría diferencial de barrido modulada (MDSC). Según la evaluación por MDSC, se logró un incremento de hasta 4,27 % en la capacidad calorífica específica con 1,0 % en peso de nanopartículas de alúmina en comparación con la sal pura, sin afectar el punto de fusión y estabilidad térmica de la sal. Este comportamiento puede estar relacionado con la buena distribución de las nanopartículas en la sal. Sin embargo, no se observó una mejora significativa en la capacidad calorífica específica del nanofluido cuando se aplicó el método estándar de DSC. Este comportamiento puede deberse a las diferentes sensibilidades de los dos métodos a pequeños cambios en la muestra, siendo MDSC la técnica más sensible, ya que establece el aporte de las dos fases que componen el nanofluido: la sal fundida como fluido base y las nanopartículas sólidas. Del mismo modo, la velocidad de calentamiento utilizada en cada una de las técnicas puede influir en la sensibilidad para determinar cambios en los nanofluidos.

Palabras clave: DSC, MDSC, nanofluidos a base de sales fundidas, capacidad calorífica específica

Received: February 2nd, 2021
Accepted: March 4th, 2022

Introduction

Due to global energy shortages and the unstable energy supply, as well as to concerns over environmental pollution, renewable energies have drawn the attention of researchers as a way to obtain sustainable energy sources. Concentrated solar power energy (CSP) stands out among the renewable energies that have been studied thanks to its advancing development and annual production, reaching 6,2 GW in 2020 (REN21, 2021). Nevertheless, as a result of the sun's intermittency, it is necessary to use a profitable storage system with which is possible to increase the efficiency and conservation of energy as well as the competitiveness

[1] Materials engineer, Universidad de Antioquia, Medellín, Colombia. PhD in Materials Engineering, Universidad de Antioquia, Medellín, Colombia. Affiliation: Microscopist, Centro de Microscopia Avanzada, CAM, Universidad de Antioquia, Medellín, Colombia. Email: marllory.isazar@udea.edu.co

[2] Metallurgical engineer, Universidad de Antioquia, Medellín, Colombia. PhD in Materials Physics, Universidad Complutense de Madrid, Madrid, España. Affiliation: Associate professor, Universidad de Antioquia, Medellín, Colombia. Email: francisco.bolivar@udea.edu.co

How to cite: Isaza-Ruiz, M., and Bolívar-Osorio, F. (2023). Development of a new method for synthesizing HITEC salt-based alumina nanofluids. *Ingeniería e Investigación, 43*(1), e93876. https://doi.org/10.15446/ing.investig.93876

of CSP compared to traditional sources. To improve the thermodynamic cycles of solar thermal energy, the use of heat transfer fluids (HTF) based on organic substances such as oils has been replaced with the use of molten salts such as nitrates and nitrites, given their high thermal stability, low vapor pressure, chemical inertness, availability, and profitability. However, these salts have low specific heat capacity and low thermal conductivity, so they are still under study (Serrano-López *et al*., 2013).

The use of solid nanoparticles (less than 100 nm in size) to obtain nanofluids with molten salt as base fluid –thereby improving the thermal properties of the molten salt– has been studied by several authors (Chieruzzi *et al*., 2017a; Hu *et al*., 2017; Zhang *et al*., 2017). Ho and Pan (2017) showed that the optimum amount to be added to commercial HITEC salt in order to obtain the best properties was 0,063 wt.% of alumina nanoparticles, through which an increase in the specific heat capacity of 19,9% is obtained. In this study, it was shown that, at higher concentrations of alumina, there is a decrease in the specific heat capacity of the salt. Schuller *et al*. (2015), on the other hand, proved that there is a parabolic relation between the specific heat and the mass fraction of alumina nanoparticles added to nitrate salts, obtaining a maximum specific heat increase of 30,6% with a 0,78 wt.% of alumina.

Although there are several reports on the use of solid additives to improve the properties of the salts used in CSP (Muñoz-Sánchez, Nieto-Maestre, Imbuluzqueta, *et al*., 2017; Schuller *et al*., 2015), only some reports (Betts, 2011; Muñoz-Sánchez *et al*., 2017) show the influence of the method on measuring thermal properties, specifically heat capacity. Regarding the synthesis method typically used for the preparation of nanofluids based on molten salts, the most common is the two-step method, the well-known *dissolution method*, which includes water as a dispersion medium in the process. For this reason, recent research has focused on improving the method by making some modifications without affecting the thermal properties of the nanofluid (Chen *et al*., 2019; Chieruzzi *et al*., 2017b; Navarrete *et al*., 2020). In this vein, different proposed methods including the ball mill dry method and a spray drying method were evaluated by Navarrete *et al*. (2020). Similarly, Chieruzzi *et al*. (2017b) determined an increase in the specific heat capacity of up to 18,6% with 1 wt.% of SiO_2-Al_2O_3 in Solar Salt at high temperatures using a twin-screw micro-compounder. None of these reports used commercial HITEC salt as base salt, and they do not propose an entirely new synthesis method.

Therefore, considering the importance of developing new synthesis methods as well as the current controversy regarding the most suitable method to measure the specific heat capacity (Cp) of molten salt, especially with nanoparticles that are molten salt-based nanofluids (MSBNFs), this work focuses on contributing to the understanding of this property, mainly concerning the commercial molten HITEC salt in comparison with MSBNFs with 0,5, 1,0, and 1,5 wt.%. Alumina nanoparticles were synthesized by means of a new two-step method. The specific heat capacity was evaluated with both scanning differential calorimetry (DSC) according to the ASTM E1269 (ASTM International, 2011) and modulated scanning differential calorimetry (MDSC) according to the ASTM E2716 (ASTM International, 2015). On the other hand, the melting temperature was measured via DSC, and the thermal stability with and without nanoparticles was evaluated through thermogravimetric analysis (TGA).

Materials and methods

Synthesis

Synthesis of ternary nitrate salt (*HITEC*)

Sodium nitrate (AR ≥ 99,5% purity, Millipore Corporation), sodium nitrite, and potassium nitrate (AR ≥ 99,0% purity, Millipore Corporation) were selected to prepare the eutectic ternary nitrate salt known as HITEC. The eutectic composition in the $NaNO_3$-$NaNO_2$-KNO_3 ternary salt system was synthesized by means of weighted amounts of 7, 40, and 53 mol.%, respectively, and mixing them uniformly in a mortar. The mixtures were then heated in a furnace at a constant heating rate of 5 °C/min from room temperature to 150 °C and held for 1 h until complete fusion was achieved to form the eutectic salts. After that, a heating rate of 3 °C/min to 270 °C and holding for 48 h were used to eliminate the water in the mixture. Finally, two heating and cooling cycles were carried out in a furnace in order to ensure homogeneity in the mixture. Finally, the molten salts were cooled rapidly and pulverized for future experiments.

Synthesis of molten salt-based nanofluids (*MSBNFs*)

To obtain a homogenous mixture between the molten salt and the alumina nanoparticles, a new synthesis method of the nitrate-nitrites molten salt-based nanofluids was developed. Hence, after moisture elimination over 48 h at 270 °C in a furnace, the HITEC molten salt was homogenized and pulverized using a mortar for 20 min and an Emax high-energy mill for 15 min at 300 rpm. Next, the pulverized molten salt was mixed with the alumina nanoparticles (0,5, 1,0, and 1,5 wt.%), which had been previously suspended in butanol and sonicated for at least one hour, using magnetic agitation for 15 min. Finally, the mixture was subjected to two heating and cooling cycles in order to ensure the homogeneity of the MSBNFs and the complete elimination of butanol, using cycles between 160 and 270 °C with 1 h holds. Figure 1 presents the new synthesis method, and Table 1 shows some thermal properties of HITEC and alumina.

Characterization

Transmission electron microscopy (*TEM*)

The size and shape of alumina nanoparticles were observed with an electron transmission microscope (Tecnai F20 Super

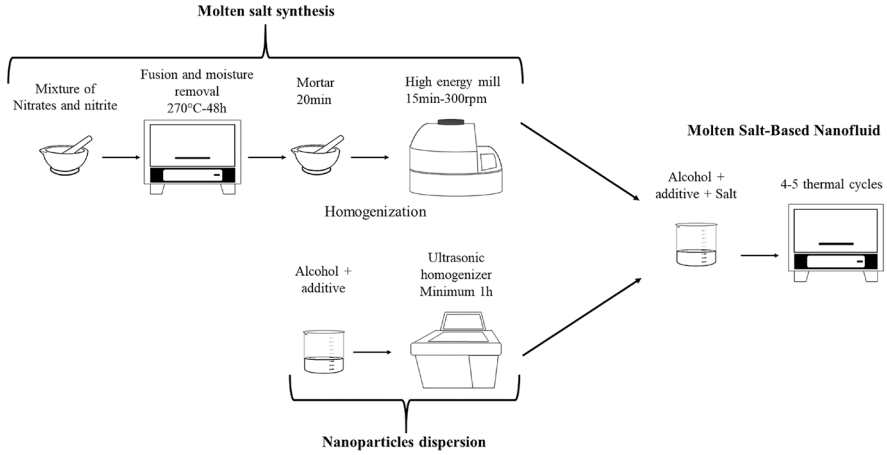

Figure 1. Synthesis method
Source: Authors

Twin, with a field emission source and a resolution of 0,1 nm in 200 Kv TMP). Considering the low solubility of alumina in butanol, the particles were dispersed in it. Then, an aliquot was placed on a copper grid (Lacey carbon mesh 200) and heated long enough to ensure solvent elimination.

Table 1. Thermal properties of HITEC and alumina

Property	HITEC	Alumina
Melting point (˚C)	145,75	2 050 2 072**
Heat capacity (J / g.℃) at 300 ˚C	1,51	0,79
Thermal conductivity (W/m K)	0,2* (at 300˚C)	16,7 (at 306,5˚C)***

* (Vignarooban *et al*., 2015)
** (Larche, 1945)
*** (Myers *et al*., 2016)
Source: Authors

Structural analysis by scanning electron microscopy (SEM)

The samples were fixed on graphite tape, and a thin gold coating (Au) was made using DENTON VACUUM Desk IV equipment. The analysis was performed in a high-vacuum scanning electron microscope (JEOL JSM 6490 LV) to obtain high-resolution images. A secondary electron detector was used to evaluate the morphology and topography of the samples. The elemental analysis was carried out by energy-dispersive X-ray spectroscopy (EDS; INCA PentaFETx3, Oxford Instruments). SEM images were taken from the pristine alumina and the MSBNFs after the DSC and MDSC measurements in order to verify the presence of the nanoparticles inside the molten salt, as well as to evaluate the agglomeration.

Differential scanning calorimetric (DSC) analysis

The melting point of the base fluid and the MSBNFs was measured using a differential scanning calorimeter (Q200, TA Instruments, Inc.). An aluminum Tzero hermetic pan/lid (TA instruments) was used to place the samples in the DSC under a nitrogen atmosphere, and these were analyzed using TA Universal Analyzer 2000, version 4,5 A. The weighting amount for each mixture was around 20 mg for both the base fluid and the MSBNFs. The measurement started at room temperature and increased linearly by 10 ˚C/min up to 400 ˚C, reaching equilibrium at 40 ˚C. The test had a sampling interval every 0,10 s/pt, and two heating and cooling runs were performed to obtain a homogeneous result.

The specific heat capacity of HITEC molten salt and the MSBNFs was measured using two different methods. The first method involved using the traditional differential scanning calorimeter (DSC; Q200, TA Instrument, Inc.) according to the ASTM E1269 standard (ASTM International, 2011). The samples were heated to 250 ˚C and held at this temperature for 5 min in order to obtain a stable heat flux signal, after which they were again heated to 350 ˚C at a rate of 20 ˚C/min. The specific heat of the sample was obtained according to (1), where m_{ref} and m_{Sample} are the standard reference and sample masses, respectively:

$$C_{p,\,sample} = \frac{Q_{sample} - Q_0}{Q_{ref} - Q_0} \cdot \frac{m_{ref}}{m_{sample}} \cdot C_{p,ref} \quad (1)$$

As a second method to measure the Cp of all samples, which involved the modulated differential scanning calorimeter (MDSC), was used according to the ASTM E2716 standard (ASTM International, 2015), with the same equipment used for the DSC analysis. This kind of method uses a sinusoidal temperature oscillation instead of the traditional linear ramp, which simultaneously provides the heat capacity of the sample and the heat flow. The sample was heated to 250 ˚C and held at this temperature for 5 min in order to obtain a stable heat flux signal. After that, the amplitude was ± 0,50 ˚C every 130 s. Finally, the sample was heated again

to 350 ˚C at 2 ˚C/min. The temperature evaluated regarding the specific heat capacity for both methods was 300 ˚C, as it is the temperature at which the salt is commonly maintained in parabolic trough plants.

Thermogravimetric analysis

The thermal stability of pure eutectic salt and the MSBNFs was determined by thermogravimetric analysis (TGA; Q500, TA Instruments, Inc.) under a constant stream of nitrogen at a flow rate of 50 ml/min, a temperature ramp of 15˚C/min in the range 25-800 ˚C, and an isotherm for 5 min. A platinum crucible was used, with weights between 7 and 10 mg for both the HITEC salt and the nanofluid.

Results

Morphology of alumina

The alumina used to synthesize the MSBNFs was obtained from clay minerals by means of an acid leaching process, followed by alkaline precipitation and an acidification process, to finally calcine and obtain mainly delta-gamma alumina with 98,5% purity. The complete procedure was reported by Botero *et al*. (2020). Figure 2a and 2b show the SEM and TEM images of the pristine alumina nanoparticles used to elaborate the MSBNFs, respectively, and Figure 2c shows the size distribution (average size of 5,1 nm). The regular shape can be observed in the SEM and TEM images.

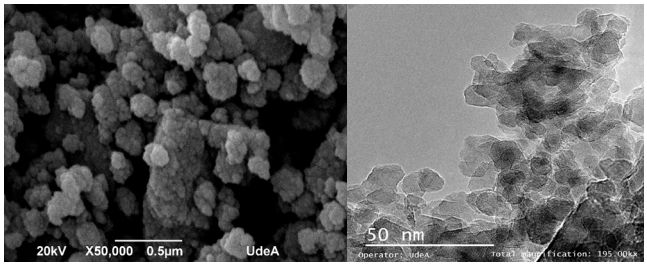

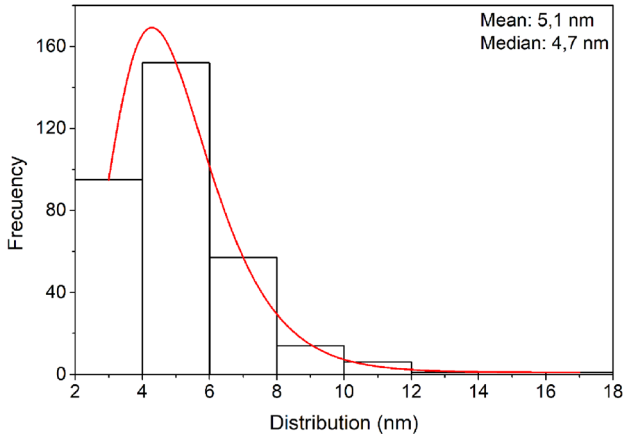

Figure 2. Pristine alumina nanoparticles are used to elaborate the MSBNFs: a) SEM image, b) TEM image, and c) the size distribution
Source: Authors

Thermal stability

The results of the TGA experiments are summarized in Table 2 and Figure 3. In order to evaluate the thermal stability of both the molten salt HITEC and the MSBNFs with 0,5, 1,0, and 1,5 wt.% of alumina nanoparticles, the maximum stability temperature criterion was used when 3% of the overall weight had been lost (Villada *et al*., 2019), whereby a temperature of 300 ˚C was chosen as the initial temperature at which the mass loss started. Based on this criterion, the thermal stability of HITEC salt under the N_2 atmosphere was 626,48 ˚C, which is higher than the results reported in the literature (about 454 ˚C, with a maximum of 535-538 ˚C) (Chen *et al*., 2018), whereas the thermal stability for the MSBNFs was higher than 636 ˚C. The discrepancies in the thermal stability of pure HITEC salt have been explained by Villada *et al*. (2018), and, in order to prevent the conversion of nitrite ions into nitrate ones, HITEC salt should be in an oxygen-free atmosphere. As it can be observed, pure HITEC salt and MSBNFs exhibit a similar decomposition behavior, with a slight increase in the maximum temperature of up to 2% with 1,5 wt.% of alumina nanoparticles. This behavior, together with the reduced melting point, extends the working temperature range of the material, which makes the resulting mixture of potential interest for CSP applications.

Table 2. TGA results for HITEC and MSBNFs with 0,5, 1,0, and 1,5 wt.% of alumina nanoparticles under a nitrogen atmosphere

Sample	Thermal decomposition (˚C)	Change percentage (%)
HITEC (H)	626,48	-
H+0,5% Al_2O_3	636,12	1,54
H+1,0% Al_2O_3	636,93	1,67
H+1,5% Al_2O_3	639,02	2,00

Source: Authors

Melting temperature

The melting temperature values of the HITEC molten salt and the MSBNFs were obtained via DSC. Two heating and cooling runs were carried out to avoid discrepancies in the melting temperature produced by the hygroscopic property of some nitrates. The first cycle was performed to achieve the perfect incorporation of the mixture, and the results from this sequence were not considered. The other cycle was analyzed, and the data from these runs are reported in Table 3.

onsidering previous reports made by Gimenez and Fereres (2015) and Mohammad *et al*. (2017), the heating rate affects the onset of melting, as well as the height and width of the peaks and transition enthalpies. As both the base molten salt (HITEC) and the nanofluids with the different alumina nanoparticle concentrations are not pure materials, the melting temperature of the sample is taken as the endset temperature of the main endothermic peak at the DSC curve

(Bonk *et al.*, 2018). Therefore, according to the literature, the melting point corresponding to the HITEC salt was 145,75 ˚C (Coastal Chemical Co. LLC, 2009; Fernández *et al.*, 2015), and the endset point was 149,82 ˚C.

Table 3. Melting point of HITEC and MSBNFs with 0,5, 1,0, and 1,5 wt.% alumina nanoparticles

Sample	Melting point (˚C)	Onset (˚C)	Endset (˚C)
HITEC (H)	145,75	139,37	149,82
H+0,5% Al_2O_3	145,42	137,13	148,88
H+1,0% Al_2O_3	140,90	133,61	147,83
H+1,5% Al_2O_3	140,52	133,31	147,41

Source: Authors

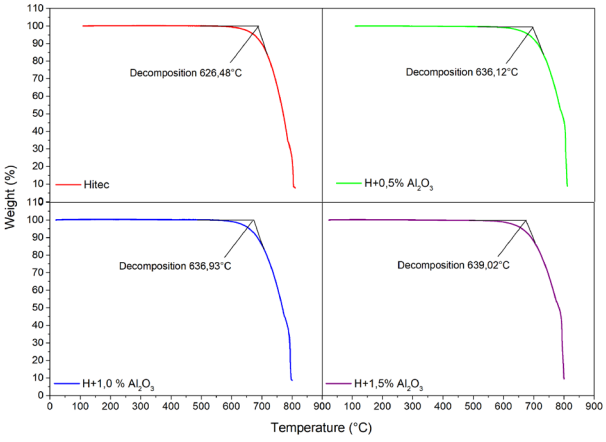

Figure 3. Decomposition temperature under N_2 atmosphere of the pure HITEC salt and the MSBNFs with 0,5, 1,0 and 1,5 wt.% of alumina nanoparticles
Source: Authors

The increase from 0,5 to 1,5 wt.% of alumina leads to a reduction of the onset, endset, and melting point temperatures. This effect was observed in all three concentrations under study, but it was more evident for 1,5 wt.% of nanoparticles (up to 3,6% compared to the base salt mixture). However, this behavior does not correspond to the reports of some authors (Chieruzzi *et al.*, 2013), in which there is a higher enhancement of the thermal properties of the molten salt with 1,0 wt.% and thermal properties start to be negatively affected with a greater amount of nanoparticles. In particular, the onset temperature decreased when Al_2O_3 was added. This means that the phase change occurs at a lower temperature in comparison with the base salt, which is a clear advantage for applications in CSP plants.

Specific heat capacity

The specific heat capacity of the MSBNFs synthesized with HITEC as a base fluid and alumina nanoparticles with a nominal size of 5,1 nm in three different proportions (0,5, 1,0, and 1,5 wt.%) was determined by two different methods: traditional differential scanning calorimetry (DSC) according to the ASTM E1269 standard (ASTM International, 2011) and modulated differential scanning calorimetry (MDSC) according to ASTM E2716 (ASTM International, 2015). The results shown in Table 4 correspond to the Cp values at 300 ˚C, a temperature chosen since it is a normal operating temperature in parabolic trough collectors at the point where the salt is completely melted and without any water content.

Table 4. Heat capacity results in DSC and MDSC

Sample	Heat Capacity (J/g ˚C)			
	DSC	Relative error	MDSC	Relative error
HITEC (H)	1,510	0,0871	1,510	0,0164
H+0,5% Al_2O_3	1,506	0,1817	1,549	0,0563
H+1,0% Al_2O_3	1,508	0,1097	1,577	0,1192
H+1,5% Al_2O_3	1,499	0,0670	1,565	0,0924

Source: Authors

To compare both methods and consider the ASTM E1269 and ASTM E2716 standards, Table 4 reports the average of three different measurements of the same sample, ensuring that the mass loss in every measure does not exceed 0,3% of the initial mass. Therefore, the average deviation is small compared to what is normally reported in the literature. In this way, the result obtained by HITEC commercial salt (1,51 J/g˚C at 300 ˚C) was consistent with the value reported by Kearney *et al.* (2002). On the other hand, the good sensitivity and low uncertainty of the MDSC method reported by Muñoz-Sánchez *et al.* (2017) are also demonstrated in this research.

It should be noted that the weighted amount for each measurement performed was 20 mg in order to ensure that, once melted, the sample remained at the center of the crucible, thus establishing good contact between the sample and the sensor throughout the test (Muñoz-Sánchez *et al.*, 2017). As shown in Table 4, the specific heat capacity of the MSBNFs evaluated through the MDSC method increased along with the proportion of nanoparticles: up to 4,56% with 1 wt.% of Al_2O_3, showing a limit close to 1 wt.% of nanoparticles, with a slight reduction of Cp with 1,5 wt.% of alumina. This behavior has been demonstrated with other kinds of nanofluids, particularly with commercial Solar Salt as base fluid (Awad *et al.*, 2018; Hu *et al.*, 2019). On the other hand, this effect is not so obvious when using standard DSC, where a similar increase in Cp was obtained for all the percentages of nanoparticles evaluated, with a maximum increase up to 0,53% with 1,0 wt.%. Furthermore, it is important to highlight that both methods were not applied

at the same heating rate because the norm for the traditional method was followed. However, this difference in speed can lead to the MDSC method being more sensitive than the traditional DSC.

The low increases in Cp obtained in this study compared to those reported by other authors may be due to several reasons. Firstly, the employed alumina was not 100% pure, and some studies have reported that impurities in the base salts can affect the thermophysical properties of the MSBNFs (Muñoz-Sánchez *et al.*, 2017; Muñoz-Sánchez *et al.*, 2018). The impurities within the alumina can also have a negative effect on the Cp of the MSBNFs, which is why this method must be verified with 100% pure alumina. Secondly, the size of the alumina was less than what is commonly used, although some authors have indicated that nanoparticle size is not a determining factor for the Cp value (Seo and Shin, 2016; Tiznobaik and Shin, 2013), while others indicate that the Cp is higher with larger nanoparticles (Dudda and Shin, 2013; Lu and Huang, 2013). However, the specific heat has been demonstrated to depend on the specific surface available, and thus on the size of the agglomerates formed during the production of the MSBNFs, as indicated by Andreu-Cabedo *et al.* (2014). It should be noted that the size of the agglomerates depends on the synthesis method, which may imply that the improvement in the specific heat may be due to the formation of agglomerates attributed to the use of butanol, which, together with the high heating rate of the DSC method, does not lead to an apparent improvement, although it is possible to observe using the MDSC method at a lower heating rate.

Finally, the new method is presented –which is used for the first time– in which the nanoparticles are dispersed by butanol. This process must be optimized and thoroughly evaluated in order to understand its repercussions. However, the increase of up to 4,56% in Cp shows that the method is suitable for use in the synthesis of MSBNFS for thermal storage, with the purpose of improving the efficiency of TES systems.

Considering the direct relationship between the behavior of the specific heat capacity with the phase and structure of the material, SEM was used to perform the microstructural analysis of both the HITEC pure molten salt and the MSBNFs. In the same way, the analysis of the degree of dispersion of nanoparticles in the molten salt after the Cp evaluation using both the DSC and MDSC methods was carried out using SEM. Figure 4 shows the SEM images of the commercial HITEC molten salt, and Figure 5 shows the SEM images of the MSBNFs, with 5a, 5b, and 5c being the samples evaluated by DSC, and 5d, 5e, and 5f corresponding to the samples evaluated by MDSC.

However, neither the interconnecting network of nanoparticles nor the needle-like structure were observed in the nanofluids, factors reported by other authors as the possible cause of Cp enhancement with nanoparticles (Shin and Banerjee, 2014; Song *et al.*, 2018). At the same time,

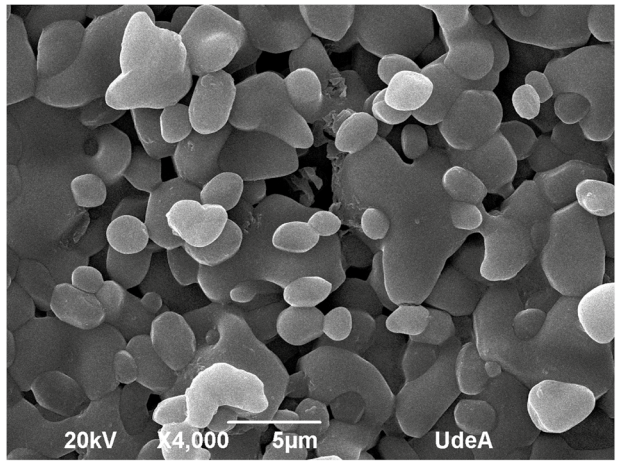

Figure 4. SEM Images of pure commercial HITEC salt
Source: Authors

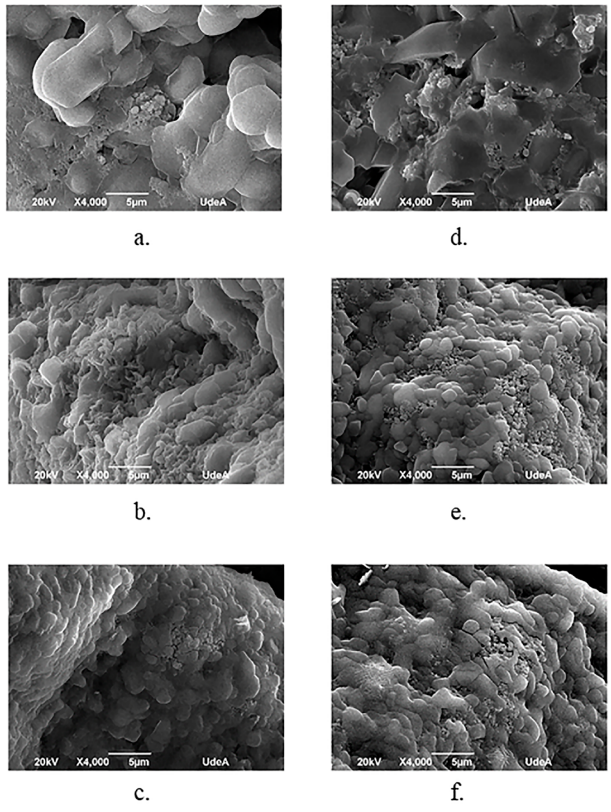

Figure 5. SEM images after DSC and MDSC evaluation. a, b, and c represent samples that were evaluated by DSC with 0,5, 1,0, and 1,5 wt.% of alumina nanoparticles, respectively; and d, e, and f are samples evaluated by MDSC with 0,5, 1,0, and 1,5 wt.% of alumina nanoparticles, respectively.
Source: Authors

other authors have reported an enhancement in specific heat capacity in the absence of a particular network, which may be due to the fact that Cp is a structure-insensitive property (Chieruzzi *et al.*, 2017a; Myers *et al.*, 2016). Thus, it can be stated that these structures are not the only factors affecting the increment of the specific heat capacity,

and it is therefore necessary to evaluate other factors that may explain the specific heat increase. By comparing the SEM images of the base HITEC (Figure 4) with the MSBNFs evaluated by DSC and MDSC (Figure 5), it is possible to observe a reduction in the grain size as the proportion of nanoparticles within it increases and the salt coalesces. It could be said that the nanoparticles are fulfilling the role of a nucleating agent. This could be linked to the increase in Cp of the MSBNFs. A similar behavior has been reported by other authors (Ho and Pan, 2014).

It is important to highlight that the microstructure of the MSBNFs is independent of the technique used to evaluate the specific heat capacity, be it DSC or MDSC. A similar morphology was also observed by other authors in a similar type of nanofluid (Chieruzzi *et al*., 2017a). Additionally, this method has the advantage of replacing the water with butanol, thus reducing the time of evaporation, and ensuring a good suspension of the nanoparticles in the alcohol before they mix with the molten salt. Possible explanations for this behavior could be the use of high-energy milling at 300 rpm for 15 minutes, which ensures good homogeneity of the molten salt and good suspension of the nanoparticles in the butanol before mixing with the molten salt; and thermal cycling, which ensures good homogeneity in the final mixture.

Conclusions

In this study, a two-step method which replaces water with butanol and uses an Emax high-energy mill to prepare molten salt-based nanofluids is proposed. HITEC molten salt was used as the base fluid with different mass fractions of Al_2O_3 nanoparticles. The thermal properties, namely melting point, specific heat capacity, and thermal stability, of the commercial molten salt and the MSBNFs were experimentally tested. The conclusions obtained are presented in this section.

According to the results, it was possible to demonstrate the viability of the synthesis of the molten salt-based nanofluids through the aforementioned method, as evidenced in the increase in specific heat capacity of up to 0,53% when measured by DSC and of 4,57% when evaluated by MDSC for 1,0 wt.% of alumina nanoparticles. The thermal stability was not affected and a melting point reduction was obtained for this sample. Similarly, a good distribution of the nanoparticles was evident in all mass fractions of alumina, especially in 1,0 wt.%, which showed a Cp higher than the other compositions evaluated. Hence, it may be stated that a better distribution of smaller aggregates tends to be correlated with an increase in specific heat capacity.

The specific heat capacity (Cp) values of both the HITEC commercial molten salt and the nanofluids were evaluated by two different methods: traditional differential scanning calorimetry (DSC) and modulated differential scanning calorimetry (MDSC). The enhancement percentage measured by the DSC method with all proportions of nanoparticles was not significant in comparison with the Cp of the pure HITEC salt. This behavior could indicate that there is no effect caused by the addition of this type of nanoparticle, which contradicts recent studies. On the other hand, the MDSC method showed a greater variation in the enhancement percentage, thus indicating that there is a positive effect attributable to the nanoparticles, in addition to a greater sensitivity of this technique to small changes in the sample, especially in non-homogeneous samples such as nanofluids. This establishes the contribution of the two phases that make up the nanofluid, the molten salt as the base fluid and the solid nanoparticles. For this reason, the MDSC technique could be more appropriate for measuring this property in this type of sample. Similarly, the heating rate used in each of the techniques can influence the sensitivity to determine changes in nanofluids.

The good distribution of the nanoparticles, together with an increase in specific heat capacity without affecting thermal stability and a reduction in the melting point, demonstrate that the proposed two-step method is viable for manufacturing molten salt-based nanofluids while avoiding the use of water and therefore its subsequent elimination, thus reducing costs and production times, without having a great influence on the dispersion and homogenization of the nanofluid. Hence, the storage capacity of the nanofluid is increased to improve the thermal storage systems of CSP plants.

Acknowledgments

The authors, particularly Marllory Isaza-Ruiz, are grateful for the financial support provided through Doctoral Grant number 727–2015 by means of the Ministry of Science, Technology, and Innovation [*Ministerio de Ciencia, Tecnología e Innovación, Minciencias*].

References

Andreu-Cabedo, P., Mondragón, R., Hernández, L., Martínez-Cuenca, R., Cabedo, L., and Julia, J. E. (2014). Increment of specific heat capacity of solar salt with SiO_2 nanoparticles. *Nanoscale Research Letters*, 9(1), 582. https://doi.org/10.1186/1556-276X-9-582

ASTM International (2011). *E1269: Standard test method for determining specific heat capacity by differential scanning*. ASTM International. https://doi.org/10.1520/E1269-11.2

ASTM International (2015). *E2716-09: Standard test method for determining specific heat capacity by sinusoidal modulated temperature differential scanning calorimetry*. ASTM International. https://doi.org/10.1520/E2716-09R14.2

Awad, A., Navarro, H., Ding, Y., and Wen, D. (2018). Thermal-physical properties of nanoparticle-seeded nitrate molten salts. *Renewable Energy*, *120*, 275-288. https://doi.org/10.1016/j.renene.2017.12.026

Betts, M. R. (2011). *The effects of nanoparticle augmentation of nitrate thermal storage materials for use in concentrating solar power applications* [Master's thesis, Texas A&M University]. https://hdl.handle.net/1969.1/ETD-TAMU-2011-05-9118

Bonk, A., Sau, S., Uranga, N., Hernaiz, M., and Bauer, T. (2018). Advanced heat transfer fluids for direct molten salt line-focusing CSP plants. *Progress in Energy and Combustion Science*, *67*, 69-87. https://doi.org/10.1016/j.pecs.2018.02.002

Botero, Y. L., López-Rendón, J. E., Ramírez, D., Zapata, D. M., and Jaramillo, F. (2020). From clay minerals to Al2O3 nanoparticles: Synthesis and colloidal stabilization for optoelectronic applications. *Minerals*, *10*(2), 118. https://doi.org/10.3390/min10020118

Chen, X., Wu, Y. ting, Zhang, L. di, Wang, X., and Ma, C. fang. (2018). Experimental study on the specific heat and stability of molten salt nanofluids prepared by high-temperature melting. *Solar Energy Materials and Solar Cells*, *176*, 42-48. https://doi.org/10.1016/j.solmat.2017.11.021

Chen, X., Wu, Y. ting, Zhang, L. di, Wang, X., and Ma, C. fang. (2019). Experimental study on thermophysical properties of molten salt nanofluids prepared by high-temperature melting. *Solar Energy Materials and Solar Cells*, *191*, 209-217. https://doi.org/10.1016/j.solmat.2018.11.003

Chieruzzi, M., Cerritelli, G. F., Miliozzi, A., and Kenny, J. M. (2013). Effect of nanoparticles on heat capacity of nanofluids based on molten salts as PCM for thermal energy storage. *Nanoscale Research Letters*, *8*(1), 448. https://doi.org/10.1186/1556-276X-8-448

Chieruzzi, M., Cerritelli, G. F., Miliozzi, A., Kenny, J. M., and Torre, L. (2017a). Heat capacity of nanofluids for solar energy storage produced by dispersing oxide nanoparticles in nitrate salt mixture directly at high temperature. *Solar Energy Materials and Solar Cells*, *167*, 60-69. https://doi.org/10.1016/j.solmat.2017.04.011

Chieruzzi, M., Cerritelli, G. F., Miliozzi, A., Kenny, J. M., and Torre, L. (2017b). Heat capacity of nanofluids for solar energy storage produced by dispersing oxide nanoparticles in nitrate salt mixture directly at high temperature. *Solar Energy Materials and Solar Cells*, *167*, 60-69. https://doi.org/10.1016/j.solmat.2017.04.011

Coastal Chemical Co. LLC. (2009). *HITEC ® Heat Transfer Salt*. http://www.skyscrubber.com/MSR%20-%20HITEC%20Heat%20Transfer%20Salt.pdf

Dudda, B., and Shin, D. (2013). Effect of nanoparticle dispersion on specific heat capacity of a binary nitrate salt eutectic for concentrated solar power applications. *International Journal of Thermal Sciences*, *69*, 37-42. https://doi.org/10.1016/j.ijthermalsci.2013.02.003

Fernández, A. G., Galleguillos, H., Fuentealba, E., and Pérez, F. J. (2015). Thermal characterization of HITEC molten salt for energy storage in solar linear concentrated technology. *Journal of Thermal Analysis and Calorimetry*, *122*(1), 3-9. https://doi.org/10.1007/s10973-015-4715-9

Gimenez, P., and Fereres, S. (2015). Effect of heating rates and composition on the thermal decomposition of nitrate based molten salts. *Energy Procedia*, *69*, 654-662. https://doi.org/10.1016/j.egypro.2015.03.075

Ho, M. X., and Pan, C. (2014). Optimal concentration of alumina nanoparticles in molten hitec salt to maximize its specific heat capacity. *International Journal of Heat and Mass Transfer*, *70*, 174-184. https://doi.org/10.1016/j.ijheatmasstransfer.2013.10.078

Ho, M. X., and Pan, C. (2017). Experimental investigation of heat transfer performance of molten HITEC salt flow with alumina nanoparticles. *International Journal of Heat and Mass Transfer*, *107*, 1094-1103. https://doi.org/10.1016/j.ijheatmasstransfer.2016.11.015

Hu, Y., He, Y., Zhang, Z., and Wen, D. (2017). Effect of Al2O3 nanoparticle dispersion on the specific heat capacity of a eutectic binary nitrate salt for solar power applications. *Energy Conversion and Management*, *142*, 366-373. https://doi.org/10.1016/j.enconman.2017.03.062

Hu, Y., He, Y., Zhang, Z., and Wen, D. (2019). Enhanced heat capacity of binary nitrate eutectic salt-silica nanofluid for solar energy storage. *Solar Energy Materials and Solar Cells*, *192*, 94-102. https://doi.org/10.1016/j.solmat.2018.12.019

Kearney, D., Herrmann, U., Nava, P., Kelly, B., Mahoney, R., Pacheco, J., Cable, R., Potrovitza, N., Blake, D., and Price, H. (2002). Assessment of a molten salt heat transfer fluid in a parabolic trough solar field. *Journal of Solar Energy Engineering*, *125*(2), 170-176. https://doi.org/10.1115/1.1565087

Larche, F. C. (1945). Melting point of alpha-alumina. *Journal of the Franklin Institute*, *139*(5), 406. https://www.sciencedirect.com/science/article/abs/pii/0016003245900238

Lu, M.-C., and Huang, C.-H. (2013). Specific heat capacity of molten salt-based alumina nanofluid. *Nanoscale Research Letters*, *8*(1), 292. https://doi.org/10.1186/1556-276X-8-292

Mohammad, M. Bin, Brooks, G. A., and Rhamdhani, M. A. (2017). Thermal analysis of molten ternary lithium-sodium-potassium nitrates. *Renewable Energy*, *104*, 76-87. https://doi.org/10.1016/j.renene.2016.12.015

Muñoz-Sánchez, B., Nieto-Maestre, J., Guerreiro, L., Julia, J. E., Collares-Pereira, M., and García-Romero, A. (2017). Molten salt based nanofluids based on solar salt and alumina nanoparticles: An industrial approach. *AIP Conference Proceedings*, *1850,* 080016. https://doi.org/10.1063/1.4984437

Muñoz-Sánchez, B., Nieto-Maestre, J., Imbuluzqueta, G., Marañón, I., Iparraguirre-Torres, I., and García-Romero, A. (2017). A precise method to measure the specific heat of solar salt-based nanofluids. *Journal of Thermal Analysis and Calorimetry*, *129*(2), 905-914. https://doi.org/10.1007/s10973-017-6272-x

Muñoz-Sánchez, B., Nieto-Maestre, J., Veca, E., Liberatore, R., Sau, S., Navarro, H., Ding, Y., Navarrete, N., Juliá, J. E., Fernández, A. G., and García-Romero, A. (2018). Rheology of Solar-Salt based nanofluids for concentrated solar power. Influence of the salt purity, nanoparticle concentration, temperature and rheometer geometry. *Solar Energy Materials and Solar Cells*, *176*, 357-373. https://doi.org/10.1016/j.solmat.2017.10.022

Myers, P. D., Alam, T. E., Kamal, R., Goswami, D. Y., and Stefanakos, E. (2016). Nitrate salts doped with CuO nanoparticles for thermal energy storage with improved heat transfer. *Applied Energy*, *165*, 225-233. https://doi.org/10.1016/j.apenergy.2015.11.045

Navarrete, N., Hernández, L., Vela, A., and Mondragón, R. (2020). Influence of the production method on the thermophysical properties of high temperature molten salt-based nanofluids. *Journal of Molecular Liquids*, *302,* 112570. https://doi.org/10.1016/j.molliq.2020.112570

REN21 (2021). *Renewables 2021 Global Status Report*. https://abdn.pure.elsevier.com/en/en/researchoutput/ren21(-5d1212f6-d863-45f7-8979-5f68a61e380e).html

Schuller, M., Shao, Q., and Lalk, T. (2015). Experimental investigation of the specific heat of a nitrate-alumina nanofluid for solar thermal energy storage systems. *International Journal of Thermal Sciences*, *91*, 142-145. https://doi.org/10.1016/j.ijthermalsci.2015.01.012

Seo, J., and Shin, D. (2016). Size effect of nanoparticle on specific heat in a ternary nitrate ($LiNO_3$-$NaNO_3$-KNO_3) salt eutectic for thermal energy storage. *Applied Thermal Engineering*, *102*, 144-148. https://doi.org/10.1016/j.applthermaleng.2016.03.134

Serrano-López, R., Fradera, J., and Cuesta-López, S. (2013). Molten salts database for energy applications. *Chemical Engineering and Processing*, *73*, 87–102. https://doi.org/10.1016/j.cep.2013.07.008

Shin, D., and Banerjee, D. (2014). Specific heat of nanofluids synthesized by dispersing alumina nanoparticles in alkali salt eutectic. *International Journal of Heat and Mass Transfer*, *74*, 210-214. https://doi.org/10.1016/j.ijheatmasstransfer.2014.02.066

Song, W., Lu, Y., Wu, Y., and Ma, C. (2018). Effect of SiO_2 nanoparticles on specific heat capacity of low-melting-point eutectic quaternary nitrate salt. *Solar Energy Materials and Solar Cells*, *179*, 66-71. https://doi.org/10.1016/j.solmat.2018.01.014

Tiznobaik, H., and Shin, D. (2013). Enhanced specific heat capacity of high-temperature molten salt-based nanofluids. *International Journal of Heat and Mass Transfer*, *57*(2), 542548. https://doi.org/10.1016/j.ijheatmasstransfer.2012.10.062

Vignarooban, K., Xu, X., Arvay, A., Hsu, K., and Kannan, A. M. (2015). Heat transfer fluids for concentrating solar power systems - A review. *Applied Energy*, *146*, 383-396. https://doi.org/10.1016/j.apenergy.2015.01.125

Villada, C., Bonk, A., Bauer, T., and Bolívar, F. (2018). High-temperature stability of nitrate/nitrite molten salt mixtures under different atmospheres. *Applied Energy, 226,* 107-115. https://doi.org/10.1016/j.apenergy.2018.05.101

Villada, C., Jaramillo, F., Castaño, J. G., Echeverría, F., and Bolívar, F. (2019). Design and development of nitrate-nitrite based molten salts for concentrating solar power applications. *Solar Energy*, *188*, 291-299. https://doi.org/10.1016/j.solener.2019.06.010

Zhang, S., Wu, W., and Wang, S. (2017). Integration highly concentrated photovoltaic module exhaust heat recovery system with adsorption air-conditioning module via phase change materials. *Energy*, *118*, 1187-1197. https://doi.org/10.1016/j.energy.2016.10.139

Research Article/Mechanical Engineering, Mechatronics, and Materials Science http://doi.org/10.15446/ing.investig.87275

Analysis and Discussion of Two-Way Coupling Effects in Particle-Laden Turbulent Channel Flow

Análisis y discusión de los efectos del acople de dos vías en el flujo turbulento de un canal cargado con partículas

Santiago Laín[1], Daniel Ortíz[2], Jesús A. Ramírez[3], and Carlos A. Duque[4]

ABSTRACT

This paper studies the turbulence modification caused by the presence of solid particles in fully developed channel flow by means of the point particle Direct Numerical Simulations (DNS) approach. Inertial particles much smaller than the smallest vortical flow structures are considered, maintaining a volume fraction of the order 10^{-4}, where inter-particle collisions are rare and have nearly no influence on flow development. To avoid concurrent effects that could mask the analysis of fluid-turbulence interaction, gravity is not included in the study, and particle-smooth wall collisions are modelled as ideal reflections. The alteration of fluid turbulence dynamics by the particles is illustrated and discussed, providing an overview of the fluid-particle interaction phenomena occurring at both microscopic and macroscopic flow levels. Finally, the relation of such phenomena with drag-reducing effects by particles is demonstrated.

Keywords: direct numerical simulation, particle-laden channel flow, turbulence, two-way coupling

RESUMEN

Este artículo estudia la modificación de la turbulencia de la fase portadora debido a la presencia de partículas sólidas en un flujo en canal totalmente desarrollado utilizando la aproximación de Simulación Numérica Directa (DNS) con partículas puntuales. Las partículas inerciales consideradas son mucho más pequeñas que la menor de las estructuras vorticales turbulentas, manteniendo una fracción volumétrica del orden de 10^{-4}, en la cual las colisiones entre partículas son esporádicas y apenas tienen influencia en el desarrollo del flujo. Con el fin de evitar efectos simultáneos que puedan enmascarar el análisis de la interacción fluido-partícula, no se incluyen los efectos gravitatorios en el estudio, y las colisiones partícula-pared lisa se modelan como reflexiones ideales. Se ilustra y discute la alteración de la dinámica turbulenta del fluido por parte de las partículas, proporcionando un panorama de los fenómenos de interacción fluido-partícula a nivel microscópico y macroscópico. Finalmente, se muestra la relación de los fenómenos descritos con los efectos de reducción de arrastre causados por las partículas en el flujo en canal.

Palabras clave: simulación numérica directa, flujo bifásico en canal, turbulencia, acoplo de dos vías

Received: May 13th, 2020
Accepted: May 23th, 2022

Introduction

Turbulent flows laden with droplets and particles are commonly found in nature and industrial processes. Examples of the first are sandstorms, clouds, particle sedimentation in rivers and oceans, among others. The evaporation of liquid drops in spray dryers and particle separation in scrubbers or cyclones are examples of the second. Such turbulent dispersed two-phase flows are investigated from both experimental and numerical approaches. This study employs the numerical perspective.

There are three main numerical approaches to such systems (Kuerten, 2016). The most detailed technique is to fully resolve the flow around the particles, whose motion is computed from the external forces and those exchanged with the carrying fluid. This method needs very fine meshes in order to compute the flow around the particles and is usually restricted to handling a small number of particles. This approach is the most adequate for dealing with particles

[1] Physicist, Mathematician, and PhD in Physical Sciences, Universidad of Zaragoza, Spain. Dr.-Ing. Habil. Martin Luther University Halle-Wittenberg, Germany. Affiliation: PAI+ Group, Fluid Mechanics Professor at Universidad Autónoma de Occidente Cali, Colombia. E-mail: slain@uao.edu.co

[2] Mechanical Engineer, Universidad Autónoma de Occidente, Colombia. Affiliation: Projects Engineer, Fundación Universidad del Valle, Colombia. E-mail: danortiz0@gmail.com

[3] Mechanical Engineer and Master in Industrial Maintenance, Universidad Experimental del Táchira, Venezuela; PhD in Mechanical Engineering, Universidad Nacional de Colombia. Affiliation: Professor at Universidad Santo Tomás, Colombia. E-mail: jesusramirez@usantotomas.edu.co

[4] Mechanical Engineer Universidad Nacional de Colombia; Master in Mechanical Engineering, Universidad de los Andes, Colombia; Ph.D. in Mechanical Engineering, University of Warwick, UK. Affiliation: GNUM Group, Professor at Universidad Nacional de Colombia, Colombia. E-mail: caduqued@unal.edu.co

How to cite: Laín, S., Ortíz, D., Ramírez, J. A., and Duque, C. A. (2023). Analysis and discussion of two-way coupling effects in particle-laden turbulent channel flow. *Ingeniería e Investigación, 43*(1), e87275. http://doi.org/10.15446/ing.investig.87275

larger than the Kolmogorov length scale. If particles are sufficiently smaller than such scale, point-mass Lagrangian approaches are usually employed. In them, each particle motion is governed by its own momentum equation, which is based on Newton's second law. Thus, millions of particles can be tracked in the computational domain. In order to deal with dense flows with many large particles, the continuum or Eulerian approaches are employed. In such methods, particles are described by continuous velocity and concentration fields, whose evolution is described by an adequate set of partial differential equations, which has to be solved in addition to the fluid equations (Lain and Aliod, 2000).

In all these numerical approaches, the description of the turbulent dynamics of the fluid can be handled by means of Direct Numerical Simulations (DNS), Large Eddy Simulations (LES), or Reynolds Averaged Navier Stokes (RANS) equations.

This study focuses on Lagrangian point-particle methods in connection with a DNS description of the turbulent flow as applied to a channel flow configuration. The interaction between the two phases (fluid and particles) can be described using different levels of coupling. The simplest approach involves considering that particles move in the fluid field without influencing it at all. This is called *one-way coupling*, and it is appropriate for a very low particle volume fraction α. For higher values, the effect of particles in the flow dynamics cannot be ignored, and the so-called *two-way coupling* (TWC) has to be considered. Finally, if the particle volume fraction is high enough, direct interactions between the particles affect the fluid and particle variables. This is known as *four-way coupling*.

Some relevant previous studies applying Lagrangian point-particle DNS methods in the configuration of channel flow are briefly reviewed herein. The first one-way coupled simulation in a channel flow using DNS with point particles was carried out by McLaughlin (1989). He considered the deposition of aerosol particles in a configuration with a bulk Reynolds number of 2 000, defined using half of the channel height as a length scale. Based on a pseudo-spectral method, Kontomaris *et al*. (1992) conducted a low-resolution DNS study of particle dispersion in a channel with a bulk Reynolds number of around 9 000. A benchmark point-particle DNS with a friction Reynolds number $Re_\tau = 150$ was performed by Marchioli *et al*. (2008). It involved five different groups, each of them with its own numerical code. Small differences were found in the mean velocity profiles, showing noticeable variations in the fluid and particle fluctuating velocities. Moreover, the dispersion of the results was larger regarding the particle concentration profiles in the near-wall region.

According to Elgobashi (1994), one-way coupling is only appropriate for very low particle volume fraction values: $\alpha \leq 10^{-5}$. Therefore, for higher values, the momentum and turbulence modification by the particles cannot be ignored and has to be considered in the fluid equations, including the force exchanged with the particles. Balachandar and Eaton (2010) complemented Elgobashi's classification (1994) by indicating that, when mass loading (defined as the ratio of particle mass to that of the fluid) is of order one or larger, even when α is still small, the effect of particles on carrier phase dynamics should be taken into account. First, research dealt with homogeneous and isotropic turbulence (Boivin *et al*., 1998), where the fluid turbulent kinetic energy and dissipation rate modification by the particles was studied. They identified the role of particle inertia (Stokes number) and mass loading in the decreasing values of both quantities, and they found that small inertia particles increased the turbulent energy spectra, albeit damped by larger inertia particles. Turbulent channel flow laden with particles while including two-way coupling was numerically studied by Pan and Banerjee (1996) with $\alpha \approx 10^{-4}$. These authors found that, for the same value of α, small particles reduced fluid turbulence, but that large particles increased it. The two-way coupled simulations performed by Zhao *et al*. (2010) in a turbulent channel flow with $Re_\tau = 360$ based on the channel height found that the bulk flow velocity was higher in the case with particles than in the particle free flow, which means that drag was reduced. Moreover, they noticed that particles enhanced the fluid Reynolds stress in the stream-wise direction but damped the components in the spam-wise and wall-normal directions. Finally, these authors observed that the velocity streaks were more regular and longer in the particle-laden flow. The constant mass loading two-coupled channel flow simulations performed by Lee and Lee (2015) at $Re_\tau = 180$ aimed to study the effect of the viscous Stokes number (τ^+) in the turbulence modification. They found that, for very low values of $\tau^+ = 0,5$, particles enhanced fluid turbulence, whereas, for $\tau^+ > 5$, it was suppressed by the presence of particles. Two values of $Re_\tau = 150,395$ were studied by Kuerten *et al*. (2011) in a two-coupled particle-laden channel flow, where also heat transfer effects were considered. They reported that particle concentration near the walls was reduced when two-way coupling was considered, a fact explained by the reduction in fluid fluctuating velocity in the wall-normal direction by the particles.

Moreover, a crucial issue that appears in TWC is estimating the fluid velocity at the particle position (Göz *et al*., 2004) because each particle locally modifies such velocity. This fact is also linked to the momentum coupling between phases. The usual approach, based on interpolation schemes and the particle in cell (PIC) method, was able to provide a qualitatively correct interpretation of the particle-fluid interaction in channel flow. However, it has been demonstrated that it suffers from some drawbacks such as a dependence on the number of available particles per computational cell and difficulties in correctly evaluating the fluid velocity at the particle position, since every single particle locally modifies the fluid velocity. In order to improve the estimation of the fluid velocity at particle position, several strategies have been proposed, such as the Force Coupling Method (FCM) by Maxey and Patel (2001), the Pairwise Interaction Extended Point-Particle (PIEP) approach by Akiki *et al*. (2017), or the Exact Regularized Point Particle (ERPP) approach by Gualtieri

et al. (2015). For instance, in wall-bounded flow, Battista *et al*. (2019) showed that ERPP provided good agreement with experimental results (Righetti and Romano, 2004; Wu *et al*., 2006; Li *et al*., 2012). Ireland and Desjardins (2017) also propose a method within the VFEL (volume filtered Euler-Lagrange) framework for estimating the undisturbed fluid velocity at the position of the particle, which provides accurate results in several theoretical limiting cases.

For values of $\alpha > 10^{-3}$, it is agreed that inter-particle interactions cannot be disregarded, since their effects are noticeable in flow development. Four-way coupled simulations of vertical pipe flow were performed by Vreman (2007). This author studied the effect of mass loading, observing that fluid turbulence decreased as mass loading increased. Vreman also realized that wall roughness modelling was the most important effect influencing the results of the particle phase. Other studies (Li *et al*., 2001; Dritselis and Vlachos, 2008) have found similar results, where the presence of particles suppresses the energy transfer from the span-wise to the transversal (span-wise and wall-normal) directions, enhancing the fluid Reynolds stress anisotropy. Moreover, inter-particle collisions reduce the concentration of particles in the near-wall region, leading to more uniform profiles. In the four-way coupled simulations performed by Vreman (2015) in a channel downward flow at $Re_\tau = 642$, it was found that rough walls improve the turbulence reduction promoted by the particles.

This study considers a particle-laden channel flow at a frictional Reynolds number of 175 and a solid particle volume fraction $\alpha \approx 4\times10^{-4}$. Periodic boundary conditions are applied in both the stream-wise and span-wise directions. The Lagrangian point particle approach is adopted, while the turbulent dynamics of the flow are described by DNS. Variations in the carrier phase variables due to the presence of particles and the modification of the dispersed phase variables given the degree of coupling between the phases are illustrated and discussed.

Summary of the numerical approach

In the particle-laden channel flow, the continuous phase consists of air, which, due to the low velocities considered, can be approximated as an incompressible Newtonian fluid. Therefore, its dynamics are governed by the continuity and Navier-Stokes equations:

$$\nabla \cdot \vec{u} = 0 \tag{1}$$

$$\frac{\partial \vec{u}}{\partial t} + \left(\vec{u}\cdot\nabla\right)\vec{u} = -\frac{1}{\rho}\nabla p + \nu\nabla^2\vec{u} + \vec{F}_p + \prod \delta_{i1} \tag{2}$$

where $\vec{u}$ is the fluid velocity, p the pressure, and ρ,ν are the fluid density and kinematic viscosity, respectively. $\vec{F}_p$ represents the feed-back force that particles exert on the fluid, and $\prod \delta_{i1}$ is the external pressure gradient necessary to keep constant mass flow rate in the channel with periodic boundaries in the stream-wise direction (Capecelatro *et al*., 2018). The particle motion equation is based on Newton's second law, and its trajectory can be built through the following expressions:

$$\frac{d\vec{x}_{pi}}{dt} = \vec{v}_i \tag{3}$$

$$m_i \frac{d\vec{v}_i}{dt} = \sum \vec{F}_i \tag{4}$$

Here, $\vec{x}_{pi}, \vec{v}_i$ denote the position and velocity of particle i, respectively, m_i is its mass, and $\vec{F}_i$ represents the different forces acting on it. For spherical particles, the Maxey and Riley equation (1983) has been well established; it includes drag, gravity-buoyancy, fluid stress, added mass, and Basset history forces. In this study, solid particles of aluminum are considered, which have a density much higher than the air, and gravity is ignored. Under such conditions, the prevalent contribution is the drag force being the rest of the aforementioned negligible forces (Lain and Sommerfeld, 2007; Sommerfeld and Lain, 2015). In this work, the drag force is written as follows:

$$\vec{F}_{Di} = m_i \frac{\vec{u}_i\left(\vec{x}_{pi}, t\right) - \vec{v}_i}{\tau_i}\left(1 + 0{,}15\, Re_i^{0{,}687}\right) \tag{5}$$

where τ_i is the Stokesian particle relaxation time and Re_i is the particle Reynolds number. Both are defined as

$$\tau_i = \frac{\rho_{pi} d_i^2}{18\rho\nu} \qquad Re_i = \frac{\left|\vec{u}_i\left(\vec{x}_{pi}, t\right) - \vec{v}_i\right| d_i}{\nu} \tag{6}$$

with ρ_{pi}, d_i being the particle density and diameter, respectively.

As the considered particle volume fraction is $\alpha \approx 4\times10^{-4}$, the presence of particles affects the turbulent dynamics of the carrier phase. However, the flow is still dilute enough to neglect the effects of inter-particle collisions (Elghobashi, 1994). Therefore, the action of particles on the fluid phase in Equation (2), $\vec{F}_p$, is computed via the method described by Zhao *et al*. (2010).

When dealing with turbulent flows constrained by walls, it is customary to work with non-dimensional numbers based on the so-called *wall units*, which are introduced hereafter. The first variables are the kinematic viscosity ν and the friction velocity u_τ, which is defined as:

$$u_\tau = \sqrt{\frac{\tau_w}{\rho}} \tag{7}$$

where τ_w denotes the wall shear stress. With these two variables, scales of length (δ_ν) and time (τ_ν) can be built as follows:

$$\text{Length} \quad \delta_\nu = \frac{\nu}{u_\tau} \qquad \text{Time} \quad \tau_\nu = \frac{\nu}{u_\tau^2} \tag{8}$$

The bulk and friction Reynolds numbers, Re and Re_τ, are defined in terms of the flow bulk velocity U_b and the friction velocity, as follows:

$$Re = \frac{U_b h}{\nu} \qquad Re_\tau = \frac{u_\tau h}{\nu} \tag{9}$$

with h being half of the channel height. Then, the non-dimensional distance to the wall z^+ and the velocity u^+ are expressed as:

$$z^+ = \frac{z u_\tau}{\nu} \qquad u^+ = \frac{u}{u_\tau} \tag{10}$$

Simulation setup

The turbulent flow developed between two infinite parallel walls in a channel, realized by imposing periodic boundary conditions in the stream-wise and span-wise directions. No-slip conditions were imposed at the walls, which were separated by a distance $2h$ along the wall-normal direction. The length of the domain was $2\pi h$ (stream-wise) and πh (span-wise), as per Dritselis and Vlachos (2008). To avoid concurrent effects that could mask the analysis of fluid-turbulence interaction, gravity effects were not included. The Friction Reynolds number was fixed at $Re_\tau = 175$ in this study.

The employed physical properties of the fluid phase were $p = 1{,}2\ \mathrm{kg/m^3}$ and $\nu = 2\times10^{-5}\ \mathrm{m^2/s}$. The resulting friction velocity of the single-phase flow was $u_\tau = 0{,}035\, m/s$. The semi-height was equal to $175\delta_\nu$, whereas the flow domain comprised $1100\times550\times350$ wall units. Such dimensions were enough to include the expected scales of the largest turbulence structures. The adopted grid resolution was 128^3, and the grid spacing Was uniform in the stream-wise and span-wise directions but stretched in the wall normal direction using a hyperbolic tangent function in the near-wall region. Additionally, the time step employed in the solution of the fluid equations was equal to $0{,}06\tau_\nu$. Both discretizations (spatial and temporal) were appropriate enough to guarantee reliable DNS results. Continuous phase equations were solved via the finite volume solver Fluent v. 17, employing the following numerical discretization schemes: a third-order scheme MUSCL for the convective, a second-order central scheme for the diffusive terms in space, and the implicit second-order scheme for time. Pressure-velocity coupling was handled by the PISO algorithm.

The flow was initialized with the intrinsically unstable velocity field introduced by Schoppa and Hussain (2002), which has been carefully explained by de Villiers (2006). It consists of imposing stream-wise and span-wise perturbations to the fully developed laminar parabolic profile. This allows fully turbulent conditions of the single-phase flow to be obtained after only 20 flow residence times, defined as $2\pi \mathrm{h}/\mathrm{U_b}$. Once such turbulent flow has reached a statistically steady state, the particles are injected randomly in the flow field. The density and diameter of the particles in this simulation were $\mathrm{p_p} = 2\,700\ \mathrm{kg/m^3}$ and $d = 264\mu m$, respectively, which, in wall units, corresponds to $\mathrm{d^+} = 0{,}462$ and a relaxation time $\mathrm{T^+} = 27$. The integration of particle motion equations (3) and (4) was performed with a Lagrangian time step around 100 times smaller than that used to solve the fluid equations. The studied particle volume fraction was $\alpha \approx 4\times10^{-4}$ which translates into $1{,}66\times10^6$ real particles in the flow domain. Moreover, for these conditions, the mass loading was around 0,9. As commented before, such value of α is low enough for inter-particle collision effects to be noticeable, but, together with the resulting mass loading, it is high enough for modulating the flow dynamics. Therefore, additional to the two-way coupled simulation, also a one-way coupled computation, *i.e.*, taking $\vec{F}_p = 0$ in Equation (2), was carried out in this study. In order to focus on the effects produced by fluid-particle interaction on the dynamics of both phases, the influence of gravity was not included, and particle-wall collisions were treated as ideal reflections.

Results

The first step was the validation of the present DNS simulations of the turbulent channel flow. Averaged profiles of the variables were obtained by averaging in time during a period of $2000\tau_\nu$ and then in the homogeneous directions (stream- and span-wise). Thus, the profiles obtained for the mean and rms (root mean square) velocities were compared with the results of Zhao *et al.* (2010), which were obtained in a channel with $Re_\tau = 180$. Figure 1a shows the non-dimensional velocity profile, together with the theoretical linear and logarithmic laws. In Figure 1a, $\mathrm{k} = 0{,}41$ refers to the von Kármán constant.

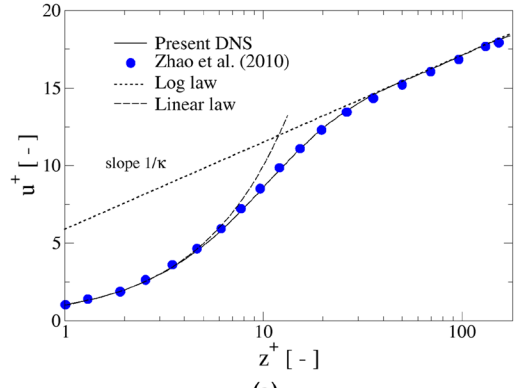

(a)

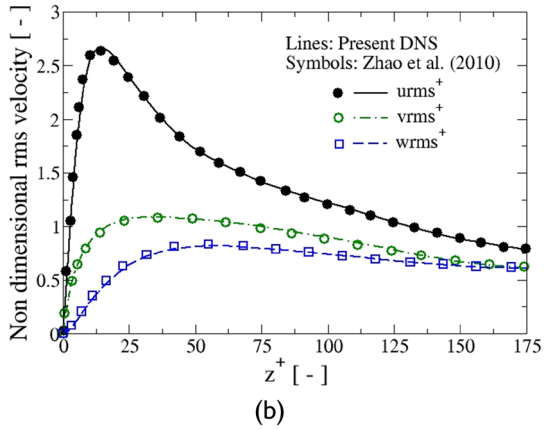

Figure 1. Non-dimensional velocity (a) and rms velocity profiles (b) for the single-phase flow. Comparison with Zhao *et al.* (2010). The theoretical linear and logarithmic laws are also shown in (a).
Source: Authors

Figure 1b shows the behavior of the non-dimensional rms velocities as compared to the results of Zhao *et al.* (2010). It can be seen that the agreement is very good for the mean and fluctuating velocities, which is why the present DNS results can be considered to be validated.

In the first approach, particles can be tracked in the previous flow field under the one-way coupling approach, *i.e.*, disregarding the particle phase influence on the carrier fluid. Afterwards, the effect of particles on the fluid phase is taken into account by the two-way coupling approach. Thus, both degrees of coupling have been performed in the present simulations, which allow describing the effects of two-way coupling between the phases not only on the fluid, but also on the particle phase.

Figure 2 shows the comparison of fluid and particle mean and fluctuating velocities regarding the degree of coupling, *i.e.*, one-way (OWC) or two-way (TWC). Figure 2a presents, in a linear scale, the results for the mean stream-wise velocity made non-dimensional with the single-phase friction velocity. It can be seen that, under two-way coupling, the fluid velocity profile is flatter than in the single-phase flow (SPF), showing two cross-over points: the first one in the buffer layer, $z^+ \approx 20$, where the fluid TWC profiles overcomes the SPF profile; and in the log layer, $z^+ \approx 100$, where the first becomes slower than the second. Such behavior is consistent with the fixed fluid mass flow imposed in the simulations. In the OWC case, particles closely follow the fluid in the viscous

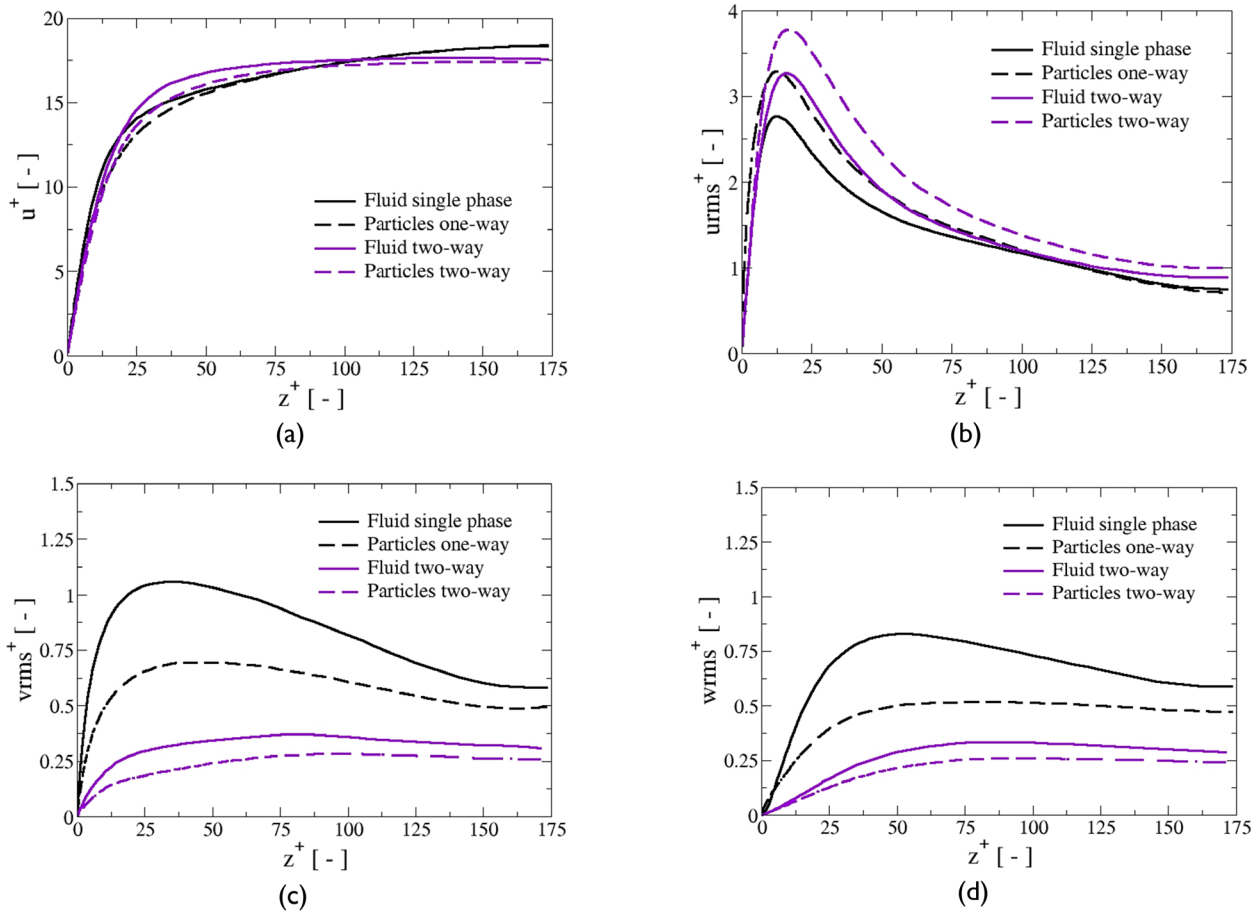

Figure 2. Non-dimensional fluid and particle mean and fluctuating velocities for one-way and two-way coupling conditions: a) stream-wise mean velocity, b) stream-wise rms velocity, (c) span-wise rms velocity, (d) wall-normal rms velocity
Source: Authors

and log layers but lag it in the buffer layer, whereas, in the TWC case, particles always lag the fluid, similar to that reported by Zhao *et al*. (2013).

Figure 2b shows the behavior of the profiles for the stream-wise rms velocity. Consistent with previous literature (*e.g.*, Dritselis and Vlachos, 2008; Zhao *et al*., 2010), the TWC fluid values of this variable are higher than those of the SPF, and the peak value is farther from the wall. The reason for this is that the particle phase, due to its inertia, presents higher values of this variable than the fluid across the whole channel, constituting a source of stream-wise fluctuating velocity for the carrier phase. Furthermore, the particle TWC $urms^+$ values are above those of the particle OWC in the buffer and log layers. On the other hand, the particle OWC profile is above the SPF profile, *i.e.*, up to $z^+ \approx 100$, and then both keep very close values, similar to what happens in the u^+ velocity.

Figures 2c and 2d present the behavior of the non-dimensional span-wise and wall-normal rms velocities, respectively. In both directions, particles are responsible for the strong reduction in the TWC fluid values regarding the SPF all across the channel cross-section, which is again an effect of particle inertia. This phenomenon can be physically explained by the fact that inertial particles tend to maintain their main direction of movement (stream-wise, in this case), not adjusting their velocity to the local flow conditions. In the wall proximity, they keep higher stream-wise velocity fluctuations than the fluid, but the contrary happens in the span-wise and wall-normal directions. Therefore, particles tend to increase fluid stream-wise velocity fluctuations but damp the velocity fluctuations of the other two components. In this way, particles affect the turbulence generation cycle, inhibiting the transfer of energy from the stream-wise to the span-wise and wall-normal directions, which eventually results in an increase in the fluid Reynolds stress anisotropy in TWC. Moreover, in two-way coupling, the near-wall peaks of fluid $vrms^+$ and $wrms^+$ are very much reduced regarding SPF, and those of particles are nearly inexistent. Additionally, it is observed that particle rms values in the span-wise and wall-normal directions are substantially higher in OWC than in TWC. Finally, in TWC, the fluid Reynolds shear stresses are also decreased with regard to SPF (Figure 4b). One last remark is that the obtained non-dimensional profiles of fluid velocity fluctuations in TWC are very close to those presented by Zhao *et al*. (2010).

The analysis of the previous results on velocity profiles cannot disregard the behavior of particle concentration profiles. It is known that, in inhomogeneous turbulent flows, particles tend to migrate to regions with low values of turbulent kinetic energy. This phenomenon has been called *turbophoresis* (Reeks, 1983), and, in the case of near-wall turbulence, it means that particles tend to move towards the wall, accumulating in the viscous sublayer. As a result, particle concentration in the vicinity of the wall can be much higher than at the center of the channel: for instance, in the OWC case shown in Figure 3, such ratio is close to 90. Two-way coupling effects are able to somewhat reduce such value –up to 23 in the TWC results presented in Figure 3 (Lee and Lee, 2015). Particle migration towards the wall depends on particle inertia and reaches a maximum for a certain Stokes number T^+. Obviously, such high particle concentration enhances fluid-particle interactions in the buffer and viscous sublayers regarding the channel center.

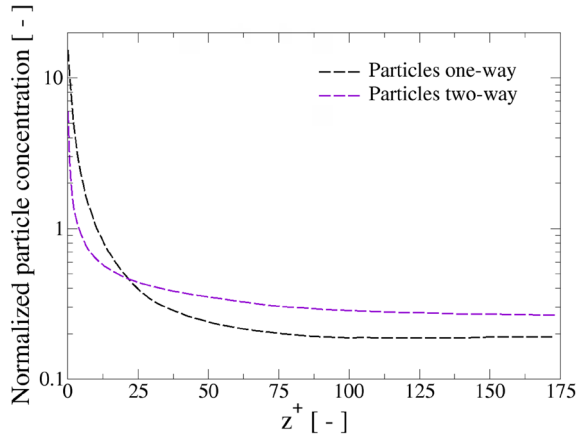

Figure 3. Normalized particle concentration profiles for one-way and two-way coupled simulations
Source: Authors

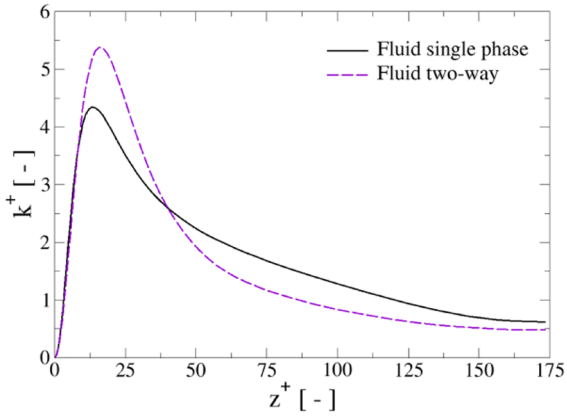

(a)

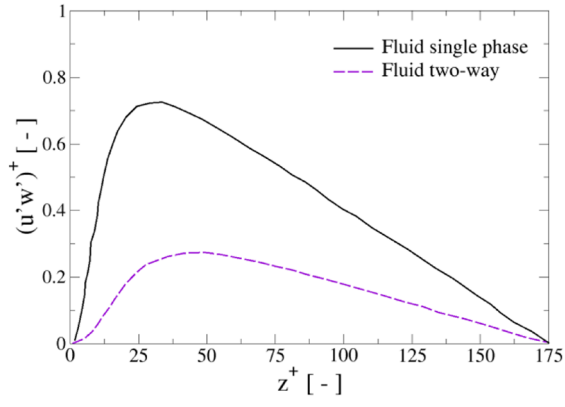

(b)

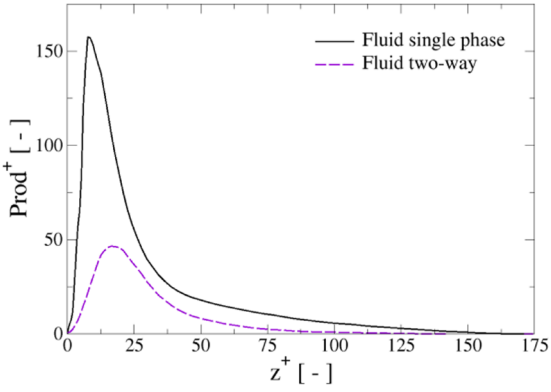

(c)

Figure 4. Non-dimensional fluid turbulent kinetic energy (a), turbulent shear stresses (b), and turbulent kinetic energy production term (c) for single phase and two-way coupling conditions
Source: Authors

Except for very small inertia particles very close to tracers, particles tend to laminarize the flow dynamics by decreasing their kinetic turbulent energy, k. Such effect is illustrated in Figure 4, which presents the comparison of the non-dimensional turbulent kinetic energies in SPF and TWC (Figure 4a), together with the profiles for the corresponding Reynolds shear stresses (Figure 4b) and production terms (Figure 4c). The process of reduction of k by the presence of particles can be explained as follows: particles tend to preferentially sample zones with low fluid velocity. This means that the conditionally averaged fluid velocity at particle position tends to be lower than the RANS averaged fluid velocity. As a result, the mean stream-wise slip velocity of particles is negative at the center of the channel but positive in the buffer and viscous layers. This, in turn, means that the fluid provides energy to the particles in the channel core but receives energy from them in the areas close to the wall ($z^+ < 30$). In fact, such energy transfer in the stream-wise direction from the particles to the fluid presents a peak in the buffer layer (Zhang *et al*., 2013). However, particles dissipate some energy, which is located in the areas with the most presence of particles, *i.e.*, close to the wall due to particles inertia (there is a non-zero slip velocity). Therefore, for the stream-wise direction, the energy extracted from the fluid by particles near the channel center is transferred back to the fluid, mainly in the buffer layer, and part of it is dissipated. Regarding the wall normal and span-wise directions, the energy that particles subtract to the fluid is totally dissipated.

As a result, the fluid Reynolds stresses in the stream-wise direction are enhanced regarding the SPF, but they are diminished in the other directions (Figure 2), as well as the Reynolds shear stresses (Figure 4b). In that context, when computing the fluid turbulent kinetic energy, the net result is that, under two-way coupling, it is higher than that of the SPF in the buffer layer but lower in the channel core and viscous regions (Figure 4a). However, because the particles actually dissipate fluctuating energy (Dritselis, 2016), the globally averaged turbulent kinetic energy in the TWC case is lower than that of the SPF, which is actually observed in the present simulations.

Apart of these facts, particles also modulate the fluid turbulence, altering the fluid velocity gradients (mean and fluctuating), which affects the different terms present in the Reynolds stress balance equations. As a consequence, the fluid production under TWC is reduced regarding the SPF (Figure 4c). However, as less turbulent kinetic energy is generated, the fluid dissipation is also reduced. All of these effects are connected with the reduction of velocity-pressure gradient correlations (Dritselis, 2016), which is the mechanism of turbulent energy redistribution among the fluid Reynolds stress components. As a result, in two-way coupled flows, not only is less turbulent kinetic energy produced with regard to the SPF, but its redistribution is also hampered. As consequence, the fluid Reynolds stress anisotropy is enhanced (Figure 2).

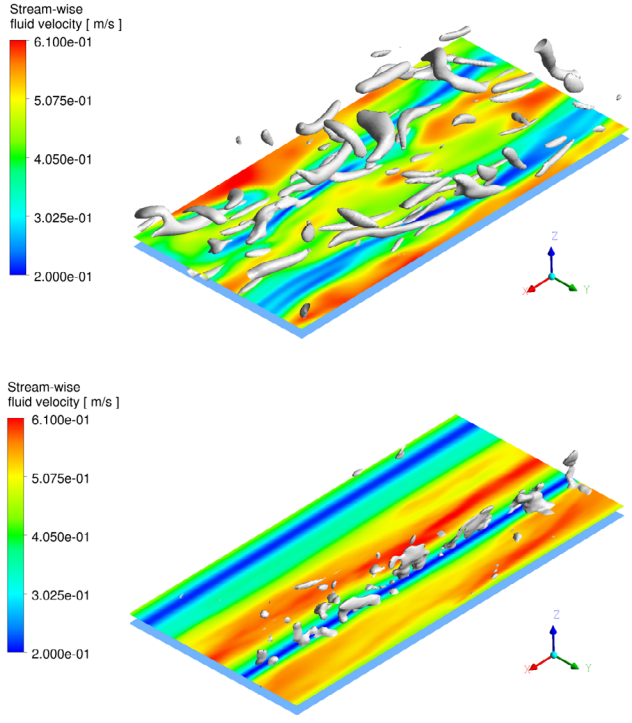

Figure 5. Illustration of the velocity field in the plane $z^+ = 18$ within the buffer layer. The turbulent structures identified by the Q criterion are included. a) Single phase flow, $Q = 50\ s^{-2}$; (b) two-phase flow, $Q = 10\ s^{-2}$. Flow is in the positive x-direction.
Source: Authors

Because of the presence of particles, the main mechanism for the production of k, vortex stretching, is inhibited, a fact that is linked to the damping of vorticity in the stream-wise direction. The consequent decrease in the stream-wise enstrophy (Dritselis, 2016) due to the particles results in a reduction in the number of turbulent structures and their weakening. As an example, Figure 5 shows the turbulent structures visualized by the Q criterion (Hunt *et al*., 1988) as grey surfaces in single-phase flow (Figure 5a) and in particle-laden flow (Figure 5b). Not only is the number of turbulent structures larger in SPF, but the intensity is also much higher. Figure 4a shows structures with $Q = 50 s^{-2}$, whereas those in Figure 4b have $Q = 10 s^{-2}$.

Another effect of particles on the fluid can also be seen in Figure 5: the length and coherence of the low and high velocity streaks in the buffer layer are increased in TWC with regard to SPF. For instance, in Figure 5, such streaks are shown for a plane located at $z^+ = 18$. In the SPF case (Figure 5a), they are noticeably wavier and shorter than in the TWC configuration (Figure 5b), where they even extend along the whole length of the computational domain. Moreover, particles tend to follow the low velocity streaks more closely than the high velocity streaks, as seen in Figure 6. In this Figure, particle positions are superimposed to the fluid velocity contours in the buffer layer slice of $z^+ = 18$. For both situations –SPF (Figure 6a) and TWC (Figure 6b)– particles are more concentrated in low-speed streaks, forming long elongated ropes, even though it is more evident in TWC. Such concentration stabilizes the low-velocity streaks (making them more inertial) against lateral perturbations, which renders them stabler and straighter (Marchioli, 2003). In the high-speed streaks, there are also particles that are clustered but more dispersed, showing shorter lengths and noticeable voids in both span-wise and stream-wise directions. A very interesting fact is that, especially in TWC, particles clustered in the low-speed streaks escape from the wall (white dots), whereas particles clustered along high-speed streaks are moving towards the wall (black dots).

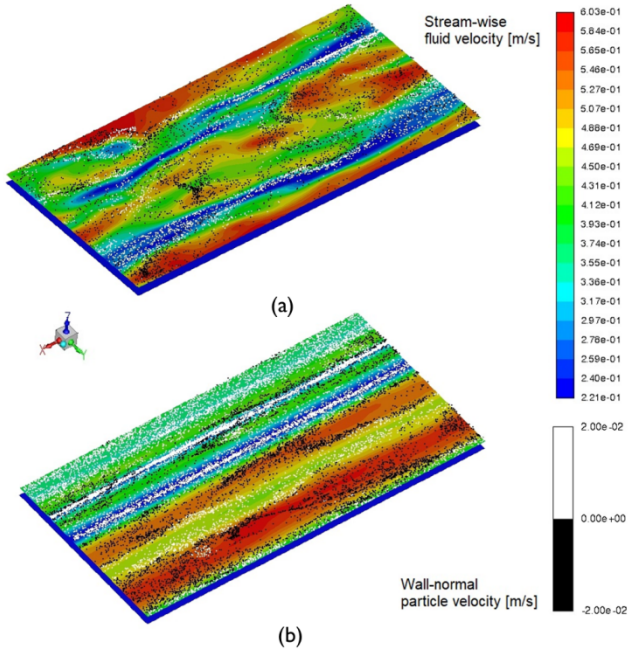

Figure 6. Illustration of the velocity field in the plane $z^+ = 18$ within the buffer layer under one-way coupling (a) and two-way coupling (b) configurations. Positions of particles around that plane are shown as colored dots. Black dots represent particles moving towards the wall, whereas white dots denote particles escaping from the wall. Flow is in the positive x-direction.
Source: Authors

Figure 7 shows the stream-wise velocity field in the middle stream-wise plane. One-way coupled flow (Figure 7a) and two-way coupled flow (Figure 7b) are presented. Moreover, the position of particles is shown as colored dots. Blue and black dots indicate particles with positive and negative wall-normal velocity, respectively. In such plots, the color transition from cyan to yellow is quite fast, indicating a high gradient of stream-wise velocity. Therefore, iso-surfaces of green color can be taken as a boundary among high- and low-speed regions. From Figure 7, it is possible to observe the following facts: 1) particle concentration at the walls is noticeably higher than at the center of the channel; 2) in the channel core, particles are not uniformly distributed, but they concentrate preferentially in clusters, which are more defined in the case of TWC; and 3) particle ejections from the wall are clearly visible thanks to the clustered particles escaping from the wall (blue dots near the lower wall and black dots near the upper wall), where the background color is cyan to green (delimiting the low speed streaks). In OWC, particle ejections are shorter and more compact than in TWC, where they penetrate deeper towards the channel core. Moreover, although it is not shown, there is a strong correlation between wall-normal particle and fluid velocities.

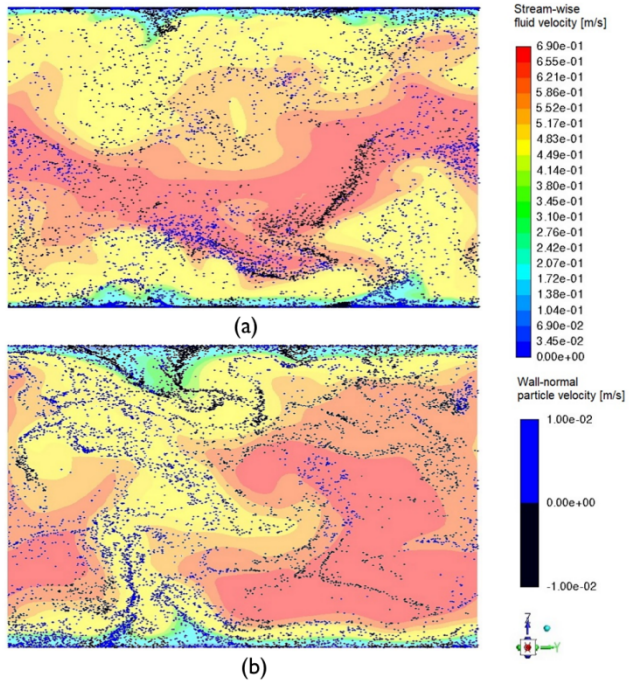

Figure 7. Illustration of the stream-wise velocity field in the middle stream-wise plane under one-way coupling (a) and two-way coupling (b) configurations. Positions of particles around that plane are shown as colored dots. Black dots represent particles with negative wall-normal velocities, whereas blue dots denote particles with positive wall normal velocities. Flow is orthogonal to the plane.
Source: Authors

Discussion

This section aims to pinpoint the main effects of inertial particles on the turbulent behavior of the flow, as well as the mechanisms that drive them. Our aim is to explain the way in which particles interrupt the turbulent generation cycle near the walls. Therefore, the turbulent flow dynamics in the vicinity of a wall are summarized.

According to Jiménez and Pinelli (1999), the self-sustained turbulent regeneration cycle in the near-wall region consists of the formation of sinuous low-velocity streaks from the advection of the mean shear profile by stream-wise vortices. Such streaks, with a typical stream-wise length of 1 000 wall units, are unstable under lateral perturbations. The result of such instability is the generation of quasi stream-wise vortices. In turn, such vortices generate strong coherent motions of fluid that control turbulent mixing near the wall, which are called *sweeps* and *ejections*. The former bring high-speed fluid from the outer flow towards the wall, whereas the latter transport low momentum fluid near the wall to the outer region. Such sweeps and ejections contribute to Reynolds stresses, increasing turbulence production (Marchioli, 2003). Low-speed streaks are longer than the quasi stream-wise vortices (with a typical length of 200 wall units) that generate them and are long-lived structures.

In a near wall particle-laden flow, the solids are driven to the wall by the sweeps and entrained in the outer flow by the ejections. However, as demonstrated by Marchioli (2003), particle exit fluxes are weaker than inlet ones due to the geometrical arrangement of the quasi stream-wise vortices flanking the low-speed streaks. The net result is that particles tend to migrate towards the wall and accumulate in the viscous layer under low-speed streaks –which are mainly related to ejection events (Figure 6)– in regions with low values of wall shear stress. In this context, low speed streaks laden with particles acquire inertia, so their meandering is reduced, which in turn has the effect of inhibiting the instability that generates the quasi stream-wise vortices. Therefore, the tripping frequency of such vortices is decreased, eventually reducing the frequency and intensity of turbulence production events (sweeps and ejections). As a result, turbulence production is diminished in a particle-laden flow.

On the other hand, the degree of turbulence suppression by particles is directly related to particle segregation near the wall, which is enhanced for maximal turbophoresis. In this region, a strong interaction between the concentration of suspended particles and coherent structures is established, thus resulting in weaker near-wall quasi-stream vortices with larger diameters and a longer stream-wise extent than in particle free flow (Dritselis and Vlachos, 2011). Such fainted quasi-stream vortices are not able to produce sweeps and ejections that are energetic enough to sustain the mechanisms of turbulence production at the same rate, and, consequently, turbulent kinetic energy is reduced. The weak intensity of the quasi stream-wise vortices in particle-laden flow also has the effect of reducing the production of coherent vorticity, which, added to the particles' direct effect of decreasing gradients of fluid velocity (Dritselis, 2016), inhibits the mechanisms of turbulence generation (*e.g.*, vortex stretching). As a consequence, the fluid dissipation rate drops accordingly to counterweight the lower turbulent kinetic energy production. Additionally, due to the lower vorticity magnitude, fluid pressure also decreases, with the consequence of lessening the pressure gradient velocity correlations, which are the mechanism responsible for the inter-component turbulent energy exchange. Thus, particles indirectly alter the development of fluid turbulence processes.

Regarding the macroscopic energy flow in the TWC situation, the picture can be summarized as follows: the fluid performs work on the particles in the log layer near the channel center, so they absorb energy from the large eddies and transfer it to the small-scale vorticity structures close to the walls (Zhao *et al.*, 2013). As a result, particles transfer energy to the fluid in the viscous and buffer layers. However, there is an energy imbalance, and the net budget is that particles extract energy from the fluid. Moreover, as commented above, in the vicinity of the wall, inertial particles tend to keep their stream-wise velocity, transferring momentum to the fluid in that direction and extracting momentum from the fluid in the transversal directions. As consequence, the Reynolds stress anisotropy is larger in TWC than in SPF.

From the previous discussion, it seems that particles disturb the near-wall autonomous turbulence regeneration cycle and, in particular, they alter the dynamics of the low velocity streaks, rendering them longer, straighter, and more regular. However, this is a typical characteristic of drag-reduced flows, regardless of the origin of such reduction. Thus, it is not surprising that particle flows laden with particles of certain inertia exhibit reduced drag regarding SPF (Zhao *et al.*, 2010, 2013). In the simulations shown in this work, where the fluid mass flow is fixed, drag reduction should manifest as a reduction in the external pressure gradient necessary to maintain such flow rate (Π in Equation (2). This is indeed the case, and it is shown in Figure 8.

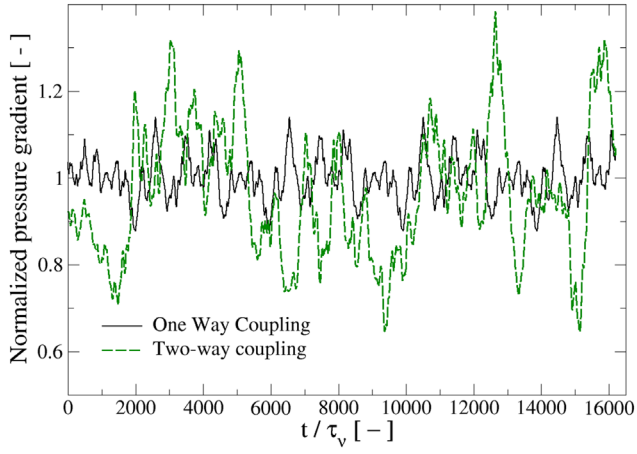

Figure 8. Time evolution of normalized pressure gradient for the one-way and two-way coupling scenarios
Source: Authors

The SPF and TWC external pressure gradient time series are plotted in Figure 8 in non-dimensional form. The pressure gradient is divided by the mean value obtained in

single-phase flow, and time is measured in wall units, *i.e.*, divided by the viscous time scale τ_ν. It can be seen that the fluctuation of the external pressure gradient in TWC flow is much higher than that of SPF. However, when its mean value is computed, it is around 4% lower than that of particle free flow. Finally, it should be mentioned that peaks in the pressure gradient under TWC correspond to bursts of turbulent activity, in which an increase in the number and intensity of turbulent structures can be observed.

Conclusions

This contribution analyzed and discussed the fluid-particle interaction effects that reduce the fluid turbulence intensity in a fully developed two-phase channel flow. Simulations were performed by combining the Direct Numerical Simulation approach and the Lagrangian tracking of point particles including two-way coupling effects. The analysis comprises not only the fluid phase variables, but also the alteration of particle phase variables when two-way coupling interaction is considered in comparison with the one-way coupling approach, *i.e.*, when the momentum feedback from the particles to the fluid is ignored. It has been shown that particles lag the fluid and that the stream-wise fluctuating particle velocity is larger than that of the fluid in the stream-wise direction, albeit lower than that of the fluid in the span-wise and wall-normal directions. Due to their inertia, particles enhance the fluid stream-wise Reynolds stresses but damp the span-wise, wall-normal, and shear stresses. In particular, it was illustrated how particles tend to be segregated in low-velocity streaks, which has the effect of perturbing the autonomous regeneration cycle of wall turbulence, thus reducing the efficiency of turbulence production processes and eventually decreasing the fluid turbulent kinetic energy while laminarizing the flow. Such effects are shown to be responsible for a decrease in the mean pressure gradient, which, in the actual configuration, implies a drag reduction effect by particles in the two-phase channel flow.

Finally, this study provided results coherent with those previously presented in the literature, which allowed presenting a global perspective of the fluid-particle interaction phenomena in the channel flow. Nevertheless, this work has several limitations. In first place, the estimation of the undisturbed fluid velocity at particle position, which is needed in point particle approaches, should be improved by using, for instance, the ERPP method described in Gualtieri *et al*. (2015). On the other hand, including the Saffman force in the particle motion equation is necessary, as it has been demonstrated in the literature (Costa *et al*., 2021). The lift force is responsible for the resuspension of particles close to the wall, causing a reduction in the particle residence time in the low-speed streaks and a diminishing of the particle concentration near the wall. Additionally, when higher particle volume fractions are of interest, inter-particle collisions must be taken into account, as they also contribute to disperse particle ropes located along the fluid streaks, promote decorrelations between fluid and particle velocities, and are a mechanism for energy redistribution among the different components of particle fluctuating velocity, especially in the vicinity of the wall. Finally, in order to approximate real flows, inelastic particle-wall collisions, wall roughness, and particle rotation should be included in the simulation approach. Such effects are to be considered in future simulations.

Acknowledgements

We would like to gratefully acknowledge the support of the Research Directorate of Universidad Autónoma de Occidente and the Research Vice-Principalship of Universidad Nacional de Colombia, through the joint project *Estudio numérico de los procesos de transporte aerodinámico de partículas sólidas en un canal rectangular con rugosidad artificial inducida* [Numerical study of the aerodynamic processes of solid particles in a rectangular channel with induced artificial roughness] (16INTER-264).

References

Akiki, G., Jackson, T. L., and Balachandar, S. (2017). Pairwise interaction extended point-particle model for a random array of monodisperse spheres. *Journal Fluid Mechanics, 813*, 882-928. https://doi.org/10.1017/jfm.2016.877

Balachandar, S., and Eaton, J. K. (2010). Turbulent dispersed multiphase flow. *Annual Review Fluid Mechanics, 42*, 111-133. https://doi.org/10.1146/annurev.fluid.010908.165243

Battista, F., Mollicone, J. P., Gualtieri, P., Messina, R., and Casciola, C.M. (2019). Exact regularised point particle (ERPP) method for particle-laden wall-bounded flows in the two-way coupling regime. *Journal Fluid Mechanics, 878*, 420-444. https://doi.org/10.1017/jfm.2019.622

Bernard, P. S., Ashmawey, M. F., and Handler, R. A. (1989). An analysis of particle trajectories in computer-simulated turbulence channel flow. *Physics of Fluids A, 1*, 1532-1540. https://doi.org/10.1063/1.857330

Boivin, M., Simonin, O., and Squires, K. D. (1998). Direct numerical simulation of turbulence modulation by particles in isotropic turbulence. *Journal Fluid Mechanics, 375*, 235-263. https://doi.org/10.1017/S0022112098002821

Capecelatro, J., Desjardins, O., and Fox, R. O. (2018). On the transition between turbulence regimes in particle-laden channel flows. *Journal Fluid Mechanics, 845*, 499-519. https://doi.org/10.1017/jfm.2018.259

Costa, P., Brandt, L., and Picano, F. (2021). Near-wall turbulence modulation by small inertial particles. *Journal Fluid Mechanics, 922*, A9. https://doi.org/10.1017/jfm.2021.507

de Villiers, E. (2006). *The potential of Large Eddy Simulation for the modeling of wall bounded flows* [Doctoral thesis, Imperial College of Science, Technology, and Medicine] https://scirp.org/reference/ReferencesPapers.aspx?ReferenceID=2169716

Dritselis, C., and Vlachos, N. S. (2008). Numerical study of educed coherent structures in the near-wall region of a particle-laden channel flow. *Physics of Fluids, 20*, 055103. https://doi.org/10.1063/1.2919108

Dritselis, C., and Vlachos, N.S. (2011). Numerical investigation of momentum exchange between particles and coherent structures in low Re turbulent channel flow. *Physics of Fluids, 23*, 025103. https://doi.org/10.1063/1.3553292

Dritselis, C. (2016). Direct numerical simulation of particle laden turbulent channel flows with two- and four-way coupling effects: budgets of Reynolds stress and streamwise enstrophy. *Fluid Dynamics Research, 48*, 015507. https://doi.org/10.1088/0169-5983/48/1/015507

Elghobashi, S. (1994). On predicting particle-laden turbulent flows. *Applied Scientific Research, 52*, 309-329. https://doi.org/10.1007/BF00936835

Göz, M. F., Laín, S., and Sommerfeld, M. (2004). Study of the numerical instabilities in Lagrangian Tracking of bubbles and particles in two-phase flow. *Computers and Chemical Engineering*, 28, 2727-2733. https://doi.org/10.1016/j.compchemeng.2004.07.035

Gualtieri, P., Picano, F., Sardina, G., and Casciola, C.M. (2015). Exact regularized point particle method for multiphase flows in the two-way coupling regime. *Journal Fluid Mechanics, 773,* 520-561. https://doi.org/10.1017/jfm.2015.258

Hunt, J. C. R., Wray, A. A., and Moin, P. (1988). Eddies, streams, and convergence zones in turbulent flows. In Center for Turbulence Research (Eds.), *Proceedings of the Summer Program 1988* (pp. 193-208). https://web.stanford.edu/group/ctr/Summer/201306111537.pdf

Ireland, P. J., and Desjardins, O. (2017). Improving particle drag predictions in Euler–Lagrange simulations with two-way coupling. *Journal Computational Physics, 338*, 405-430. https://doi.org/10.1016/j.jcp.2017.02.070

Jiménez, J., and Pinelli, A. (1999). The autonomous cycle of near-wall turbulence. *Journal Fluid Mechanics, 389*, 335-359. https://doi.org/10.1017/S0022112099005066

Kontomaris, K., Hanratty, T. J., and McLaughlin, J. B. (1992). An algorithm for tracking fluid particles in a spectral simulation of turbulent channel flow. *Journal Computational Physics, 103*, 231-242. https://doi.org/10.1016/0021-9991(92)90398-I

Kuerten, J. G. M., van der Geld, C. W. M., and Geurts, B. J. (2011). Turbulence modification and heat transfer enhancement by inertial particles in turbulent channel flow. *Physics of Fluids, 23*, 123301. https://doi.org/10.1063/1.3663308

Kuerten, J. G. M. (2016). Point-particle DNS and LES of particle-laden turbulent flow – A state-of-the-art review. *Flow, Turbulence and Combustion, 97*, 689-713. https://doi.org/10.1007/s10494-016-9765-y

Laín, S., and Aliod, R. (2000). Study on the Eulerian dispersed phase equations in non-uniform turbulent two-phase flows: Discussion and comparison with experiments. *International Journal of Heat and Fluid Flow, 21*, 374-380. https://doi.org/10.1016/S0142-727X(00)00023-0

Laín, S., and Sommerfeld, M. (2007). A study of pneumatic conveying of non-spherical particles in a turbulent horizontal channel flow. *Brazilian Journal of Chemical Engineering, 24*, 535-546.

Lee, J., and Lee, C. (2015). Modification of particle-laden near-wall turbulence; effect of Stokes number. *Physics of Fluids, 27*, 023303. https://doi.org/10.1063/1.4908277

Li, Y., McLaughlin, J. B., Kontomaris, K., and Portela, L. (2001). Numerical simulation of particle-laden turbulent channel flow. *Physics of Fluids, 13*, 2957-2967. https://doi.org/10.1063/1.1396846

Li, J., Wang, H., Liu, Z., Chen, S., and Zheng, C. (2012). An experimental study on turbulence modification in the near-wall boundary layer of a dilute gas-particle channel flow. *Experiments in Fluids, 53*, 1385-1403. https://doi.org/10.1007/s00348-012-1364-7

Marchioli, C. (2003). *Mechanisms for transfer, segregation and deposition of heavy particles in turbulent boundary layers* [Doctoral thesis, University of Udine] http://calliope.dem.uniud.it/PEOPLE/cris.html

Marchioli, C., Soldati, A., Kuerten, J. G. M., Arcen, B., Tanière, A., Goldensoph, G., Squires, K. D., Cargnelutti, M. F., and Portela, L. M. (2008). Statistics of particle dispersion in direct numerical simulations of wall bounded turbulence: Results of an international collaborative benchmark test. *International Journal of Multiphase Flow, 34*(9), 879-893. https://doi.org/10.1016/j.ijmultiphaseflow.2008.01.009

Maxey, M. R., and Patel, B. K. (2001). Localized force representations for particles sedimenting in Stokes flow. *International Journal of Multiphase Flow, 27*, 1603-1626. https://doi.org/10.1016/S0301-9322(01)00014-3

Maxey, M. R., and Riley, J. J. (1983). Equation of motion for a small rigid sphere in a nonuniform flow. *Physics of Fluids, 26*, 883-889. https://doi.org/10.1063/1.864230

McLaughlin, J.B. (1989). Aerosol particle deposition in numerically simulated channel flow. *Physics of Fluids A, 1*, 1211-1224. https://doi.org/10.1063/1.857344

Pan, Y., and Banerjee, S. (1996). Numerical simulation of particle interactions with wall turbulence. *Physics of Fluids, 8*, 2733-2755. https://doi.org/10.1063/1.869059

Reeks, M. W. (1983). The transport of discrete particles in inhomogeneous turbulence. *Journal of Aerosol Science, 14*, 729-739. https://doi.org/10.1016/0021-8502(83)90055-1

Righetti, M., and Romano, G. P. (2004). Particle–fluid interactions in a plane near-wall turbulent flow. *Journal Fluid Mechanics*. https://doi.org/10.1017/S0022112004008304

Schoppa, W., and Hussain, F. (2002). Coherent structure generation in near-wall turbulence. *Journal of Fluid Mechanics, 453*, 57-108. https://doi.org/10.1017/S002211200100667X

Sommerfeld, M., and Laín, S. (2015). Parameters influencing dilute-phase pneumatic conveying through pipe systems: A computational study by the Euler/Lagrange approach. *Canadian Journal of Chemical Engineering, 93*, 1-17. https://doi.org/10.1002/cjce.22105

Vreman, A. W. (2007). Turbulence characteristics of particle-laden pipe flow. *Journal Fluid Mechanics, 584*, 235-279. https://doi.org/10.1017/S0022112007006556

Vreman, A. W. (2015). Turbulence attenuation in particle-laden flow in smooth and rough channels. *Journal Fluid Mechanics, 773*, 103-136. https://doi.org/10.1017/jfm.2015.208

Wu, Y., Wang, H., Liu, Z., Li, J., Zhang, L., and Zheng, C. (2006). Experimental investigation on turbulence modification in a horizontal channel flow at relatively low mass loading. *Acta Mechanica Sinica, 22*, 99-108. https://doi.org/10.1007/s10409-006-0103-9

Zhao, L. H., Andersson, H. I., and Gillissen, J. J. J. (2010). Turbulence modulation and drag reduction by spherical particles. *Physics of Fluids, 22*, 081702. https://doi.org/10.1063/1.3478308

Zhao, L. H., Andersson, H. I., and Gillissen, J. J. J. (2013). Interphasial energy transfer and particle dissipation in particle-laden wall turbulence. *Journal Fluid Mechanics, 715*, 32-59. https://doi.org/10.1017/jfm.2012.492

Research Article/Mechanical Engineering, Mechatronics, and Materials Science https://doi.org/10.15446/ing.investig.94361

Effects of Variations in Operating Conditions on the Precision and Accuracy of Standardless Elemental Analysis of Stainless Steel by SEM-EDS

Efectos de cambios en las condiciones de operación en la precisión y la exactitud del microanálisis químico sin patrones de acero inoxidable por MEB-EDE

Carlos M. Garzón[1], Juan P. Cruz[2], Johan K. Noreña[3], Eduar F. Pineda[4], and Juan S. Cachaya[5]

ABSTRACT

It is a customary practice to carry out standardless elemental microanalysis by energy dispersive spectroscopy (EDS) under the very same operational conditions as those used for scanning electron microscope (SEM) imaging. In this article, EDS experiments were carried out with stainless steel (SS), varying the EDS testing operating conditions. The results showed that, if X-ray spectra are acquired under operating conditions that are very dissimilar to those optimized for microanalysis, both the detectability limit of minor species (Si, Mo, and Mn) and the uncertainty in the concentration of major alloying elements (Cr and Ni) are noticeably impaired. It was observed that, by improving the signal-to-noise (S-to-N) ratio (*i.e.*, by increasing the accelerating voltage, beam intensity, and total acquisition time, or when the working distance is optimized), the precision of the elemental concentration increases, but the accuracy is only marginally affected. For the major alloying elements, 25% of the measurements showed a percent discrepancy higher than three times the standard deviation, which is inconsistent with a normal statistical distribution.

Keywords: scanning electron microscopy, energy dispersive spectroscopy, SDD detector, elemental analysis, accuracy

RESUMEN

Es común que el microanálisis químico por espectroscopia por dispersión de energía (EDE) se realice en las mismas condiciones en las usadas para la adquisición de imágenes mediante el microscopio electrónico de barrido (MEB). En este artículo se realizaron experimentos de EDE sobre acero inoxidable, variando las condiciones de operación. Los resultados mostraron que, cuando se adquieren espectros de rayos X bajo condiciones de operación muy disímiles de aquellas optimizadas para el microanálisis, tanto la detectabilidad de las especies minoritarias (Si, Mo y MN) como la incertidumbre en la concentración de los principales elementos de aleación (Cr y Ni) se ven notoriamente afectadas. Se observó que, al mejorar la relación señal a ruido (S-R) (i.e., aumentando el voltaje de aceleración, la intensidad del haz y el tiempo de adquisición total, o cuando se optimiza la distancia de trabajo), aumenta la precisión en la concentración elemental, pero la exactitud se ve afectada solo de manera marginal. Para los elementos de aleación principales (Cr y Ni), 25% de las medidas presentaron discrepancias porcentuales mayores a tres veces la desviación estándar, lo cual no es consistente con una distribución estadística normal.

Palabras clave: microscopía electrónica de barrido, espectroscopía por dispersión de energía, detector SDD, análisis elemental, exactitud

Received: March 14th, 2021
Accepted: June 28th, 2022

Introduction

Scanning electron microscopes (SEMs) are a key tool in materials engineering departments worldwide. A SEM allows analyzing technological materials with a resolution down a to few nanometers. It can be equipped with different analyzing tools (*i.e.*, the so-called Analytical-SEM). This includes backscattering electron diffraction EBSD, energy dispersive spectroscopy, EDS, wave-length dispersive spectroscopy, WDS, X-ray tomography, XRT, X-ray fluorescence, XRF, cathodoluminescence, CL, among others. Although elemental analysis using EDS in SEM is intrinsically less accurate than either WDS or XRF (or even other techniques not implemented in SEM), EDS

[1] PhD in Metallurgical and Materials Engineering, Sao Paulo University, Sao Paulo, Brazil. Affiliation: Departamento de Física, Universidad Nacional de Colombia. Email: cmgarzono@unal.edu.co

[2] Physicist, Universidad Nacional de Colombia. Affiliation: Departamento de Física, Universidad Nacional de Colombia, Colombia. Email: jpcruzca@unal.edu.co

[3] Physicist, Universidad Nacional de Colombia. Affiliation: Departamento de Física, Universidad Nacional de Colombia, Colombia. Email: jknorenab@unal.edu.co

[4] Chemist, Universidad Nacional de Colombia. Affiliation: Departamento de Química, Universidad Nacional de Colombia, Colombia. Email: efpinedab@unal.edu.co

[5] Physicist, Universidad Nacional de Colombia. Affiliation: Departamento de Física, Universidad Nacional de Colombia, Colombia. Email: jscachayam@unal.edu.co

How to cite: Garzón, C. M., Cruz, J. P., Noreña, J. K., Pineda, E. F., and Chachaya, J. S. (2023). Effects of variations in operating conditions on the precision and accuracy of standardless elemental analysis of stainless steel by SEM-EDS. *Ingeniería e Investigación, 43*(1), e94361. https://doi.org/10.15446/ing.investig.94361

microanalysis is the most used among them, as it is an inexpensive, less time-consuming, simpler technique that demands less operator training (Newbury and Ritchie, 2015). Most SEM facilities worldwide are equipped with EDS detectors. The concentration of atomic species is carried out by EDS, both with and without standards (Newbury and Ritchie, 2013). On the one hand, elemental analysis with standards typically leads up to a 5% standard error in the mean concentration for major elements. This is known as *quantitative analysis* (Newbury and Ritchie, 2013). On the other hand, standardless analysis could lead up to a 50% standard error in the mean concentration for major elements, which is why this approach is called *semiquantitative* or *qualitative analysis* (Newbury and Ritchie, 2013). Despite the inaccurate nature of the standardless approach, more than 98% of EDS microanalyses are performed with it (Newbury and Ritchie, 2015). In recent years, the structure of EDS detectors has been significantly improved, as is the case of the development of silicon drift detectors (SDD). This recently developed family of EDS detectors has an improved energy resolution, is more sensible to low energy photons, operates with negligible dead times, and has better pulse processing electronics than the former Si(Li) detectors (Burgess and Holland 2013; Carlton 200; Gernet, 2008; Maniguet *et al*., 2012, Streli *et al*., 2004). Quantitative EDS elemental analysis with SDD detectors could potentially exhibit an accuracy similar to the concomitant accuracy of WDS analysis (Cubukçu *et al*., 2008; Newbury and Ritchie, 2015; Ritchie *et al*., 2012).

The precision of EDS elemental analysis is very dependent on the signal-to-noise (S-to-N) ratio and the background-corrected count intensity of the peaks in the spectrum (Lifshin and Gauvin, 2003; Newbury and Ritchie, 2019; Wassilkowska 2014). On the one hand, such peaks in the EDS spectrum show a Gaussian behavior (Franchi, 2017; Rackwitz, 2010; Scholze, 2009), which allows relating the background-corrected count intensity to the elemental concentration uncertainty. Here, the higher the counts, the lower the uncertainty. On the other hand, the detectability of minor species is related to the S-to-N ratio, with threshold values being established for defining major species, minor species, and traces, as well as for defining the detection limit as a function of the S-to-N ratio. A complete presentation of these computations is outside the scope of this work, and the reader is advised to consult the works by Goldstein *et al*. (2018) and Liao (2006).

In SEM facilities worldwide, the standard error of the mean EDS concentration is commonly reported as an integer factor of the concentration uncertainty (Goldstein *et al*. 2018; Liao 2006). As the concentration uncertainty is straightforwardly correlated to the S-to-N ratio, when accurate measurements are desired, it is a common practice to conduct EDS elemental analysis under SEM-EDS operating conditions, which leads to high S-to-N values. Further research is needed to establish the actual relationship between precision and accuracy in standardless EDS analysis with SDD detectors.

In general terms, the operating conditions optimized for high-resolution and high-quality SEM morphological analyses are not the same as those needed for optimized accurate elemental analyses (Goldstein *et al*., 2018; Liao, 2006). Although that disagreement between optimal operational conditions for either morphological or elemental analysis is well known for microscopists, it is a customary practice to carry out EDS standardless elemental microanalysis under the very same operational conditions as those used for imaging. Further research is needed to quantitatively determine how much is the accuracy of standardless EDS analysis affected when the SEM-EDS operational conditions are far from optimal for chemical microanalysis.

In this study, EDS experiments were carried out with stainless steel (SS), varying the operational conditions for acquiring EDS spectra, *i.e.*, the acceleration voltage (V_0), working distance (WD), electron beam intensity, and count number (the latter through variations in the live acquisition time). The aim of this work was to appraise the effects of variations in EDS operating conditions regarding both the percent uncertainty and percent discrepancy of the elemental analysis of UNS 31603 SS.

Experimentation

SEM-EDS experiments were carried out with UNS S31603 SS. The SS samples were 2 mm-thick cylinders cut from a commercial hot-worked bar of 19 mm in diameter. For reference, the SS's chemical composition was assessed by optical spectroscopy (at-%): 18,0 Cr, 9,1 Ni, 1,8 Mn, 0,8 Si, 1,2 Mo, 0,14 C, and bal. Fe. The samples were initially ground in emery paper, increasing the mesh number up to 1 200, and finally polished in diamond paste slurry, with the final stage in slurries with an average particle size of 1 μm. The RMS roughness parameter of polished samples was around 2-5 nm (as assessed by atomic force microscopy).

EDS experiments were carried out in a Tescan Vega 3 scanning electron microscope (SEM) equipped with an XFlash 410-M SDD detector from Bruker, which was cooled by a Peltier. The FWHM for $Mn_{k\alpha}$ was 128,0 eV. The energy scale division was 5 eV/channel. No electron dose was registered. The acquisition and post-processing of EDS spectra were carried out by using the ESPRIT 1,9 software. By means of this software, a deconvolution of the Bremsstrahlung *vs.* the characteristic X-ray radiation in the raw EDS spectra was performed, and the background-corrected peak intensity for every radiation line in the EDS spectra was recorded. An automatic analysis setup was used. From both the background-corrected peak intensities recorded and the intensity of the Bremsstrahlung, the S-to-N ratio was computed. From the peak characteristic intensity, the percent uncertainty was calculated as the standard deviation of the counts in the peak while assuming it followed a Gaussian distribution (Liao, 2006). The percent discrepancy was computed as the percent difference between the reference

chemical composition assessed by optical spectroscopy and the chemical composition assessed by EDS. This percent discrepancy is usually called *relative error* in EDS analysis (Newbury and Ritchie, 2015). This research assumed that the lower the relative error, the more accurate the elemental concentration assessed. The following were set as the initial EDS operating conditions: V_0 25 kV, WD 15 mm, electron beam intensity 12 a.u., spot size 150 nm, live time 60 s. From those initial operating conditions, experiments were carried out, varying only one of the following parameters: (i) V_0 between 5 and 25 kV, (ii) beam intensity between 6 and 14 a.u., (iii) WD between 10 and 20 mm, and (iv) count number between $3x10^3$ and $8x10^5$ a.u.

Results and analysis

Figure 1 shows typical EDS spectra obtained by varying V_0. It depicts the characterization of Mo via the L line, the characterization of Si is shown by means of the K line, and the characterization of Cr, Mn, and Fe is shown by the K_α line at V_0 between 10 and 25 kV and by the L line at 5 kV. The characterization of Ni is shown by the K_α line at V_0 between 15 and 25 kV and by the L line at 5 and 10 kV. In the EDS spectra (Figure 1), it can be observed that the $Mn_{k\alpha}$ and $Cr_{k\beta}$ lines strongly overlap. Therefore, Mn was characterized after deconvoluting of those two lines, which makes its quantification strongly unprecise. The EDS spectra show that the major alloying elements are Cr and Ni (bal. Fe), while Si, Mo, and Mn are minor alloying elements, which is in trivial accordance with the chemical composition assessed by optical spectroscopy.

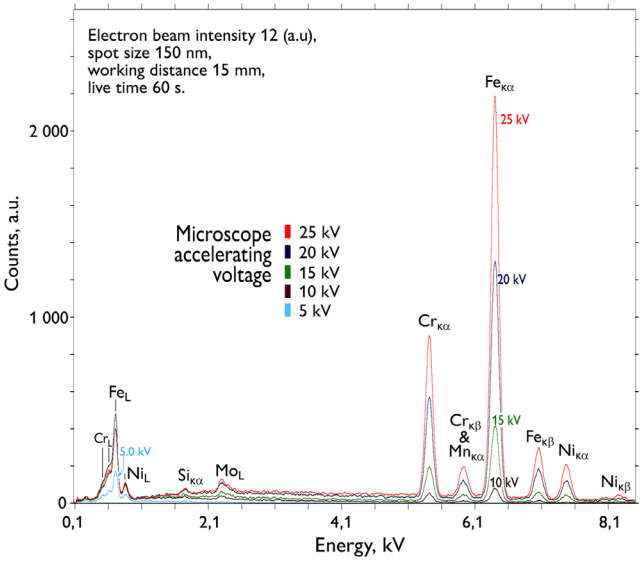

Figure 1. Effects of V_0 variations on the energy spectra
Source: Authors

Figures 2 to 5 show the percent uncertainty, percent discrepancy, and S-to-N ratio as a function of variations in V_0 (Figure 2), electron beam intensity (Figure 3), WD (Figure 4), and count number (Figure 5).

The results of this research regarding the S-to-N ratio (Figure 2 to 5) follow the trends well-known for microscopists worldwide: the S-to-N ratio increases as the (i) V_0, (ii) beam intensity, and (iii) counts number increase, or (iv) when the WD is closer to a factory-reference optimal value. As the S-to-N ratio increases, the precision of elemental concentration increases (*i.e.*, the percent uncertainty decreases), which is also a classical result in the realm of EDS error analysis. However, the accuracy of the elemental concentration (analyzed on the basis of the percent discrepancy) did not show a monotonic relationship with the precision, which is not consistent with the common conception at SEM facilities, where it is assumed that the standard error of the mean EDS concentration is proportional to the percent uncertainty (EDS analysis software have a report routine where the SEM microscopist can choose the confidence interval for the chemical composition, and then the software routine associates the concentration percent error to an integer factor of the percent uncertainty). The results of this work contradict this rule of proportionality, and, to the best of our knowledge, this is the very first report with actual experimental data where the precision and accuracy are compared for standardless EDS microanalysis carried out with a SDD detector.

The percent discrepancy of the Cr and Ni concentrations shows a smooth decreasing relationship with the increase in the S-to-N ratio when V_0 varies (Figure 2), as well as a roughly decreasing relationship with the S-to-N ratio when the beam intensity varies (Figure 3). However, there is a not well-defined relationship between the percent discrepancy of the Cr and Ni concentrations and the S-to-N ratio. Regarding the minor species (Si, Mo, and Mn), an overall decrease in the percent discrepancy takes place as the S-to-N ratio increases, but that relationship is also not well-defined.

The results (Figures 2 to 5) show that, if X-ray spectra are acquired under SEM operating conditions that are very dissimilar to the optimal conditions for microanalysis, which leads to a decreased S-to-N ratio (*i.e.*, when the V_0, beam intensity, or count number are lower, or when the WD is far from 15 mm), both the detectability limit of minor species (Si, Mo, and Mn) and the uncertainty of the concentration of major alloying elements (Cr and Ni) are appreciably impaired. In particular, the morphological analysis of nanometric phases or particles is generally carried out in the SEM with low values of V_0 (around 6-12 kV), beam intensity (around 6-10 a.u), and working distance (around 6-10 mm), conditions which are not well suited for EDS analysis. On the other hand, failure and coarse microstructures analyses are carried out at high values of V_0 (20-30 kV), beam intensity (10-14 a.u.), and working distance (14-20 mm). The results of this study show that the latter are adequate operating conditions for EDS analysis, provided that the WD is limited to around 16 mm.

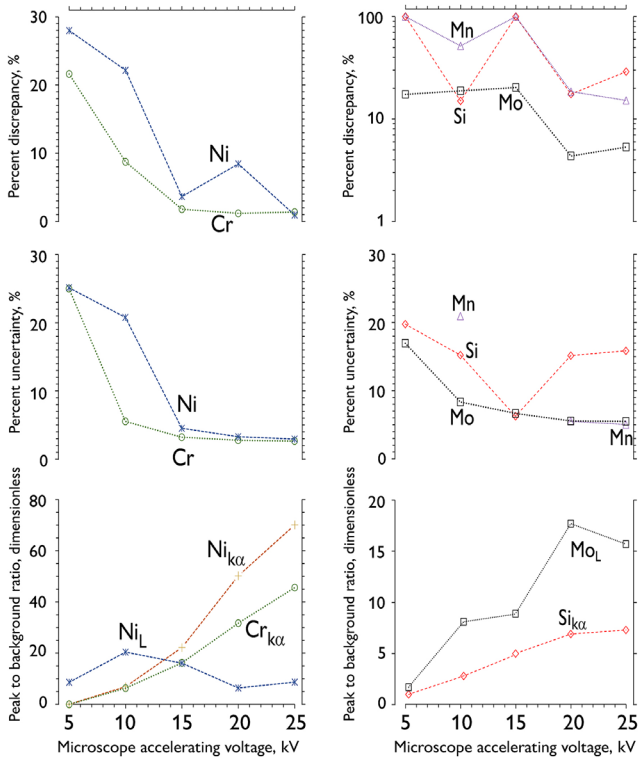

Figure 2. Effects of V_0 variations on the discrepancy and uncertainty of the assessed elemental composition and the S-to-N ratio of spectral peaks. Left: major elements; right: minor elements. Beam intensity: 12 (a.u.); spot size: 150 nm; WD: 15 mm; and live time: 60 s.
Source: Authors

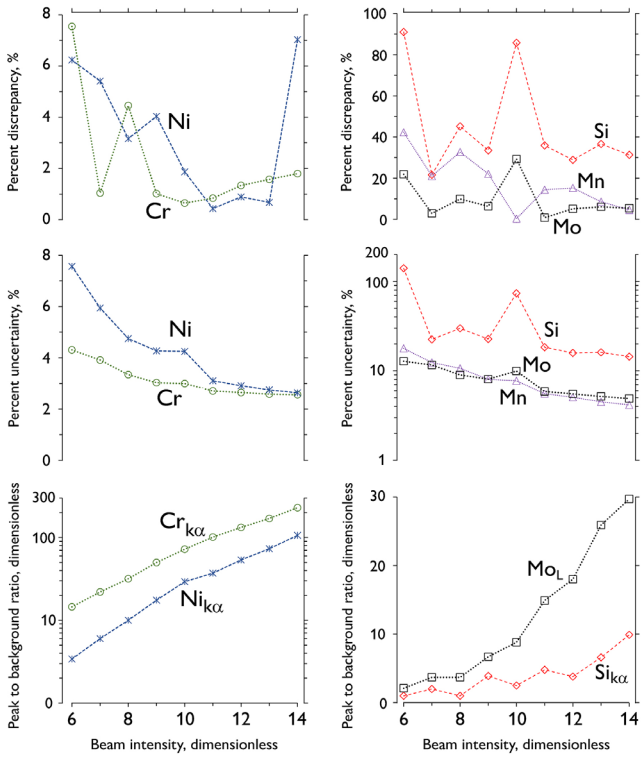

Figure 3. Effects of variations in the electron beam intensity on the discrepancy and uncertainty of the assessed elemental composition and the S-to-N ratio of spectral peaks. Left: major elements; right: minor elements. V_0: 25 kV; WD: 15 mm; and live time: 60 s.
Source: Authors

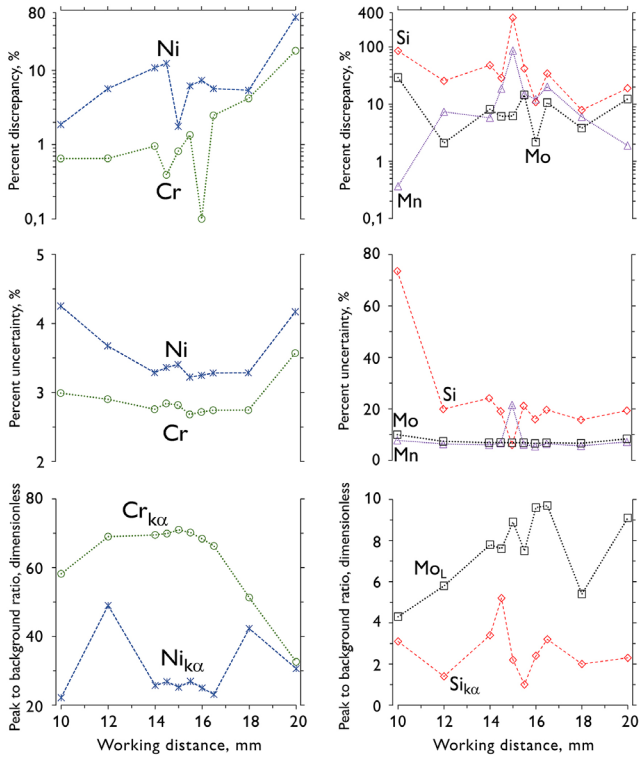

Figure 4. Effects of WD variations on the discrepancy and uncertainty of the assessed elemental composition and the S-to-N ratio of spectral peaks. Left: major elements; right: minor elements. Beam intensity: 12 (a.u.); spot size: 150 nm; V_0: 25 kV; and live time: 60 s.
Source: Authors

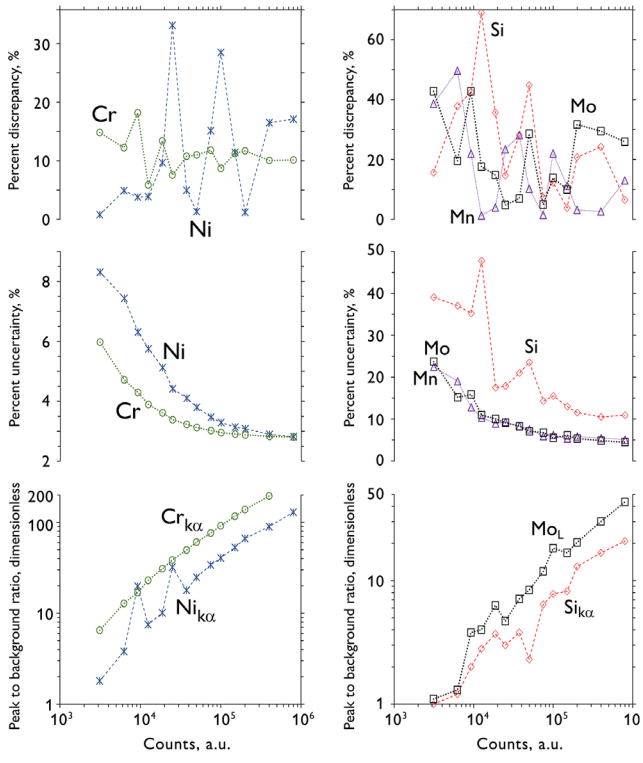

Figure 5. Effects of variations in the count number on the discrepancy and uncertainty of the assessed elemental composition and the S-to-N ratio of spectral peaks. Left: major elements; right: minor elements. Beam intensity: 12 (a.u.); spot size: 150 nm; V_0: 25 kV; WD: 15 mm.
Source: Authors

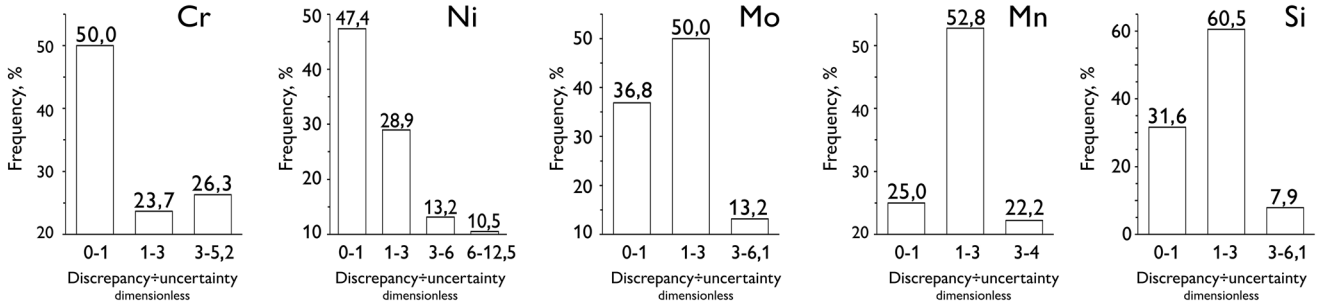

Figure 6. Overview of the ratio between the percent discrepancy and the percent uncertainty
Source: Authors

Figure 6 shows the distribution histograms for the ratio between the percent discrepancy and the percent uncertainty. It can be seen that the analysis of the major alloying elements is more accurate than that of the minor species. For Cr and Ni, around 25% of the data points have percent discrepancies higher than three times the percent uncertainty. Thus, it is concluded that the relationship between the percent discrepancy and the uncertainty does not follow a normal statistic distribution.

Figure 7 shows the effect of variations in the S-to-N ratio on the percent discrepancy, the percent uncertainty, and the ratio between the percent discrepancy and the percent uncertainty. On the one hand, a clear and smooth decrease in uncertainty can be observed as the S-to-N increases. On the other hand, a rough decrease in the discrepancy can be seen when the S-to-N ratio increases from 1 to around 20 (dimensionless). However, when the S-to-N ratio increases from around 20 to 300 (dimensionless), the discrepancy decreases only marginally. For lower S-to-N ratios (*i.e.*, lower than around 20) the percent discrepancy randomly oscillates between zero and three times the uncertainty (which is in accordance with a normal distribution). Nonetheless, for higher S-to-N ratios (*i.e.*, higher than around 20), the percent discrepancy randomly oscillates between zero and six times the uncertainty (which is not in accordance with a normal distribution). When the percent uncertainty is very low (lower than around 3%), it becomes clear that the standard error of the mean EDS concentration does not follow a normal distribution. It is worth highlighting this result, as it does not agree with the common practice in SEM lab facilities, where the error of the elemental concentration is reported as either ±1 or ±3 (said standard deviation is assessed via a Gaussian analysis of the characteristic peaks in the EDS spectra).

Conclusions

The S-to-N ratio could be improved by increasing the acceleration voltage, beam intensity, and total acquisition time, or setting the working distance near 15 mm. This increase in the S-to-N ratio is associated with an increase in the precision of the elemental concentration, but there is no clear increase in accuracy when the S-to-N ratio increases.

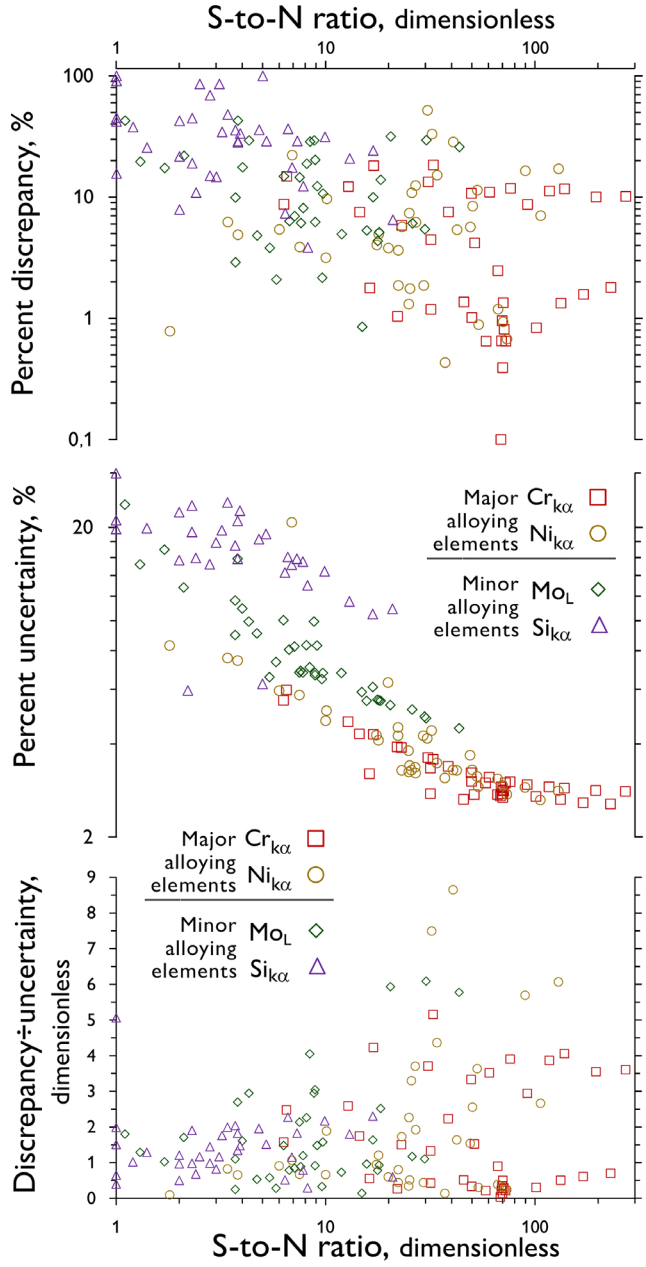

Figure 7. Effects of variations in the S-to-N ratio on the percent discrepancy, the percent uncertainty, and the ratio between discrepancy and uncertainty, putting together all the measurements made in this study
Source: Authors

If X-ray spectra are acquired under operating conditions that are very dissimilar to the interval optimal conditions for EDS microanalysis, which leads to a decreased S-to-N ratio, both the detectability limit of minor species and of the uncertainty in the concentration of major alloying elements are significantly impaired.

When the percent uncertainty is lower than around 3%, the standard error of the mean EDS concentration does not follow a normal distribution concerning the percent uncertainty. It was observed that, for the major alloying elements, 25% of the measurements had a percent discrepancy higher than three times the standard deviation.

References

Burgess S., Li X., and Holland J. (2013). High spatial resolution energy dispersive X-ray spectrometry in the SEM and the detection of light elements including lithium. *Microscopy and Analysis 27*(4) S8-S13. https://analyticalscience.wiley.com/do/10.1002/micro.620/full/id0f755c16020bfdbfe-4de8804e569337.pdf

Carlton, R. (2009). Comparison of SiLi and SDD Detectors for Pharmaceutical Applications. *Microscopy and Microanalysis, 15*(S2), 382-383. https://doi.org/10.1017/S1431927609096731

Çubukçu H. E., Ersoy O, Ayudar E., and Çakir U. (2008). WDS versus silicon drift detector EDS: A case report for the comparison of quantitative chemical analyses of natural silicate minerals. *Micron, 39*(2), 88-94. https://doi.org/10.1016/j.micron.2006.11.004

Franchi G., Angulo J., Moreaud M., and Sorbier I. (2017). Enhanced EDX images by fusion of multimodal SEM images using pansharpening techniques. *Journal of Microscopy, 269*(1), 94-112. https://doi.org/10.1111/jmi.12612

Gernet U. (2008, September 1-5). *Comparing the Si(Li)-detector and the silicon drift detector (SDD) using EDX in SEM* [Conference presentation]. EMC 2008 14th European Microscopy Congress, Aachen, Germany. https://doi.org/10.1007/978-3-540-85156-1_349

Goldstein, J. I., Newbury, D. E., Michael, J. R., Ritchie, N. W. M., Scott, J. H. J., and Joy, D.C. (2018). *Scanning electron microscopy and X-ray microanalysis*. Springer. https://doi.org/10.1007/978-1-4939-6676-9

Liao, Y. (2006). *Practical electron microscopy and database*. https://www.globalsino.com/EM/

Lifshin, E., and Gauvin, R. (2003). Precision and detection limits for EDS analysis in the SEM. *Microscopy Today, 11*(5), 46-49. https://doi.org/10.1017/S1551929500053256

Maniguet, L., Robaut, F., Meuris, A., Roussel-Dherbey, F., and Charlot, F. (2012). X-ray microanalysis: The state of the art of SDD detectors and WDS systems on scanning electron microscopes (SEM). *IOP Conference Series: Materials Science and Engineering, 32*, 012015. https://doi.org/10.1088/1757-899X/32/1/012015

Newbury, D. E., and Ritchie, N. W. M. (2013). Is scanning electron microscopy/energy dispersive X-ray spectrometry (SEM/EDS) quantitative? *Scanning, 35*(3),141-68. https://doi.org/10.1002/sca.21041

Newbury, D. E., and Ritchie, N. W. M. (2015). Performing elemental microanalysis with high accuracy and high precision by scanning electron microscopy/silicon drift detector energy-dispersive X-ray spectrometry (SEM/SDD-EDS). *Journal of Materials Science, 50*, 493-518. https://doi.org/10.1007/s10853-014-8685-2

Newbury, D., and Ritchie, N. W. M. (2019). Electron-excited X-ray microanalysis by energy dispersive spectrometry at 50: Analytical accuracy, precision, trace sensitivity, and quantitative compositional mapping. *Microscopy and Microanalysis, 25*(5), 1075-1105. https://doi.org/10.1017/S143192761901482X

Rackwitz V., Procop M., Bjeoumikhova S., Panneac U., and Hodoroabaa V. (2010). A routine procedure for the characterisation of polycapillary X-ray semi-lenses in parallelising mode with SEM/EDS. *Journal of Analytical Atomic Spectrometry, 26*, 499-504. https://doi.org/10.1039/C0JA00135J

Ritchie, N. W. M., Newbury, D. E., and Davis J. M. (2012). EDS measurements of X-Ray intensity at WDS precision and accuracy using a silicon drift detector. *Microscopy and Microanalysis, 18*(4), 892-904. https://doi.org/10.1017/S1431927612001109

Scholze, F., and Procop, M. (2009). Modelling the response function of energy dispersive X-ray spectrometers with silicon detectors. *X-Ray Spectrometry, 38*(4), 312-321. https://doi.org/10.1002/xrs.1165

Streli, C., Wobrauschek, P., and Schraik, I. (2004) Comparison of SiLi detector and silicon drift detector for the determination of low Z elements in total reflection X-ray fluorescence. *Spectrochimica Acta Part B: Atomic Spectroscopy, 59*(8), 1211-1213. https://doi.org/10.1016/j.sab.2004.01.018

Wassilkowska, A., Czaplicka-Kotas, A., Bielski, A., and Zielina, M. (2014). An analysis of the elemental composition of micro-samples using eds technique. *Technical Transactions, Czasopismo Techniczne, 18*, 133-148. https://www.ejournals.eu/pliki/art/4168/

Research Article/Mechanical Engineering, Mechatronics, and Materials Science http://doi.org/10.15446/ing.investig.92288

Estimating the Electrical Conductivity of Human Tissue in Radiofrequency Hyperthermia Therapy

Estimación de la conductividad eléctrica del tejido humano en la terapia de hipertermia por radiofrecuencia

Jorge I. López-Pérez[1], and Leonardo A. Bermeo Varón[2]

ABSTRACT

The use of mathematical models to study complex systems such as physical and biological phenomena allows understanding their behavior, specifically regarding variables and parameters that are difficult to obtain. Additionally, studying optimization techniques has made it possible to approximate the characteristics of these systems by correlating numerical simulations and experimentation. Radiofrequency hyperthermia therapy for cancer treatment is currently under consideration for future medical applications. However, some of its properties are complex to measure, which could prevent their control. This is the case of electrical conductivity, which depends on the induction frequency and the tissue characteristics. In this paper, radiofrequency hyperthermia therapy was simulated via the finite element method. Then, an estimation of the electrical conductivity involved in the treatment was performed using the particle swarm optimization method. The execution time and the difference between the estimated parameter and the exact value were evaluated and compared with those obtained using the Levenberg-Marquardt method. The results indicate a significant agreement between the estimated and exact values in three different cases. The Levenberg-Marquardt method has a difference of 0,1942% and a performance time of 22 minutes, whereas the particle swarm optimization method has a difference of 0,0967% and a performance time of 327 minutes. The latter performs better in terms of parameter value estimation, whereas the former has better computational times. These techniques may help medical doctors to prescribe treatment protocols and may open the possibility of devising control strategies for hyperthermia therapy as a cancer treatment.

Keywords: electrical conductivity, parameter estimation, hyperthermia, Levenberg-Marquardt, radiofrequency, particle swarm optimization

RESUMEN

El uso de modelos matemáticos para el estudio de sistemas complejos como los fenómenos físicos y biológicos permite comprender su comportamiento, específicamente con respecto a variables y parámetros difíciles de obtener. Adicionalmente, el estudio de técnicas de optimización ha permitido aproximar las características de estos sistemas por medio de la correlación de simulaciones numéricas y la experimentación. La terapia de hipertermia por radiofrecuencia para el tratamiento del cáncer está actualmente en consideración para su futura aplicación médica. Sin embargo, algunas de sus propiedades son difíciles de medir, lo cual impediría su control. Este es el caso de la conductividad eléctrica, que depende de la frecuencia de inducción y de las características del tejido. En este artículo se simuló la terapia de hipertermia por radiofrecuencia mediante el método de elementos finitos. Luego se realizó una estimación de la conductividad eléctrica en el tratamiento mediante el método de optimización por enjambres de partículas. Se evaluaron el tiempo de ejecución y la diferencia del valor estimado con respecto al valor exacto, y se compararon sus valores estimados con los obtenidos mediante el método de Levenberg-Marquardt. Los resultados indican una concordancia significativa entre los valores estimados y los exactos en tres casos diferentes. El método de Levenberg-Marquardt tiene una diferencia de 0,1942% y un tiempo de ejecución de 22 minutos, mientras que el método de optimización de enjambres de partículas tiene una diferencia de 0,0967% y un tiempo de ejecución de 327 minutos. Este último tiene un mejor rendimiento en términos de estimación del valor de los parámetros, mientras que el otro tiene un mejor tiempo de ejecución computacional. Estas técnicas podrían ayudar a los médicos a prescribir protocolos de tratamiento y abrir la posibilidad de diseñar estrategias de control para la terapia de hipertermia como tratamiento para el cáncer.

Palabras clave: conductividad eléctrica, estimación de parámetros, hipertermia, Levenberg-Marquardt, radiofrecuencia, optimización por enjambre de partículas

Received: December 09th, 2020
Accepted: June 03rd, 2022

[1] Bioengineer, Universidad Santiago de Cali, Colombia. Affiliation: Young researcher, Universidad Santiago de Cali, Colombia. E-mail: jorge.lopez06@usc.edu.co

[2] Electronic Engineer and MSc in Electronic Engineering, Universidad del Valle, Colombia. PhD in Mechanical Engineering, Universidade Federal de Rio de Janeiro, Brazil. Affiliation: Full professor, Universidad Santiago de Cali, Colombia. E-mail: leonardo.bermeo00@usc.edu.co

How to cite: López-Pérez, J., and Bermeo, L. (2023). Estimating the Electrical Conductivity of Human Tissue in Radiofrequency Hyperthermia Therapy. *Ingeniería e Investigación, 43*(1), e92288. http://doi.org/10.15446/ing.investig.92288

Introduction

Mathematical modeling techniques are a tool to provide solutions to complex systems in different fields of medicine and physiology (Bratus *et al*., 2017). In these fields, it is possible to obtain a mathematical model of any system using the principles of physics, chemistry, and biology (Selişteanu *et al*., 2015). However, these models represent the approximate physical problem (Akhmedova and Semenkin, 2013), a behavior that suggests the implementation of optimization algorithms that correlate mathematical models and experimental data in order to obtain a better understanding of the system (Rasdi *et al*., 2016).

A considerable number of researchers use optimization algorithms such as the Levenberg-Marquardt (LM) and Particle Swarm Optimization (PSO) methods to obtain information from systems that are difficult to measure (Chen *et al*., 2010; Pereyra *et al*., 2013). An optimization problem consists of minimizing or maximizing an objective function, with the purpose of finding the best available information to solve a problem. In the case of a complex problem with a unique solution, an optimization algorithm might find a local minimum that does not represent the feasible solution. The PSO method avoids these local minimums, allowing to find the global optimum of the objective function (Matajira-Rueda *et al*., 2018; Zhang, 2003).

Classical algorithms extract information sequentially, exploring the solution space in a unique direction (Chuang *et al*., 2012), whereas optimization algorithms can explore the solution space in different directions, increasing the probability of finding a feasible solution (Cornejo and Rebolledo, 2016).

Optimization algorithms do not need to detail the structure or behavior of the system: their function is to make random changes to the probable solutions, using an adjustment function in multiple variables in order to decide which solutions are optimal and computationally efficient. The implementation of optimization algorithms allows estimating the value of a variable in order to understand the behavior of a system's parameters under different conditions.

Radiofrequency (RF) hyperthermia therapy is a treatment for the partial or total elimination of cancer cells. It consists of increasing the tissue temperature between 40 and 45 °C via the induction of radiofrequency waves. This therapy is used as adjuvant therapy in traditional cancer treatments (Colombo *et al*., 2003; Curto, 2010; Horsman and Overgaard, 2007). Several researchers have conducted simulations of RF hyperthermia therapies in order to understand its behavior. These include the use of the finite element method (Gas, 2010; Gas and Miaskowski, 2015; Kurgan and Gas, 2009, 2010, 2011, 2015, 2016; Lv *et al*., 2005; Miaskowski *et al*., 2010; Miaskowski and Krawczyk, 2011; Miaskowski and Sawicki, 2013; Paruch and Turchan, 2018; Sawicki and Miaskowski, 2014; Yang *et al*., 2005), the boundary element method (Majchrzak, Drozdek, *et al*., 2008; Majchrzak, *et al*., 2008; Majchrzak and Paruch, 2009, 2010), and the finite-difference method (Deng and Liu, 2002). Other works have performed state variables and parameter estimation, which correlates numerical simulations and experimental data through algorithms based on Bayesian inference.

In the study by Bermeo *et al*. (2015a), particle filters were used for the temperature field and heat source estimation. Lamien *et al*. (2017) and Bermeo *et al*. (2016a, 2016b) employed simultaneous parameters and state variables estimation while using the Liu and West filter, and Pacheco *et al*. (2020) the used Kalman filter to estimate temperature distribution. These analyses only consider a single frequency for the treatment. In the study by López *et al*. (2020), the estimation of electrical conductivity with three frequencies was performed via the LM method, with acceptable results in terms of accuracy.

Mathematical models in RF hyperthermia involve Maxwell's equations (Maxwell, 1865) and the bioheat transfer equation (Pennes, 1948). The modeling process poses a difficulty in the case of electrical conductivity in Maxwell's equations, as the values are different in intracellular and extracellular fluids, and, when the tissue is exposed to a uniform field, this behavior indicates that human tissue is inhomogeneous at a cellular scale (Ohmine *et al*., 2004; Peters *et al*., 2001). However, electrical conductivity can be assumed as constant in specific frequency ranges of the treatment because the differences are negligible, *i.e.*, for each frequency value, there is a value of electrical conductivity. This assumption allows the evaluation of the model under certain conditions, considering that its environment is homogeneous (Gabriel, *et al*., 1996; Gabriel, Lau, *et al*., 1996; Haueisen *et al*., 1997; Kurup *et al*., 2012; Schepps and Foster, 1980).

Thus, in this work, electrical conductivity is estimated via the PSO algorithm, and the results are compared with the estimation process performed by means of the LM method. The inverse problem was performed via simulated temperature measurements in RF hyperthermia therapy with three different frequencies and powers. The results include the analysis of the sensitivity coefficients of the system and the statistical summary of the estimation process.

Particle Swarm Optimization method (PSO)

PSO is a stochastic method for the continuous optimization of parameters based on population behavior. The algorithm imitates the interactive behavior of the flocks of birds and banks of fish to reach an optimal solution (Kennedy and Eberhart, 1995). The method solves by improving a candidate solution, updating its velocity and position according to its individual experiences, as well as those of its neighbors (Chen *et al*., 2010). The PSO is a widely used tool for continuous optimization problems (Aazim *et al*., 2017; Alfi, 2011; Bermeo *et al*., 2015b; Muñoz *et al*., 2008; J. Tang *et al*., 2021).

In the PSO algorithm, the *i-th* particle is treated as a point within a space of N dimensions, and it is represented by a vector $x_{i,j}$. The best position found by the *i-th* particle is the position that produces the best value of the objective function, represented by $Pbest_{i,j}$, while the best position found by the entire population is represented by $Gbest_{i,j}$. The velocity for the *i-th* particle is represented by $V_{i,j}$. The velocity and position of the particles are calculated via Equations (1) and (2) (Kennedy and Eberhart, 1995):

$$V_{i,j}(k+1) = wV_{i,j}(k) + C_1R_1\left[Pbest_{i,j} - x_{i,j}(k)\right] + C_2R_2\left[Gbest_{i,j} - x_{i,j}(k)\right] \quad (1)$$

$$x_{i,j}(k+1) = x_{i,j}(k) + V_{i,j}(k+1) \quad (2)$$

where C_1 and C_2 are positive constants called the *acceleration coefficients*, and R_1 and R_2 are uniform random values for the interval [0;1] (Lashkari and Moattar, 2016). Equation (1) calculates the new velocity at which the particle moves in the solution area as a function of the current velocity and the position. *w* is the inertia coefficient that influences particle velocity, which affects the exploration capability of each individual towards the best location found by it (local best) and by the swarm in the search space (global best) (Kennedy and Eberhart, 1995). It allows particles to compensate their exploration ranges between particular and global in order to locate the optimal solution within a reasonable number of iterations. Algorithm 1 shows the canonical form of the conventional PSO algorithm, where *S* is the objective function, *Np* is the number of particles population, *Pbest* is the particle position, and *Gbest* is the best position of the particle.

Algorithm 1. Particle swarm optimization algorithm

Initial randomization for particle positions and velocities
WHILE *termination criteria*
FOR *i*=1 **TO** *Np*
Calculate S, of P_{best} *particle*
IF $S_i < S_{i-1}$
$S_{i-1} = S_i$
END IF
Calculate the velocity of the P_{best} *particle with* (1)
Calculate the position of the P_{best} *particle with* (2)
END FOR
Calculate G_{best}
END WHILE

Source: Authors

According to Li *et al*. (2019), the implementation of an adaptive inertia coefficient (*w*) allows the particle population to adjust more precisely and quickly the exploration of the optimal solution, reducing the search times for particular and global values in the conventional implementation of the PSO algorithm. On the other hand, the variation in the acceleration coefficients is used to improve the speed of convergence towards the optimal global solution, thus allowing to reach this solution efficiently. Z. Tang and Zhang (2009) proposed a temporal variation of the acceleration coefficients in order to improve the exploration of the global optimum in the first stage of the optimization process and thus facilitate the convergence of the particles towards it. Equations (3)-(5) describe this proposal.

$$w = w_{\max} - i / i_{\max}\left(w_{\max} - w_{\min}\right) \quad (3)$$

$$C_1 = C_{\min} + \left(C_{\max} - C_{\min}\right) / i_{th} + C_{\max} \quad (4)$$

$$C_2 = C_{\max} + \left(C_{\max} - C_{\min}\right) / i_{th} + C_{\min} \quad (5)$$

The modified algorithm is shown in Algorithm 2.

Algorithm 2. Modified particle swarm optimization algorithm

Initial randomization for particle positions and velocities
WHILE *termination criteria*
Calculate w with (3)
Calculate C_1 *with* (4)
Calculate C_2 *with* (5)
FOR *i*=1 **TO** *Np*
Calculate S of P_{best} *particle*
IF $S_i < S_{i-1}$
$S_{i-1} = S_i$
END IF
Calculate the velocity of the P_{best} *particle with* (1)
Calculate the position of the P_{best} *particle with* (2)
END FOR
Calculate G_{best}
END WHILE

Source: Authors

The Levenberg-Marquardt method (LM)

The LM method is used to iteratively solve nonlinear least-squares and linear problems for parameter estimation in highly complex inverse problems (Huang and Huang, 2007). This method combines the Gauss-Newton and gradient descent methods (Dattner and Gugushvili, 2018; Kanzow *et al*., 2005) controlled by a damping factor (μ). If the damping factor tends to zero, the speed of convergence increases, and, if this factor tends to infinity, its convergence is slow and stepwise (Zhang, 2003). Equations (6) and (7) describe the parameter update and the objective function, respectively (Rouquette *et al*., 2007).

$$P^{k+1} = P^k + \left[\mathbf{J}^T\mathbf{J} + \mu\Omega\right]^{-1}\mathbf{J}^T\left[Y - T_{P^k}\right] \quad (6)$$

$$S_{k+1} = \left[Y - T_{P^{k+1}}\right]^T\left[Y - T_{P^{k+1}}\right] \quad (7)$$

where P^{k+1} is the candidate parameter, J is the sensitivity matrix, Ω is the diagonal of the matrix J^TJ, S_{k+1} is the likelihood function, *Y* is the experimental temperature, and T_{pk} is the numerical temperature. This method for estimating electrical conductivity is described in Algorithm 3.

Algorithm 3. Levenberg–Marquardt method

Initial randomization for the parameter
WHILE *termination criteria*
Calculate S_{k+1} *with (7)*
Calculate P^{k+1} *with (6)*
Calculate
IF $S_k < S_{k+1}$
$\mu = 10 \times \mu$
ELSE
$P^k = P^{k+1}$
$\mu = 0{,}1 \times \mu$
END IF
END WHILE

Source: Authors

Physical problem and mathematical formulation

The physical problem considered in this work involves a cylindrical domain with the physical properties of human muscle. The heating is generated using RF through a copper coil of three spirals with a radius of 8 mm and a cross-section of 70 mm, as presented in Figure 1. The heat in the domain is due to the electrical and magnetic loss of the therapy. The boundary conditions for the material are considered to be convective heat flux in the lower and upper surfaces and adiabatic boundary conditions around the domain. The solution of the direct (forward) problem was obtained using COMSOL Multiphysics® 5.3 and verified against the results presented by Hand *et al*. (1982) and Paruch and Turchan (2018). These processes were performed on a computer with 16 GB RAM and an i7-9750H processor.

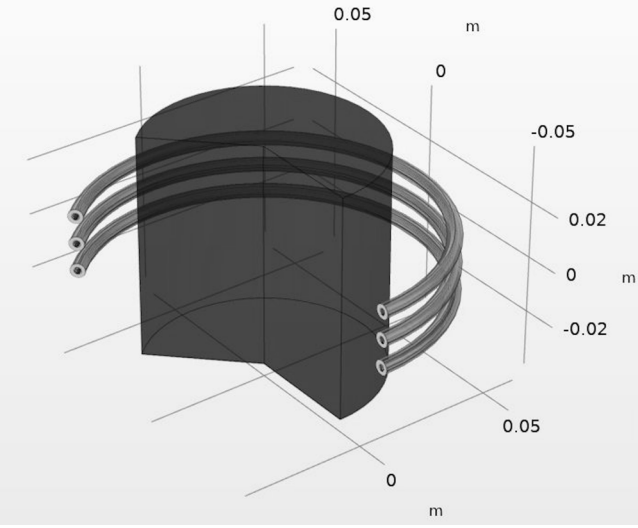

Figure 1. Domain system
Source: Authors

The electromagnetic and thermal models of the domain were obtained via Maxwell's equations (Gratiy *et al*., 2017) and the bioheat transfer equation, respectively (Charny, 1992; Nakayama and Kuwahara, 2008; Pennes, 1948). Maxwell's equations are described in Equations (8)-(11).

$$\nabla \times \mathbf{H} = \mathbf{J} \tag{8}$$

$$\mathbf{B} = \nabla \times \mathbf{A} \tag{9}$$

$$\mathbf{J} = \sigma \mathbf{E} + \frac{\partial \mathbf{D}}{\partial t} \tag{10}$$

$$\mathbf{E} = -\frac{\partial \mathbf{A}}{\partial t} \tag{11}$$

where H is the magnetic field, J is the electric current density, B is the magnetic flux density, A is the magnetic vector potential, E is the electric field, σ is the electrical conductivity, and D is the electric displacement field.

The biological heat transfer is defined by Pennes (1948) as shown in Equation (12). Equation (13) presents the boundary conditions in the domain length L and the directions r, z.

$$\rho c \frac{\partial T}{\partial t} = \nabla \cdot k \nabla T - \omega_b c_b (T - T_a) + Q_m + Q \tag{12}$$

$$\left.\begin{aligned} -k\frac{\partial T}{\partial r} = h(T - T_t) \quad r \geq 0 \quad z = 0 \quad z = L_z \\ T_{(r,z)} = T_0 \qquad\qquad r = L_r \quad z \geq 0 \end{aligned}\right\} \tag{13}$$

where ρ is the density, c_b is the specific heat capacity, k is the thermal conductivity, T_0 is the initial temperature, ω_b is the blood perfusion, Q_m is the metabolic heat source, and Q is the heat source, as determined through Equations (14)-(16).

$$Q = Q_{rh} + Q_{ml} \tag{14}$$

$$Q_{rh} = \frac{1}{2}\mathrm{Re}\left(\mathbf{J} \cdot \mathbf{E}^{'}\right) \tag{15}$$

$$Q_{ml} = \frac{1}{2}\mathrm{Re}\left(i\omega \mathbf{B} \cdot \mathbf{H}^{'}\right) \tag{16}$$

where Q_{rh} is the electrical loss, Q_{ml} is the magnetic loss, and Re is the real part of the losses (Lakhssassi *et al*., 2010).

The heat source inside of the copper coil to avoid overheating is calculated by means of Equation (17).

$$Q_0 = M_t c_{pw} \frac{T_{in} - T}{2\pi r A_c} \tag{17}$$

where M_t is the mass flow, c_{pw} is the heat capacity of water, T_{in} is the initial temperature, r is the inner radius, and A_c is the cross section of the coil.

Results

In the estimation process of the electrical conductivity, the PSO and LM methods were evaluated using different

frequencies and powers (Table 1). The simulated temperature measurements were considered in the inverse problem available at the center of the domain every 30 s. To avoid an inverse crime (Kaipio and Somersalo, 2004), the simulated temperature measurements were produced on a grid of 9 128 elements, while the inverse problem solution was performed on a grid of 3 091 elements. The initial conditions of the hyperthermia model were as follows: the temperature of the environment was $T_i = 24^{\circ}C$, the initial temperature of the cooling pad was $T_{in} = 20^{\circ}C$, the convection coefficient was $h = 10$ W/m^2 K, the temperature in the domain was 24 °C ($r = 0{,}04$; $-0{,}04 < z < 0{,}04$), and the thermal properties of the biological tissue Q_m, c_b, and ω_b were zero because the domain was simulated as a solid material. The parameter values were assumed constant because the effects of temperature variation on the thermal and electrical properties are negligible (Rossmann and Haemmerich, 2014). This assumption is not possible at 10,0 MHz because the temperature increase is too high. Table 1 presents the electrical properties of the phantom with three different frequencies and powers, and Table 2 shows the physical properties of the domain.

Table 1. Electric properties of the phantom (muscle properties)

Nominal frequency [MHz]	0,1	1,0	10,0
Power [W]	1 000	600	300
Electrical conductivity [S/m]	0,362	0,503	0,617
Permittivity	8 090	1 840	1 710

Source: Hasgall *et al*. (2018)

Table 2. Physical properties of the domain

	k[W/(m.K)]	c_p[J/(kg.K]	ρ[kg/m^3]	σ [S/m]	εr	μ_r
Copper	400	385	1 090	5,998x10^7	1	1
Air	0,024	0,240	1,086	0	1	1
Water	0,580	4,230	997	5,500x10^{-6}	1	80
Phantom	0,49*	3 421*	1 090*	**Table 1**		159

Source: Comsol Multiphysics (2012) and Hasgall *et al*. (2018)

Temperature field

Figures 2 to 4 show the simulated temperature measurements and numerical simulation at the center of the domain {0,0; 0,0} at 0,1, 1,0, and 10,0 MHz. These results indicate an increase in the temperature as the frequency increases. For 0,1 MHz, the temperature increase was 0,13 °C; 3,23 °C for 1,0 MHz; and 45 °C for 10,0 MHz. In terms of power, the temperature rises as the power increases.

To establish the appropriate frequency and power to perform RF hyperthermia, it is necessary to consider the thermal dose in the treatment. Experimental studies have revealed that patients are comfortable when the heating rate is 1,0 °C/min, which does not cause considerable pain or severe damage (de Oliveira, 2014). In this study, the mean rate at 0,1 MHz was 0,02 °C/min and 0,64 °C/min at 1,0 MHz. These rates are suitable for performing mild RF hyperthermia therapy. For the case of 10,0 MHz, the rate was 1,8°C/min, which does not allow performing therapy. However, it is possible to modify the power to reach an adequate thermal dose, *e.g.*, a frequency of 10,0 MHz at 100 W in approximately 9 minutes (López and Bermeo, 2021).

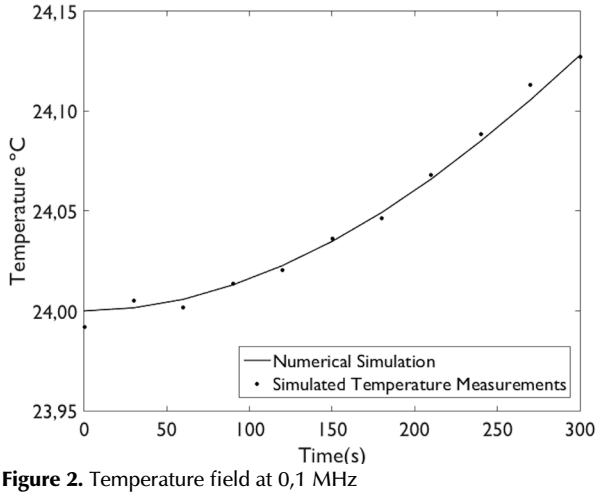

Figure 2. Temperature field at 0,1 MHz
Source: Authors

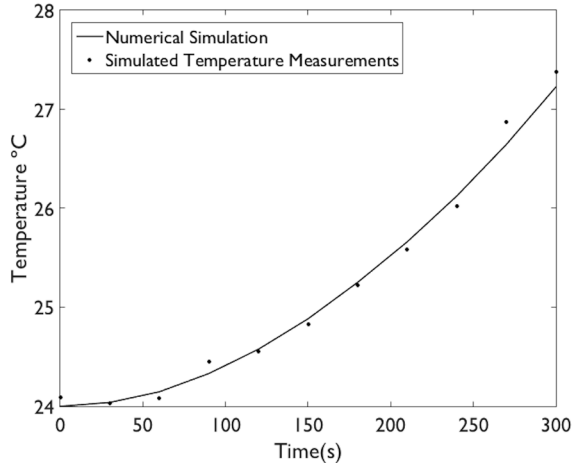

Figure 3. Temperature field at 1,0 MHz
Source: Authors

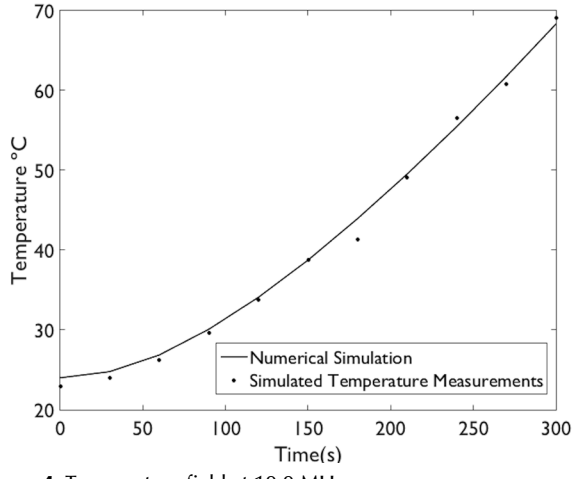

Figure 4. Temperature field at 10,0 MHz
Source: Authors

To establish the appropriate frequency and power to perform RF hyperthermia, it is necessary to consider the thermal dose in the treatment. Experimental studies have revealed that patients are comfortable when the heating rate is 1,0 ˚C/min, which does not cause considerable pain or severe damage (de Oliveira, 2014). In this study, the mean rate at 0,1 MHz was 0,02 ˚C/min and 0,64 ˚C/min at 1,0 MHz. These rates are suitable for performing mild RF hyperthermia therapy. For the case of 10,0 MHz, the rate was 1,8˚C/min, which does not allow performing therapy. However, it is possible to modify the power to reach an adequate thermal dose, *e.g.*, a frequency of 10,0 MHz at 100 W in approximately 9 minutes (López and Bermeo, 2021).

Analyzing the sensitivity coefficients

The sensitivity coefficients were analyzed in order to determine the parameters that influenced the temperature field in terms of dependence and magnitude (Özisik and Orlande, 2018). The coefficients were calculated using the finite-difference approximation method, as presented in Equation (18), which indicates the changes that occur in the temperature due to a low variation in the value of the parameters.

$$J_{ij}=\left[\frac{\partial T_i(P)}{\partial P_j}\right]\cong\frac{T_i(P_1,P_2,...,P_j+\varepsilon P_j,...,P_N)-T_i(P_1,P_2,...,P_j-\varepsilon P_j,...,P_N)}{2\varepsilon P_j} \quad (18)$$

where J is the sensitivity matrix, i is the time instant, j is the number of the parameter, and ε is the perturbation of the parameter, represented at 10% of its nominal value.

Figure 5 shows the behavior of the sensitivity coefficients of k (thermal conductivity), ρ (density), σ (electrical conductivity), μ_r (relative permeability), ε_r (relative permittivity), and c_p (heat capacity). Note that those of μ_r and ε_r have small magnitudes, indicating a low influence on the temperature field, and the remaining parameters exhibit linear dependence and large magnitudes. This behavior reveals that a single parameter can be estimated. As mentioned in this paper, electrical conductivity was estimated despite the limited information on this parameter in the literature.

Results of the estimation using the LM Method

The LM method was implemented with three different frequencies and powers (Table 1). The method was executed 50 times, and a statistical analysis was conducted in order to determine the electrical conductivity. The stopping criterion was likelihood. The study included the Shapiro-Wilk test (Shapiro and Wilk, 1965). Then, the mean, the standard deviation, and a confidence interval of 95% were calculated. Table 3 summarizes the estimation values. Note that the p-value in the Shapiro-Wilk test for the total cases is higher than 0,05, indicating that the results of 50 performances correspond to a normal distribution. In this sense, the estimation of electrical conductivity was represented by the mean, observing that the value was very close to the exact value, which indicates that the method accurately performed the estimation. Concerning the confidence interval, note that the exact and estimated values are within this interval.

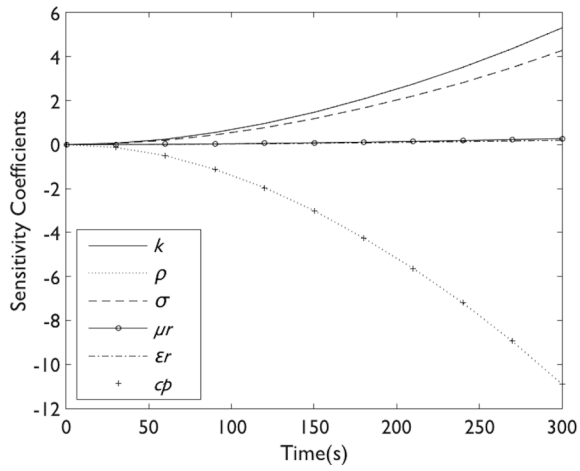

Figure 5. Sensitivity analysis
Source: Authors

Table 3. Results of the estimation of σ via the LM method

Nominal frequency (MHz)	0,1	1,0	10,0
Shapiro-Wilk test (p-value)	0,4643	0,1057	0,2615
Exact σ (S/m)	0,3620	0,5030	0,6170
Mean (S/m)	0,3604	0,5055	0,6175
Standard deviation (S/m)	0,0065	0,0130	0,0013
Confidence interval (S/m)	0,3513-0,3641	0,5009-0,5102	0,6170-0,6210
Computational time (min)	20,0856	22,1876	23,9812

Source: Authors

Results of the estimation using the PSO Method

The PSO method was implemented using the same condition as the LM method. The algorithm was executed 50 times with a population of 50 particles for every computer simulation. The stopping criterion was the maximum number of iterations (50 by default). The study included the Shapiro-Wilk normality test, and the results are presented in Table 4. Note that the results of the 50 performances correspond to a normal distribution. Thus, the mean of a global best was very close to the exact value. The results of estimates are similar to those found by the LM method.

Discussions

Tables 3 and 4 show the statistical analysis for the methods implemented in RF hyperthermia therapy, demonstrating that the results obtained from the estimation are close to the exact value of electrical conductivity, with a difference of

0,1942%. Note that the maximum standard deviation of the total cases was 0,0130 S/m, indicating that the estimation values have good precision. This behavior was verified with the 95% confidence interval, which reveals that, within the range obtained, the exact value of the parameter lies within 95% certainty.

Table 4. Results of the estimation of σ via PSO

Nominal frequency (MHz)	**0,1**	**1,0**	**10,0**
Shapiro Wilk test (p-value)	0,0764	0,2177	0,1432
Exact σ (S/m)	0,3620	0,5030	0,6170
Mean (S/m)	0,3614	0,5033	0,6166
Standard deviation (S/m)	0,0021	0,0009	0,0016
Confidence interval (S/m)	0,3606-0,3621	0,5031-0,5036	0,6160-0,6171
Computational time (min)	315,1985	380,3298	286,1487

Source: Authors

In the case of the LM method, 50 estimations were performed. Note that the mean values were very close to the estimated parameter. The estimated values were as follows: 0,3604, 0,5055, and 0,6175 S/m for 0,1, 1,0, and 10,0 MHz, respectively. These results indicate that the algorithm has a good convergence to the exact value. In terms of the computational time, the mean time of each estimation process was approximately 22 minutes, indicating that it is a fast-convergence algorithm. The PSO method was evaluated on a population of 50 particles and 50 iterations as a stopping criterion. Also, 50 estimation processes were performed, where the solution was obtained from the position of the best particle. The estimated values were 0,3614, 0,5033, and 0,6166 S/m for 0,1, 1,0, and 10,0 MHz, respectively. Note that this algorithm achieved an excellent convergence of the electrical conductivity value, with a difference of 0,0967%. In terms of the computational time, the mean time of each estimation process was approximately 327 minutes, which indicates that it is an acceptable convergence algorithm. This time could be lower if another stopping criterion were considered instead of the number of iterations, (*e.g.*, the mean square error).

These results aim to predict the electrical conductivity in biological tissues using mathematical simulations and optimization algorithms on phantoms, where the final goal is to improve RF hyperthermia in terms of frequency and exposure time values, which may help medical doctors with the planning of individual treatment protocols. This also opens the possibility to design real-time control strategies.

Conclusions

This paper presents the application of two methods for estimating electrical conductivity in RF hyperthermia therapy for cancer treatment. The estimation problem was performed using the LM and PSO methods on a rectangular 2D axisymmetric system with temperature measurements available at one single location inside the domain. The estimation process was executed with three different frequencies and powers. The results were more accurate and smoother with the PSO method, and an excellent agreement with the exact values was obtained. In terms of computational time, the LM method performed better because its stopping criterion depends on the likelihood, whereas, for the PSO method, it is the number of iterations.

Acknowledgements

The authors are thankful for the support provided by DGI of Universidad Santiago de Cali, Colombia, project No. 819-621120-1767 and young researcher grant No. 05-2021.

References

Aazim, R., Liu, C., Haaris, R., and Mansoor, A. (2017). Rapid generation of control parameters of multi-infeed system through online simulation. *Ingeniería e Investigación*, *37*(2), 67-73. https://doi.org/10.15446/ing.investig.v37n2.61822

Akhmedova, S., and Semenkin, E. (2013). Co-operation of biology related algorithms. In IEEE (Eds.), *2013 IEEE Congress on Evolutionary Computation, CEC 2013* (pp. 2207-2214). IEEE. https://doi.org/10.1109/CEC.2013.6557831

Alfi, A. (2011). PSO with adaptive mutation and inertia weight and its application in parameter estimation of dynamic systems. *Acta Automatica Sinica*, *37*(5), 541-549. https://doi.org/10.1016/s1874-1029(11)60205-x

Bermeo, L. A., Caicedo, E., Clementi, L., and Vega, J. (2015). Estimation of the particle size distribution of colloids from multiangle dynamic light scattering measurements with particle swarm optimization. *Ingeniería e Investigación*, *35*(1), 49-54. https://doi.org/10.15446/ing.investig.v35n1.45213

Bermeo, L. A., Orlande, H. R. B., and Eliçabe, G. E. (2015). Estimation of state variables in the hyperthermia therapy of cancer with heating imposed by radiofrequency electromagnetic waves. *International Journal of Thermal Sciencies*, *98*, 228-236. https://doi.org/10.1016/j.ijthermalsci.2015.06.022

Bermeo, L. A., Orlande, H. R. B., and Eliçabe, G. E. (2016a). Combined parameter and state estimation in the radiofrequency hyperthermia treatment of cancer. *Heat Transfer, Part A: Aplicattions*, *70*(6), 581-594. https://doi.org/10.1080/10407782.2016.1193342

Bermeo, L. A., Orlande, H. R. B., and Eliçabe, G. E. (2016b). Combined parameter and state estimation problem in a complex domain: RF hyperthermia treatment using nanoparticles. *Journal of Physics: Conferences Series*, *745*(032014), 1-8. https://doi.org/10.1088/1742-6596/745/3/032014

Bratus, A., Samokhin, I., Yegorov, I., and Yurchenko, D. (2017). Maximization of viability time in a mathematical model of cancer therapy. *Mathematical Biosciences*, *294*, 110-119. https://doi.org/10.1016/j.mbs.2017.10.011

Charny, C. K. (1992). Mathematical models of bioheat transfer. *Advances in Heat Transfer*, *22*(C), 19-155. https://doi.org/10.1016/S0065-2717(08)70344-7

Chen, W. N., Zhang, J., Chung, H. S. H., Zhong, W. L., Wu, W. G., and Shi, Y. H. (2010). A novel set-based particle swarm optimization method for discrete optimization problems. *IEEE Transactions on Evolutionary Computation*, *14*(2), 278-300. https://doi.org/10.1109/TEVC.2009.2030331

Chuang, L. Y., Lin, Y. Da, Chang, H. W., and Yang, C. H. (2012). An improved PSO algorithm for generating protective SNP barcodes in breast cancer. *PLoS ONE*, *7*(5), 0037018. https://doi.org/10.1371/journal.pone.0037018

Colombo, R., da Pozzo, L. F., Salonia, A., Rigatti, P., Leib, Z., Baniel, J., Caldarera, E., and Pavone-Macaluso, M. (2003). Multicentric study comparing intravesical chemotherapy alone and with local microwave hyperthermia for prophylaxis of recurrence of superficial transitional cell carcinoma. *Journal of Clinical Oncology : Official Journal of the American Society of Clinical Oncology*, *21*(23), 4270-4276. https://doi.org/10.1200/JCO.2003.01.089

Comsol Multiphysiscs (2012). *The RF module user's guide*. https://doc.comsol.com/5.3/doc/com.comsol.help.rf/RFModuleUsersGuide.pdf

Cornejo, O., and Rebolledo, R. (2016). Estimación de parámetros en modelos no lineales: algoritmos y aplicaciones. *Revista EIA*, *13*(25), 81-98. https://doi.org/10.14508/reia.2016.13.25.81-98

Curto, S. (2010). *Antenna development for radio frequency hyperthermia applications* [Doctoral thesis, Dublin Institute of Tecnology]. https://doi.org/10.21427/D7CP6S

Dattner, I., and Gugushvili, S. (2018). Application of one-step method to parameter estimation in ODE models. *Statistica Neerlandica*, *72*(2), 126-156. https://doi.org/10.1111/stan.12124

Deng, Z.-S., and Liu, J. (2002). Monte Carlo method to solve multidimensional bioheat transfer problem. *Numerical Heat Transfer, Part B*, *42*, 543-567. https://doi.org/10.1080/10407790190054076

Gabriel, S., Gabriel, C., and Corthout, E. (1996). The dielectric properties of biological tissues: I. Literature survey. *Physics in Medicine and Biology*, *41*(11), 2231-2249. https://doi.org/10.1088/0031-9155/41/11/001

Gabriel, S., Lau, R. W., and Gabriel, C. (1996). The dielectric properties of biological tissues: III. Parametric models for the dielectric spectrum of tissues. *Physics in Medicine and Biology*, *41*(11), 2271-2293. https://doi.org/10.1088/0031-9155/41/11/003

Gas, P. (2010). Temperature inside tumor as time function in RF hyperthermia. *Przeglad Elektrotechniczny*, *86*(12), 42-45.

Gas, P., and Miaskowski, A. (2015, September 17-19). *Specifying the ferrofluid parameters important from the viewpoint of Magnetic Fluid Hyperthermia* [Conference presentation]. 2015 Selected Problems of Electrical Engineering and Electronics (WZEE), Kielce, Poland. https://doi.org/10.1109/WZEE.2015.7394040

Gratiy, S. L., Halnes, G., Denman, D., Hawrylycz, M. J., Koch, C., Einevoll, G. T., and Anastassiou, C. A. (2017). From Maxwell's equations to the theory of current-source density analysis. *European Journal of Neuroscience*, *45*(8), 1013-1023. https://doi.org/10.1111/ejn.13534

Hand, J. W., Ledda, J. L., and Evans, N. T. S. (1982). Considerations of radiofrequency induction heating for localised hyperthermia. *Physics in Medicine and Biology*, *27*(1), 1-16. https://doi.org/10.1088/0031-9155/27/1/001

Hasgall, P. A., di Gennaro, F., Baumgartner, C., Neufeld, E., Lloyd, B., Gosselin, M., Payne, D., Klingenböck, A., and Kuster, N. (2018). *IT'IS Database for thermal and electromagnetic parameters of biological tissues, Version 4.0*. https://doi.org/10.13099/VIP21000-04-0

Haueisen, J., Ramon, C., Eiselt, M., Brauer, H., and Nowak, H. (1997). Influence of tissue resistivities on neuromagnetic fields and electric potentials studied with a finite element model of the head. *IEEE Transactions on Biomedical Engineering*, *44*(8), 727-735. https://doi.org/10.1109/10.605429

Horsman, M. R., and Overgaard, J. (2007). Hyperthermia: A potent enhancer of radiotherapy. *Clinical Oncology*, *19*, 418-426. https://doi.org/10.1016/j.clon.2007.03.015

Huang, C. H., and Huang, C. Y. (2007). An inverse problem in estimating simultaneously the effective thermal conductivity and volumetric heat capacity of biological tissue. *Applied Mathematical Modelling*, *31*(9), 1785-1797. https://doi.org/10.1016/j.apm.2006.06.002

Kaipio, J. P., and Somersalo, E. (2004). *Computational and statistical methods for inverse problems*. Springer.

Kanzow, C., Yamashita, N., and Fukushima, M. (2005). Levenberg-Marquardt methods with strong local convergence properties for solving nonlinear equations with convex constraints. *Journal of Computational and Applied Mathematics*, *173*(2), 321-343. https://doi.org/10.1016/j.cam.2004.03.015

Kennedy, J., and Eberhart, R. (1995). Particle swarm optimization. *Proceedings of ICNN'95 - International Conference on Neural Networks*, *4*(2), 1942-1948. https://doi.org/10.1109/ICNN.1995.488968

Kurgan, E., and Gas, P. (2009). Distribution of the temperature in human body in RF hyperthermia. *Przeglad Elektrotechniczny*, *85*(12), 96-99.

Kurgan, E., and Gas, P. (2010). Estimation of temperature distribution inside tissues in external RF hyperthermia. *Przeglad Elektrotechniczny*, *86*(01), 100-102.

Kurgan, E., and Gas, P. (2011). Treatment of tumors located in the human thigh using RF hyperthermia. *Przeglad Elektrotechniczny*, *87*(12), 103-106.

Kurgan, E., and Gas, P. (2015). Simulation of the electromagnetic field and temperature distribution in human tissue in RF hyperthermia. *Przeglad Elektrotechniczny*, *91*(1), 169-172. https://doi.org/10.15199/48.2015.01.37

Kurgan, E., and Gas, P. (2016, September 14-17). *Analysis of electromagnetic heating in magnetic fluid deep hyperthermia* [Conference presentation]. 7th International Conference Computational Problems of Electrical Engineering (CPEE), Sandomierz, Poland. https://doi.org/10.1109/CPEE.2016.7738756

Kurup, D., Joseph, W., Vermeeren, G., and Martens, L. (2012). In-body path loss model for homogeneous human tissues. *IEEE Transactions on Electromagnetic Compatibility*, *54*(3), 556-564. https://doi.org/10.1109/TEMC.2011.2164803

Lakhssassi, A., Kengne, E., and Semmaoui, H. (2010). Modifed pennes' equation modelling bio-heat transfer in living tissues: analytical and numerical analysis. *Natural Science*, *02*(12), 1375-1385. https://doi.org/10.4236/ns.2010.212168

Lamien, B., Bermeo, L. A., Orlande, H. R. B., and Eliçabe, G. E. (2017). State estimation in bioheat transfer : A comparison of particle filter algorithms. *International Journal of Numerical Methods for Heat & Fluid Flow*, *27*(3), 615-638. https://doi.org/10.1108/HFF-03-2016-0118

Lashkari, M., and Moattar, M. H. (2016, November 11-12). *The improved K-means clustering algorithm using the proposed extended PSO algorithm* [Conference presentation]. 2015 International Congress on Technology, Communication and Knowledge (ICTCK), Mashhad, Iran. https://doi.org/10.1109/ICTCK.2015.7582708

Li, C., Liu, C., Yang, L., He, L., and Wu, T. (2019). Particle swarm optimization for positioning the coil of transcranial magnetic stimulation. *BioMed Research International*, *2019*, 9461018. https://doi.org/10.1155/2019/9461018

López, J. I., and Bermeo, L. A. (2021). Parametric study of thermal damage in the hyperthermia treatment by radiofrequency. *2021 IEEE 2nd International Congress of Biomedical Engineering and Bioengineering* (*CI-IB&BI*), *7*, 1-4. https://doi.org/10.1109/CI-IBBI54220.2021.9626117

López, J. I., Serna, R. D., Bermeo, L. A., and Castillo, J. F. (2020). Estimation of electrical conductivity from radiofrequency hyperthermia therapy for cancer treatment by Levenberg Marquardt method. *Communications in Computer and Information Science*, *1195*, 141-152. https://doi.org/10.1007/978-3-030-42531-9_12

Lv, Y. G., Deng, Z. S., and Liu, J. (2005). 3-D Numerical study on the induced heating effects of embedded micro/nanoparticles on human body subject to external medical electromagnetic field. *IEEE Transactions on Nanobioscience*, *4*(4), 284-294. https://doi.org/10.1109/TNB.2005.859549

Majchrzak, E., Drozdek, J., and Paruch, M. (2008). Heating of tissue by means of the electric field: Numerical model basing on the BEM. *Scientific Research of the Institute of Mathematics and Computer Science*, *7*(1), 99-110.

Majchrzak, E., Dziatkiewicz, G., and Paruch, M. (2008). The modelling of heating a tissue subjected to external electromagnetic field. *Acta of Bioengineering and Biomechanics/ Wroc aw University of Technology*, *10*(2), 29-37.

Majchrzak, E., and Paruch, M. (2009). Numerical modelling of temperature field in the tissue with a tumor subjected to the action of two external electrodes. *Scientific Research of the Institute of Mathematics and Computer Science*, *8*(1), 137-145.

Majchrzak, E., and Paruch, M. (2010). Numerical modelling of tissue heating by means of the electromagnetic field. *Scientific Research of the Institute of Mathematics and Computer Science*, *9*(1), 89-97.

Matajira-Rueda, D., Cruz-Duarte, J., Aviña-Cervantes, J., and Correa-Cely, C. (2018). Global optimization algorithms applied in a parameter estimation strategy. *Revista UIS Ingenierías*, *17*(1), 233-242. https://doi.org/10.18273/revuin.v17n1-2018023

Maxwell, J. C. (1865). A dynamical theory of the electromagnetic field. *Philosophical Transactions of the Royal Society of London*, *155*, 459-512. https://doi.org/10.5479/sil.423156.39088007130693

Miaskowski, A., and Krawczyk, A. (2011). Magnetic fluid hyperthermia for cancer therapy. *Przeglad Elektrotechniczny*, *87*(12), 125-127.

Miaskowski, A., and Sawicki, B. (2013). Magnetic fluid hyperthermia modeling based on phantom measurements and realistic breast model. *IEEE Transactions on Biomedical Engineering*, *60*(7), 1806-1813. https://doi.org/10.1109/TBME.2013.2242071

Miaskowski, A., Sawicki, B., Krawczyk, A., and Yamada, S. (2010). The application of magnetic fluid hyperthermia to breast cancer treatment. *Przeglad Elektrotechniczny*, *86*(12), 99-101.

Muñoz, M. A., López, J. A., and Caicedo, E. F. (2008). Swarm intelligence problem-solving societies (a review). *Ingeniería e Investigación*, *28*(2), 119-130. https://doi.org/10.15446/ing.investig.v28n2.14901

Nakayama, A., and Kuwahara, F. (2008). A general bioheat transfer model based on the theory of porous media. *International Journal of Heat and Mass Transfer*, *51*(11-12), 3190-3199. https://doi.org/10.1016/j.ijheatmasstransfer.2007.05.030

Ohmine, Y., Morimoto, T., Kinouchi, Y., Iritani, T., Takeuchi, M., Haku, M., and Nishitani, H. (2004). Basic study of new diagnostic modality according to noninvasive measurement of the electrical conductivity of tissues. *The Journal of Medical Investigation*, *51*(3,4), 218-225. https://doi.org/10.2152/jmi.51.218

Özisik, M. N., and Orlande, H. R. B. (2018). *Inverse heat transfer: Fundamentals and applications*. Routledge. https://doi.org/10.1201/9780203749784

Pacheco, C. C., Orlande, H. R. B., Colaço, M. J., Dulikravich, G. S., Varon, L. A. B., and Lamien, B. (2020). Real-time temperature estimation with enhanced spatial resolution during MR-guided hyperthermia therapy. *Numerical Heat Transfer, Part A: Applications*, *77*(8), 782-806. https://doi.org/10.1080/10407782.2020.1720409

Paruch, M., and Turchan, Ł. (2018). Mathematical modelling of the destruction degree of cancer under the influence of a RF hyperthermia. *AIP Conference Proceedings*, *1922,* 060003. https://doi.org/10.1063/1.5019064

Pennes, H. H. (1948). Analysis of tissue and arterial blood temperatures. *Journal of Applied Physiology*, *1*(2), 93-122. https://doi.org/10.1152/jappl.1948.1.2.93

Pereyra, S., Lombera, G. A., Frontini, G., and Urquiza, S. A. (2013). Sensitivity analysis and parameter estimation of heat transfer and material flow models in friction stir welding. *Materials Research*, *17*(2), 397-404. https://doi.org/10.1590/s1516-14392013005000184

Peters, M. J., Stinstra, J. G., and Hendriks, M. (2001). Estimation of the electrical conductivity of human tissue. *Electromagnetics*, *21*(7-8), 545-557. https://doi.org/10.1080/027263401752246199

Rasdi, L. M., Fanany, M. I., and Arymurthy, A. M. (2016). Metaheuristic algorithms for convolution neural network. *Computational Intelligence and Neuroscience*, *2016*, 1537325. https://doi.org/10.1155/2016/1537325

Rossmann, C., and Haemmerich, D. (2014). Review of temperature dependence of thermal properties, dielectric properties, and perfusion of biological tissues at hyperthermic and ablation temperatures. *Critical Reviews in Biomedical Engineering*, *42*(6), 467-492. https://doi.org/10.1615/critrevbiomedeng.2015012486

Rouquette, S., Guo, J., and Le Masson, P. (2007). Estimation of the parameters of a Gaussian heat source by the Levenberg–Marquardt method: Application to the electron beam welding. *International Journal of Thermal Sciences*, *46*(2), 128-138. https://doi.org/10.1016/j.ijthermalsci.2006.04.015

Sawicki, B., and Miaskowski, A. (2014). Nonlinear higher-order transient solver for magnetic fluid hyperthermia. *Journal of Computational and Applied Mathematics*, *270*, 143-151. https://doi.org/10.1016/j.cam.2014.02.008

Schepps, J. L., and Foster, K. R. (1980). The UHF and microwave dielectric properties of normal and tumour tissues: Variation in dielectric properties with tissue water content. *Physics in Medicine and Biology*, *25*(6), 1149-1159. https://doi.org/10.1088/0031-9155/25/6/012

Selişteanu, D., Endrescu, D., Georgeanu, V., and Roman, M. (2015). Mammalian cell culture process for monoclonal antibody production: Nonlinear modelling and parameter estimation. *BioMed Research International*, *2015*, 598721. https://doi.org/10.1155/2015/598721

Shapiro, S. S., & Wilk, M. B. (1965). An Analysis of Variance Test for Normality (Complete Samples). *Biometrika*, *52*(3/4), 591. https://doi.org/10.2307/2333709

Tang, J., Liu, G., and Pan, Q. (2021). A review on representative swarm intelligence algorithms for solving optimization problems: Applications and trends. *IEEE/CAA Journal of Automatica Sinica*, *8*(10), 1627-1643. https://doi.org/10.1109/JAS.2021.1004129

Tang, Z., and Zhang, D. (2009). A modified particle swarm optimization with an adaptive acceleration coefficients. *Proceedings - 2009 Asia-Pacific Conference on Information Processing, APCIP 2009*, *2*, 330-332. https://doi.org/10.1109/APCIP.2009.217

Yang, X., Du, J., and Liu, Y. (2005). Advances in hyperthermia technology. *Proceedings of the 2005 IEEE Engineering in Medicine and Biology 27th Annual Conference*, *7*, 6766-6769. https://doi.org/10.1109/IEMBS.2005.1616058

Zhang, J.-L. (2003). On the convergence properties of the Levenberg–Marquardt method. *Optimization*, *52*(6), 739-756. https://doi.org/10.1080/0233193031000163993

Instructions for Authors

The Editorial Committee reserves the copyright to printing any material and its total or partial reproduction, as well as the right to accept submitted material or reject it. It also reserves the right to make any editorial modification which it thinks fit. In such event, the author of the submitted material will receive the evaluators' recommendations in writing. If an author accepts them, the revised (or rewritten) article must be submitted with the suggested changes having been made by the date on the date set by the journal in order to guarantee its publication in the scheduled issue.

The process to be followed for publishing an article in the journal

The article must be uploaded into the journal's OJS website (see the guidelines for article submission in the Authors guide section in our website http://www.revistas.unal.edu.co/index.php/ingeinv/article/view/59291/56815). Any manuscript must be submitted using journal's template (with a maximum length of six pages) and must be accompanied by the license agreement, addressed to the journal's editor, Prof. Andrés Pavas, stating that all authors involved in the work in question agree to its submission for consideration in the *Ingeniería e Investigación*.

Article and License templates are available on:

http://www.revistas.unal.edu.co/index.php/ingeinv/index

Once an article has been received by the journal, the corresponding author will be notified via Email and the peerreview process will begin. Following this evaluation, authors will then be informed whether their article has been accepted or not. If accepted, authors must deal with the respective corrections recommended by the evaluators and the Editorial Committee's final decision –if the article is to be published.

Content

All articles considered by the committee for possible publication in the *Ingeniería e Investigación* must consist of the following parts:

- Title, abstract and keywords must be written in Spanish and English. The title must clearly explain the contents of the article in question, it must be written in normal title form, and it must be preferably brief. The abstract should contain around 200 words in Spanish and English, in addition to the methods and materials used, results obtained, and conclusions drawn.
- An introduction must be given. It must describe the article's general purpose, including its main objective, referring to any previous work and the scope of the current article.
- Conclusions must be drawn. This section must provide the implications of the results found and their relationship to the proposed objective.
- Bibliographical references must be given (an explanation and example of how to set them out is given later on).
- Acknowledgements (optional). These should be brief and mention any essential support received for carrying out the work being reported.
- Appendix (optional).

Scientific and technological research articles must also include:

- Experimental development. This must be written giving sufficient details for the subject to be fully understood by readers, including the descriptions of any procedures involved.
- Results. These must give a clear explanation and interpretation of the findings. If necessary, a brief, focused discussion may be provided with regard to the way in which results can be interpreted.

It is required that the bibliographical references for all articles be included at the end of the article, given in alphabetical order of first authors' surnames, and mentioned in the text, and since May 2014, authors are required use the American Psychological Association (APA) style for citation and references:

- Articles published in journals:

Author, A. A., Author, B. B., and Author, C. C. (year). Article title. *Journal Title, volume number* (issue number), page numbers.

Del Sasso, L. A., Bey, L. G., and Renzel, D. (1958). Low-scale flight ballistic measurements for guided missiles. *Journal of the Aeronautical Sciences, 15*(10), 605-608.

Author, A. A., and Author, B. B. (year). Article title. *Journal Title, volume number* (issue number), page numbers. http://www.xxxxxxxxxxxxxxxx

Gaona, P. A. (2014). Information visualization: A proposal to improve search and access digital resources in repositories. *Ingeniería e Investigación*, *34*(1), 83-89. http://www.revistas.unal.edu.co/index.php/ingeinv/article/ view/39449

- Books:

Author, A. A., and Author, B. B. (year). Title of work. Publisher.

Turner, M. J., Martin, H. C., and Leible, R. C. (1964). Further development and applications of the stiffness method, Matrix Methods of Structural Analysis. Macmillan Co.

- Conference papers and symposium contributions:

Author, A. A., and Author, A. A. (year). *Title* [Conference presentation]. Name of conference, City, State, Country. http://xxxxxxxxxxxxxxx

- Theses or undergraduate projects:

Author, A. A., and Author, A. A. (year). *Title* [Type of thesis, University]. http://xxxxxxxxxxxxxxx

Further information can be obtained by:

Contacting the Editorial Team (Email: revii_bog@unal.edu.co) or Prof. Andrés Pavas (Editor-in-Chief. Email: fapavasm@unal.edu.co)

The office of the journal *Ingeniería e Investigación* is located at: Ciudad Universitaria, Facultad de Ingeniería, Edificio CADE. Telefax: (57-1) 3165000 Ext. 13674. Bogotá - Colombia.